Mission-Oriented Seismic Research Program

Annual Report

2010

M-OSRP

University of Houston

Sponsors and Advisory Board representatives

Corporate Sponsors

Amerada Hess ..... Scott Morton, Jacques Leveille
Anadarko ..... Roger Reagan
BP ..... Uwe Albertin
BHP ..... Michael Richardson
ChevronTexaco ..... Debbie Bones
ConocoPhillips ..... Douglas Foster, Robert Stolt
Devon Energy ..... Kenneth Beeney
Encana ..... William Goodway, David Mackidd
ENI-Agip ..... Michele Buia
ExxonMobil ..... Peter Traynin
GX Technology ..... Nick Bernitsas, Robert Bloor
IBM ..... Tom McClure
Landmark ..... Dave Diller
Petrochina Company Limited ..... Jixiang Xu
Petrobras ..... Neiva Zago
PGS ..... Martin Widmaier, Steve Kelly
Repsol ..... Gladys Gonzalez, Francisco Ortigosa
Saudi Aramco ..... Yi Luo
Shell ..... Jonathan Sheiman
Statoil ..... Lasse Amundsen
Total ..... Wafik Beydoun
WesternGeco ..... William Dragoset

Federal Support

DOE Basic Sciences award DE-FG02-05ER15697 ..... Nick Woodward
NSF-CMG award DMS-0327778 ..... Henry A. Warchall

M-OSRP Personnel

Faculty

Lasse Amundsen (Statoil) ..... Adjunct Professor (Physics)
Douglas J. Foster[1] (ConocoPhillips) ..... Adjunct Professor (Physics)
Kristopher A. Innanen (Associate Professor, University of Calgary) .. Adjunct Professor (Physics)
Robert G. Keys (ConocoPhillips) ..... Adjunct Professor (Physics)
Jacques Leveille (Amerada Hess) ..... Adjunct Professor (Physics)
Fang Liu ..... Research Assistant Professor (Physics)
Ken H. Matson (Shell) ..... Adjunct Associate Professor (Physics)
Bogdan Nita (Assistant Professor, Montclair State U.) ..... Adjunct Assistant Professor (Physics)
Partha Routh ..... Adjunct Professor (Physics)
Jon Sheiman (Shell) ..... Adjunct Professor (Physics)
Robert H. Stolt (ConocoPhillips) ..... Adjunct Professor (Physics)
T. Hing Tan (Shell) ..... Adjunct Professor (Physics)
Paolo Terenghi ..... PostDoc Fellow (Physics)
Arthur B. Weglein ..... Cullen Professor (Physics)
Daniel Whitmore (PGS) ..... Adjunct Professor (Physics)

[1] Chair, M-OSRP Advisory Board

Graduate Students

Andre Ferreira[2] ..... Geosciences
Chao Ma ..... Physics
Di Chang ..... Physics
Hong Liang ..... Physics
Jim Mayhan ..... Physics
Jinlong Yang ..... Physics
Lin Tang ..... Physics
Mozhdeh Niazmand ..... Physics
Shih-Ying Hsu ..... Physics
Xu Li ..... Physics
Zhiqiang Wang ..... Physics

Recent Alumni

Adriana Citlali Ramirez ..... Physics
Fang Liu ..... Physics
Francisco Miranda ..... Physics
Haiyan Zhang ..... Physics
Jingfeng Zhang ..... Physics
Jose Eduardo Lira[2] ..... Geosciences
Simon A. Shaw ..... Geosciences
Zhiqiang Guo ..... Geosciences

Administrative Support

Jennifer Chin-Davis ..... Business Administrator
Nguyen Tran ..... Program Accountant
Angela Cowan ..... Program Coordinator
Andrew Fortney, Marco Moncada ..... Computer/IT Support
Jesse Weglein ..... Webmaster/TLC^2
Adam Blount ..... TLC^2

[2] Petrobras, Brazil

Table of Contents

2010 M-OSRP Annual Report Introduction and Summary

This Annual Report describes the progress, status, and plans of the Mission-Oriented Seismic Research Program for the Fall 2010-Spring 2011 academic year. The Introduction provides a perspective and program overview that includes: (1) code release to sponsors and (2) technical highlights from the projects within the program, which are detailed in individual reports within the Report.

This year was another good, productive year for M-OSRP with significant contributions and progress to report. Among contributions/advances are :

1. Preprocessing: delivery of proprietary M-OSRP software for 3D wave theoretic preprocessing for source and receiver deghosting;

2. On-shore internal multiples: the historic first onshore tests, analysis, and evaluation of ISS internal multiple effectiveness, both in absolute terms and in comparison with other methods, continued and was reported;

3. On-shore near-surface complexity: good progress to report on testing and evaluating the sensitivity of the ISS internal multiple attenuation algorithm to ill-defined near-surface complexity;

4. First field data tests, ISS direct depth imaging: progress on the theory and practical fronts on the inverse scattering series imaging methods continued, and the ISS imaging algorithm had its first field data test, with early encouraging results. The entire M-OSRP group was involved in this first ISS first field data imaging test;

5. Including exclusively laterally varying subsurface imaging challenges in the depth imaging: an extension of the previous inverse scattering depth imaging method was extended to accommodate imaging challenges that only arise with a laterally variable earth, and have no function in a laterally invariant earth. Encouraging results on synthetic data showed added-value in comparison with previous ISS imaging capability;

6. Consequences of the difference between the appropriate model of a seismic data set and a model type match-mismatch in processing: this project addressed the issue of how far below the water bottom can a two-parameter ISS acoustic model provide value in an elastic earth;

7. New projects/New students: projects were launched that began to examine: (a) the inclusion of a source signature radiation pattern in ISS methods, beginning with free-surface multiple removal; (b) the inadvertent effect of the concept of 'event' on various wave theory processing methods, including ISS algorithms; (c) bringing the removal of density-only reflections to a laterally variable earth, to allow ISS depth imaging; (d) ocean bottom seismics for soft sea floor acquisition and processing, and when can P data alone be useful and adequate; (e) why internal multiples do not contribute to ISS direct depth imaging; and (f) onshore acquisition and vertical component measurements, acoustic versus elastic Green's theorem for land wavelet estimation.

The details of these projects and initiatives are provided in the individual reports (please refer to the Annual Report Table of Contents) and also within presentations at the Annual Meeting. A video of the Annual Meeting and the presentation slides will be on the sponsor-only section of the M-OSRP website.

The Annual Report will be distributed to sponsor attendees at the Annual Meeting in the form of a USB pen drive, and will be sent to sponsors unable to attend, and will also be available on the sponsor-only section of the M-OSRP web-site. The papers and authors that contributed to the above projects, and initiatives, can be readily located from the Table of Contents of the Annual Report.

Publications/Books/Abstracts submitted this past year:

Two invited papers for an upcoming special edition of SEG's The Leading Edge on multiple suppression: (1) "Elimination of land internal multiples based on Inverse Scattering Series" by Yi Luo, Panos G. Kelamis, Qiang Fu, ShouDong Huo, Ghada Sindi, Shih-Ying Hsu, and Arthur B. Weglein; and (2) "Multiple attenuation: Recent advances and the road ahead (2011)" by Arthur B. Weglein, Shih-Ying Hsu, Paolo Terenghi, Xu Li and Robert H. Stolt.

A new and for the first time consistent Green's theorem method for reverse-time migration (RTM) that addresses shortcomings in the theory and application of current RTM methods. Those papers provide a Green's function that simultaneous allows two-way propagation and has no contribution from the lower boundary. The latter property avoids issues and imaging artifacts from, for example, absorbing boundary conditions or perfectly matched layer (PML), A.B. Weglein, R.H. Stolt and J.D. Mayhan, "Reverse-time migration and Green's theorem: Part I - The evolution of concepts, and setting the stage for the new RTM method", Journal of Seismic Exploration 20: 73-90; A.B. Weglein, R.H. Stolt and J.D. Mayhan, "Reverse-time migration and Green's theorem: Part II - A new and consisten theory that progresses and corrects current RTM concepts and methods", Journal of Seismic Exploration 20: 135-159.

The first of a two-volume set on "Seismic Imaging and Inversion" by R. H. Stolt and A. B. Weglein is soon to appear, published by Cambridge University Press.

Three SEG Abstracts were submitted in 2011: (1) "Green's theorem derived methods for preprocessing seismic data when the presure P and its normal derivative are measured" by J. D. Mayhan, P. Terenghi, A. B. Weglein, and Nizar Chemingui; (2) "The inverse scattering series approach to removing internal multiples: Delineating and defining its current stand-alone capability, and proposing a plan for additional added value for land application" by A. B. Weglein, P. Terenghi, S.-Y. Hsu, Y. Luo, and P.G. Kelamis; and (3) "Inverse scattering depth imaging: First field data examples" by Fang Liu, X. Li, A. B. Weglein, P. Terenghi, Ed Kragh, Hong Liang, James D. Mayhan, Lin Tang, S.-Y. Hsu, Zhiqiang Wang, Joachim Mispel, and Lasse Amundsen.

Welcome

Please join me in extending a very warm welcome to Repsol and Total as new sponsors of M-OSRP, and Gladys Gonzalez, Francisco Ortigosa, and Wafik Beydoun as the newest members of the M-OSRP Advisory Board. We are also happy to announce that Dr. Wilberth Herrera (from Steven Weinberg's group at UT Austin) and Dr. Lujian Peng (from the Department of Material Science and Engineering, University of Tennessee), have joined our research group as research scientists. We very much look forward to working together with Lujian and Wilberth.

Summary

It has been a very good and productive year. Among the highlights mentioned above is the first field data test of inverse scattering series imaging, that demonstrated the method's viability. In addition to reviewing the progress of the past year, at the Annual Meeting, June 1-3, 2011, at the Barton Creek Hotel in Austin, Texas, we will also describe our strategy to move from demonstrating viability to providing relevant added-value within the seismic imaging tool-box. The development, testing and delivery of new capability in response to pressing seismic exploration challenges has had another good year and the campaign continues. On behalf of the students, staff and faculty of M-OSRP, I want to thank you for your encouragement and your constant and strong support.

Sincere best regards, Art

Arthur B. Weglein

Green's theorem derived method for deghosting seismic data when the pressure P and its normal derivative are measured along the cable

James D. Mayhan, Paolo Terenghi, Arthur B. Weglein, and Nizar Chemingui

Abstract

We discuss deghosting of marine seismic data using Green's theorem. Deghosting is put into context in the complete M-OSRP processing chain, Green's theorem derived theory is presented, and an algorithm implementing the theory is discussed. The algorithm has been tested on field data and several kinds of synthetic data with positive and encouraging results. This algorithm is the first of a set of deliverables based on Green's theorem in 3D. Release 1 (deghosting) has been delivered to the sponsors (via the sponsors only section at mosrp.uh.edu).

1 Introduction

Green's theorem offers a flexible framework for defining a number of useful algorithms — ghost removal, wavefield separation (into reference P_0 and scattered P_s), wavelet estimation, and two way wavefield continuation (RTM) — because it allows the freedom of choosing a convenient reference medium (Weglein and Secrest (1990), Zhang and Weglein (2005), Zhang and Weglein (2006), Zhang (2007), Ramírez and Weglein (2009)). Green's theorem methods are exact (fully consistent with the wave equation), multidimensional, make no assumptions about the earth, and work in the $(\omega, \mathbf{r})$ data space (and hence are simple to extend to irregularly spaced data). Therefore, Green's theorem preprocessing methods and inverse scattering series (ISS) isolated task subseries are fully consistent.

Deghosting is important because (1) it is a prerequisite for many processing algorithms including data driven multiple elimination (ISS free surface multiples and internal multiples and conventional surface related multiple elimination (SRME)) and imaging (wavefield continuation often assumes one way waves), and (2) removing the downward component of the field enhances seismic resolution and boosts the low frequencies. Hence, deghosting has benefit for traditional seismic processing and also provides an important role in all ISS based isolated task processing. This report is focused on deghosting.

Deghosting is a prerequisite for the ISS. The ISS can perform certain tasks (e.g., free surface multiple elimination) without a priori estimates of the spatial distribution of velocity. The Mission-Oriented Seismic Research Program (M-OSRP) has generated algorithms to accomplish seismic data processing goals based on the ISS (free surface multiple elimination, internal multiple removal, depth imaging, nonlinear direct amplitude variation with offset (AVO), and Q compensation) and Green's theorem (deghosting, source signature estimation, and data reconstruction). While the ISS is independent of subsurface velocity (and in fact of all subsurface properties), it is data dependent and makes certain assumptions about its input data. Weglein et al. (2003) describe how every ISS isolated task subseries requires (1) the removal of the reference wavefield, (2) an estimate of the source signature and radiation pattern, and (3) source and receiver deghosting and how the ISS has a nonlinear cascaded dependence on these preprocessing steps. Therefore, the Green's theorem

deghosting methods are critically important to the success of the inverse series methods since they may be used to bring seismic data in line with the assumptions of inverse scattering. The fact that the ISS is nonlinear places a higher bar on preprocessing. An error in the input to a linear process creates a linear error in its output, but the same error in ISS input creates linear, quadratic, cubic, and higher order errors in its output.

1.1 Terminology

A brief aside on terminology. (1) The total wavefield P consists of the reference wavefield P_0 (which doesn't experience the earth) and the scattered wavefield P_s (which does experience the earth). (2) Ghosts begin their propagation moving upward from the source (source ghosts) or end their propagation moving downward to the receiver (receiver ghosts) or both (source/receiver ghosts) and have at least one upward reflection from the earth. (3) Free surface multiples have at least one downward reflection from the free surface (air-water interface) and at least one upward reflection from the earth. (4) Internal multiples have no downward reflections from the free surface, more than one upward reflection from the earth, and at least one downward reflection from inside the earth. An nth order internal multiple has n downward reflections from inside the earth. (5) Primaries have only one upward reflection from the earth.

2 Deghosting tutorial

The ISS is based on perturbation theory, and Green's theorem derived preprocessing utilizes perturbation theory. A reference medium (and its associated Green's function) is chosen to facilitate solving the problem at hand, and the perturbation is the real world properties minus the reference medium. Within that framework, Green's theorem based preprocessing is remarkably wide ranging. For example, Figure 1 shows the configuration chosen for Green's theorem deghosting. Choosing a reference medium consisting of a whole space of water, a hemispherical surface of integration bounded below by the measurement surface, and the prediction/observation point inside the surface of integration gives deghosted data $P^{\text{deghosted}}$. A different choice of a reference medium (a half space of air and a half space of water) and the prediction/observation point outside/inside the surface of integration gives wavefield separation in which the total wavefield P is separated into the reference wavefield P_0 and scattered wavefield P_s. It should be noted that several processing algorithms for multiple elimination (including the ISS) assume deghosting has been performed on the data and that an accurate estimate of the source wavelet is available. (The latter can be computed using P_0.)

Deghosting (both receiver and source side) is based on Zhang and Weglein (2005), Zhang and Weglein (2006), and Zhang (2007). The theory assumes measurement of the pressure wavefield P and its normal derivative $\partial P/\partial n \equiv \nabla' P(\mathbf{r}', \mathbf{r}_s, \omega) \cdot \hat{n}$ where $\mathbf{r}'$ is the measurement point, $\mathbf{r}_s$ is the source location, and $\hat{n}$ is the normal to the measurement surface. The reference medium is chosen as a whole space of water (where a causal, analytic solution exists for the acoustic wave equation). In 3D the whole space Green's function is

$$G_0^d(\mathbf{r}, \mathbf{r}', \omega) = -\frac{1}{4\pi} \frac{\exp(ikR_+)}{R_+}$$

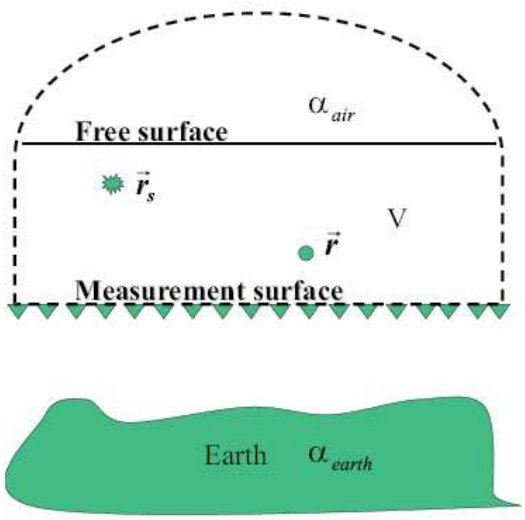

Figure 1: *Configuration for deghosting using Green's theorem (Zhang, 2007). α_{air} and α_{earth} are perturbations, the differences between the actual medium (air, water, earth) and reference medium (water). The closed surface S of integration is the measurement surface plus dashed line.*

where $k = \omega/c_0$, c_0 is the wave speed in the reference medium, and $R_+ = |\mathbf{r} - \mathbf{r}'|$. In 2D

$$G_0^d(\mathbf{r}, \mathbf{r}', \omega) = -\frac{i}{4} H_0^{(1)}(kR_+)$$

where $H_0^{(1)}$ is the zeroth order Hankel function of the first kind (Morse and Feshbach, 1953, pp. 810-811). The observation/prediction point is between the free surface and the measurement surface, i.e., inside the volume V bounded by the closed surface of integration consisting of the measurement surface and dashed line in Figure 1.

Using the above configuration and Green's theorem gives the key equation (Zhang, 2007, equation 2.23),

$$P^{\text{deghosted}}(\mathbf{r}, \mathbf{r}_s, \omega) = \oint_S dS\, \hat{n} \cdot [P(\mathbf{r}', \mathbf{r}_s, \omega)\nabla' G_0^d(\mathbf{r}, \mathbf{r}', \omega) - G_0^d(\mathbf{r}, \mathbf{r}', \omega)\nabla' P(\mathbf{r}', \mathbf{r}_s, \omega)], \qquad (1)$$

where $\mathbf{r}$ is the prediction point, $\mathbf{r}_s$ is the location of the air gun array, S is the closed surface consisting of the measurement surface and dashed line in Figure 1, $\hat{n}$ is the normal to S (pointing away from the enclosed volume V), $\mathbf{r}'$ is the measurement point, and G_0^d is a whole space Green's function. Extending the radius of the hemisphere to infinity, invoking the Sommerfeld radiation condition, and assuming a horizontal measurement surface, the integral over the closed surface becomes an integral over the measurement surface (Zhang, 2007, equation 2.24),

$$P^{\text{deghosted}}(\mathbf{r}, \mathbf{r}_s, \omega) = \int_{m.s.} dS\, [P(\mathbf{r}', \mathbf{r}_s, \omega)\frac{\partial}{\partial z'} G_0^d(\mathbf{r}, \mathbf{r}', \omega) - G_0^d(\mathbf{r}, \mathbf{r}', \omega)\frac{\partial}{\partial z'} P(\mathbf{r}', \mathbf{r}_s, \omega)]. \qquad (2)$$

The algorithm as given in equation 2 lends itself to application in a marine single shot experiment.

3 The code

The implementation of the above theory is done in a straightforward manner. The Green's theorem algorithm computes the surface integral in equation 2. The method requires two wavefields as input, the pressure measurements P and their normal derivatives $\partial P/\partial z'$. The latter require dual sensor cables or dual streamer cables. Source side deghosting is straightforward and amounts to applying reciprocity to exchange sources and receivers. Our examples will focus on receiver side deghosting.

This code is the first of a set of deliverables based on Green's theorem in 3D. The new programs use data in the Seismic Unix (SU) format and integrate with all native SU programs. Release 1 consists of the following components: (1) Code (sujim.c) which calculates the surface integral in equation 2 (deghosting), reduced to the contribution from the measurement surface as explained previously. (2) Code (sugreen.c) which computes the Green's function for a homogeneous half space or whole space, and optionally convolves with a Ricker wavelet. The output is in the t, x domain, while calculations are performed in the ω, x domain. (3) Synthetic data created from the flat layer model and used to create Figure 2. (4) Files required to compile sujim.c and sugreen.c, a script that can be used to submit the two programs, and code documentation are also included. The above items are in directory Jim_Greens.tar in the sponsors only section of mosrp.uh.edu.

The same code can also perform source wavelet estimation, the documentation for which will be included in Release 2 to the sponsors. A discussion of source wavelet estimation is in the appendix.

3.1 Example: Flat layer model

The left panel of Figure 2 shows synthetic data (produced using ray tracing in a flat layer model) designed so that deghosting is easy to demonstrate. (More detail about the input data is in the Appendix.) The depth of the receivers is chosen such that primaries and ghosts appear as distinct seismic events. The right panel of Figure 2 shows Green's theorem output using equation 2; note the primary's receiver side ghost at 0.45 s and the free surface multiple's receiver side ghost at 0.85 s are suppressed. Figure 3 shows the spectra of the input data (blue) and receiver side deghosted output (red). As expected, the receiver side deghosted data fills in notches related to receiver ghosts.

3.2 Example: SEAM application

Green's theorem was applied to the SEAM data set generated based on a deepwater Gulf of Mexico earth model (Figure 4) (Society of Exploration Geophysicists, 2011). We used the special SEAM classic data set modeled to simulate dual sensor acquisition by recording the pressure wavefield at two different depths, 15 m and 17 m respectively. This dual sensor data consisted of nine sail lines for an equivalent wide azimuth towed streamer survey. The source interval is 150 m by 150 m while the receiver interval is 30 m in both inline and crossline directions. Figure 5 displays a typical shot gather from the SEAM model. Given the low frequency of the data (less than 30 Hz) and the source and receiver depths of 15 m and 17 m, the ghost reflections are not as separable as in the previous flat layer model. In this situation, successful deghosting would correspond to a change in the wavelet shape. Figure 6 shows SEAM input (a window of Figure 5) and receiver side

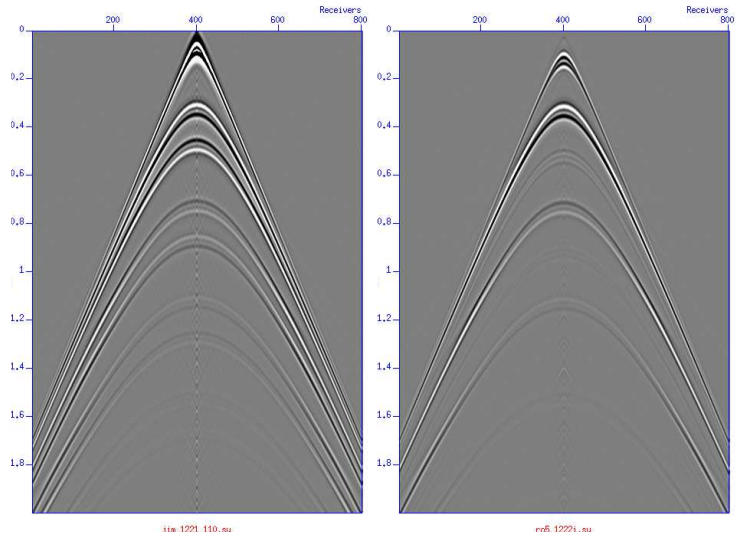

Figure 2: *Flat layer model (source at 30 m, cable at 140 m, water bottom at 300 m): input data at 110 m (left), receiver side deghosted at 100 m (right).*

deghosted output computed by the Green's theorem approach. In the right panel of Figure 6, note the collapsed wavelet. In Figure 7, note the increased amplitude in lower frequencies and decreased amplitude in higher frequencies, i.e., the shift of the amplitude spectrum towards low frequencies.

3.3 Example: Field data

We also applied the deghosting approach to a field survey from the deep water Gulf of Mexico. The data were acquired using dual sensor streamers comprised of hydrophones and vertical geophones. The left panel in Figure 8 shows a close up of an input shot record while the right panel displays the same traces after receiver side deghosting. Note the collapsed wavelet in the output image. This is also demonstrated in Figure 9 that shows the amplitude spectra before and after receiver side deghosting. The receiver depth is about 25 m which corresponds to notches in the input spectra around 30 Hz, 60 Hz, and 90 Hz. Figure 9 displays the spectra of the hydrophones before and after receiver side deghosting. In the bandwidth from 20 Hz to 100 Hz, note the removal of the receiver notches by receiver side deghosting.

4 Conclusions

We have implemented deghosting based on Green's theorem and have tested the algorithm on field data and several kinds of synthetic data. Testing to date has shown the algorithm works with positive and encouraging results.

Suggestions for improving the code are appreciated. (The first author can be reached via e-mail at jdmhou1@sbcglobal.net.)

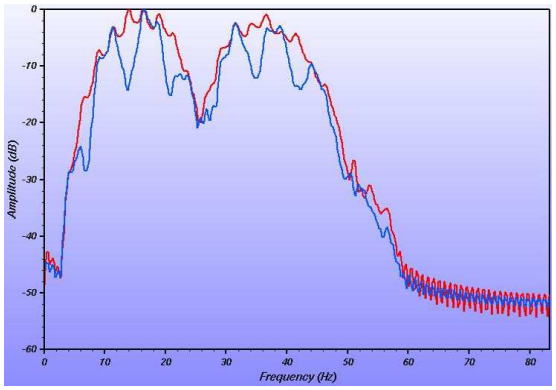

Figure 3: *Flat layer model: muted input data (blue), receiver side deghosted (red). The receiver notches (at intervals of 5.4 Hz) have been filled in; the notch at 25 Hz is a source notch.*

5 Acknowledgements

We are grateful to the M-OSRP sponsors for their support of this research. The first author (JDM) is grateful to Arthur B. Weglein for his mentoring, Fang Liu and Paolo Terenghi for their teaching, and ExxonMobil and PGS for internships.

A Source wavelet estimation

Source wavelet estimation is based on Weglein and Secrest (1990) which uses the geometry shown in Figure 10. The reference medium is chosen to be a half space of water plus a half space of air separated by a free surface, and the observation/prediction point $\mathbf{r}$ is below the towed cable, i.e., outside the integration volume V.

The key equation is:

$$P_0(\mathbf{r},\mathbf{r}_s,\omega) = \int_{m.s.} dS\,\hat{n}\cdot[P(\mathbf{r}',\mathbf{r}_s,\omega)\nabla' G_0^D(\mathbf{r},\mathbf{r}',\omega) - G_0^D(\mathbf{r},\mathbf{r}',\omega)\nabla' P(\mathbf{r}',\mathbf{r}_s,\omega)], \tag{3}$$

where G_0^D is a Dirichlet Green's function constructed to vanish on the free surface. In 3D

$$G_0^D(\mathbf{r},\mathbf{r}',\omega) = -\frac{1}{4\pi}\left(\frac{\exp(ikR_+)}{R_+} - \frac{\exp(ikR_-)}{R_-}\right),$$

in 2D

$$G_0^D(\mathbf{r},\mathbf{r}',\omega) = -\frac{i}{4}(H_0^{(1)}(kR_+) - H_0^{(1)}(kR_-)),$$

and $R_\pm = \sqrt{(x-x')^2+(y-y')^2+(z\mp z')^2}$.

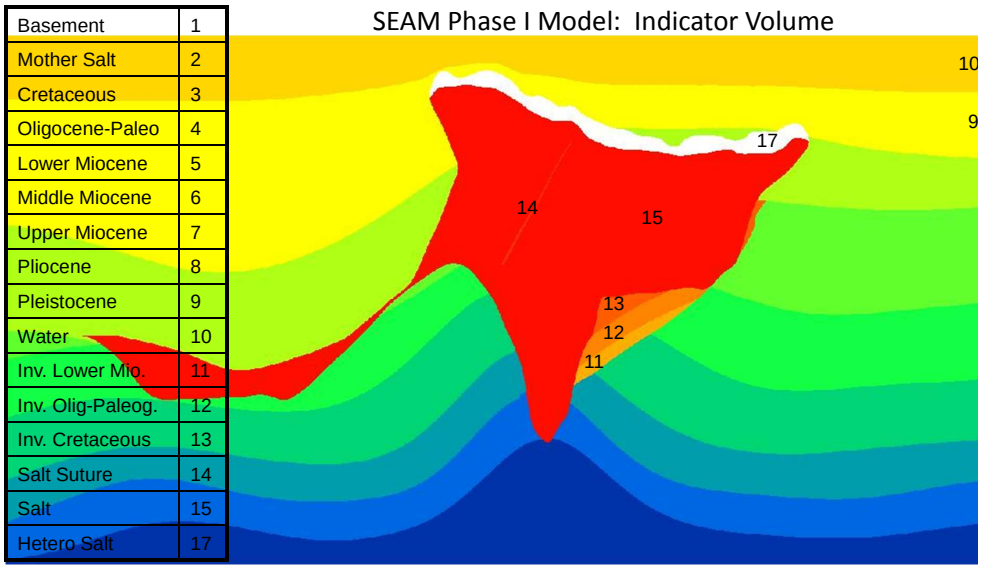

Figure 4: *SEAM deepwater Gulf of Mexico model: inline section from the middle of the model. Figure courtesy of SEAM.*

The source wavelet $A(\omega)$ can be estimated by averaging the reference wavefield divided by a Green's function:

$$A(\omega) = \frac{1}{N} \sum_{i=1}^{N} \frac{P_0(\mathbf{r}_i, \mathbf{r}_s, \omega)}{G_0^+(\mathbf{r}_i, \mathbf{r}_s, \omega)}.$$

It is worth noting that inside/outside the integration volume is an important concept. The surface of integration S divides all space into inside and outside the integration volume V. The integral over S of $(P\nabla' G_0^D - G_0^D \nabla' P) \cdot \hat{n}$ gives the field inside (outside) the integration volume due to sources outside (inside) the integration volume, a result called the extinction theorem (Born and Wolf, 1964, pp. 101–102). Selecting the integration volume V between the free surface and measurement surface (Figure 10) gives the reference wavefield P_0 (if the observation/prediction point is outside V/below the cable) or the scattered wavefield P_s (if the observation point is inside V/above the cable). An electromagnetic analogy is shown in Figure 11. Sources outside (inside) the integration volume induce sources on the measurement surface that create the field inside (outside) the integration volume (Orfanidis, 2008, pp. 679-681), (Jackson, 1999, pp. 36-37).

B Input data characteristics

The flat layer model has the following parameters:
Free surface, 3D source, water bottom at 300 m, 1D constant density acoustic earth (c = 2250 m/s)

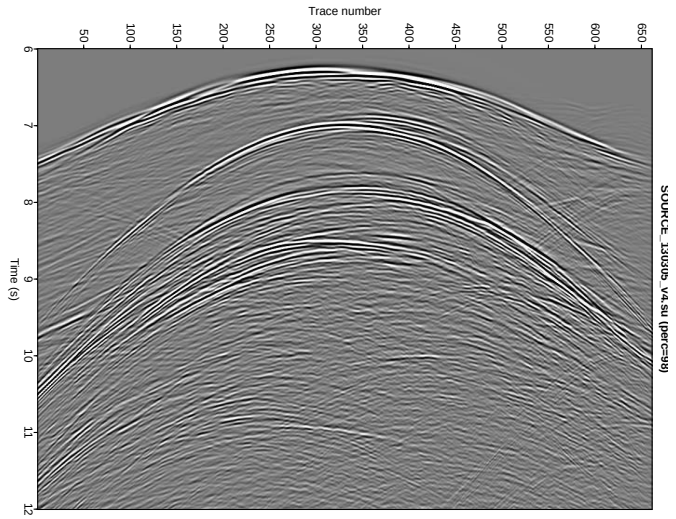

Figure 5: *SEAM data, shot 130305 (located at sx=16,975 m, sy=20,000 m, sz=15 m, i.e., near the center of the shot grid).*

Depth of source: 30 m
Frequency of source at peak amplitude: 20 Hz
1 towed streamer, 801 receivers
Distance between receivers: 6.25 m
Depth of towed streamer: 140 m
Sampling rate: 4 ms
Record length: 1500 samples

$$\frac{dP}{dz'} = \frac{P(140m) - P(145m)}{140m - 145m}$$

The SEAM model has the following parameters:
Free surface, 3D source, variable water depth, 3D variable density acoustic earth
Depth of source: 15 m
Frequency of source: 1-30 Hz
661×661 receivers
Distance between towed streamers: 30 m
Distance between receivers: 30 m
Depth of receivers: 15 m and 17 m
Sampling rate: 8 ms
Record length: 16 s (2001 samples)

$$\frac{dP}{dz'} = \frac{P(17m) - P(15m)}{17m - 15m}$$

The field data has the following parameters:
Free surface, 3D source, variable water depth, actual earth
Depth of source: 9 m

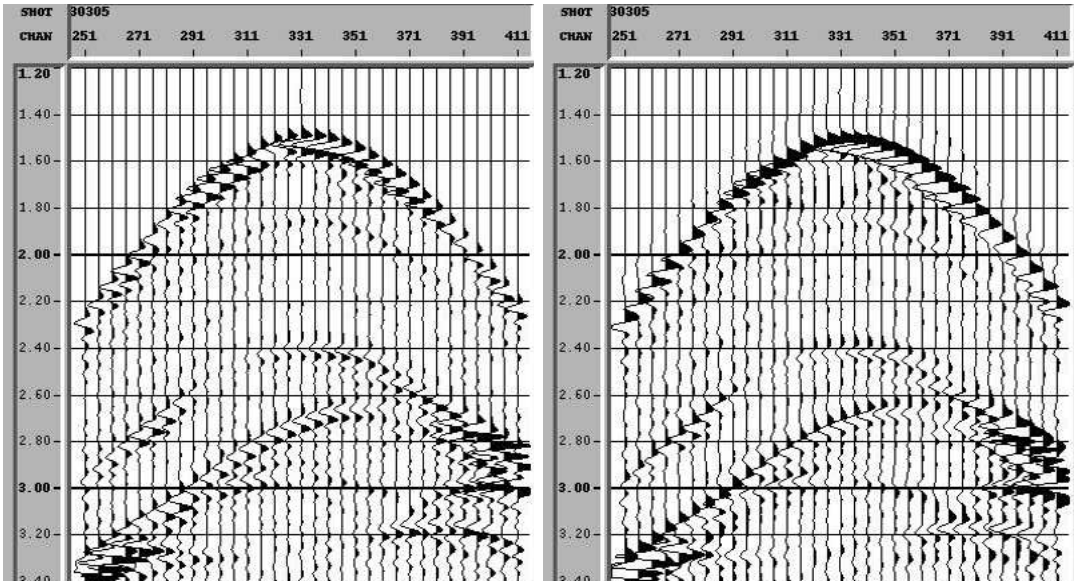

Figure 6: *SEAM data, shot 130305: recorded data at 17 m (left), receiver side deghosted at free surface (right). Note the collapsed wavelet in the right panel.*

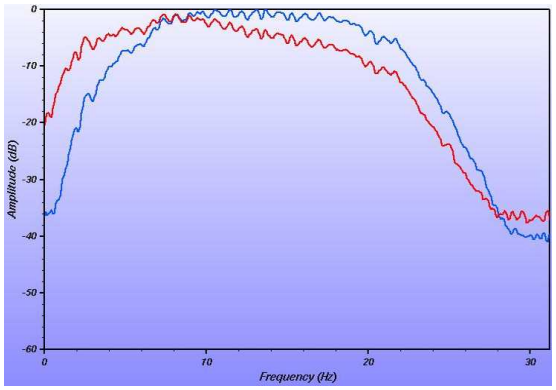

Figure 7: *SEAM data: shot 130305: recorded data at 17 m (blue), receiver side deghosted at free surface (red). Note the shift of the spectrum towards lower frequencies (first receiver notch is at 50 Hz).*

1 towed streamer, 960 receivers
Distance between receivers (after grouping): 12.5 m
Depth of towed streamer: 22–25 m
Sampling rate: 4 ms
Record length: 3585 samples
2 input files: P and V_z

$$\frac{dP}{dz'} = i\omega\rho V_z$$

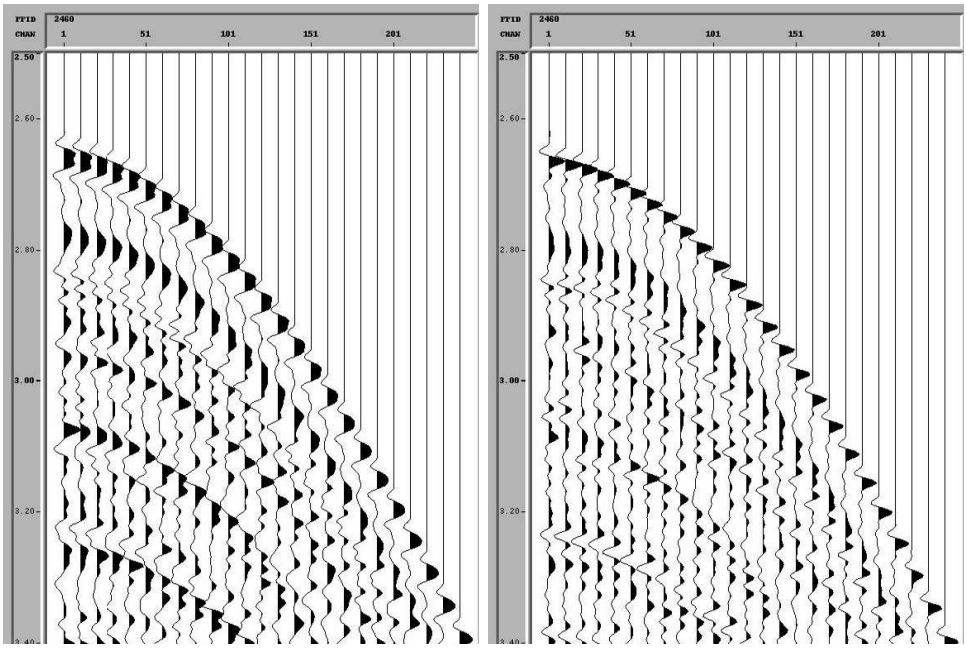

Figure 8: *Field data: hydrophones (top), receiver side deghosted at free surface (bottom). Note the collapsed wavelet in the right panel. Input data courtesy of PGS.*

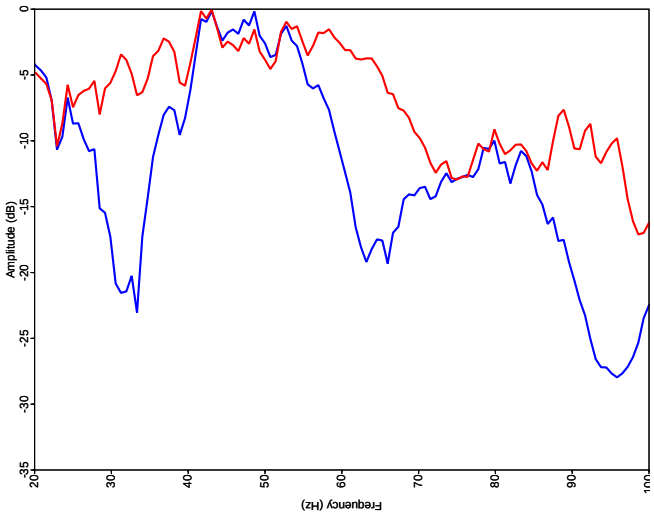

Figure 9: *Input hydrophones (blue), receiver side deghosted (red). The receiver notches around 30 Hz, 60 Hz, and 90 Hz have been filled in. Input data courtesy of PGS.*

where ρ is the density of the reference medium (seawater).

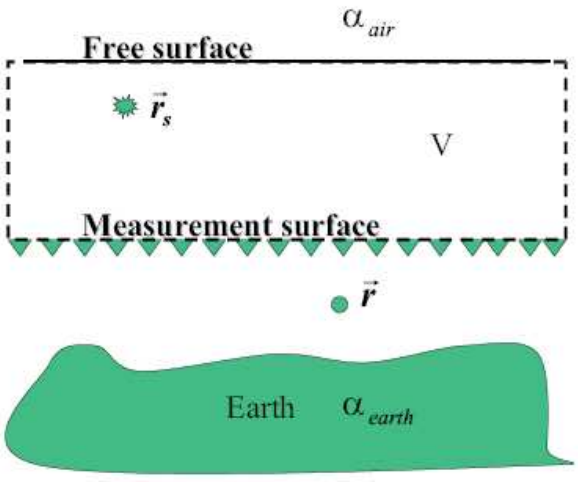

Figure 10: *Configuration for estimating the source wavelet $A(\omega)$ (Zhang, 2007). The closed surface S of integration consists of the measurement surface, free surface, and dashed lines.*

References

Born, Max and Emil Wolf. *Principles of Optics: Electromagnetic Theory of Propagation, Interference, and Diffraction of Light*. 2nd (revised) edition. New York: The MacMillan Company, 1964.

Jackson, J. D. *Classical Electrodynamics*. Third edition. New York: John Wiley & Sons, Inc., 1999.

Morse, P. M. and H. Feshbach. *Methods of theoretical physics*. McGraw-Hill Book Co., 1953.

Orfanidis, S. J. *Electromagnetic Waves and Antennas*. http://www.ece.rutgers.edu/~orfanidi/ewa/. distributed via url, 2008.

Ramírez, Adriana Citlali and Arthur B. Weglein. "Green's theorem as a comprehensive framework for data reconstruction, regularization, wavefield separation, seismic interferometry, and wavelet estimation: a tutorial." *Geophysics* 74 (November-December 2009): W35–W62.

Society of Exploration Geophysicists. 2011 "The SEG Advanced Modeling Corporation.". http://www.seg.org/resources/research/seam.

Weglein, A. B., F. V. Araújo, P. M. Carvalho, R. H. Stolt, K. H. Matson, R. T. Coates, D. Corrigan, D. J. Foster, S. A. Shaw, and H. Zhang. "Inverse Scattering Series and Seismic Exploration." *Inverse Problems* (2003): R27–R83.

Weglein, Arthur B. and Bruce G. Secrest. "Wavelet estimation for a multidimensional acoustic earth model." *Geophysics* 55 (July 1990): 902–913.

Zhang, Jingfeng. *Wave theory based data preparation for inverse scattering multiple removal, depth imaging and parameter estimation: analysis and numerical tests of Green's theorem deghosting theory*. PhD thesis, University of Houston, 2007.

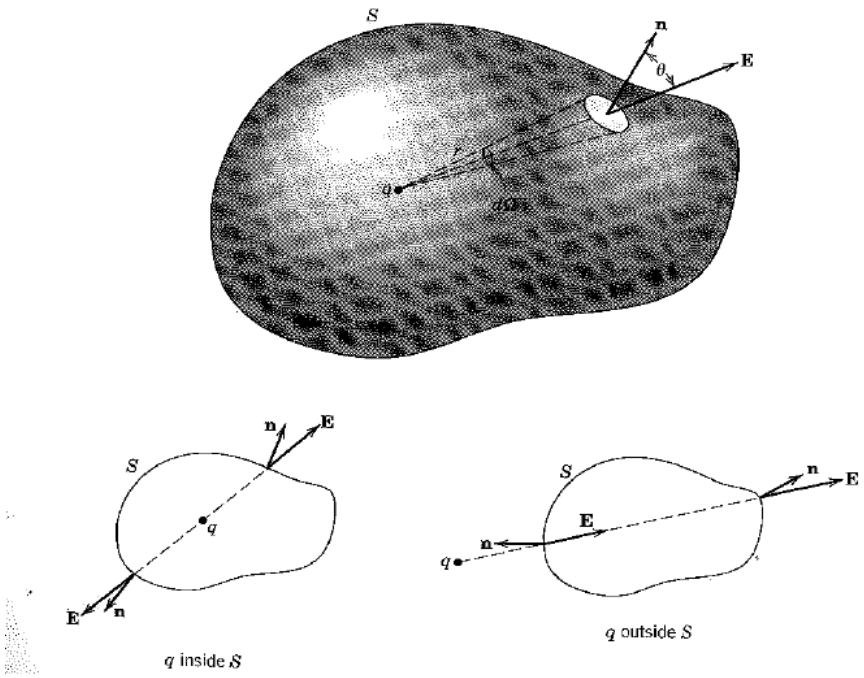

Figure 11: *Gauss' law (Jackson, 1999). The normal component of the electric field* $\mathbf{E} \cdot \hat{n}$ *is integrated over the closed surface S. If the charge is inside (outside) S, the total solid angle subtended at the charge is* 4π *(zero).*

Zhang, Jingfeng and Arthur B. Weglein. "Extinction theorem deghosting method using towed streamer pressure data: analysis of the receiver array effect on deghosting and subsequent free surface multiple removal." *75th Annual International Meeting, SEG, Expanded Abstracts.* . Volume 24 . Soc. Expl. Geophys., 2005. 2095–2098.

Zhang, Jingfeng and Arthur B. Weglein. "Application of extinction theorem deghosting method on ocean bottom data." *76th Annual International Meeting, SEG, Expanded Abstracts.* . Volume 25 . Soc. Expl. Geophys., 2006. 2674–2678.

The properties of the inverse scattering series internal multiple attenuation algorithm: Analysis and evaluation on synthetic data with lateral variations, choosing reference velocity and examining its sensitivity to near surface properties

Shih-Ying Hsu, Paolo Terenghi and Arthur B. Weglein

Abstract

We present three examples to demonstrate the capability of the inverse scattering series internal multiple attenuation algorithm. Example 1 shows that the algorithm resolves complicated wave phenomena by transforming the input wavefield into pseudodepth domain. The key to this algorithm's automated scheme is to allow all combinations of events that satisfy lower-higher-lower relationship in pseudodepth domain to contribute to internal multiple prediction. The algorithm's strength of handling all internal multiples for all horizons at the same time without any interpretive intervention is shown in example 2. In example 3, the algorithm's insensitivity to reference velocity error is demonstrated by the numerical results using both accurate and inaccurate reference velocity.

1 Introduction

Multiple removal is a long-standing problem in seismic processing. When exploring offshore areas, the most dominant multiples are associated with reflections at the free surface; thus, performing free surface de-multiple is often sufficient. As there is an increasing demand for energy it becomes necessary to explore more challenging areas (*e.g.* deep water/complex marine environments and onshore areas) where internal multiples often predominate. The inability to attenuate/remove internal multiples can cause destructive interference with primaries or multiples can be misinterpreted as primaries leading to poor drilling decisions. Hence, an adequate internal multiple attenuation/removal method in complex geology is required.

Methods for internal multiple attenuation/removal can be divided into two group. The first group of methods requires the user to identify the primaries as internal multiple sub-events or the portion of the earth responsible for the internal multiple's downward reflection. Typically, the interpretation consists in the picking of the travel-time of the event corresponding to a chosen reflector, often referred to as the internal multiple *generator*. In one case, the interpretation can be used directly to isolate the chosen generator from other events corresponding to deeper reflectors (Keydar et al., 1997; Jakubowicz, 1998). Another group of algorithms use the picked travel-times to downward continue the wave-field towards the generator (Berkhout and Verschuur, 2005; Verschuur and Berkhout, 2005) [common-focus-point or CFP boundary approach] or towards a chosen reference level (Berkhout and Verschuur, 2005; Verschuur and Berkhout, 2005) [CFP layer approach]. The reference level is chosen to separate the regions of the earth that act as downward reflectors from those that act as upward reflectors in the prediction of internal multiples. The layer approach

predicts internal multiples composed of a downward reflection above the chosen level and upward reflections below the level. It will not predict the internal multiple with at least one of its upward reflections above the chosen reference level.

The second group of internal multiple attenuation/removal methods does not require generator identification and the internal multiples are constructed by combining three events that satisfy an automated constraint. In the method based on the inverse scattering series (ISS), the constraint is a lower-higher-lower relationship in pseudo-depth or vertical travel time (Araújo et al., 1994; Weglein et al., 1997, 2003; Nita and Weglein, 2007). ten Kroode (2002) proposed an asymptotic derivation of the results in Weglein et al. (1997), where the constraint is a longer-shorter-longer relationship between total travel-times under the assumption of travel-time monotonicity (deeper events yield longer travel time). The automated constraint enables the algorithms in the second group to predict internal multiples for all possible generators in one step and can be considered truly independent of subsurface information. It should be mentioned that the latter method will not predict internal multiples generated within the area that does not satisfy travel-time monotonicity.

The leading order ISS internal multiple attenuation algorithm was first proposed by Araújo et al. (1994) and Weglein et al. (1997). This multi-D algorithm does not require subsurface information or interpretive intervention. It predicts internal multiples for all horizons at once. This algorithm is independent of earth model type and it predicts the correct traveltimes and an approximated amplitude of the true internal multiples in the data, including converted wave internal multiples (Coates and Weglein, 1996). Ramírez and Weglein (2005) captured a portion of the higher order terms in a closed form, thus improving the amplitude of the prediction. Matson (1997) extended the theory to the case of land and ocean-bottom surveying (Matson and Weglein, 1996). Other implementations were proposed in Otnes et al. (2004), Kaplan et al. (2005) and Hsu et al. (2010). The first towed-streamer field data example using the $2D$ version of the algorithm was shown by Matson et al. (1999) and the first land field data example appeared in Fu et al. (2010). The encouraging results demonstrate the effectiveness of this algorithm and the latter paper represents an important step in demonstrating the ISS algorithm in cases where the choice of the reference medium is problematic, due to near surface heterogeneity.

In this paper, we briefly review the ISS internal multiple attenuation algorithm followed by numerical examples. The first example demonstrates the advantage of using vertical travel-time instead of total travel-time as the automated constraint for the case of multiples generating at a highly curved boundary. In the second numerical example we illustrate the properties of the ISS internal multiple attenuation algorithm and the difference between ISS method and the CFP layer approach. In particular, we highlight how the ISS method can predict all internal multiples generated by all reflectors in a single step. In the third example we demonstrate this algorithm to be robust even with incorrect reference velocity, which accommodates the error due to near surface complexity.

2 Theory

The ISS provide a family of data-processing algorithms firmly rooted into the wave equation and all based on the intuitive idea that the earth properties can be divided into a known (typically homogeneous) background component, where the propagation of waves can be described analytically, and

an unknown perturbation, which is the object to the investigation. The wave-equation allows the sought for perturbation to be determined as a series of terms of increasing power in the input scattered field. Within this framework, the removal of internal multiples can be regarded as a particular task within the general inversion scheme and it is possible to identify a sub-series to construct the internal multiple-free data starting from the input wave-field with all internal multiples.

The internal multiple attenuation series starts with an uncollapsed FK migration of the wave-field with all its internal multiples untouched. After the first order term is determined, all higher order terms can also be determined in a cascade. The leading order contribution to the prediction of the internal multiples can be found within the third order term, which combines three instances of the first-order FK migration, constrained by a lower-higher-lower relationship. All subsequent terms reside in the odd-numbered terms in the series, similarly constrained by the lower-higher-lower relationship.

The ISS internal multiple attenuation algorithm for first order internal multiple prediction in a 2D earth is given by Araújo (1994) and Weglein et al. (1997),

$$\begin{aligned} b_3(k_g,k_s,\omega) = \frac{1}{(2\pi)^2}\int_{-\infty}^{\infty}\int_{-\infty}^{\infty} dk_1 e^{-iq_1(z_g-z_s)} dk_2 e^{iq_2(z_g-z_s)} \\ \times \int_{-\infty}^{\infty} dz_1 b_1(k_g,k_1,z_1) e^{i(q_g+q_1)z_1} \\ \times \int_{-\infty}^{z_1-\epsilon} dz_2 b_1(k_1,k_2,z_2) e^{-i(q_1+q_2)z_2} \\ \times \int_{z_2+\epsilon}^{\infty} dz_3 b_1(k_2,k_s,z_3) e^{i(q_2+q_s)z_3}, \end{aligned} \tag{1}$$

where ω is temporal frequency; k_g and k_s are the horizontal wavenumbers for source and receiver coordinates, respectively; the vertical source and receiver wavenumbers, q_g and q_s, are given by $q_i = sgn(\omega)\sqrt{\frac{\omega^2}{c_0^2} - k_i^2}$ for $i = (g, s)$; c_0 is the constant background velocity; z_s and z_g are source and receiver depths; and z_i $(i = 1, 2, 3)$ represents pseudodepth (depth location given by migration with background velocity). The quantity $b_1(k_g, k_s, z)$ corresponds to an uncollapsed migration (Weglein et al., 1997) of an effective plane-wave incident data, $b_1(k_g, k_s, q_g + q_s) = -2iq_sD(k_g, k_s, \omega)$, where $D(k_g, k_s, \omega)$ is the Fourier transformed prestack data.

3 Properties of the first order term - uncollapsed FK migration

The first order term in the ISS internal multiple attenuation series can be regarded as an uncollapsed Stolt migration of the input wave-field with all its internal multiples. It is worth reminding that Stolt migration provides an exact one-way wave-equation method for a constant-velocity acoustic medium. Therefore, where the chosen constant velocity adequately describes the properties of the actual medium all reflections and diffractions are collapsed to their exact image location. However, where the constant velocity is inadequate, waves will still focus, albeit at a smeared-out area near the correct image location. In general, the pseudo-depth of a geologic feature determined through FK migration in the constant velocity background medium does not necessarily match the true

location of that feature in the actual earth. Unlike the original pre-stack Stolt migration, however, the first order term in the ISS internal multiple series does not perform the final stack over all reflection angles which finalizes all traditional imaging processes. Rather it preserves the pre-stack information that allows an exact de-migration to be performed within the third and higher order terms even in the case of inadequate velocity.

Stolt uncollapsed migration resolves many complicated wave phenomena within a constant velocity overburden such as diffractions and multi-pathing. One example of such phenomena is the bow-tie pattern generated by reflections over a sufficiently curved boundary. These effects are common in seismic exploration data, as they can occur in a variety of known geologic settings, including highly curved reflectors (*e.g.* salt domes), faults, layer terminations, pinch-outs, fractured and/or irregular volcanic layers and even at the sea bottom in the case of rough topography. Several algorithms published in the literature for the attenuation of internal multiples require the user to pick the travel-time of the seismic event interpreted as the internal multiple generator, defined as the location of a downward reflection generally associated with the definition of internal multiples. In some of those methods the picked travel-times are directly used to mute the wave-field at earlier or later times with respect to the generator and internal multiples are then predicted using auto and cross-correlation operations between traces from the resulting fields (Keydar et al., 1997; Jakubowicz, 1998). In other methods traveltimes are used to determine approximated re-datuming operators in a data-driven manner, capable of 'sinking' the measurement surface down into the earth, where the prediction of internal multiples is resorted to the known free-surface case (Berkhout and Verschuur, 2005; Verschuur and Berkhout, 2005). However, all these approaches are based on the implicit assumption that a one-to-one relationship exists between seismic events (their travel-time) and the earth features that create them (such as layer boundaries). In the presence of diffractions or multi-pathing, a one-to-one relationship does not exist, as a single curved interface can produce several seismic arrivals. In that case picking of traveltimes becomes an issue and those methods are inadequate wherever the interpretation is required with a certain degree of accuracy.

Example 1: Internal multiples from curved or rugose surfaces

We propose an example based on a simple three-layer earth model where the shallower interface is sine-shaped. The model in Figure 1(a) produces the data in Figure 1(b) where all seismic events except the second primary at $2.2s$ can be traced back to their origin at the shallow reflector. Clearly, in this example it is an issue to pick a unique travel-time to represent the curved reflector, as many events are generated, which interfere among themselves and even with the second primary. The ISS method provides an elegant solution to that problem, by allowing an un-collapsed image to represent the input wave-field in the pseudo-depth domain rather than in the total-time domain (Figure 1(c)). In such representation, the order of events along the vertical axis can be trusted to agree with the order of reflectors along the actual depth axis (Nita and Weglein, 2007).

Figure 2 describes the case of an internal multiple which would not be predicted if total travel-times were taken into considerations. The multiple can be shown to an earth feature where the relationship between total traveltimes and vertical traveltimes (pseudodepth) is inverted due to the presence of a high velocity layer at depth.

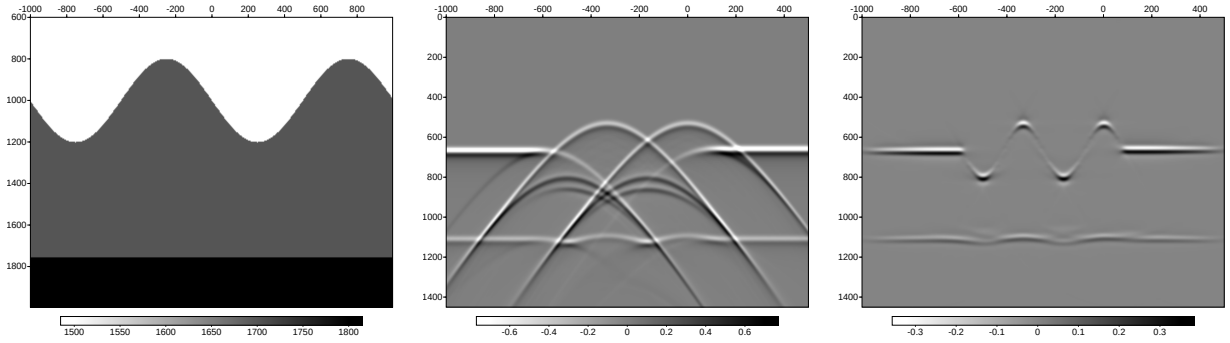

(a) (b) (c)

Figure 1: (a) Velocity model, (b) zero offset sections of the input data, (c) input wavefield in the pseudo-depth domain.

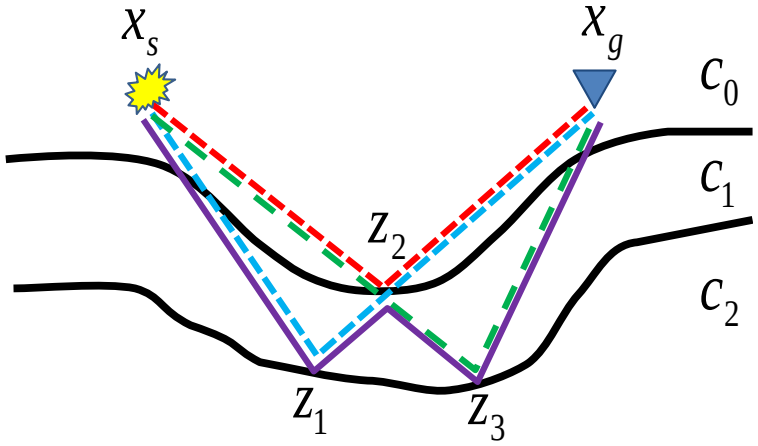

Figure 2: An internal multiple (solid blue) satisfying monotonicity in vertical time but not in total travel time. If wave-speed c_1 is much greater than c_0, the (dashed blue) and (dashed green) primaries arrive at the surface earlier than the (dashed red) primary. The multiple is removed by the ISS method, but not by methods based on total traveltime monotonicity.

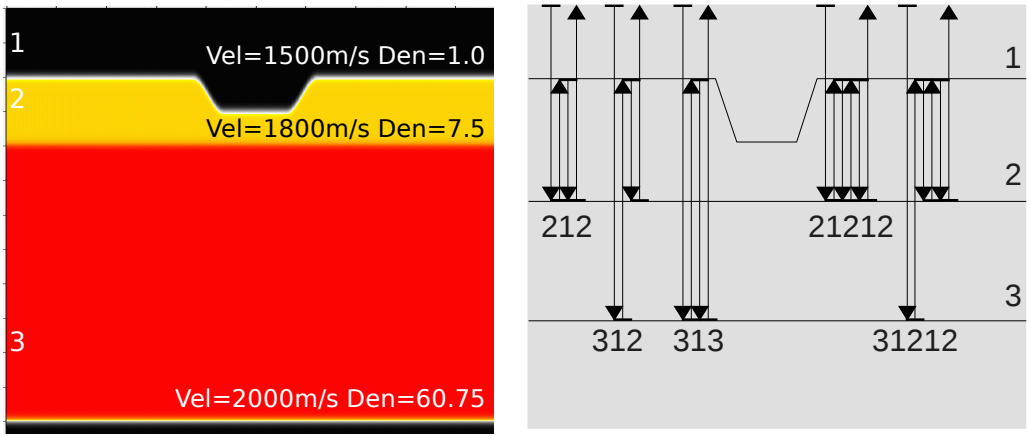

(a) (b)

Figure 3: earth model (a) and event labeling (b) used in example2. Densities are chosen to yield a vertical-incidence reflection coefficient of 0.8 at all layer boundaries.

4 Properties of the leading (third) order term

Let z_1, z_2 and z_3 be the pseudodepths of three generic points in the first order term of the internal multiples series (uncollapsed constant-velocity pre-stack migration). As those points span the entire data volume, the leading order (third order) algorithm allows any combination such that $z_1 > z_2$ and $z_3 > z_2$ to contribute the prediction (lower-higher-lower constraint). In contrast with the methods based on the convolution and correlation of wave-fields, where the definition of the generator is static, the ISS algorithm's lower-higher-lower constraint does not refer to any particular interface or event in the data. On the contrary, it applies to all of them and therefore allows the simultaneous prediction of a variety of internal multiples at once without requiring interpretation and traveltime picking of the data or knowledge of the medium.

Example 2: A complete one-step prediction

We demonstrate the properties of the ISS internal multiple prediction algorithm using a set of acoustic finite-difference data. The model (shown in Figure 3(a)) consists of four media delimited by three interfaces, the first of which has a gap approximately 1.5km long and 100m deep. In Figure 3(b), the travel paths of some internal multiples are drawn schematically using up- and downgoing arrows representing wave propagation. In a zero offset section of the data (Figure 4(a)) a first train of closely spaced internal multiples (characterized by the pattern $2[12]_n$) can be shown to originate from the energy reflected between the two shallow reflectors (1) and (2). A deeper reflector (3) causes the entire train to begin again at around $1.4s$ ($3[12]_n$ trend) and once more at $2.1s$ ($313[12]_n$ and $323[12]_n$ trends). In general, even in a simple three-interface earth model, the number of reverberations recorded at the surface is extremely large as a result of the various ways three reflectors can be combined to form internal multiples. The ISS internal multiple algorithm predicts

all of them at once, without any interpretation required on the data, as shown in Figures 4(b) and 4(c).

It is useful to observe that CFP layer-related approach would not achieve the same result in a single step. Figure 5(a) shows the four types of first-order internal multiples generated within a three-reflector earth. If the reference level that separates an internal multiple's upward and downward reflections is chosen to close between the first and the second reflectors, the layer-related method would predict the three types of first-order internal multiples shown in Figure 5(b). If we use the layer-related method and choose the reference level between events (1) and (2) in the example shown in Figure 4, all multiples characterized by trend $3[23]_n$ would be absent in the prediction. Figure 5(c) shows a different prediction produced by selecting the reference level to close between second and third reflectors. Similarly, in the example in Figure 4, if the downward reflecting layer was chosen to close between events (2) and (3), all $2[12]_n$ trend would not be predicted. Notice that once the reference level is chosen, the events above this level can only act as downward reflectors; similarly, the events below this level can only contribute as upward reflectors. In Figure 5(a), however, the second reflector contributes both as an upward reflector, for the two internal multiples in the middle, and as a downward reflector, for the right most internal multiple. Therefore, for any choice of downward-reflecting layer, there is at least one trend of first-order internal multiple which cannot be predicted in one step.

In contrast, there is no such kind of restriction in ISS internal multiple attenuation algorithm. Any combination of three events that satisfy the lower-higher-lower relationship in pseudodepth will contribute to the prediction. Hence, the reflections associated to the second reflector in 5(a) can be used as upward and downward reflections in predicting different type of internal multiples within a single step.

Example 3: Reference velocity insensitivity

The ISS solves the perturbation using only the reference Green's function and measured data. One reasonable question to ask is what to choose for the reference medium. The ISS needs the reference medium to agree with the actual medium at and above the measurement surface so the perturbation may exist only below the source-receiver plane. Hence, the known near surface properties, including reference velocity, are required. In the marine case, the requirement is easily satisfied by choosing water as a reference medium. On the other hand, the requirement may be difficult to obtain for onshore application where the near surface complexity often produces unavoidable errors in reference velocity measurement. However, it is reasonable to expect that the requirement may not be as stringent for the internal multiple attenuation subseries as it can be for the entire inverse series, which have the direct determination of the earth properties as a target. Hsu and Weglein (2008) have shown that the ISS internal multiple attenuation algorithm is independent of the reference velocity for an 1D earth. Here, we evaluate the algorithm's reference velocity insensitivity using different reference velocity to perform the prediction on the same acoustic finite-difference data as example 2.

The zero-offset section of the predictions obtained using different reference velocity are shown in Figure 6. The predictions using lower reference velocity 1300 m/s and 1400 m/s are shown in Figures 6(b) and 6(c). The prediction with correct reference velocity 1500 m/s is shown in Figure 6(d).

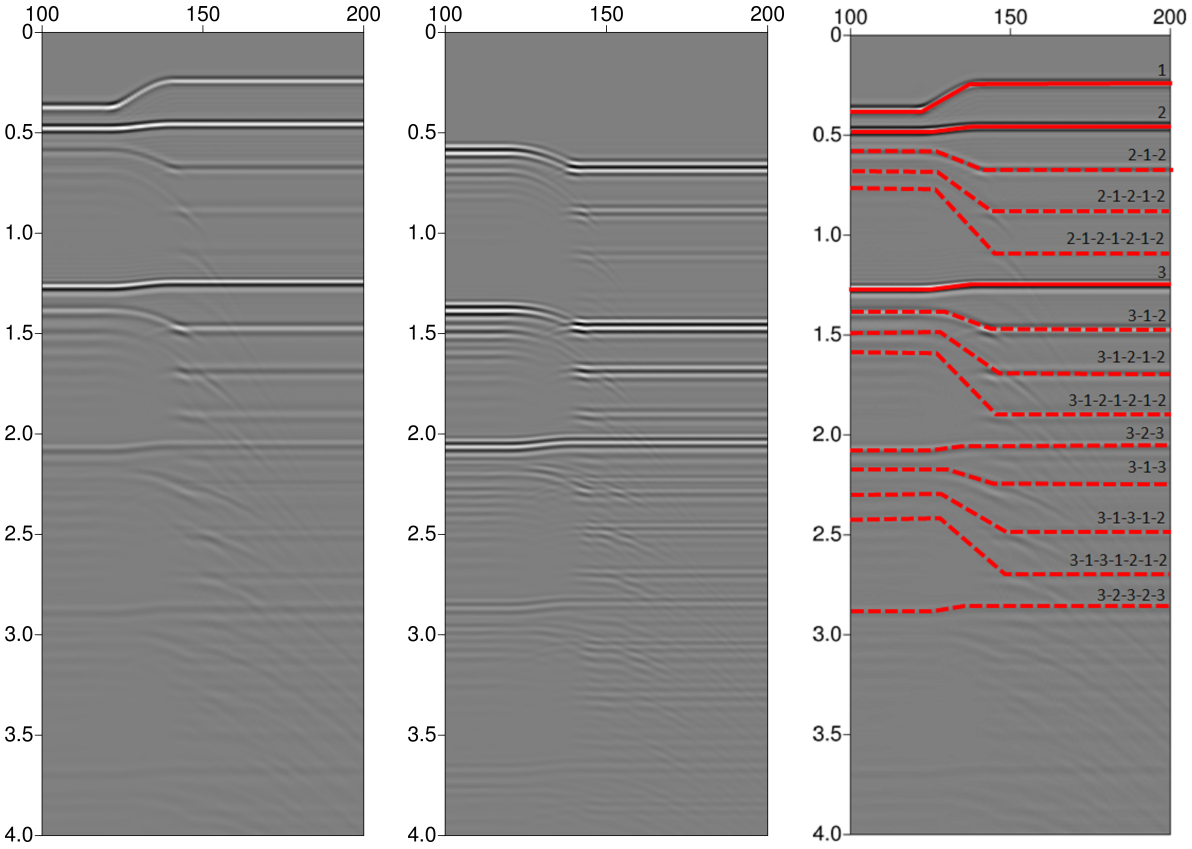

(a) (b) (c)

Figure 4: zero offset sections from example2: (a) input data, (b) predicted multiples and (c) labeling of events.

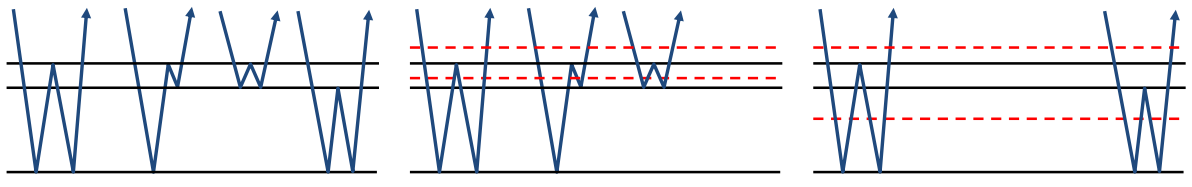

(a) (b) (c)

Figure 5: (a) Four types of first-order internal multiples are generated by three reflectors. (b) and (c) The first-order internal multiples predicted by the feedback layer method using different definitions of the downward generator layer (red dashed lines).

The results using higher reference velocities, 1600 m/s and 1700 m/s, are displayed in Figure 6(e) and 6(f). The zero offset sections of the five results are very similar, which confirms our previous study of reference velocity insensitivity in 1D. In Figure 7 we compare the single shot gather of the five results. The predictions are also very similar but notice that the amplitudes of the far offset in Figures 7(e) and 7(f) are slightly weaker than that in Figure 7(d). We relate this phenomenon to the fact that our current implementation only uses the nonevanescent portion of the data, corresponding to real values of vertical wavenumber q, given by $q = sgn(\omega)\sqrt{\frac{\omega^2}{c_0^2} - k^2}$. For higher reference velocity, the nonevanescent portion is smaller; therefore, it excludes the computations of the steepest slopes associated with the far offsets of the first primary. For the same reason, with high reference velocities, the algorithm also becomes faster to compute.

The ISS internal multiple attenuation algorithm produces similar predictions for different reference velocities. For onshore cases, the velocity independence of the ISS algorithm is particularly important as it may accommodate the local heterogeneity of the near surface medium.

5 Conclusions

In this work, we demonstrated through simple numerical examples some of the strengths of the ISS internal multiple attenuation method. The algorithm (1) works in the pseudodepth domain, where complicated wave phenomena are resolved, (2) is characterized by an automatic constraint which is key to providing a prediction of all internal multiple at once, and (3) we discussed the algorithm's insensitivity to reference velocity, confirmed by a set of numerical tests on 2D acoustic data.

Acknowledgments

The authors wish to thank Bill Dragoset of WesternGeco (Houston) for providing the data shown in example 2 and for permission to publish the results. We thank all M-OSRP sponsors for constant support and encouragement.

References

Araújo, F. V. *Linear and non-linear methods derived from scattering theory: backscattered tomography and internal multiple attenuation.* PhD thesis, Universidade Federal da Bahia, 1994.

Araújo, Fernanda V., Arthur B. Weglein, Paulo Marcus Carvalho, and R. H. Stolt. "Inverse scattering series for multiple attenuation: An example with surface and internal multiples." *SEG Technical Program Expanded Abstracts* 13 (1994): 1039–1041.

Berkhout, A. J. and D. J. Verschuur. "Removal of internal multiples with the common-focus-point (CFP) approach: Part 1 — Explanation of the theory." *Geophysics* 70 (2005): V45–V60.

Coates, R. T. and A. B. Weglein. "Internal multiple attenuation using inverse scattering: Results from prestack 1 & 2D acoustic and elastic synthetics." *SEG Technical Program Expanded Abstracts* 15 (1996): 1522–1525.

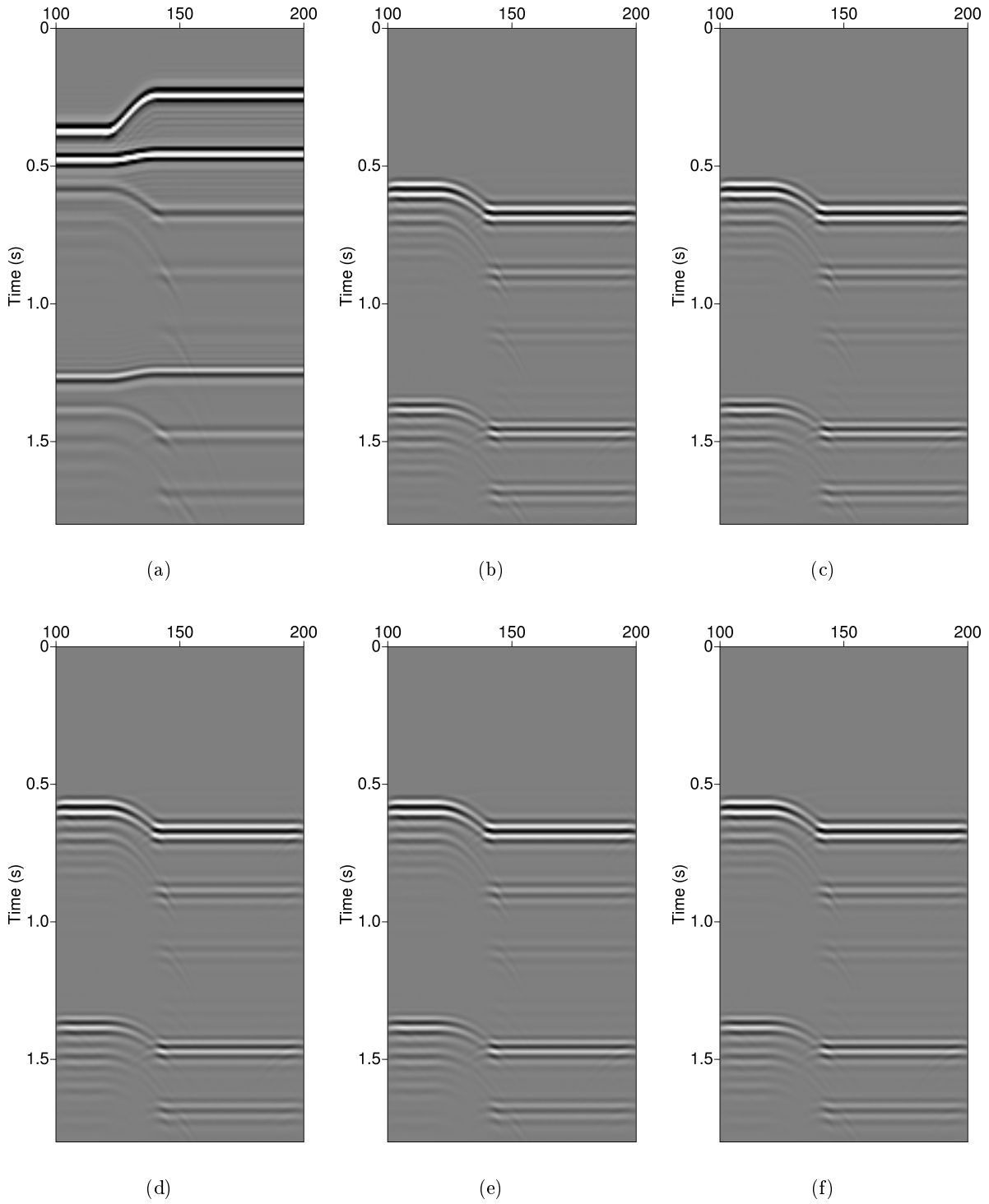

Figure 6: Zero offset section of predictions using different reference velocity: (a) raw data, (b) $c = 1300\, m/s$, (c) $c = 1400\ m/s$, (d) $c = 1500\ m/s$, (e) $c = 1600\ m/s$, (f) $c = 1700\ m/s$.

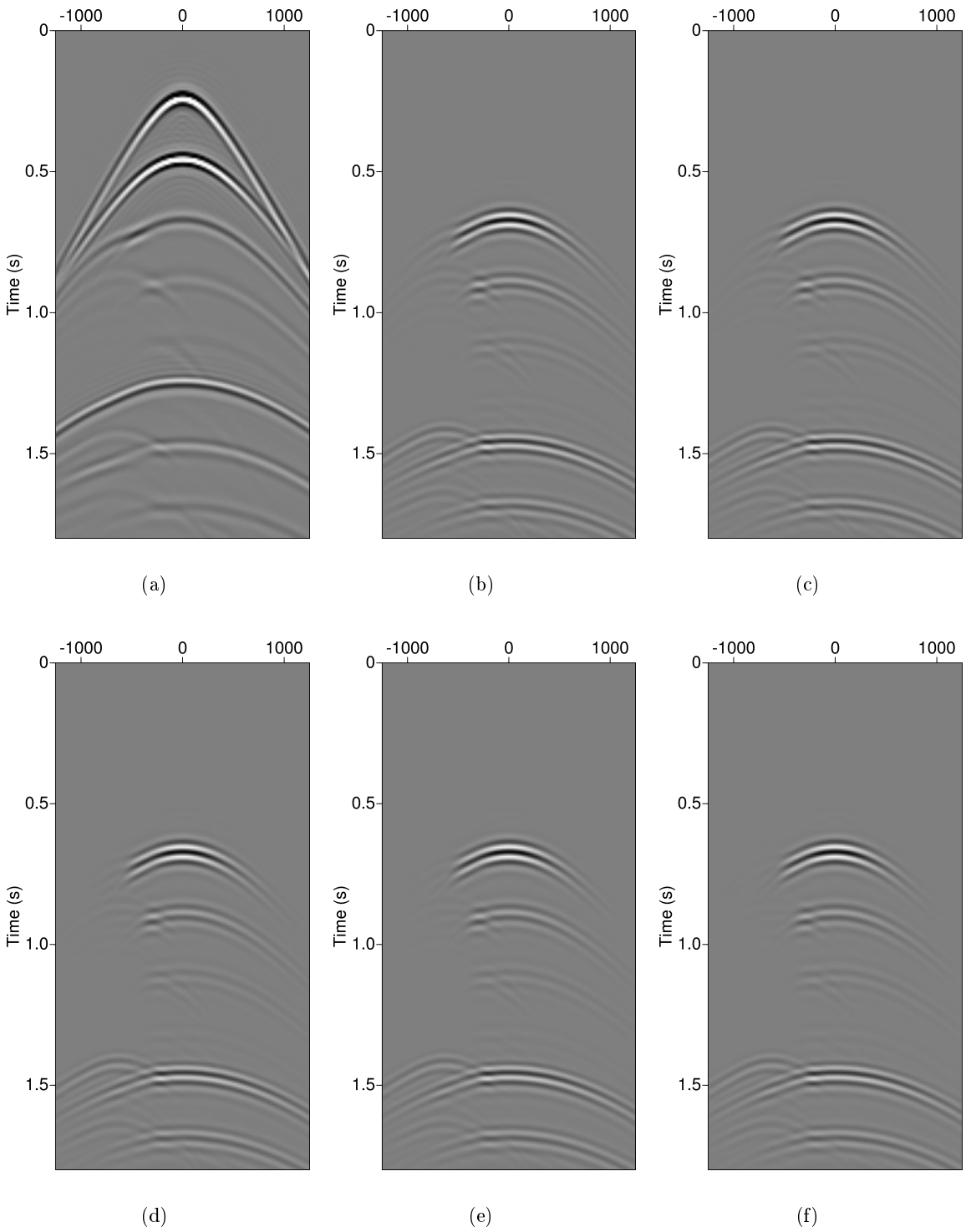

Figure 7: Single shot gather results using different reference velocity: (a) raw data, (b) $c = 1300\ m/s$, (c) $c = 1400\ m/s$, (d) $c = 1500\ m/s$, (e) $c = 1600\ m/s$, (f) $c = 1700\ m/s$.

Fu, Qiang, Yi Luo, Panos G. Kelamis, ShouDong Huo, Ghada Sindi, Shih-Ying Hsu, and Arthur B. Weglein. "The inverse scattering series approach towards the elimination of land internal multiples." *SEG Technical Program Expanded Abstracts* 29 (2010): 3456–3461.

Hsu, S.-Y. and A. B. Weglein. An analysis example examining the reference velocity sensitivity of the elastic internal multiple attenuation algorithm. Technical report, Mission-Oriented Seismic Research Project, University of Houst on, 2008.

Hsu, Shih-Ying, Einar Otnes, and Adriana C. Ramírez. "Quasi-Monte Carlo integration for the inverse scattering internal multiple attenuation algorithm." *SEG Technical Program Expanded Abstracts* 29 (2010): 3462–3467.

Jakubowicz, Helmut. "Wave equation prediction and removal of interbed multiples." *SEG Technical Program Expanded Abstracts* 17 (1998): 1527–1530.

Kaplan, Sam T., Billy Robinson, and Kristopher A. Innanen. "Optimizing internal multiple attenuation algorithms for large distributed computing systems." *Mission-Oriented Seismic Research Program (M-OSRP), Annual Report.* 2005.

Keydar, S., E. Landa, B. Gurevich, and B. Gelchinsky. "Multiple prediction using wavefront characteristics of primary reflections." *EAGE Expanded Abstracts* (1997).

Matson, K. H. *An inverse-scattering series method for attenuating elastic multiples from multicomponent land and ocean bottom seismic data.* PhD thesis, University of British Columbia, 1997.

Matson, Ken, Dennis Corrigan, Arthur Weglein, Chi-Yuh Young, and Paulo Carvalho. "Inverse scattering internal multiple attenuation: Results from complex synthetic and field data examples." *SEG Technical Program Expanded Abstracts* 18 (1999): 1060–1063.

Matson, Ken and Arthur B. Weglein. "Removal of elastic interface multiples from land and ocean bottom data using inverse scattering." *SEG Technical Program Expanded Abstracts* 15 (1996): 1526–1530.

Nita, Bogdan G. and Arthur B. Weglein. "Inverse-scattering internal multiple-attenuation algorithm: An analysis of the pseudo-depth and time-monotonicity requirements." *SEG Technical Program Expanded Abstracts* 26 (2007): 2461–2465.

Otnes, Einar, Ketil Hokstad, and Roger Sollie. "Attenuation of internal multiples for multicomponent- and towed streamer data.." *SEG Technical Program Expanded Abstracts* 23 (2004): 1297–1300.

Ramírez, Adriana Citlali and Arthur B. Weglein. "An inverse scattering internal multiple elimination method: beyond attenuation, a new algorithm and initial tests." *SEG Technical Program Expanded Abstracts* 24 (2005): 2115–2118.

Kroode, Fonsten . "Prediction of internal multiples." *Wave Motion* 35 (2002): 315–338.

Verschuur, D. J. and A. J. Berkhout. "Removal of internal multiples with the common-focus-point (CFP) approach: Part 2 — Application strategies and data examples." *Geophysics* 70 (2005): V61–V72.

Weglein, A. B., F. V. Araújo, P. M. Carvalho, R. H. Stolt, K. H. Matson, R. T. Coates, D. Corrigan, D. J. Foster, S. A. Shaw, and H. Zhang. "Inverse Scattering Series and Seismic Exploration." *Inverse Problems* (2003): R27–R83.

Weglein, A. B., F. A. Gasparotto, P. M. Carvalho, and R. H. Stolt. "An Inverse-Scattering Series Method for Attenuating Multiples in Seismic Reflection Data." *Geophysics* 62 (November-December 1997): 1975–1989.

Wavelet estimation from the reference wave in the Kristin data set

L. Tang, A. B. Weglein, P. Terenghi and J. D. Mayhan

Abstract

Wavelet estimation is an important issue in the process of seismic exploration. One possible approach consists in deconvolving the direct wave in the data by a Green's function. This approach is used with the Kristin field data tests. The estimated wavelet has been further used in multiple removal and imaging work.

1 Introduction

In seismic exploration, reflection data recorded on the measurement surface depend on both the properties of the subsurface medium and the source signature. In order to extract information about the properties of the subsurface medium from the recorded data, the contribution of the source signature must be removed. Therefore, it is important to obtain accurate wavelet information.

Weglein and Secrest (1990) provided an algorithm for wavelet extraction using the pressure field and its normal derivative on the measurement surface without knowledge of the properties of the earth. This algorithm has been implemented by Mayhan and Weglein (2009). For the Kristin data, since the normal derivative of the wavefield on the measurement surface is unknown, we choose to extract wavelet information directly from field data by exploiting the physical separation between the direct and reflected wavefield. The method used in this report has a straightforward physical meaning and does not involve complicated numerical calculation. However, its applicability is limited since the direct and reflected wavefield can only be separated in the near offset region. In the far offset area the two wavefields display an overlap. In this report we will focus our calculation in the near offset region.

2 Method

In scattering theory, we treat the actual medium as a combination of an unperturbed medium, called the reference medium, plus a perturbation. Correspondingly, the total measured wavefield P is the summation of the reference wave P_0 and the scattered wave P_s. The inverse scattering series (ISS) algorithm requires that the reference medium agree with the actual medium at and above the measurement surface (Weglein et al. (2003)). In the marine environment, such as in the case of Kristin data, since sources and receivers are located underwater, we may treat a half-space water with speed c_0, plus a half space of air as the reference medium. We consider a 1D homogeneous acoustic medium and assume that a point source and receivers are located at $\vec{r_s} = (x_s, y_s, z_s)$ and

$\vec{r} = (x, y, z)$, where z_s and z are the depths of the source and receivers, respectively. The reference wave P_0 satisfies the differential equation

$$\left(\nabla^2 - \frac{1}{c_0^2}\frac{\partial^2}{\partial t^2}\right) P_0(\vec{r}, \vec{r}_s, t) = A(t)\delta(x - x_s)\delta(y - y_s)\big\{\delta(z - z_s) - \delta(z + z_s)\big\}, \tag{1}$$

where $A(t)$ is the source signature that we pursue in this report. The corresponding Green's function satisfies

$$\left(\nabla^2 - \frac{1}{c_0^2}\frac{\partial^2}{\partial t^2}\right) G_0(\vec{r}, \vec{r}^{\,'}; t) = \delta(x - x')\delta(y - y')\big\{\delta(z - z') - \delta(z + z')\big\}\delta(t), \tag{2}$$

Fourier transforming from the time domain to the frequency domain gives

$$\left(\nabla^2 + \frac{\omega^2}{c_0^2}\right) P_0(\vec{r}, \vec{r}_s, \omega) = \tilde{A}(\omega)\delta(x - x_s)\delta(y - y_s)\big\{\delta(z - z_s) - \delta(z + z_s)\big\}, \tag{3}$$

$$\left(\nabla^2 + \frac{\omega^2}{c_0^2}\right) G_0(\vec{r}, \vec{r}^{\,'}, \omega) = \delta(x - x')\delta(y - y')\big\{\delta(z - z') - \delta(z + z')\big\}. \tag{4}$$

The expression of G_0 will be discussed in section 2.2. Thus, the reference wavefield P_0 can be calculated by

$$\begin{aligned} P_0(\vec{r}, \vec{r}_s, \omega) &= \int \tilde{A}(\omega)\delta(x' - x_s)\delta(y' - y_s)\big\{\delta(z' - z_s) - \delta(z' + z_s)\big\}G_0(\vec{r}, \vec{r}^{\,'}, \omega)dx'dy'dz' \\ &= \tilde{A}(\omega)G_0(\vec{r}, \vec{r}_s, \omega). \end{aligned} \tag{5}$$

Therefore, the wavelet can be obtained by

$$\tilde{A}(\omega) = \frac{P_0(\omega)}{G_0(\omega)} \tag{6}$$

Alternatively, in the time domain, the wavelet is the convolution of the direct wave and inverse reference Green's function,

$$A(t) = P_0(t) * G_0^{-1}(t). \tag{7}$$

Equation 7 is the method used to calculate the wavelet from Kristin data. The following two sections in this document discuss how to obtain an estimation of the direct wave on field data, and how to calculate the Green's functions. The test result of wavelet is then shown, with discussions of its angle variation and the presence of free-surface.

2.1 Direct Wave

In Kristin data, direct wave P_0 can be identified from the raw data directly where P_0 and scattered wave P_s do not overlap, as shown in Figure.1. In the more general case of an overlap, P_0 can still be isolated using the algorithm proposed by Weglein and Secrest (1990), and this algorithm has been implemented by Mayhan and Weglein (2009).

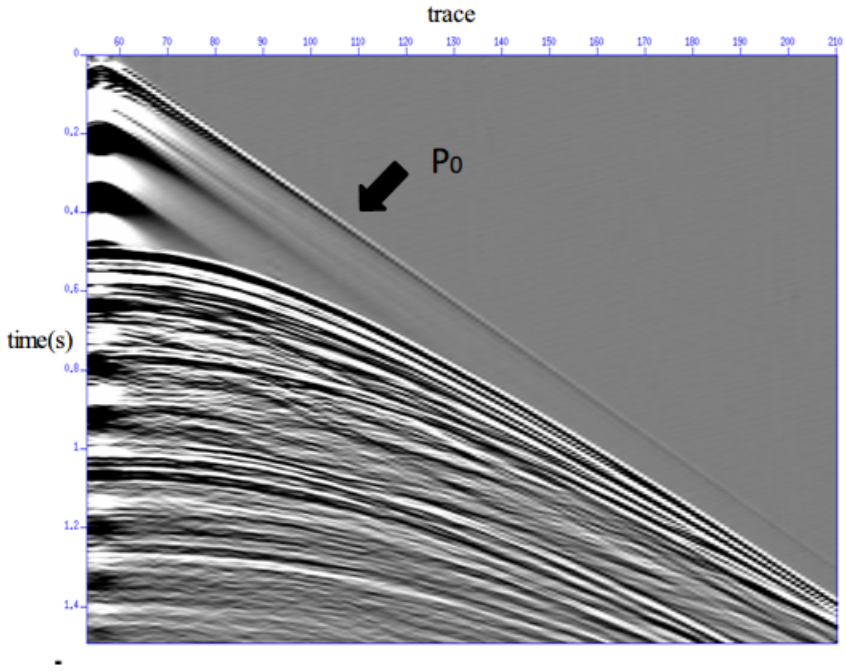

Figure 1: Kristin data, type I, cable II (sources at depth 7 m and receivers at depth 18 m).

2.2 Green's function

The reference Green's function is the causal solution of equation 4 (Morse and Feshbach (1953), chapter 7), which is

$$G_0(\vec{r},\vec{r}',\omega) = \frac{1}{4\pi}\left(\frac{e^{ikR}}{R} - \frac{e^{ikR_I}}{R_I}\right) \quad (8)$$

$$= G_0^d + G_0^{FS}, \quad (9)$$

where $k = \omega/c_0$, $\vec{r} = (x, y, z)$, $\vec{r}' = (x', y', z')$ and

$$R = \sqrt{(x-x')^2 + (y-y')^2 + (z-z')^2} \quad (10)$$

$$R_I = \sqrt{(x-x')^2 + (y-y')^2 + (z+z')^2}. \quad (11)$$

Here G_0^d represents the portion of the direct arrival from the source to the receiver, and G_0^{FS} represents the wave that experiences a reflection at the air-water interface in the reference medium. The only information required for calculating Green's function is the location of the source and receiver, therefore the reference Green's function can be calculated directly.

3 Wavelet Estimation Result

Having the reference wave P_0 obtained directly from the raw data, the reference Green's function G_0 calculated from the configuration of source and receiver, and using equation 7, the wavelet $A(t)$

can be extracted independently from each trace. In Kristin data cable II with sources located at depth 7 m and receivers at depth18 m, the wavelet is calculated as shown in Figure 2. For the deep cable (sources at depth 7 m, receivers at depth 25 m) the same method is applied, and wavelet is shown in Figure 3.

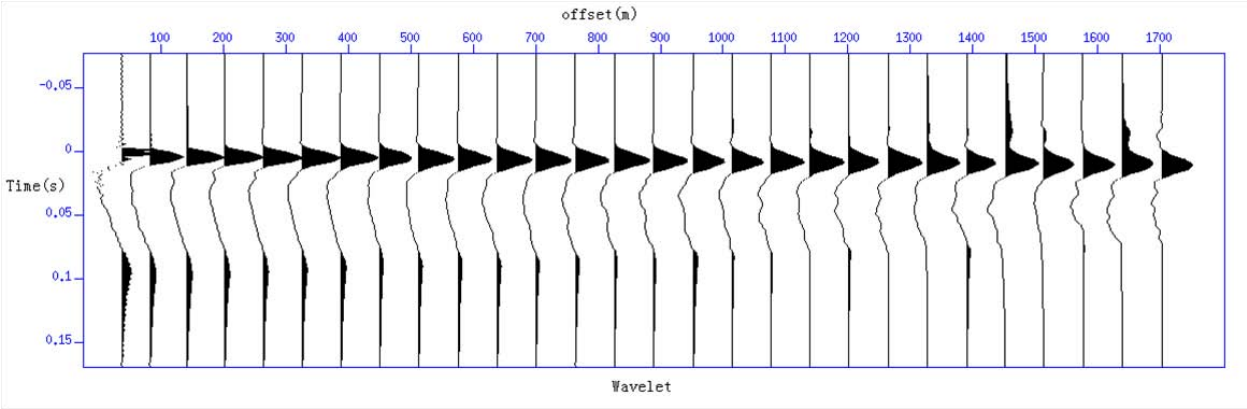

Figure 2: Wavelet $A(t)$, cable II (sources at depth 7 m and receivers at depth 18 m).

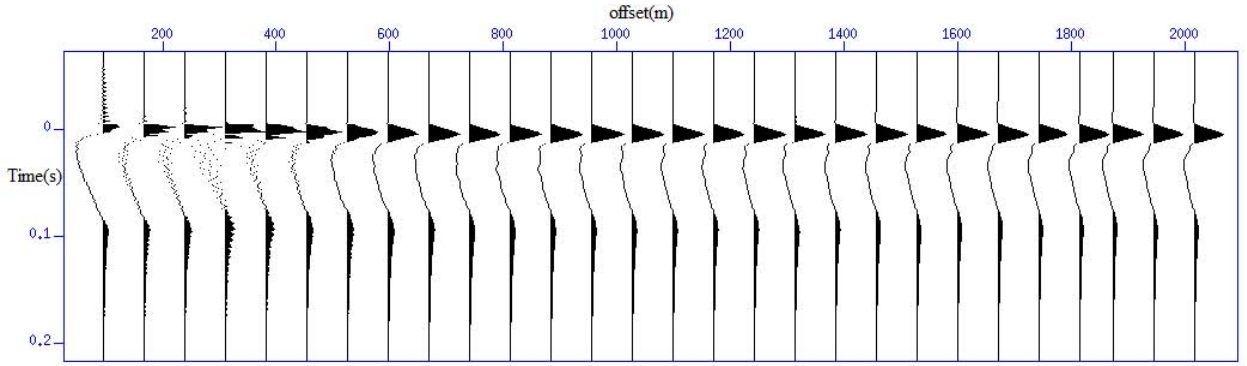

Figure 3: Wavelet $A(t)$, cable III (sources at depth 7 m and receivers at depth 25 m).

4 Discussion

4.1 Angle Variation Property

The source signature displays angle variation. A propagation angle can be obtained from the coordinates of the source and receivers. Since the wavelet is estimated independently at each receiver, its variations can be seen as a description of the air gun array's radiation pattern. From our test results of both cables, the wavelet is fairly consistent within individual shot record, not showing strong variations with angle.

We notice that in the near offset some receivers might be located very close to the shock area created by the air gun. The corresponding traces show disturbance, which reflect into the estimated wavelets. Also in the further offset area, the reference wave P_0 is getting smaller due to destructive interference between the reference wave and the scattered wave. When P_0 is comparable to the noise around them, the wavelet result is disturbed, too.

4.2 Using Direct Green's Function

The results shown so far were obtained using the total Green's function G_0 for a homogeneous half space of water, which is composed of a direct Green's function G_0^d plus a free surface Green's function G_0^{FS}. If the direct Green's function G_0^d is used instead of the total Green's function G_0 in equation 7, the result is shown in Figure 4.

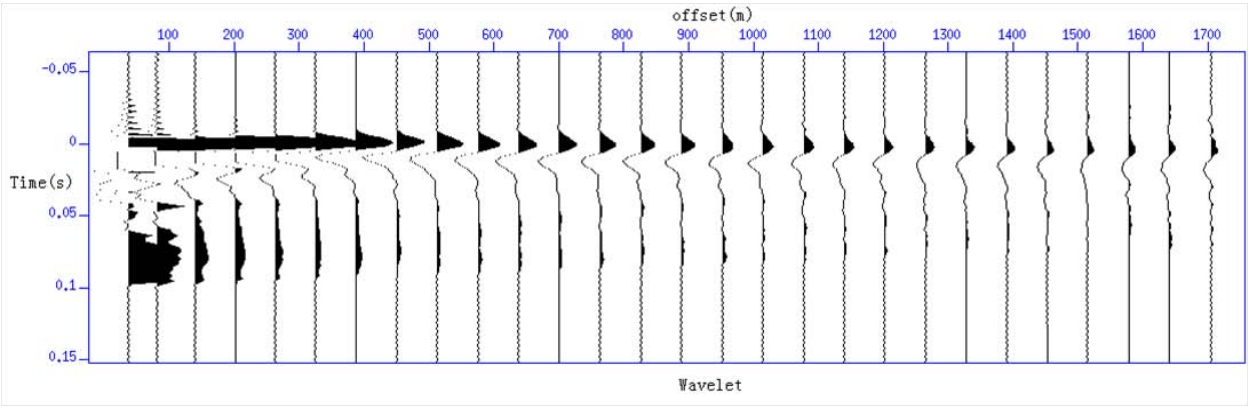

Figure 4: Wavelet $A(t)$, cable II (sources at depth 7 m and receivers at depth 18 m), using direct Green's function G_0^d.

The result in Figure 4 can be interpreted as estimates of the effect of the source in the presence of a free surface as proven by the decreasing amplitude trends for increasing offsets. The reason can be found in the expression of G_0^d. As

$$G_0^d(\vec{r}, \vec{r'}, \omega) = \frac{1}{4\pi}\frac{e^{ikR}}{R} \tag{12}$$

and

$$G_0(\vec{r}, \vec{r'}, \omega) = \frac{1}{4\pi}(\frac{e^{ikR}}{R} - \frac{e^{ikR_I}}{R_I}), \tag{13}$$

at large offset, the two terms of total G_0 tend to cancel each other, thus G_0 gets smaller, whereas G_0^d still gets larger as distance grows. On the other hand, reference wave P_0 also consist of direct arrival and free surface ghost, which will cancel each other at large offset, too. Therefore, when using total G_0 the amplitude of the wavelet is stable, while G_0^d makes the wavelet vanish.

5 Acknowledgements

We are grateful to all M-OSRP sponsors for long-term encouragement and support in this research. In particular, Statoil ASA, Petoro, ExxonMobil, Eni, Total and WesternGeco are thanked for granting access to the Kristin data and permission to publish this work. The first author would like to thank Dr. Paolo Terenghi, Jim Mayhan, and Xu Li for valuable discussion and generous help in this report, and owes deepest gratitude to Dr. Weglein for his guidance, encouragement, and support.

References

Mayhan, J. D. and A. B. Weglein. "Preprocessing 3D seismic data." *Mission-Oriented Seismic Research Program Annual Report* (2009): 10–39.

Morse, P. M. and H. Feshbach. *Methods of theoretical physics*. McGraw-Hill Book Co., 1953.

Weglein, A. B., F. V. Araújo, P. M. Carvalho, R. H. Stolt, K. H. Matson, R. T. Coates, D. Corrigan, D. J. Foster, S. A. Shaw, and H. Zhang. "Inverse Scattering Series and Seismic Exploration." *Inverse Problems* (2003): R27–R83.

Weglein, Arthur B. and Bruce G. Secrest. "Wavelet estimation for a multidimensional acoustic earth model." *Geophysics* 55 (July 1990): 902–913.

1D preprocessing of Kristin data

P. Terenghi, X. Li, Shih-Ying Hsu and Arthur B. Weglein

Abstract

We document the processing applied to a set of seismic exploration data, the Kristin survey, chosen for the first field test of the inverse scattering series direct depth imaging algorithm. As an initial approach, we choose to operate certain processing steps under the assumption of a horizontally layered earth. In order to minimize the necessary inaccuracies, we implement a filtering methodology in the Fourier domain which seeks to attenuate the portions in the data related to rapid structural or lithological variations, such as the diffractions caused by small-scale heterogeneities in the shallow overburden. The applied processing flow begins from previously de-ghosted data, and features free-surface and internal multiple attenuation using the 1D versions of the inverse scattering series multiple prediction methods.

1 Introduction

Kristin is a marine seismic exploration survey carried out in an area of the North Sea (Figure 1a) characterized by gentle structural variations and moderate reflector dips. The acquisition apparatus (Figure 1b) features multiple streamer cables towed at different depths and arranged in an asymmetric split-spread, designed to avoid the problem of near offset extrapolation (Majdanski et al., 2010). Because of both its acquisition setup and its geologic setting, the Kristin survey was chosen to demonstrate the inverse scattering series (ISS) direct depth imaging algorithm (Liu et al., 2004, 2005; Liu, 2006; Zhang et al., 2007; Wang et al., 2009) in its first field data test.

In this first approach to the Kristin data we choose to perform some of the key processing steps under a 1D earth assumption. The choice is motivated by the necessity to allow a fast turnaround for parameter testing, and enabled by the observation of the moderate dips and gentle curvatures of many reflectors of interest. Additionally, the current capture in the ISS direct depth imaging algorithm has a limited capability of handling purely multidimensional wave-propagation effects, such as diffractions, which are therefore to be attenuated or suppressed.

Although the 1D earth assumption is hardly ever true in any real-life scenarios, in an earth with mild lateral changes the 1D approach can sometimes represent a reasonable compromise between cost and benefits. Also, using data sorted in common midpoint gathers may offer symmetries which can help minimizing the inaccuracies. Moreover, in certain geologic settings, seismic exploration data are often treated with blunt noise reduction tools, such as multichannel coherency filters, to increase the signal-to-noise level, or subject to preconditioning processes which often implicitly or explicitly make a 1D earth assumption. One example of such processes is the normal moveout correction, which is often used in connection with Radon transform-based tools. Although we advocate that processing methods should accomodate the complexity of the medium, we are confident that this 1D approach represents a worthwhile experience and a viable choice for certain real-life seismic exploration problems.

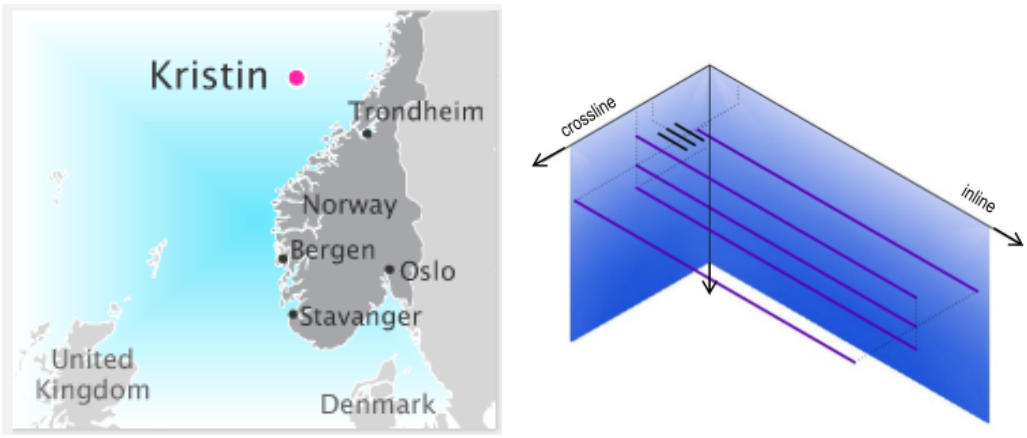

(a) (b)

Figure 1: (a) Location of the Kristin survey, off-shore Trondheim in the North Sea, and (b) layout of streamer cables for the Kristin survey (after Majdanski et al. (2010)). Three cables are towed in the vertical plane of the sail line; two more are towed laterally. The airgun array is towed within the length of the cables to form an asymmetric split spread. Courtesy of Statoil ASA and Schlumberger.

The processing chain applied to the Kristin data begins with the deghosted up-going field. The initial steps include: (1) regularization of the geometries, (2) interpolation of constant offset gathers (increase CMP fold and equalize source and receiver spacing), (3) CMP binning, (4) redatuming of source and receivers to a common depth of 7m, (5) application of source-receiver reciprocity to obtain two-sided CMP gathers. Ultimately, a subset of the data composed of 301 shots of 301 traces each, is selected and carried through the subsequent processing steps.

The above operations are performed using well-established traditional processing techniques whose detailed description is beyond the scope of this document. Here, the focus is rather on the traditional as well as ISS-based processing steps specifically aimed at conditioning the Kristin data in a way suitable for the current capture in the ISS direct depth imaging series.

The body of this report will first describe a filtering technique which mitigates the errors a 1D processing chain may produce on real-life data. Then, the prediction and subtraction of multiples related to the free surface will be documented and examples will be shown. The last section will discuss the result and issues in the current effort to suppress internal multiples.

2 Wavefield conditioning

This section describes a filtering technique based on concepts outlined in Weglein and Stolt (1999), in the context of a discussion on the *uncollapsed* imaging condition. Those ideas are used here with the aim to attenuate the portions in the data related to rapid lateral variations in the properties of

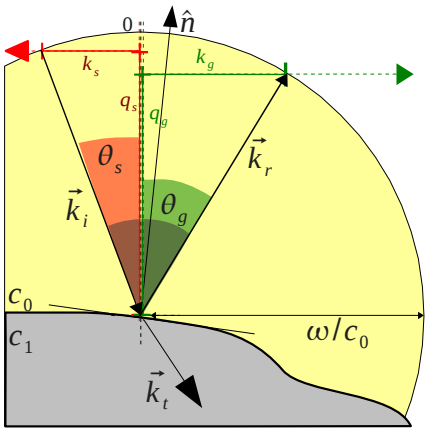

Figure 2: Wavefield conditioning. A sketch representing the portion of the wavefield that yields $|k_g - k_s|$ small, untouched in the output.

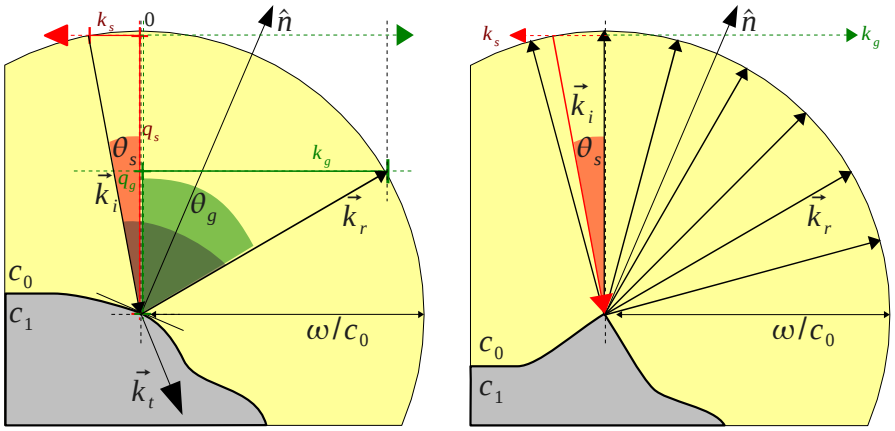

(a) (b)

Figure 3: Wavefield conditioning. Sketches representing the portion of the wavefield that yields $|k_g - k_s|$ large, suppressed in the output: (a) plane wave incident on a dipping, smooth, locally planar reflector, obeying Snell's law; (b) plane wave scattering in all directions at a highly curved feature of the earth.

the earth, such as diffractions or reflections at steeply dipping interfaces. Those wave phenomena are incompatible with the assumption of a horizontally layered earth and are likely to act as sources of error if treated with 1D algorithms.

Our approach is based on a full plane wave decomposition of the entire dataset $D(x_g, x_s, \omega)$, through Fourier transforms on time t, receiver coordinate x_g, and source coordinate x_s,

$$D(k_g, k_s, \omega) = \int\int\int_{\infty} dt\ dx_g\ dx_s e^{i\omega t - ik_g x_g + ik_s x_s}\ D(x_g, x_s, t), \tag{1}$$

where ω is the angular frequency, and k_g and k_s are the receiver-side and source-side horizontal wavenumbers. If every reflector in the earth is simplistically treated as a boundary between a homogeneous overburden with velocity c_0, and an underlying medium with velocity c_1, then k_s and k_g may also be seen as horizontal components of incident and reflected wavenumber vectors $\overrightarrow{k_i}$, $\overrightarrow{k_r}$,

$$\overrightarrow{k_i} = \{k_s, q_s\}, \quad \overrightarrow{k_r} = \{k_g, q_g\}, \tag{2}$$

where the quantities q_g and q_s represent the receiver and source-side vertical wavenumbers, constrained by the dispersion relationship (Stolt and Jacobs, 1980; Etgen, 1988)

$$q_g = signum(\omega)\ \sqrt{\frac{\omega^2}{c_0^2} - k_g^2}\ , \qquad q_s = signum(\omega)\ \sqrt{\frac{\omega^2}{c_0^2} - k_s^2}.$$

Consider a down-going plane wave, reflected upwards by a locally plane reflector characterized by an out-going normal $\widehat{n}$ (Figures 2 and 3a). The relationship between the propagation directions of the incident, reflected, and transmitted waves are governed by the equations (Cerveny, 2001),

$$\overrightarrow{k_r} = \overrightarrow{k_i} - \widehat{n}[2\overrightarrow{k_i} \cdot \widehat{n}], \tag{3}$$

$$\overrightarrow{k_t} = \overrightarrow{k_i} - \widehat{n}\left[(\overrightarrow{k_i} \cdot \widehat{n}) - \epsilon\sqrt{1/c_1^2 - 1/c_0^2 + (\overrightarrow{k_i} \cdot \widehat{n})^2}\right], \tag{4}$$

where $\epsilon = signum(\widehat{n} \cdot \overrightarrow{k_i})$ and c_0 and c_1 are the acoustic velocities in the incidence and transmission media. A plane wave traveling down from the source conserves its horizontal wavenumber when reflected upwards by a horizontal interface, so that $k_g = k_s$. In the more general case of a dipping plane reflector, the difference between k_s and k_g is proportional to the magnitude of the horizontal component of the reflector's outgoing normal. Additionally, a similar argument can be shown to hold for the relationship between the incident and transmitted wave.

Following that reasoning, and assuming the earth is characterized by moderate dips and gently curved reflectors, a filtering procedure can be devised that attenuates the regions of the Fourier transformed data volume $D(k_g, k_s, \omega)$ characterized by arbitrarily large absolute values of $k_g - k_s$. Requesting that the quantity $|k_g - k_s|$ be small amounts to discarding waves that either reflect at steeply dipping interfaces or scatter where the interface is highly curved (Figures 3a and 3b). Therefore, this procedure attenuates those portions in the data related to rapid lateral variations in the properties of the earth, such as diffractions caused by small-scale heterogeneities in the shallow overburden or steeply dipping interfaces.

Since quantities k_s and k_g can be simply related to the incidence and reflection angles θ_s (positive clockwise from the vertical) and θ_g (positive anti-clockwise from the vertical),

$$k_s = \frac{\omega}{c_0} sin\theta_s \qquad k_g = \frac{\omega}{c_0} sin\theta_g,$$

it is also possible to further characterize the effect of the filter as selectively attenuating waves that yield large differences between their take-off angle θ_s at the source and emergence angle θ_g at the receiver. It is ultimately important to emphasize how the proposed methodology takes simultaneously into account the properties of the wavefield on the source and receiver side, and therefore substantially differs from using traditional FK filters sequentially in the shot domain and receiver domain.

Examples of the effects of this procedure applied to the Kristin data are shown in Figure 4 and Figure 5.

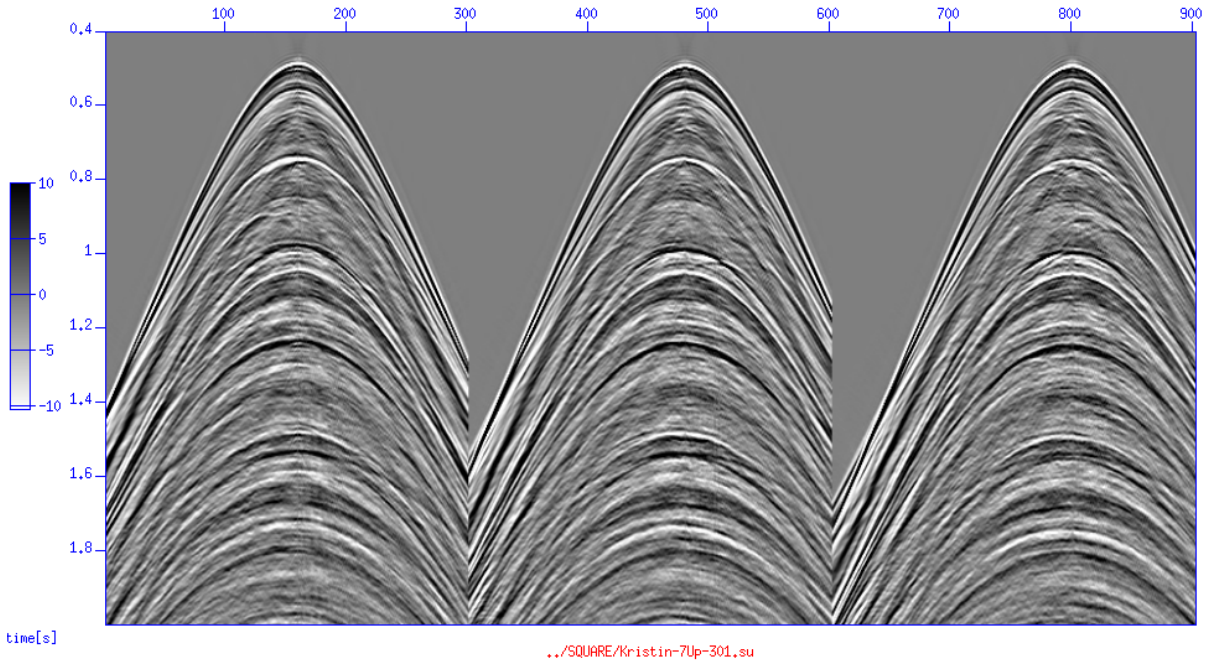

(a)

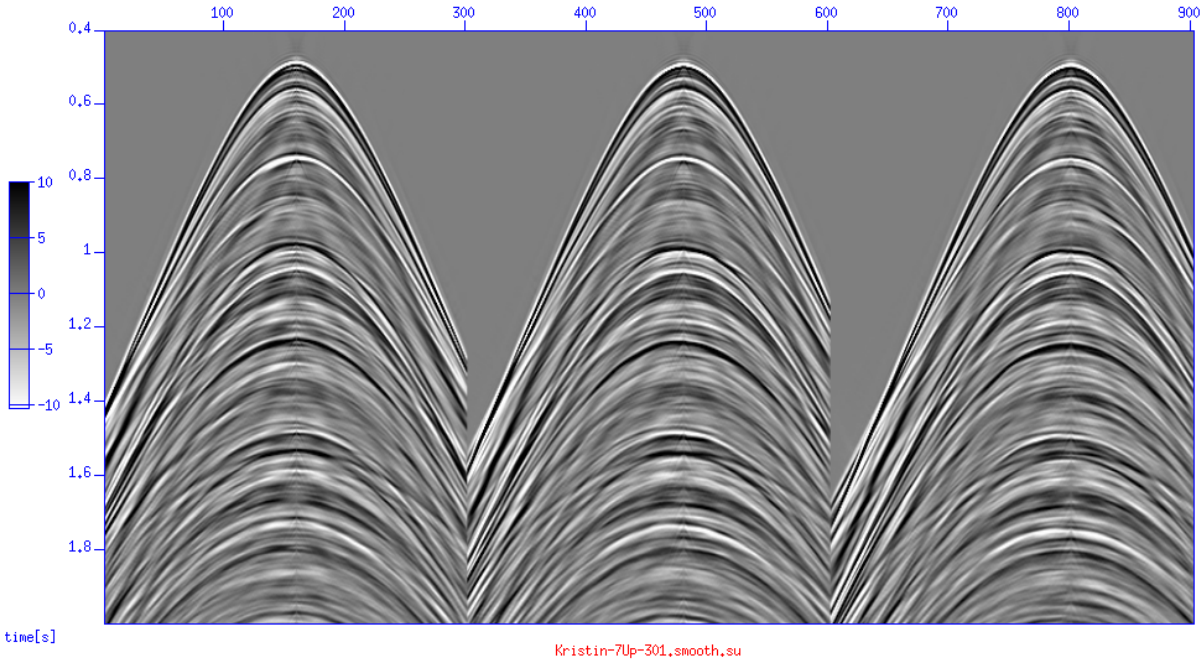

(b)

Figure 4: Attenuation of the portion of the data related to rapid lateral variations in the earth. Three shot gathers selected from the Kristin data before (a) and after (b) filtering in the Fourier domain. The comparison of (a) and (b) demonstrates the attenuation of diffracted energy, in particular between 0.5 and 0.9 s in the near offset traces. Data plotted with a t^2 gain applied.

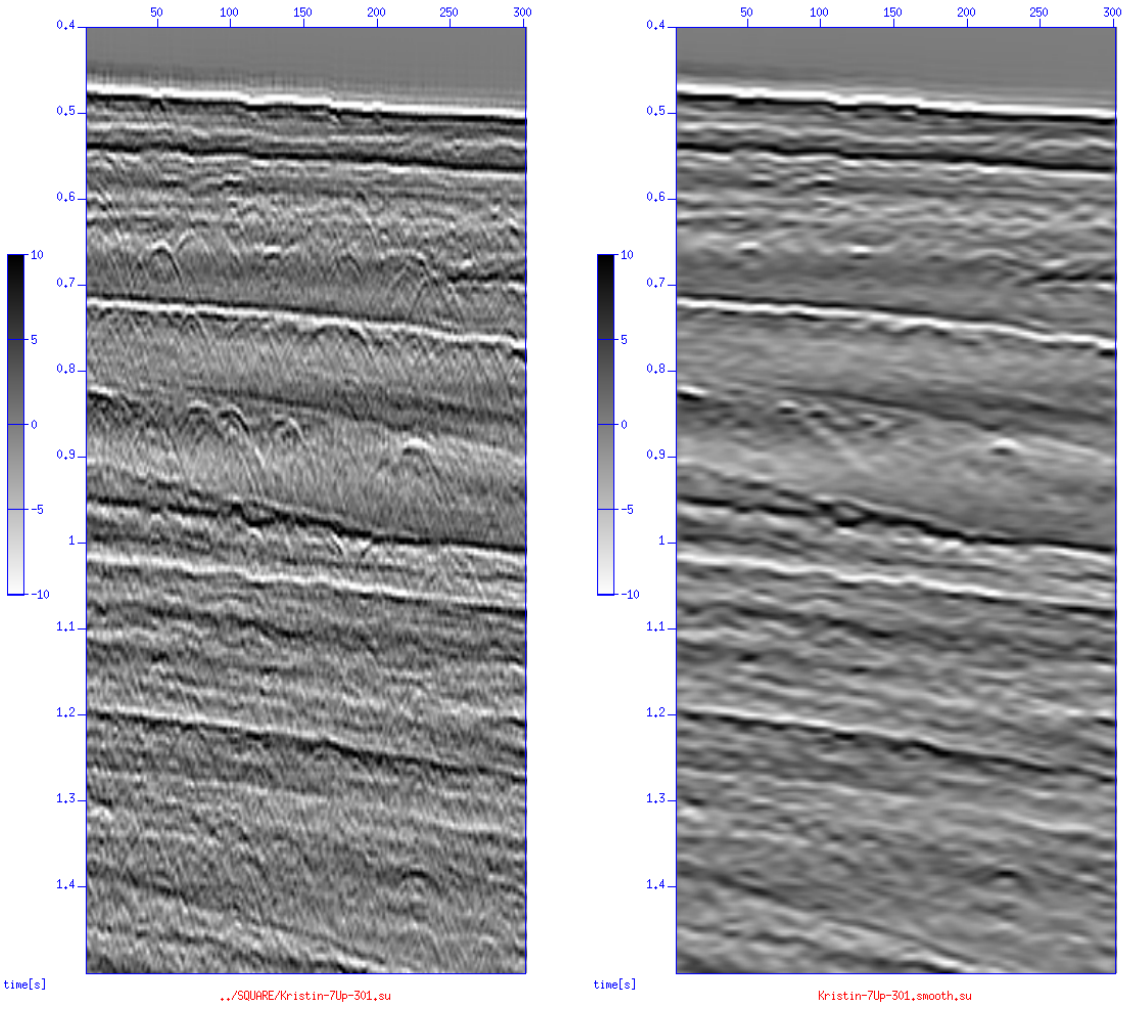

(a) (b)

Figure 5: Attenuation of the portion of the data related to rapid lateral variations in the earth. Zero offset sections of the Kristin data before (a) and after (b) filtering in the Fourier domain. The comparison of (a) and (b) demonstrates the attenuation of diffracted energy, apparent in the shallow zone between 0.5 and 0.9 s. Data plotted with a t^2 gain applied.

3 1D free-surface multiple prediction

The ISS free surface multiple prediction series is a wave-theoretical method for the removal of surface-related multiples in a multidimensional earth. Its formulation (Carvalho, 1992; Weglein et al., 1997) consists of an infinite series, having as first term D'_1 a de-ghosted version of the input data D. All higher order terms ($n = 2, 3, ...$) are defined by the recursive expression

$$D'_n(k_g, k_s, \omega) = \frac{A^{-1}(\omega)}{i\pi\rho_0} \int_\infty dk\ e^{iq(z_s+z_g)}\ D'_1(k_g, k, \omega) q(k, \omega) D'_{n-1}(k, k_s, \omega), \tag{5}$$

where ω is the angular frequency, k, k_g, and k_s are the horizontal wavenumbers, z_g and z_s the depths of receivers and sources, ρ_0 and c_0 are the reference medium's density and acoustic velocity, $A^{-1}(\omega)$ is the inverse of the source signature and

$$q(k, \omega) = sign(\omega)\ \sqrt{\omega^2/c_0^2 - k^2}.$$

Under the assumption of a horizontally layered (1D) earth, the data become invariant with respect to the midpoint location, but conserve their dependency on source-to-receiver offset,

$$D'_n = D'_n(x_g - x_s, \omega). \tag{6}$$

Thus, the integral method in equation 5 reduces to a simple analytic algorithm in the frequency-wavenumber domain (Carvalho, 1992, section 5.1),

$$D'_n(k, \omega) = \frac{2q(k, \omega)A^{-1}(\omega)}{i\rho_0}\ e^{iq(z_s+z_g)}\ D'_1(k, \omega) D'_{n-1}(k, \omega) \tag{7}$$

where k represents the Fourier conjugate to the offset variable $x_g - x_s$.

For the Kristin data, the prediction of free surface multiples is obtained using the leading order 1D ISS algorithm (equation 7 with $n = 2$), evaluated independently over each common midpoint (CMP) gather, and subsequently adjusted using a 1D (trace-by-trace) traditional least-square adaptive subtraction algorithm.

A selection of input CMP gathers and corresponding demultipled results are shown in Figures 6a and 6b. An alternative view is provided in the zero-offset section in Figures 7a and 7b. The earliest free surface multiple (related to the water bottom reflection) appears at a recording time of 0.95-1.0 s, characterized by a gentle dip towards the right-hand side of Figure 7(a,b), and closely followed by other water-column reverberations. Specifically in the interval between 0.9 and 2 s, the removal of free surface multiples reveals events which were previously hidden by large amplitude free surface multiples. The most noticeable examples are the newly visible reflectors (emphasized by arrows) at 0.9, 1.1, 1.5, and 2s.

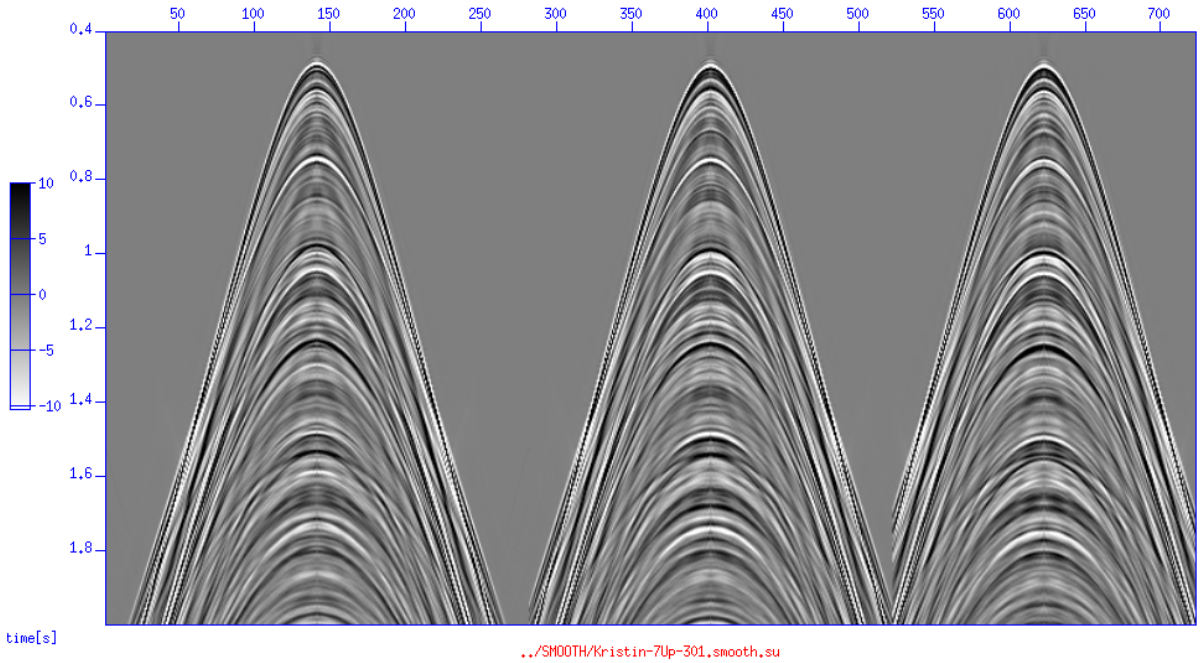

(a)

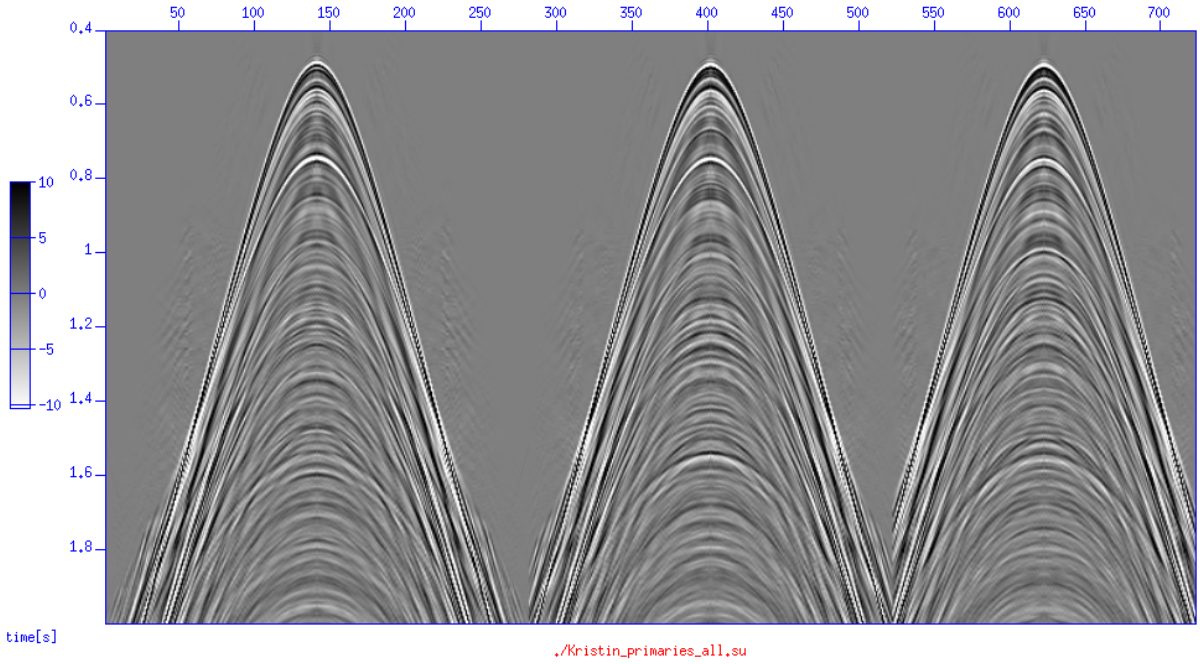

(b)

Figure 6: free surface multiple elimination. CMP gathers from the Kristin data before (a) and after ISS free surface multiple prediction and adaptive subtraction (b). The single-channel subtraction algorithm was parametrized to act on 1.5 s long temporal windows, sliding of 0.25 s. Data displayed after t^2 gain.

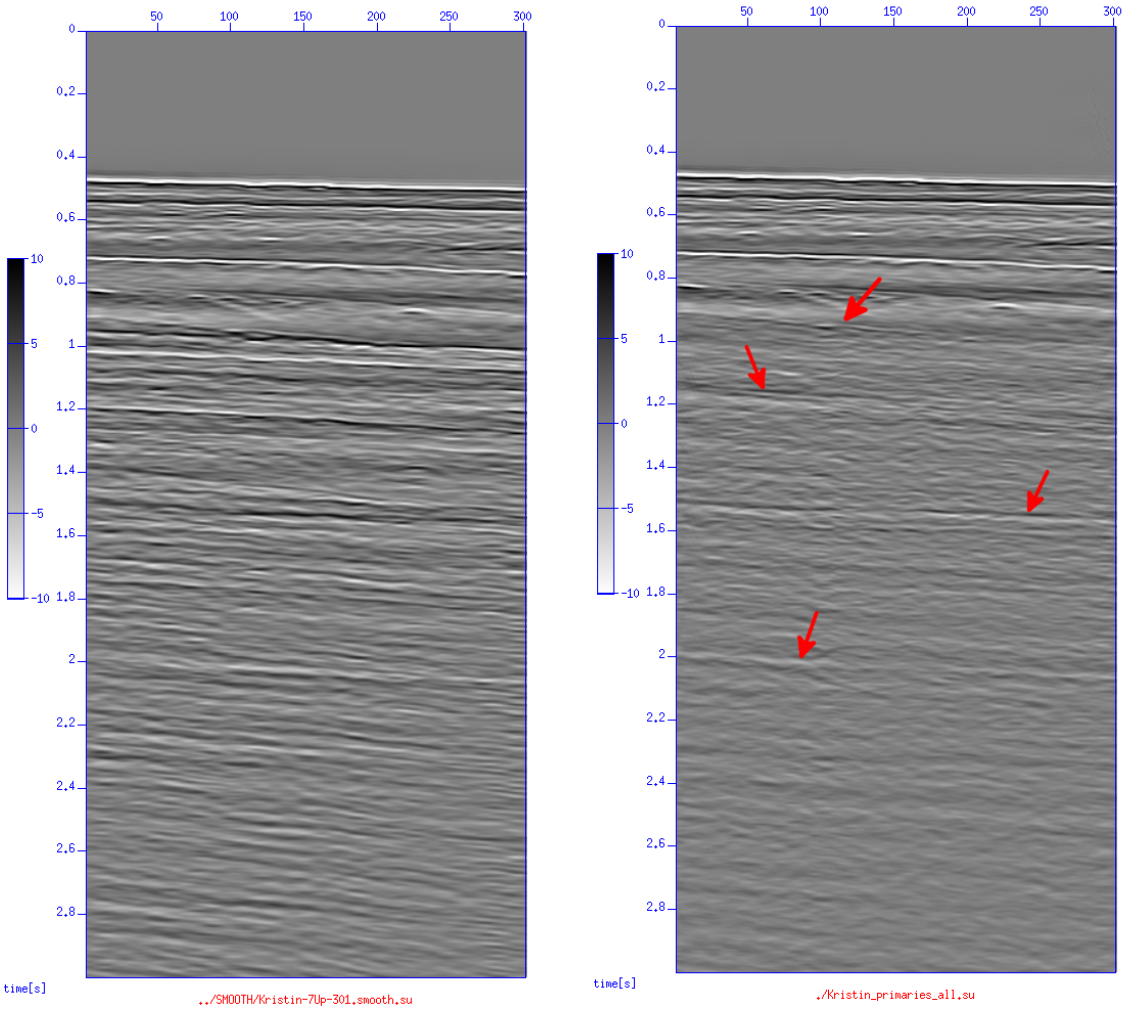

(a) (b)

Figure 7: free surface multiple elimination. Zero offset sections of the data before (a) and after ISS free surface multiple prediction and adaptive subtraction (b). The single-channel subtraction algorithm was parametrized to act on 1.5 s long temporal windows, sliding of 0.25 s. The arrows indicate reflections revealed after the removal of free surface multiples (0.9, 1.1, 1.5, and 2.0 s). Data displayed after t^2 gain.

4 1D internal multiple prediction

The ISS provide a wave-theoretical method for the attenuation of internal multiples in a multi-dimensional earth. The internal multiple algorithm provides an accurate prediction of the travel time of all internal multiples, and an approximated estimate of their amplitudes, without requiring a priori subsurface information, nor an interpretation of the portions of the earth chosen to provide the subevents to construct the prediction (Weglein et al., 2003). A more detailed description accompanied by explicatory numerical examples may be found elsewhere in this volume.

Specific 2D formulations of inverse scattering multiple attenuation series appear in Araújo (1994); Araújo et al. (1994); Weglein et al. (1997); Kaplan et al. (2004, 2005). The leading order term in the series is

$$\begin{aligned} b_3^{IM}(k_g,k_s,\omega) = \frac{1}{(2\pi)^2}\int_{-\infty}^{\infty}\int_{-\infty}^{\infty} dk_1 e^{-iq_1(z_g-z_s)} dk_2 e^{iq_2(z_g-z_s)} \\ \int_{-\infty}^{\infty} dz_1 b_1(k_g,k_1,z_1) e^{i(q_g+q_1)z_1} \\ \int_{-\infty}^{z_1-\epsilon} dz_2 b_1(k_1,k_2,z_2) e^{-i(q_1+q_2)z_2} \\ \int_{z_2+\epsilon}^{\infty} dz_3 b_1(k_2,k_s,z_3) e^{i(q_2+q_s)z_3}, \end{aligned} \tag{8}$$

where ω is the temporal frequency; k_g and k_s are the horizontal wavenumbers for source and receiver coordinates, respectively; the vertical source and receiver wavenumbers, q_g and q_s, are defined as $q_i = sgn(\omega)\sqrt{\omega^2/c_0^2 - k_i^2}$ for $i = (g,s)$; c_0 is the constant background velocity; z_s and z_g are source and receiver depths; and z_i $(i = 1,2,3)$ represents pseudodepth (depth location given by migration with background velocity). The quantity b_1 is the first order term in the series for internal multiple-free result and corresponds to an uncollapsed prestack Stolt migration (Stolt, 1978; Weglein et al., 2003) of an effective plane-wave incident data and scaled by an obliquity factor,

$$b_1(k_g,k_s,q_g+q_s) = -2iq_s D(k_g,k_s,\omega), \tag{9}$$

where $D(k_g,k_s,\omega)$ is the Fourier transformed prestack data.

In analogy to the free surface case, the method for a horizontally layered earth can be obtained by allowing the effective data to vary only as a function of source-to-receiver offset, and dropping the dependence on midpoint. In that case, nonzero values of b_1 may solely be found along the diagonal of the k_g, k_s plane (Araújo, 1994, section 4.5)

$$b_1(k_g,k_s,q_g+q_s) = 2\pi\delta(k_g-k_s) b_1(k_g,2q_g) \tag{10}$$

where $k_g - k_s$ can be seen as the Fourier-conjugate of the midpoint variable $(x_g + x_s)/2$.

Thus, the expression for the ISS internal multiple prediction algorithm for horizontally layered media may be written as

$$b_3^{IM}(k,\omega) = \int_{-\infty}^{+\infty} dz_1 b_1(k,z_1) e^{2iqz_1} \int_{-\infty}^{z_1-\epsilon} dz_2 b_1(k,z_2) e^{-2iqz_2} \int_{z_2+\epsilon}^{\infty} dz_3 b_1(k,z_3) e^{2iqz_3}, \tag{11}$$

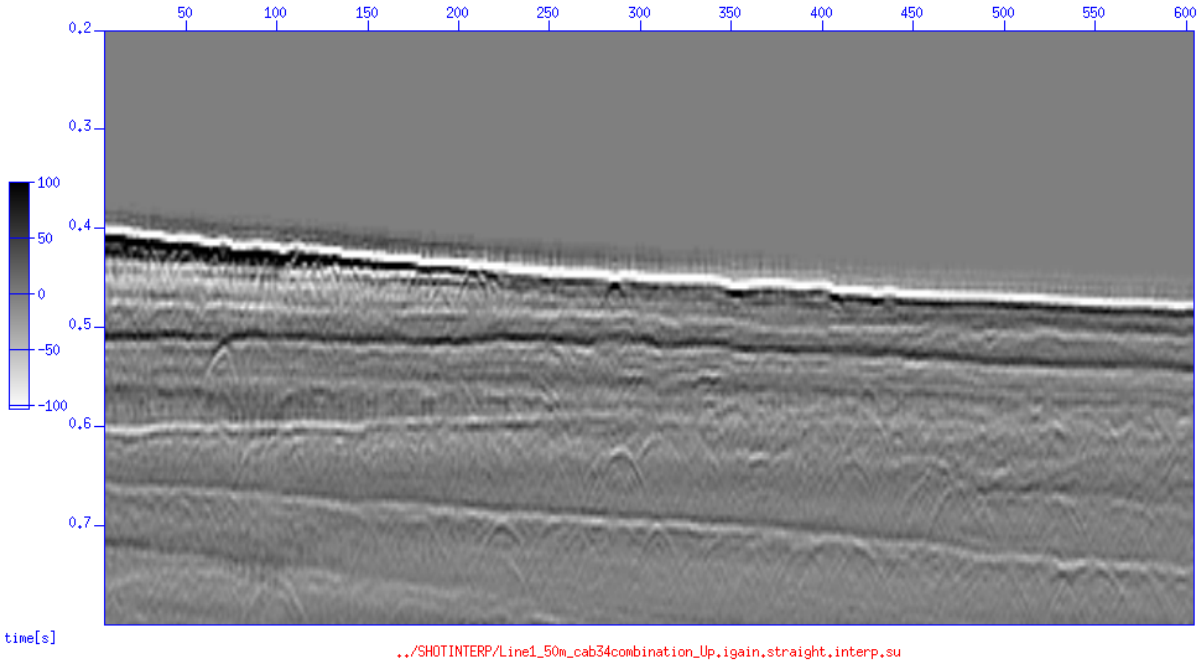

Figure 8: A zero offset section featuring the shallow reflectors in the Kristin data. At the southern end of the survey (left on of figure), a continuous internal multiple can be recognized near 0.6 s. Towards the north, the internal multiple fades out to be replaced by a discontinuous event which occasionally displays diffraction hyperbolas.

where all horizontal integrals have disappeared and the three remaining integrals operate along the pseudodepth axis. In equation 11, k represents the Fourier conjugate to the offset variable and the algorithm may be applied to a single shot record or to a common midpoint gather.

Keeping in mind that one of the main purposes of this processing effort is to condition the data to best accommodate the characteristics of the ISS depth imaging algorithm, the internal multiples of highest concern are those located in the shallow portion of the seismic records, which yield the largest amplitudes and can affect the ISS imaging the most. Therefore we bring the attention to the internal multiple originating between the water bottom and the reflectors immediately underneath (Figure 8).

At the time of writing this report, internal multiple attenuation on the Kristin data is work in progress and what follows is a discussion of the issues being faced. At the southern end of the survey, where the sea bottom is shallower and dipping more steeply than in other areas, the event with vertical traveltime around 0.6 s (left on of Figure 8) can be interpreted as an internal multiple reverberating between the water-bottom and a strong reflector at 0.51 s. Further north along the sail-line (left of Figure 8), in the area used in the examples shown in the earlier portion of this document, the interpreted internal multiple looses its continuity. Our initial attempts to treat the sub-water-bottom internal multiple in those two subregions of the Kristin data using a 1D approach have met difficulties for reasons specific to the characteristics of the multiples in those two areas.

In the northern area, the considerable slope of the sea bottom is probably at the origin of the inaccuracy of the 1D predictions. In the southern area, the sub-water-bottom internal multiple can be recognized as a cluster of tangled low-amplitude events, rather than a coherent one. The latter observation indicates that the portion of the wavefield related to that multiple should be described in terms of diffractions at the earth's most irregular features, rather than in terms of reflections at smooth interfaces, as is the case under a 1D earth assumption and within the constraints applied through the processing described in section 2.

In both scenarios the nature of the issues suggests that treating the earth as a horizontally layered medium will not yield a satisfactory result. The internal multiple removal effort on the Kristin data will therefore continue, using the 2D version of the ISS algorithm which accommodates both the steep dips in the northern area and the diffractive character of the medium in the southern end.

5 Conclusions

The Kristin survey was selected for the first field data test of the ISS direct imaging algorithm, because of its moderate structural complexity and gentle reflector dips. In the first approach to field data, a choice was made to perform some of the key processing steps under the assumption of a 1D horizontally layered earth. That choice allows a substantial reduction in the computational cost and a shorter turnaround time for the testing of parameters. A filtering methodology was implemented on the data after Fourier transforms on both source and receiver sides, to mitigate the inaccuracies which can arise in those circumstances. The filter selectively suppresses the portion of the wavefield related to the earth's rapid lateral variations, such as diffractions and reflections at steeply dipping interfaces. The removal of free surface multiples using the 1D version of the ISS algorithm, followed by trace-by-trace adaptive subtraction, proved successful at all offsets and revealed events previously swamped amid higher amplitude reverberations. The removal of internal multiples turned out to be difficult to perform under 1D earth approximation. In one case, the slant nature of the water-bottom is believed to be at the base of the 1D predictions. In another case, the multiples are thought to originate mostly by diffraction, an exclusive phenomenon of multidimensional media, and therefore unaccounted for in the 1D version of the ISS internal multiple prediction algorithm. The internal multiple removal effort on the Kristin data will therefore continue using a 2D approach, which will accommodate both the steep dips in the northern area and the diffractive character of the medium in the southern end.

6 Acknowledgements

We gratefully acknowledge Statoil ASA, Petoro, ExxonMobil, Eni, Total and WesternGeco Schlumberger Cambridge Research for the access to the Kristin data and for the permission to publish these results. Special thanks are due to Joachim Mispel, Mariusz Majdanski, and Ed Kragh, in appreciation for the time they kindly dedicated to this project.

References

Araújo, Fernanda V. *Linear and non-linear methods derived from scattering theory: backscattered tomography and internal multiple attenuation.* PhD thesis, Universidade Federal da Bahia, 1994.

Araújo, Fernanda V., Arthur B. Weglein, Paulo Marcus Carvalho, and R. H. Stolt. "Inverse scattering series for multiple attenuation: An example with surface and internal multiples." *SEG Technical Program Expanded Abstracts* 13 (1994): 1039–1041.

Carvalho, P. M. *Free-surface multiple reflection elimination method based on nonlinear inversion of seismic data.* PhD thesis, Universidade Federal da Bahia, 1992.

Cerveny, V. *Seismic ray theory.* Cambridge University Press, 2001.

Etgen, John T. Elastic Prestack Migration of Two Component Data. Technical Report 57, Stanford Exploration Project (SEP), 1988.

Kaplan, Sam T., Kristopher A. Innanen, Einar Otnes, and Arthur Weglein. "Internal multiple attenuation code-development and implementation." *Mission-Oriented Seismic Research Program (M-OSRP) Annual Report.* 2004, 83–102.

Kaplan, Sam T., Billy Robinson, and Kristopher A. Innanen. "Optimizing internal multiple attenuation algorithms for large distributed computing systems." *Mission-Oriented Seismic Research Program (M-OSRP) Annual Report.* 2005.

Liu, F., B. G. Nita, A. B. Weglein, and K. A. Innanen. "Inverse Scattering Series in the presence of lateral variations." *Mission-Oriented Seismic Research Program (M-OSRP) Annual Report* 3 (2004).

Liu, F., A.B. Weglein, K.A. Innanen, and B.G Nita. "Extension of the non-linear depth imaging capability of the inverse scattering series to multidimensional media: strategies and numerical results." 2005.

Liu, Fang. *Multi-dimensional depth imaging without an adequate velocity model.* PhD thesis, University of Houston, 2006.

Majdanski, M., C. Kostov, E. Kragh, I. Moore, M. Thompson, and J. Mispel. "Field data results of elimination of free-surface-related events for marine Over/Under streamer data." *EAGE Extended Abstract.* 2010.

Stolt, R. H. "Migration by Fourier transform." *Geophysics* 43 (1978): 23–48.

Stolt, R. H. and B. Jacobs. "An approach to the inverse seismic problem." *Stanford Exploration Project (SEP)* 25 (1980).

Wang, Zhiqiang, Arthur B. Weglein, and Fang Liu. "Note: A derivation of the HOIS closed form." *Mission-Oriented Seismic Research Program (M-OSRP) Annual Report.* 2009.

Weglein, A. B., F. V. Araújo, P. M. Carvalho, R. H. Stolt, K. H. Matson, R. T. Coates, D. Corrigan, D. J. Foster, S. A. Shaw, and H. Zhang. "Inverse Scattering Series and Seismic Exploration." *Inverse Problems* (2003): R27–R83.

Weglein, A. B., F. A. Gasparotto, P. M. Carvalho, and R. H. Stolt. "An Inverse-Scattering Series Method for Attenuating Multiples in Seismic Reflection Data." *Geophysics* 62 (November-December 1997): 1975–1989.

Weglein, A. B. and R. H. Stolt. "Migration-inversion revisited (1999)." *The Leading Edge* 18 (1999): 950–975.

Zhang, Jingfeng, Fang Liu, Kristopher Innanen, and Arthur B. Weglein. "Comprehending and analyzing the leading order and higher order imaging closed forms derived from inverse scattering series." *Mission-Oriented Seismic Research Program (M-OSRP) Annual Report* (2007): 149–159.

Addressing innate data limitations in ISS imaging algorithms: distinct data regularization methods to address different types of data limitations, to facilitate and allow specific ISS imaging steps and goals

Fang Liu, Xu Li, and Arthur B. Weglein

Abstract

MOSRP's first field data test of the inverse scattering series imaging algorithm was arranged for the Kristin condensed gas field in the Norwegian Sea. Although the acquisition on a 2D line is far from the area coverage required by our wave theoretical data processing initiative, a relatively flat subsurface allows us to extrapolate the existing measurement to other azimuths and to procure an extensive area coverage by taking advantage of the radial symmetry. We construct the amplitude profile with sufficient low frequency content to further move subsurface events without velocity information. This field data test is very encouraging: The subsurface target event is migrated towards its actual depth and the event is flattened in the angle gather using the ISS imaging algorithm derived from the simplest velocity only acoustic formalism.

1 Introduction

The inverse scattering series (ISS) is a comprehensive framework for processing primaries and multiples without knowing subsurface information, with many task-specific subseries that focus on an individual objective in the seismic processing flow and is much less demanding on the frequency content of the seismic data. Its application in removing free surface and internal multiples, for example Weglein et al. (1997); Matson et al. (1999); Weglein et al. (2003); Weglein and Dragoset (2005); Ramírez and Weglein (2005); Ramírez (2007); Hsu and Weglein (2009, 2010); Fu et al. (2010), has provided significant added value and additional capabilities to the current multiple removal methods, especially retaining effectiveness in complicated geology and not demanding knowledge of the velocity field.

The seismic imaging subseries, first proposed in Weglein et al. (2000, 2002), was progressed in the velocity-only (single parameter) framework by Shaw et al. (2003); Innanen (2004); Shaw (2005); Liu et al. (2005); Liu (2006). It was later expanded for multiple parameter by Jiang and Weglein (2007); Li et al. (2008); Jiang et al. (2008); Li and Weglein (2010); Wang et al. (2009); Liang et al. (2009). The objective of this article is to study the viability of the ISS imaging algorithm in field data, especially the lack of low frequency information in the field measurements. A detailed documentation of the issues caused by missing low frequencies information can be found in Shaw (2005).

In seismic exploration, regularization procedure is often needed to convert the irregular field measurement to a regular form prefered by algorithms, or in other words to fix certain issues in the field data. For example: to regularize the non-uniform sampled data to have uniform sampling, or to fill in the mising gap in the frequency band or the measurement surrface. To address data issues discussed in this article, the following regularization methods are popular in exploration seismology,

1. Using nearest neighbor, or NMO based method to obtain uniform sampling in space.
2. Auto regression or interpolation algorithms to fill the frequency gap.
3. Deconvolution methods.
4. Asymptotics, stationary phase approximation to reduce the burden on wave theoretical processing that demands measurement everywhere.

All ISS imaging algorithms are currently formulated as a Taylor series expansion of a box and have certain innate data limitations/sensitivities/issues,

- The current form (Taylor expansion of boxes) requires low frequency information since a box contains the zero frequency information. This issue is present for all our current imaging subseries. The solution in Kristin is demonstrated in this report.
- The inconsistence between events from different angles. This issue exists for multiparameter imaging subseries, and has been addressed in Liu and Weglein (2010).

The regularization methods documented in this article to address field data limitations are oriented toward maximizing physics (in terms of both amplitude and phase) in the data and minimizing adaptive measure in processing. The major contributions of this article to allow the ISS imaging to function in the face of innate limitations are,

1. Fourier Bessel transform,
   - synthesizes a plane wave experiment with many sources, much higher energe, and much more low frequency information,
   - offers a simple and robust solution for data reconstruction and reduces the burden on offset regularization,
   - provides a fast and easy implementation of deghosting.
2. Source signature regularization,
   - makes the field experiment consistent with the ISS world,
   - greatly improves the quality of image,
   - reduces the negative impact of sparse sampling in x.
3. Source side deghosting,
   - improves low frequency,
   - implemented in the plane wave world.
4. The three steps above provide us with a quantity physically comparable to α_1 in the language of ISS, pave the way for the adaptive factor of 0.34.

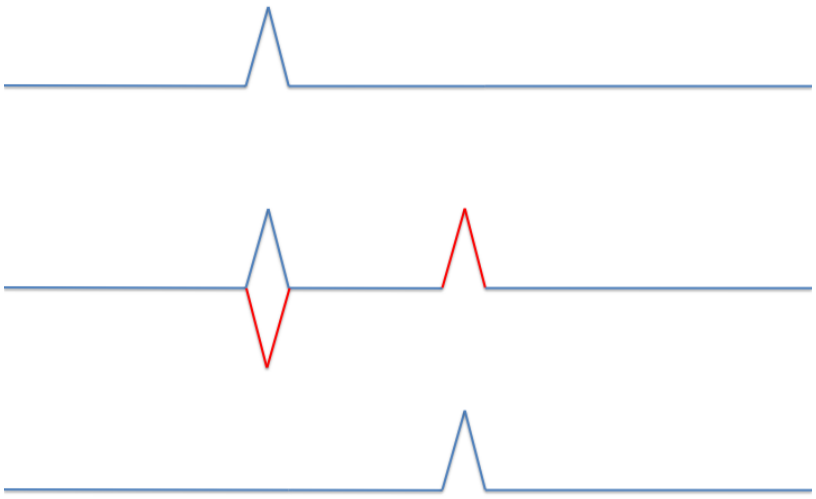

Figure 1: Top: the original spike. Middle: Add a function (in red) without zero frequency information to the original spike. Bottom: the resulting migrated spike.

One of M-OSRP's future direction is to avoid this innate limitations for low frequency information by formulating algorithms to move spikes rather than boxes. The ISS internal multiple removal subseries is operated on spike events, and has much less dependency on low frequency information. The internal multiple subseries takes advantage of structures very similar to cross correlation rather than a simple integral in the imaging subseries. The difference between two boxes has zero frequency information, that is why the current imaging subseries demands low frequency to be effective. One the other hand, the difference between two spikes has no zero frequency information, this fundamental difference implies that the effectiveness of the new imaging form should remain without low frequency as illustrated in Figure 1.

The following items are some unfavorable facts we faced in this experiment.

- Compared with the original field data, the input data at our stage went through a gain of approximately the order of t^2 to boost the deeper events. It is highly possible that this gain was applied to convert the 3D propagation in the data to 2D propagation favored by many seismic processing packages. Our wave theoretical methods are derived for real propagation in the actual 3D world. Upon the advice of Terenghi, we applied a t^{-2} gain to undo its effect.
- In the process of regularizing the acquisition into a relatively uniform sampling in space, the amplitude of our input data was altered by NMO like operations based on the velocity model.
- The original Q-marine data were grouped to enhance signal/noise ratio. This operation changes the recording at the physical location and causes array effects. Our wave theoretical methods prefer single sensor measurement obtained in each physical location. Feng et al. (2002) described some unfavorable impacts of array effects on inverse series.

- Missing zero offset data: the minimum offset for the towed streamers is 35 m in the example presented in this article. In the previous numerical examples we tried, we have split spread synthetic data with zero minimum offset.
- 2D acquisition in a three dimensional world.
- The original lateral sampling interval is very big: 37.09 m. By increasing the size of the CDP bin, Terenghi produces CMP gathers with many more traces. The lateral sampling interval is decreased to 12.32 m after CDP rebinning. We prefer this smaller offset sampling interval for the accurate implementation of transforms over lateral coordinates.
- We used the simplest data reconstruction method (assuming a 1D earth) used to procure an area coverage of measurement. More sophisticated procedures, for example Stolt and Benson (1986); Wapenaar et al. (1992); Ramírez (2007); Wang et al. (2008), should be considered for more complicated geology.
- We applied the simplest deghosting algorithm (assuming a 1D earth) to remove the source ghost.
- The simplest ISS imaging method (velocity-only formalism) is used without any cross communication between events from different angles[1]. No curvature information is used to achieve the flattened common image gather.

Considering the amount of compromising we had to accept or make in the data processing, the richness in deterministic physics exceeds our original expectations: The target is solidly migrated toward its actual location and the ISS imaging algorithms are shown to be viable under the current field data conditions.

2 Preprocessing

In the inverse scattering series the imaging task assumes the information of the source signature (wavelet), the exclusion of direct arrivals, and the removal of ghosts and multiples.

We received Kristin field data in three stages:

- Stage I data: Three cables of measurement with irregular geometry at different depths ($z_g = 9$, 18, and 25 m, respectively) after group forming, with temporal sampling rate $\Delta t = 2$ ms. It had been used by Tang et al. (2011) to calculate the source signature (wavelet) used in this paper.
- Stage II data: Removal of direct wave and offset regularization.
- Stage III data: Separated up- and down-wavefield at another fixed depth ($z_g = 50$ m), with bigger temporal sampling rate $\Delta t = 4$ ms. We only used the up-going wavefield. Minimum offset: 35 m, maximum offset 5948 m.

[1] In more advanced ISS imaging formalism, for example Zhang and Weglein (2004); Zhang (2006); Li et al. (2008); Wang et al. (2010); Liang et al. (2010), events from different angles will communicate to kick out density contribution.

- Angle dependent wavelet from 0° to 90°: The technical details in Ziolkowski et al. (1982). It is obvious that this wavelet (defined as the radiation pattern of a seismic source in the presence of the free surface) describes the recorded wave at a very large distance from the source and has a different definition from our objective.

3 Conventions, notations, and definitions

In this article we use c_0 to denote the constant unchanged reference velocity[2]. The symbol $\stackrel{\triangle}{=}$ denotes the definition of a variable or function.

We use t to denote time and ω to denote its Fourier conjugate (temporal frequency). We put the $\widetilde{\ }$ sign above a function to denote its Fourier transform. Due to historical reasons we often use distinct Fourier convention for different situations. The Fourier transform of a function $f(t)$ in the time domain into its spectrum in the frequency domain is defined as:

$$\widetilde{f}(\omega) = \int_{-\infty}^{\infty} f(t) e^{i\omega t} dt. \tag{1}$$

The corresponding inverse Fourier transform is defined as:

$$f(t) = \frac{1}{2\pi} \int_{-\infty}^{\infty} \widetilde{f}(\omega) e^{-i\omega t} d\omega. \tag{2}$$

We use z to denote depth (the vertical coordinate), and its Fourier conjugate is denoted as vertical wavenumber k_z. z_g and z_s denote the depth of receiver and source, respectively. The forward and inverse Fourier transforms between z and k_z are respectively defined as:

$$\widetilde{f}(k_z) \stackrel{\triangle}{=} \int_{-\infty}^{\infty} f(z) e^{ik_z z} dz \quad , \quad f(z) \stackrel{\triangle}{=} \frac{1}{2\pi} \int_{-\infty}^{\infty} \widetilde{f}(k_z) e^{-ik_z z} dk_z. \tag{3}$$

On the other hand, the Fourier transform between $\vec{x} = (x, y)$ (the horizontal coordinates) and $\vec{k}_m = (k_{mx}, k_{my})$ (the horizontal wavenumbers) is defined with a different sign convention:

$$\widetilde{f}(k_{mx}) \stackrel{\triangle}{=} \int_{-\infty}^{\infty} f(x) e^{-ik_{mx} x} dx \quad , \quad f(x) \stackrel{\triangle}{=} \frac{1}{2\pi} \int_{-\infty}^{\infty} \widetilde{f}(k_{mx}) e^{ik_{mx} x} dk_{mx}, \tag{4}$$

$$\widetilde{f}(k_{my}) \stackrel{\triangle}{=} \int_{-\infty}^{\infty} f(y) e^{-ik_{my} y} dx \quad , \quad f(y) \stackrel{\triangle}{=} \frac{1}{2\pi} \int_{-\infty}^{\infty} \widetilde{f}(k_{my}) e^{ik_{my} y} dk_{my}, \tag{5}$$

[2]It is also called migration velocity since it is the constant velocity field input into our imaging algorithm.

$$\widetilde{f}(\vec{k}_m) \triangleq \int_{-\infty}^{\infty} f(\vec{x}) e^{-i\vec{k}_m \bullet \vec{x}} d\vec{x} \quad , \quad f(\vec{x}) \triangleq \frac{1}{4\pi^2} \int_{-\infty}^{\infty} \widetilde{f}(\vec{k}_m) e^{i\vec{k}_m \bullet \vec{x}} d\vec{k}_m. \tag{6}$$

We use x_m to denote the x-coordinate the midpoint and x_h denote the offset (source-receiver distance) in the x direction.

We use the function $c(x, y, z)$ to denote the subsurface velocity field. The difference between c and the often homogeneous reference velocity c_0 is the perturbation α,

$$\alpha(x, y, z) = 1 - \frac{c_0^2}{c^2(x, y, z)}, \tag{7}$$

which is expanded in an infinite series,

$$\alpha = \alpha_1 + \alpha_2 + \alpha_3 + \cdots, \tag{8}$$

where the first term α_1 is the part of α linear in terms of measured data, the second term α_2 is the quadratic contribution in terms of measured data, etc. α_1 is more commonly named water speed FK migration in the geophysical literature.

4 Theory

4.1 Radon transform

The Radon transform[3] is one of the critical steps in our work; the purpose of this operation is to construct an α_1 image in the velocity-only framework. Its derivation and physical meaning can be found in equation 31 of Liu and Weglein (2007) more detail can be found in Liu (2006). The Radon transform is a natural and convenient step in our parameterization. For a function with radial symmetry it reduces to the Fourier Bessel form, as described below.

A function $f(\vec{x}, t)$ can be transformed from $(\vec{x}, t)$ to $(\vec{p}, \tau)$ domain via a Radon transform:

$$F(\vec{p}, \tau) \triangleq \int_{-\infty}^{\infty} dx \int_{-\infty}^{\infty} dy f(\vec{x}, \tau + \vec{p} \bullet \vec{x}). \tag{9}$$

The equation above can also be computed from the spectrum in the frequency domain using a fast Fourier transform,

[3] It is also named (τ, p) transform or slant stack.

$$F(\vec{p},\tau) = \int_{-\infty}^{\infty}\int_{-\infty}^{\infty} dxdyf(\vec{x},\tau+\vec{p}\bullet\vec{x}) = \int_{-\infty}^{\infty} dx \int_{-\infty}^{\infty} dy \frac{1}{2\pi}\int_{-\infty}^{\infty} d\omega \widetilde{f}(\vec{x},\omega)e^{-i\omega(\tau+\vec{p}\bullet\vec{x})}$$
$$= \frac{1}{2\pi}\int_{-\infty}^{\infty} d\omega e^{-i\omega\tau}\int_{-\infty}^{\infty} dx \int_{-\infty}^{\infty} dy e^{-i\omega\vec{p}\bullet\vec{x}}\widetilde{f}(\vec{x},\omega). \tag{10}$$

By definition $F(\vec{p},\tau)$ can also be calculated from its frequency domain spectrum $\widetilde{F}(\vec{p},\omega)$ as,

$$F(\vec{p},\tau) = \frac{1}{2\pi}\int_{-\infty}^{\infty} d\omega e^{-i\omega\tau}\widetilde{F}(\vec{p},\omega). \tag{11}$$

Note that equations 10 and 11 are both Fourier transforms of the same form, and both result in the same function $F(\vec{p},\tau)$. Due to the properties of the Fourier transform, they must have the same kernel. Hence we have,

$$\widetilde{F}(\vec{p},\omega) = \int_{-\infty}^{\infty} dx \int_{-\infty}^{\infty} dy e^{-i\omega\vec{p}\bullet\vec{x}}\widetilde{f}(\vec{x},\omega). \tag{12}$$

Note that the double integral in the above expression is also a forward Fourier transform over $\vec{x}$ defined in equation 6, applied on the frequency spectrum $\widetilde{f}(\vec{x},\omega)$, with the wavenumber vector set as $\vec{k} = \omega\vec{p}$. Consequently, in the frequency domain the Radon transform in equation 9 can be calculated as a Fourier transform over $\vec{x}$ with restriction $\vec{k} = \omega\vec{p}$.

For our specific purpose, we take the p_y-component of $\vec{p}$ to be zero and use $\vec{p} = (p, 0)$ and assume radial symmetry: $f(x, y, t) = f(\rho, t)$ where $\rho = \sqrt{x^2+y^2} = |\vec{x}|$, and the above transform can be written as:

$$F(p,0,\tau) = \int_{-\infty}^{\infty} dx \int_{-\infty}^{\infty} dy f(\rho,\tau+px) = \int_{0}^{\infty} \rho d\rho \int_{0}^{2\pi} d\theta f(\rho,\tau+p\rho\cos\theta). \tag{13}$$

We evaluate the time-domain function $f(\rho,\tau+p\rho\cos\theta)$ by the inverse Fourier transform [4] from its spectrum $\widetilde{f}(\rho,\omega)$, and the expression above becomes,

[4] It is defined in equation 2.

$$
\begin{aligned}
&= \int_0^{\infty} \rho d\rho \int_0^{2\pi} d\theta \frac{1}{2\pi} \int_{-\infty}^{\infty} d\omega \widetilde{f}(\rho,\omega) e^{-i\omega(\tau + p\rho\cos\theta)} \\
&= \frac{1}{2\pi} \int_{-\infty}^{\infty} d\omega e^{-i\omega\tau} \int_0^{\infty} \rho d\rho \widetilde{f}(\rho,\omega) \int_0^{2\pi} d\theta e^{-i\omega p\rho\cos\theta}.
\end{aligned} \tag{14}
$$

The innermost integral in equation 14 can be further simplified as,

$$
\begin{aligned}
\int_0^{2\pi} d\theta e^{-i\omega p\rho\cos\theta} &= \int_0^{\pi} d\theta \left[e^{-i\omega p\rho\cos\theta} + e^{-i\omega p\rho\cos(\theta+\pi)} \right] = \int_0^{\pi} d\theta \left[e^{-i\omega p\rho\cos\theta} + e^{i\omega p\rho\cos(\theta)} \right] \\
&= 2\int_0^{\pi} d\theta \cos\left[\omega p\rho\cos\theta\right],
\end{aligned}
$$

and the original transform reduces to,

$$
\begin{aligned}
F(p,0,\tau) &= \int_{-\infty}^{\infty} d\omega e^{-i\omega\tau} \rho d\rho \widetilde{f}(\rho,\omega) \frac{1}{\pi} \int_0^{\pi} d\theta \cos\left[\omega p\rho\cos\theta\right] \\
&= \int_{-\infty}^{\infty} d\omega e^{-i\omega\tau} \int_0^{\infty} \rho d\rho \widetilde{f}(\rho,\omega) J_0(\omega p\rho).
\end{aligned} \tag{15}
$$

The last step in the above drivation uses the integral definition of the Bessel function, for example equation 9.1.18 of Abramowitz and Stegun (1965).

In this article, the angle θ is also used[5]. Its relation with p is as follows,

$$
\begin{aligned}
p &= \frac{\sin\theta}{c_0}, \\
\theta &= \arcsin\left[c_0 p\right],
\end{aligned} \tag{16}
$$

where c_0 is the reference velocity (homogeneous whole-space water speed in this example).

Assuming a bandlimited seismic source with signature equal to the first derivative of a Gaussian located at $z_s = 0$,

[5]For example, the image is carried out in the angle gather.

$$w(t) = -\frac{a^3 t}{4\sqrt{\pi}} e^{-a^2 t^2/4} \qquad \Leftrightarrow \qquad \widetilde{w}(\omega) = -i\omega e^{-\omega^2/a^2}. \tag{17}$$

According to equation 7.3.8 of Morse and Feshbach (1953), the causal Green's function in a 3D medium with homogeneous velocity field $c(x, y, z) \equiv c_0$ is: $G_0(r, t) = -\frac{1}{4\pi}\frac{\delta(t - r/c_0)}{r}$, where r is the distance of the receiver from the source. For receivers located near the surface with depth $z_g = h$, the recording will be:

$$f(\rho, t) = -\frac{1}{4\pi}\frac{A(t - \frac{r}{c_0})}{r} = -\frac{1}{4\pi}\frac{A\left(t - \sqrt{\rho^2 + h^2}/c_0\right)}{\sqrt{\rho^2 + h^2}}, \tag{18}$$

which can be transformed into frequency domain to have,

$$\widetilde{f}(\rho, \omega) = -\frac{1}{4\pi}\frac{\widetilde{A}(\omega)\, e^{i\omega\sqrt{\rho^2+h^2}/c_0}}{\sqrt{\rho^2 + h^2}} = \frac{i\omega}{4\pi}\frac{e^{-\omega^2/a^2 + i\omega\sqrt{\rho^2+h^2}/c_0}}{\sqrt{\rho^2 + h^2}}, \tag{19}$$

where ρ is the horizontal distance of the receiver from the source. Figure 4 shows the recorded wavefield at depth $z_g = h = 500\,\mathtt{m}$. Calculating equation 15 with equation 19 as the input, we have the corresponding transform result, shown in Figure 5.

The effectiveness of the 3D Radon transform in recovering the low frequency information from the data produced by a source without zero frequency is presented in Figure 6.

The 3D Radon trasform can perfectly recover 3D spherical divergence. For example, for both direct and reflected waves, the event will have the same amplitude regardless of the distance of the source, receiver, or reflectors. This is not true for a 2D Radon transform applied on a 3D data set.

In exploration seismology, 2D Radon transforms are more commonly used. For a function $f(x, t)$, its Radon transform $F(p, \tau)$ is defined as,

$$F(p, \tau) \triangleq \int_{-\infty}^{\infty} f(x, \tau + px)dx, \tag{20}$$

and can be computed in the frequency domain as a fast Fourier transform over τ,

$$\begin{aligned} F(p, \tau) &= \int_{-\infty}^{\infty} f(x, \tau + px)dx = \int_{-\infty}^{\infty} dx \frac{1}{2\pi} \int_{-\infty}^{\infty} d\omega e^{-i\omega(\tau+px)} \widetilde{f}(x, \omega) \\ &= \frac{1}{2\pi} \int_{-\infty}^{\infty} e^{-i\omega\tau} d\omega \int_{-\infty}^{\infty} e^{-i\omega px} \widetilde{f}(x, \omega)dx. \end{aligned} \tag{21}$$

4.2 The effects of Radon transforming a 3D wave equation

Collectively denoting the lateral variables x and y as a vector $\vec{x} = (x, y)$, we consider a 3D wave propagation in a velocity-only acoustic medium without lateral variations,

$$\left(\frac{\partial^2}{\partial x^2} + \frac{\partial^2}{\partial y^2} + \frac{\partial^2}{\partial z^2} - \frac{1}{c^2(z)}\frac{\partial^2}{\partial t^2}\right) P(\vec{x}, z, t) = A(t)\delta(x)\delta(y)\delta(z). \tag{22}$$

We apply the time-domain Fourier transform defined in equation 1 to the above wave equation to obtain a Helmholtz equation,

$$\left(\frac{\partial^2}{\partial x^2} + \frac{\partial^2}{\partial y^2} + \frac{\partial^2}{\partial z^2} + \frac{\omega^2}{c^2(z)}\right) \widetilde{P}(\vec{x}, z, \omega) = \widetilde{A}(\omega)\delta(x)\delta(y)\delta(z). \tag{23}$$

Applying the frequency domain Radon transform specified in equation 12, with $\vec{p} = (p, 0)$, the following relations are straightforward: $p_x = p$, $p_y = 0$, $k_x = \omega p_x = \omega p$, $k_y = \omega p_y = 0$, and equation 23 becomes[6],

$$\left(\frac{\partial^2}{\partial z^2} + \omega^2\left[c^{-2}(z) - p^2\right]\right) \widetilde{P}(\vec{p}, z, \omega) = \widetilde{A}(\omega)\delta(z). \tag{24}$$

Transformed back into the (τ, p) domain by applying the $\frac{1}{2\pi}\int_{-\infty}^{\infty} e^{-i\omega\tau}$ integration, equation 24 will become a 1D wave equation with velocity $\left[c^{-2}(z) - p^2\right]^{-1/2}$,

$$\left(\frac{\partial^2}{\partial z^2} + \left[c^{-2}(z) - p^2\right]\frac{\partial^2}{\partial \tau^2}\right) \hat{P}(\vec{p}, z, \tau) = \widetilde{A}(\tau)\delta(z). \tag{25}$$

In the above equation, $\hat{P}(\vec{p}, z, \tau)$ is the Radon transform of the wavefield in equation 22 in the space-time domain. From the derivations above, it is clear that a 3D wave propagation problem can be transformed into a 1D one if the earth has no lateral variation. Since the geology in the Kristin field is relatively flat, for our initial test, we assume it has no lateral variation and derive the simplest deghosting algorithm in the next subsection[7].

4.3 Source signature regularization

Within the velocity-only framework, let us consider a 3D wave equation,

$$\left(\frac{\partial^2}{\partial x^2} + \frac{\partial^2}{\partial y^2} + \frac{\partial^2}{\partial z^2} - \frac{1}{c^2(x, y, z)}\frac{\partial^2}{\partial t^2}\right) P(\vec{x}, z, t) = A(t)\delta(x)\delta(y)\delta(z), \tag{26}$$

[6] In this case we use the symbol $\widetilde{P}$ to denote the wavefield in equations 23 and 24, although in the former case it is a function of $\vec{x}$, in the latter case it is a function of $\vec{p}$.

[7] Obviously, more complete deghosting procedures without assuming the earth is 1D, such as Zhang (2007); Mayhan and Weglein (2010); Mayhan et al. (2011), should be considered in the future for more complex geology.

which can be transformed into a Helmholtz equation in the frequency domain,

$$\left(\frac{\partial^2}{\partial x^2}+\frac{\partial^2}{\partial y^2}+\frac{\partial^2}{\partial z^2}+\frac{\omega^2}{c^2(x,y,z)}\right)\widetilde{P}(\vec{x},z,\omega)=\widetilde{A}(\omega)\delta(x)\delta(y)\delta(z). \tag{27}$$

The term source signature (wavelet) needs special attention. By wavelet we mean the one temporal function on the right hand side (source term) of the wave equation that has no spatial dependency, not the seismic event (or wave packet) propagating through the earth. To be more specific, we consider the function $A(t)$ in equation 26 as the wavelet[8]. In many situations, $\widetilde{A}(\omega)$, or the Fourier transform of $A(t)$ is used in the context without any clarification since $A(t)$ and $\widetilde{A}(\omega)$ are prepresentations of the same wavelet in different domain.

With this definition, replacing the original wavelet $\widetilde{A}(\omega)$ with a target wavelet $\widetilde{B}(\omega)$ is very straightforward: if their ratio,

$$\widetilde{f}(\omega)\triangleq\frac{\widetilde{B}(\omega)}{\widetilde{A}(\omega)}, \tag{28}$$

is stable for all frequencies[9], it can be multiplied to both sides of equation 27 to change the right hand side to $\widetilde{B}(\omega)$,

$$\begin{aligned}\left(\frac{\partial^2}{\partial x^2}+\frac{\partial^2}{\partial y^2}+\frac{\partial^2}{\partial z^2}+\frac{\omega^2}{c^2(x,y,z)}\right)\widetilde{P}(\vec{x},z,\omega)\widetilde{f}(\omega)&=\widetilde{A}(\omega)\delta(x)\delta(y)\delta(z)\widetilde{f}(\omega)\\&=\widetilde{B}(\omega)\delta(x)\delta(y)\delta(z).\end{aligned} \tag{29}$$

And consequently the wavelet in the experiment had been changed to $\widetilde{B}(\omega)$. The data we received can be obtained by multiplying the original data with the factor $\widetilde{f}(\omega)$. This operation is very simple and can be quickly implemented in the frequency domain.

4.4 Regularization of source signature: Changing the source signature to a Gaussian function

The inverse scatering series is written for an ideal source with a full bandwidth. The idea of regularization was also proposed in Liu and Weglein (2010) to address another issue incured by a bandlimited wavelet: the inconsistence between events from different angles, and it was termed as "source regularization" in that paper. In retrospect, we think it should be more specifically and appropriately named "source regularization for angle inconsistence".

[8]The meaning of the term "wavelet" is very important in this situation. The simple source signature regularization method proposed here which is derived from the simple and convenient convolution relation in the wave equation, may lead to very confusing conclusions if we have other convention of wavelet in mind.

[9]The wavelet $\widetilde{A}(\omega)$ may lack both low- and high-frequency information. We can choose the Gaussian wavelet or its various derivatives with proper frequency range that decay much faster than $\widetilde{A}(\omega)$ for high frequency, and take its derivatives to make it decay faster than $\widetilde{A}(\omega)$ in the low-frequency range.

- In the limiting case, it becomes a Dirac δ-function, the ideal form of source in the original derivation of the ISS.
- It has only one peak, is symmetrical and has good resolution.
- It is very smooth and well-suited for interpolation methods.
- A Ricker wavelet, or the second derivative of a Gaussian, is the most commonly encountered wavelet in field data.
- For a Gaussian type wavelet, for example, the first derivative and second derivative (Ricker), the low frequencies can be recovered through integration. Several examples can be found in Liu (2006).
- The spectrum of a Gaussian function: $e^{-\omega^2/a^2}$ decays much faster than the usually numerically obtained wavelet at high frequency. We can also take its n^{th} order derivative, which is equivalent to multiplying the spectrum by $(i\omega)^n$ in the frequency domain, to produce a decay faster than that of the original wavelet at the low frequency range. This makes a Gaussian type wavelet a good choice for source regularization detailed in equation 28.

The benefits of regularization are demonstrated in Figure 3 from the comparison between before and after changing the wavelet to a Gaussian: After source regularization the events become much more continuous, i.e., more favorable for the operations to kick out the density contribution[10] from the data.

5 Low-frequency analysis

The importance of low frequency is a very important issue in seismic acquisition, data processing, and interpretation is well explained in the collective report "*Low frequencies, their value and challenges*", distributed by the SEG/EAGE 2010 summer research workshop (15-20 August 2010) in Snowbird, Utah. Missing low frequencies had been regarded as an insurmountable barrier for the effectiveness of the seismic imaging subseries. The dependencies of each ISS task on the frequency content of data is shown in Table 1, and the ISS imaging subseries in the current form shows more dependency on low frequencies than both multiple removal subseries. A very important mission of our Kristin experiment is to study the viability of the ISS imaging algorithm under the current seismic acquisition conditions.

What we learned from this field data experiment is that the ability to handle missing low frequencies to a large extent depends on the algorithms themselves, especially the amount of attention paid to preserve the physics. We observed the lack of low frequency for a trace in the $(\vec{x}, t)$ domain, together with the presence of low frequency information in the (τ, p) domain, for both synthetic and field data examples. This seemingly conflicting picture about low frequency is like the two different faces of the same coin, they appear different but are two different aspects of the same wave. The solid movment of the target event towards its actual depth without using the actual velocity in

[10] Interested readers can confer Li and Weglein (2010); Wang et al. (2009); Liang et al. (2009) for further detail of this step in ISS imaging.

Dependence on temporal frequency content of the data	Task specific subseries
None	Free surface multiple removal
Very mild	Internal multiple removal
Some	Depth imaging

Table 1: The degree to which each ISS task specific subseries depends on the temporal frequency content of the data.

this experiment demonstrates that the ISS imaging algorithms, together with the proper seismic acquisition and processing methods, should not be stopped from further migrating reflection events without actual velocity velocity information by the issue of missing low frequencies.

5.1 The effects of source and receiver ghosts

The free surface (air/water boundary), with a reflection coefficient very close to -1, causes great attenuation at low frequencies. Consequently deghosting has a significant impact on boosting low frequencies andi, very importantly, in retaining the critical low-frequency information.

In a 1D experiment our simple deghosting algorithm can be derived as follows:

- The reflection coefficient of the air/water surface is -1, and water velocity is c_0;
- z_s and z_g are the depths of the source and receiver, respectively;
- and the recorded data (excluding direct wave) in the frequency domain is $\widetilde{f}(\omega)$ if the free surface is absent.

It is easy to find out that if the free surface is present, the recorded data will be[11],

$$\widetilde{f}(\omega)\left[1-e^{i2\omega z_s/c_0}\right]\left[1-e^{i2\omega z_g/c_0}\right].$$

Both factors the $1-e^{i2\omega z_s/c_0}$ multiplier caused by the source ghost, and the $1-e^{i2\omega z_g/c_0}$ multiplier caused by the receiver ghost, vanish quickly towards zero frequency and are among the major reasons for lack of low frequencies in the field data.

In this field data test, we only use the up-going wavefield, the direct wave and receiver ghost had been removed by up/down separation. We do not need to remove the second multiplier caused by the receiver ghost. The deghosting operation upon the source ghost is done by dividing the factor $1-e^{i2\omega z_s/c_0}$ from each trace in the angle domain, as described in equation 30:

[11]The effect of the free surface on the source can be described by a multiplicative factor $-e^{i2z_s\omega/c_0}$ in the frequency domain, or an image source with opposite polarity at distance $2z_s$ from the original. The total contribution of the original and image source can be described by a $1-e^{i2z_s\omega/c_0}$ multiplicative factor in the frequency domain. The same logic also applies for the effect of receiver ghost, and results in another $1-e^{i2z_g\omega/c_0}$ multiplier.

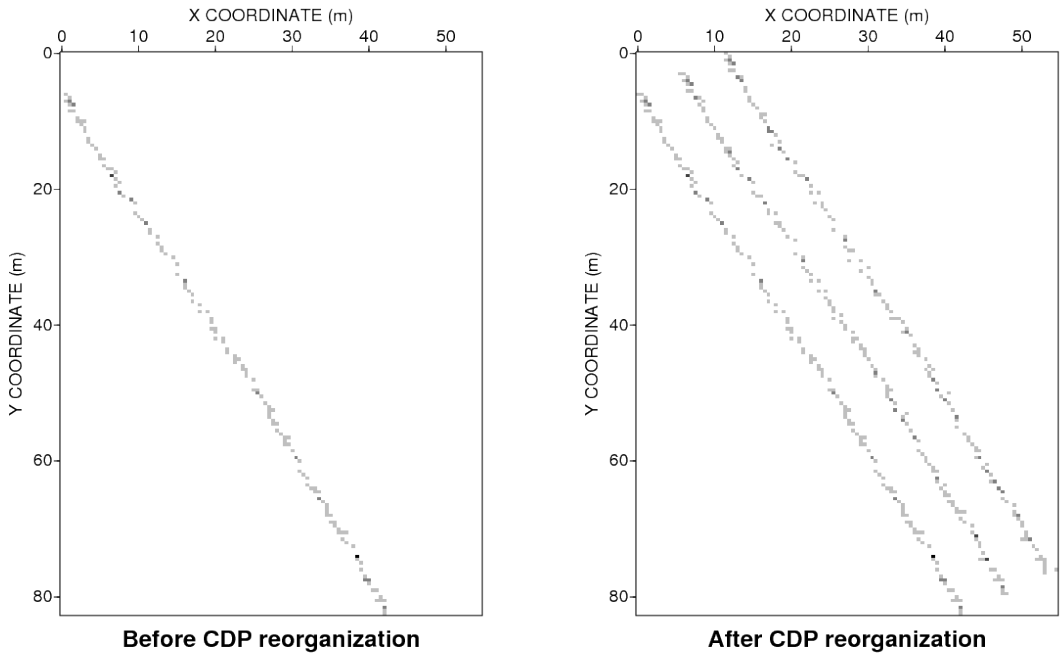

Figure 2: Distribution of midpoint coordinates. Left: before CDP rebinning, right: after rebinning. The size of the new CDP gather is three times of the old one.

$$\widetilde{B}(\omega) = \frac{\widetilde{A}(\omega)}{1 - e^{i2\omega z_s/c_0}}, \tag{30}$$

where $\widetilde{A}(\omega)$ and $\widetilde{B}(\omega)$ are the spectrum of the input and output for the deghosting operation, respectively.

The effect of the source ghost on the data can be described as multiplying by a $1 - e^{i2\omega z_s/c_0}$ factor, which is very similar to the ∂_z (partial derivative over the depth) operation. Our current ISS imaging subseries utlizes the box-like (very similar to impedance log) α_1 to do the imaging. A geological boundary between two boxes is much more difficult for visualization than a spike boundary between two empty regions. We often use the ∂_z operation on α_1 to convert the boxes into spikes and make the imaging results more familiar to the general geophysicist. We take advantage of this fact to use data without deghosting for showing spikelike events familiar to the general geophysical audience.

5.2 Critical steps in retaining low-frequency information

- High accuracy wavelet estimation
- Deghosting
- Source signature regularization

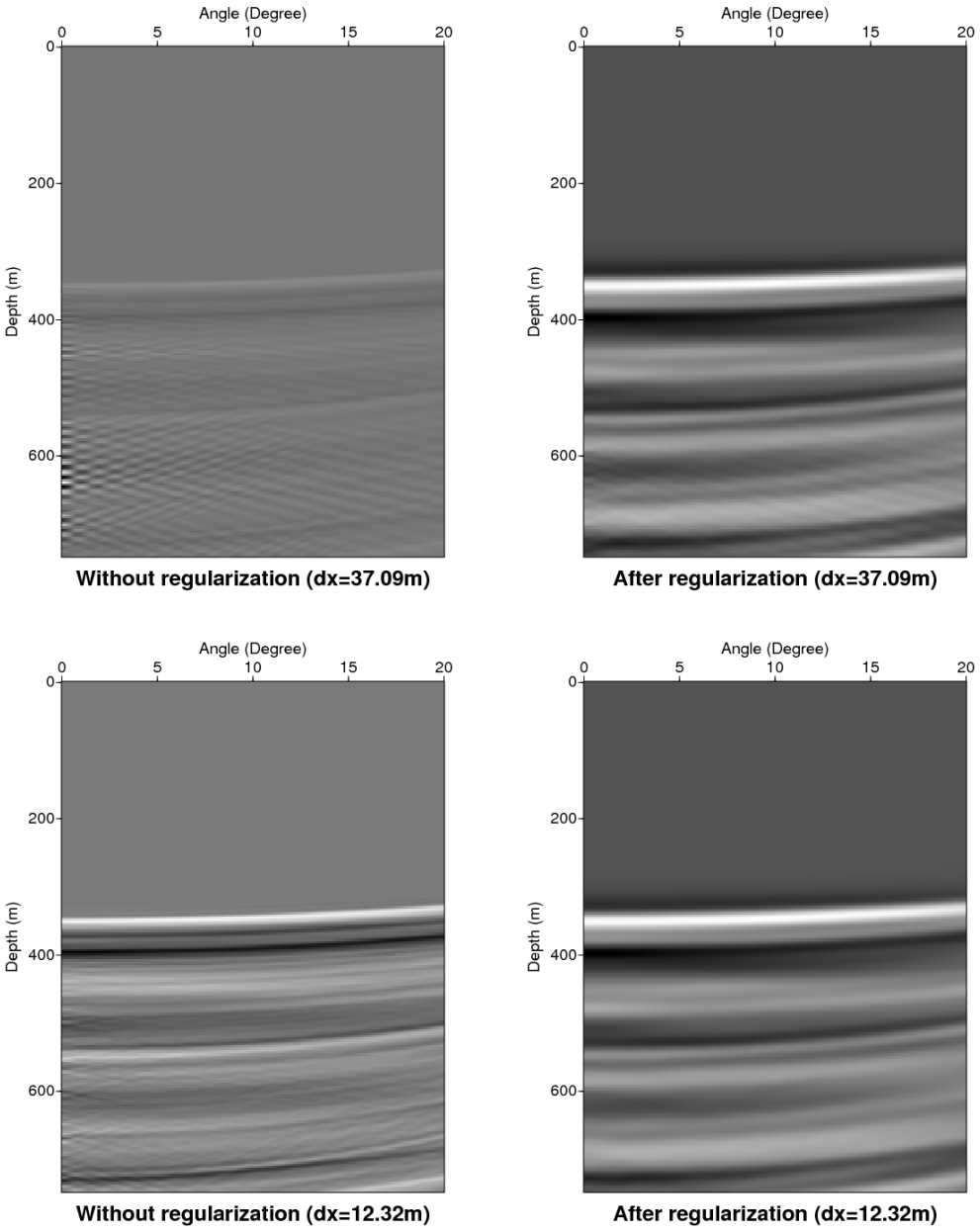

Figure 3: Four different 3D Radon transform demonstrate the benefit of source regularization described in equation 28. The smaller the value of the spatial sampling interval Δx, the better the image. Top: $\Delta x = 37.09$ m provided by the original CDP, bottom $\Delta x = 12.32$ m provided by the new CDP after rebinning. Left: without regularization, right: after regularization. Note that the deeper the depth, the more problematic the image.

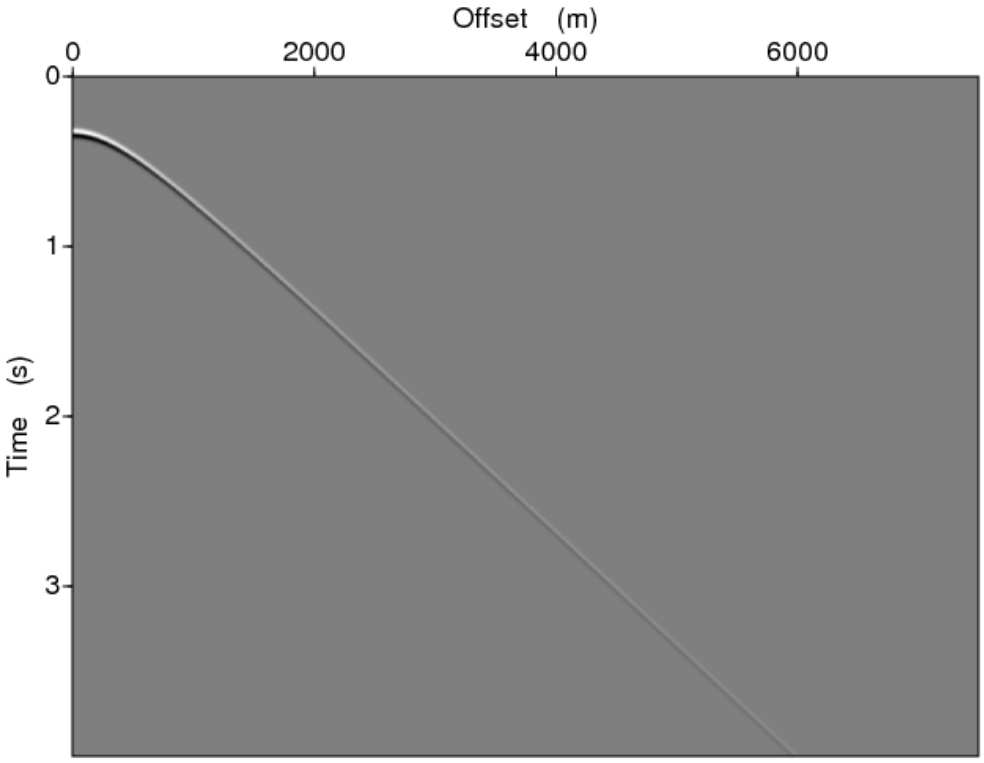

Figure 4: Input data for the Radon transform described in equation 18 with $z_s = 0\,\mathtt{m}$, $z_g = 500\,\mathtt{m}$, $a = 80\pi$.

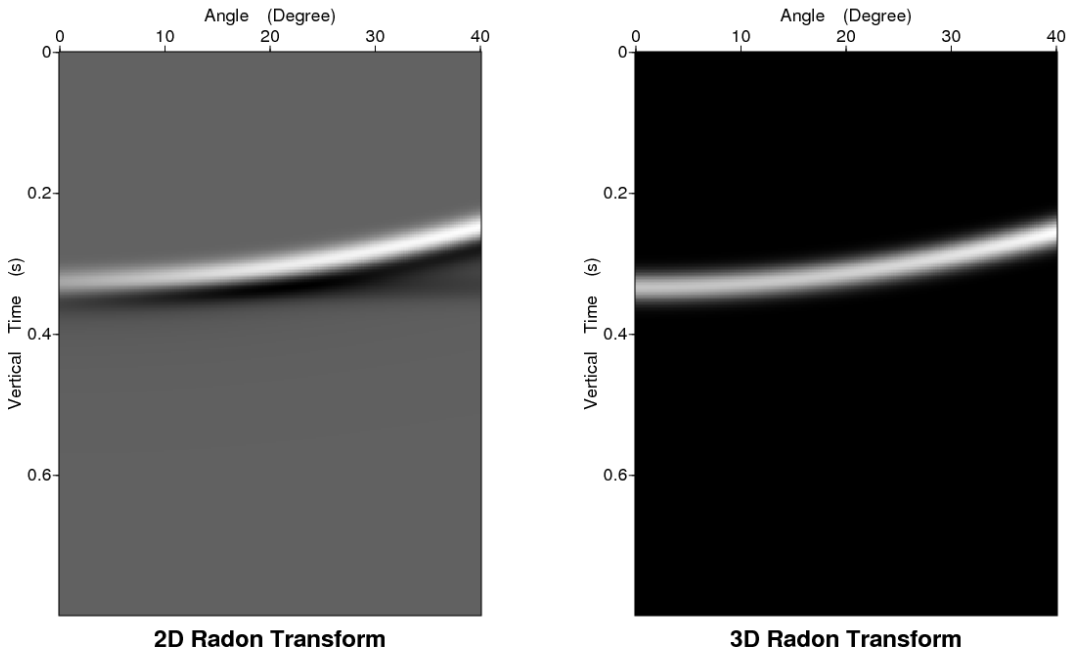

Figure 5: Radon transform comparison. Left: 2D Radon (see equation 20), right: 3D Radon (see equation 9). The input data is from Figure 4, the offset variable is regarded as the x-coordinate in the 2D Radon, and $\rho = \sqrt{x^2 + y^2}$ in 3D Radon. Note that although in both cases the traveltimes are identical for all angles, the waveform in the 3D Radon is perfectly uniform, whereas the shape of the event in the 2D Radon has a noticeable change from 0° to 40°.

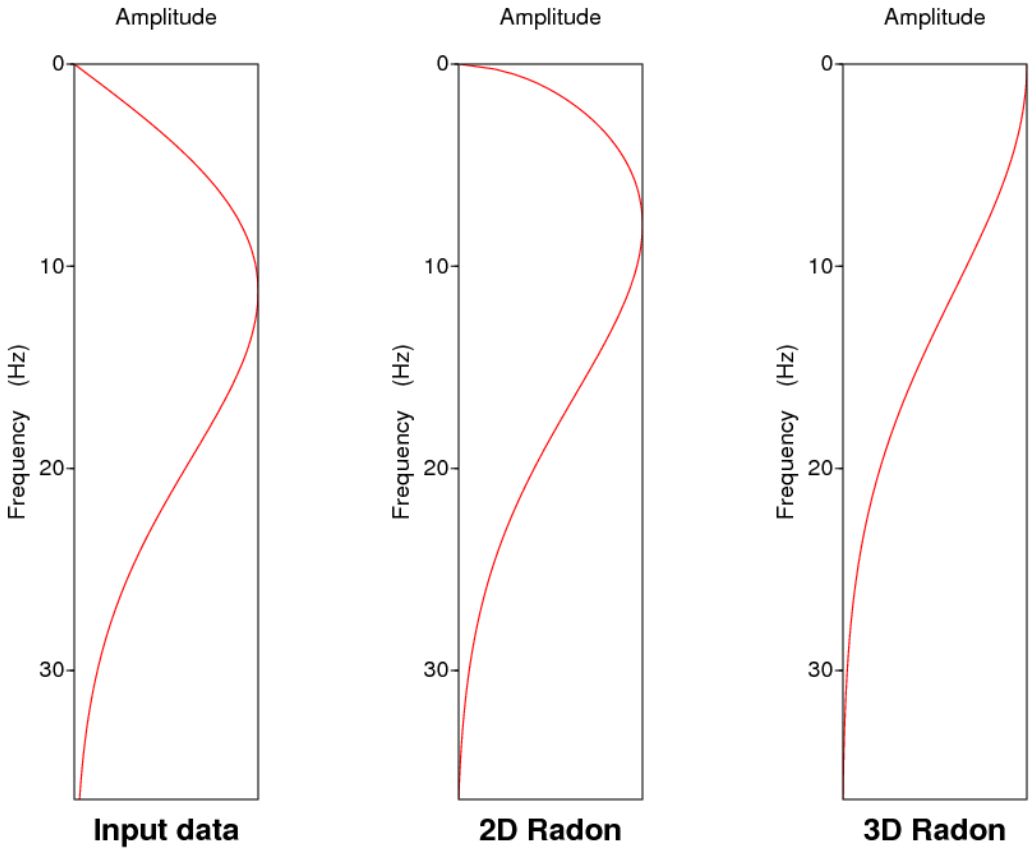

Figure 6: Comparison of amplitude spectra (left) of the input data at any fixed spatial location in Figure 4, (center) of 2D Radon (the left panel of Figure 5), and (right) of the 3D Radon (the right panel of Figure 5). Although the low frequency region is generally improved after the 2D Radon, the amplitude at $\omega = 0$ remains zero. In the 3D Radon, however, not only the improvement in low frequency is much more significant, also the amplitude at $\omega = 0$ is fully recovered. In this example we observed the lack of low frequency in the $(\vec{x}, t)$ domain, and the presence of low frequency in the (τ, p) domain.

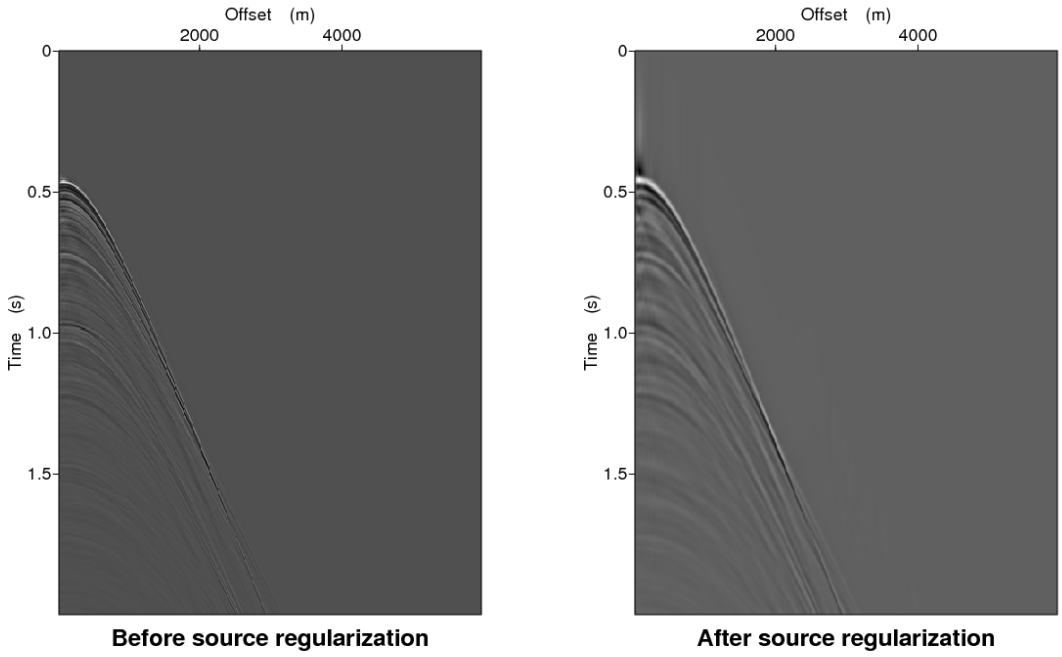

Figure 7: CMP gather used in the Radon transform. Left: without source regularization. Right: with source regularization. The minimum and maximum offsets in the gather are 35 and 5948 m, respectively. The data in the right panel is obtained in the frequency domain by multiplying the spectrum of the data on the left panel by the factor defined in equation 28 and displayed in Figure 9. A more detailed analysis can be found in Figure 10 and 11.

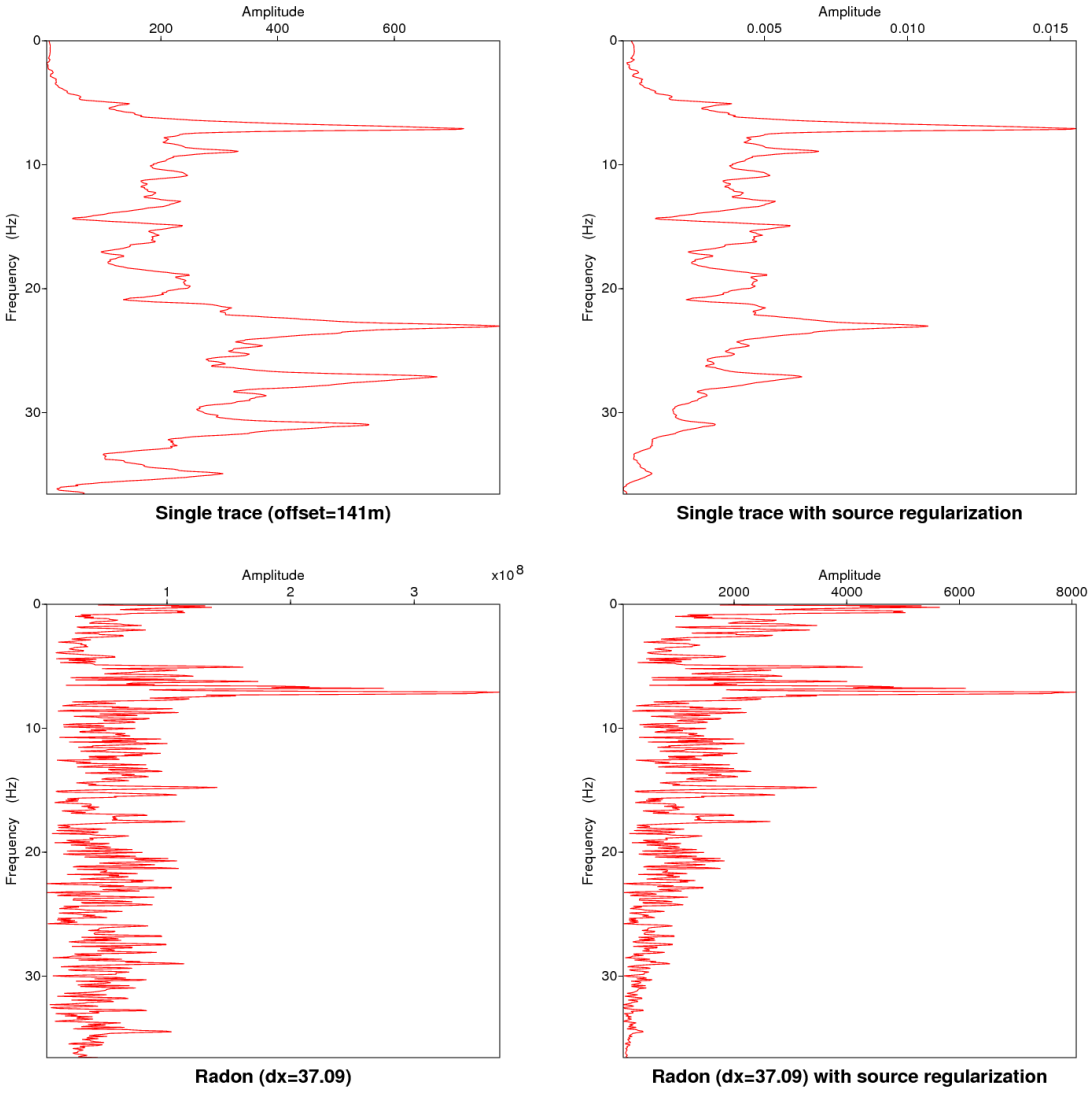

Figure 8: Comparison of amplitude spectra. Input data is from the trace with offset $x_h = 141$ m. Left: before regularization, right: after regularization.

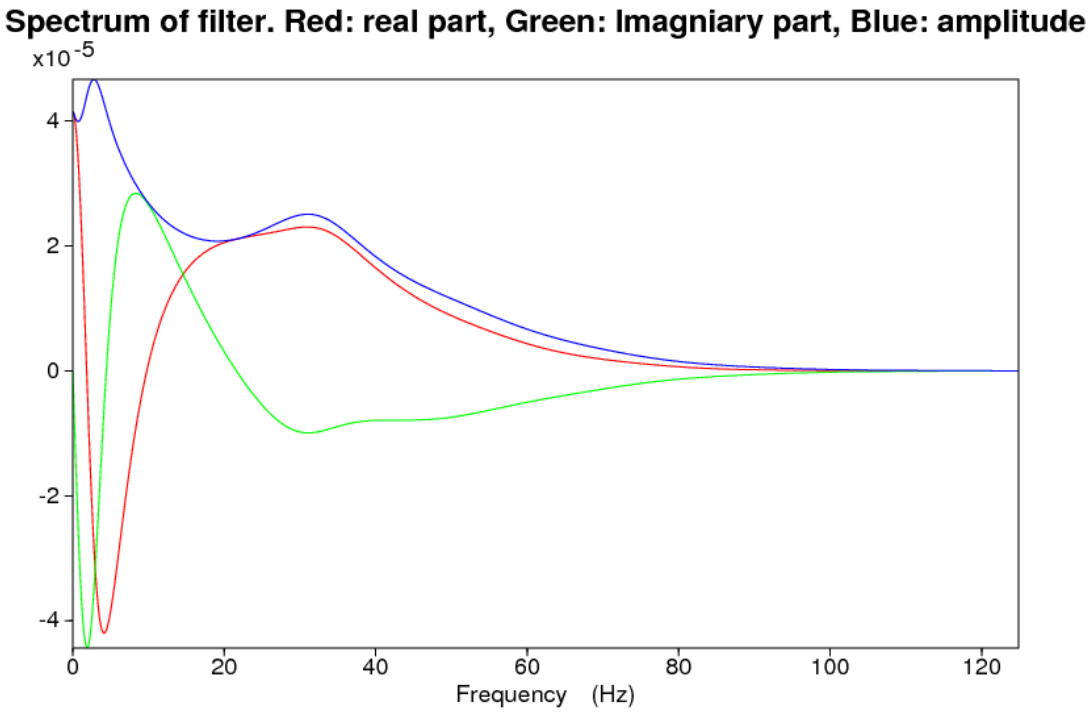

Figure 9: Diagram of the filter for source regularization in the frequency domain. Its technical detail can be found in equation 28.

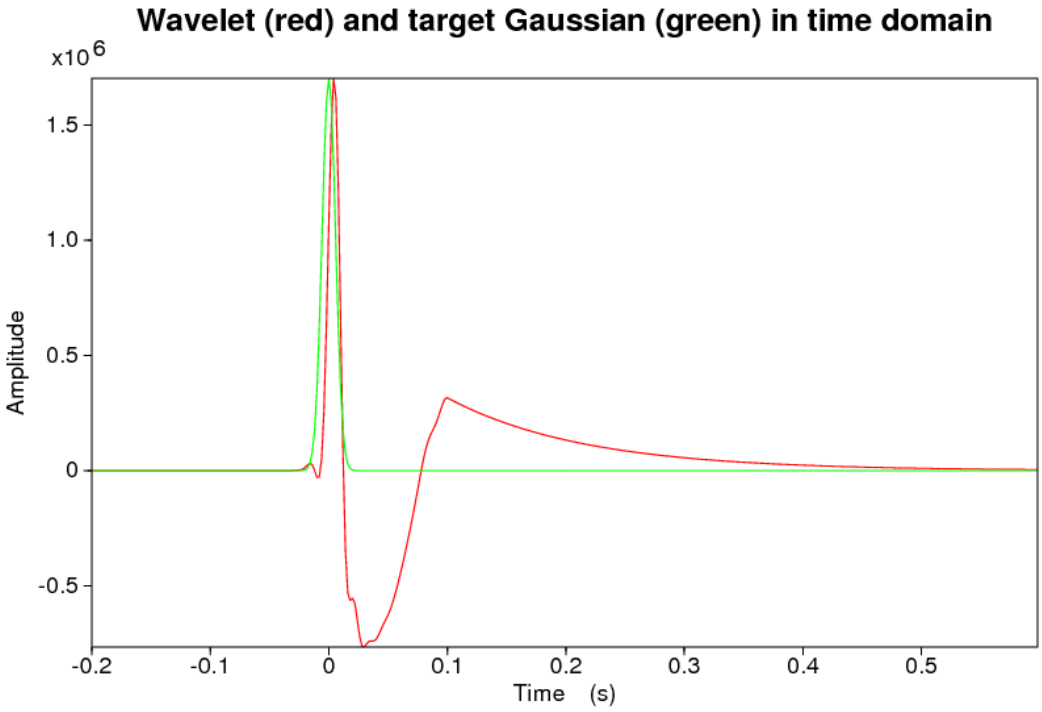

Figure 10: Original wavelet (in red) and the target wavelet we wish to have (in green). The target wavelet is $-\frac{a^2}{2\sqrt{\pi}}e^{-a^2t^2/4}$, where $a = 80\pi$. We adjust its maximum value to be the same as that of the original wavelet for easy graphical comparison.

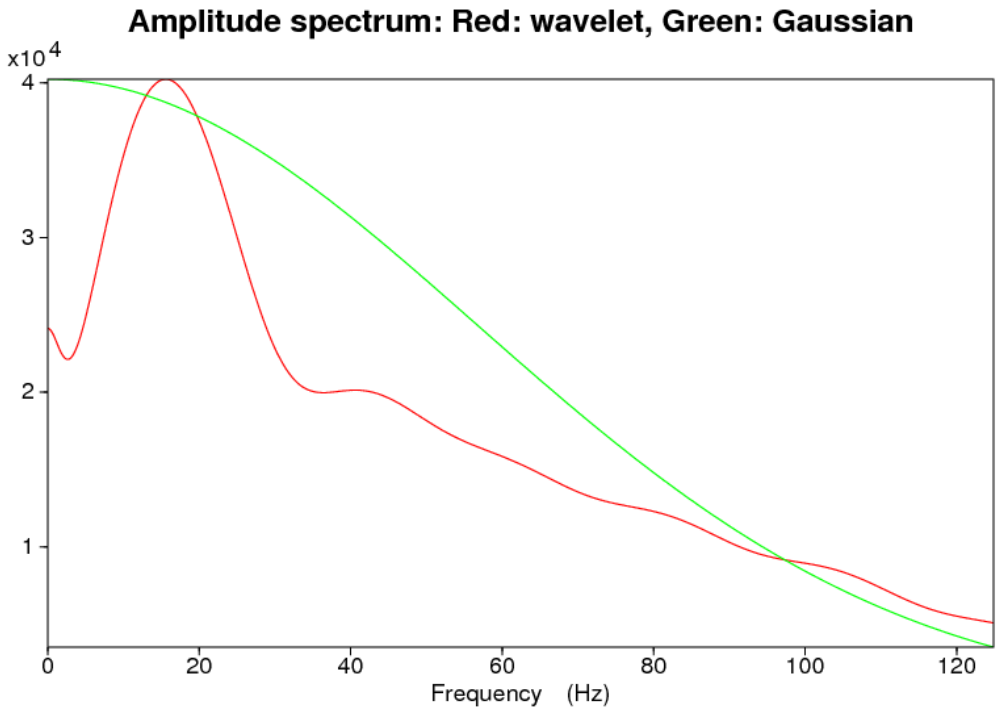

Figure 11: Amplitude spectrum of original wavelet (in red) and the target wavelet we wish to have (in green). We scale the spectrum of the target wavelet ($e^{-\omega^2/a^2}$, where $a = 80\pi$) to be of the same magnitude as that of the original wavelet for easy comparison.

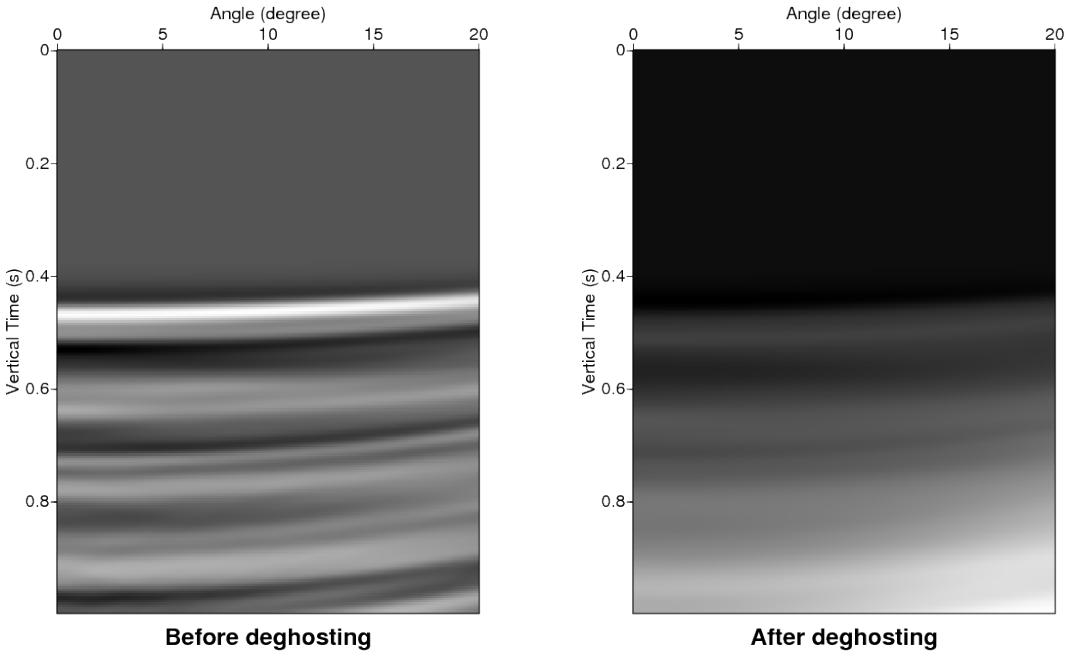

Figure 12: The extensive boxes appear after the deghosting operation.

- Sufficient sampling density in the measurement surface

6 Data processing flow

We keep one principle in mind: Extract as much deterministic physics information as possible. Maximize the predictive capability applying minimum adaptive measure. In this experiment the only adaptive measure we used is the 0.34 factor multiplied to the data to undo the amplitude alterations already existed in the data we received. The processing steps are documented in Table 2.

6.1 Processing range

Our processing is carried out for a CMP gather of the up-going wavefield. We choose the middle part of the section where maximum fold is reached. We consider the time above the first-order water-bottom free surface multiple, i.e., above 1000 `ms`.

7 Conclusions

The subsurface event is further migrated towards its actual location and becomes flattened in the angle gather using the ISS imaging algorithm without using the actual velocity field. The flattening

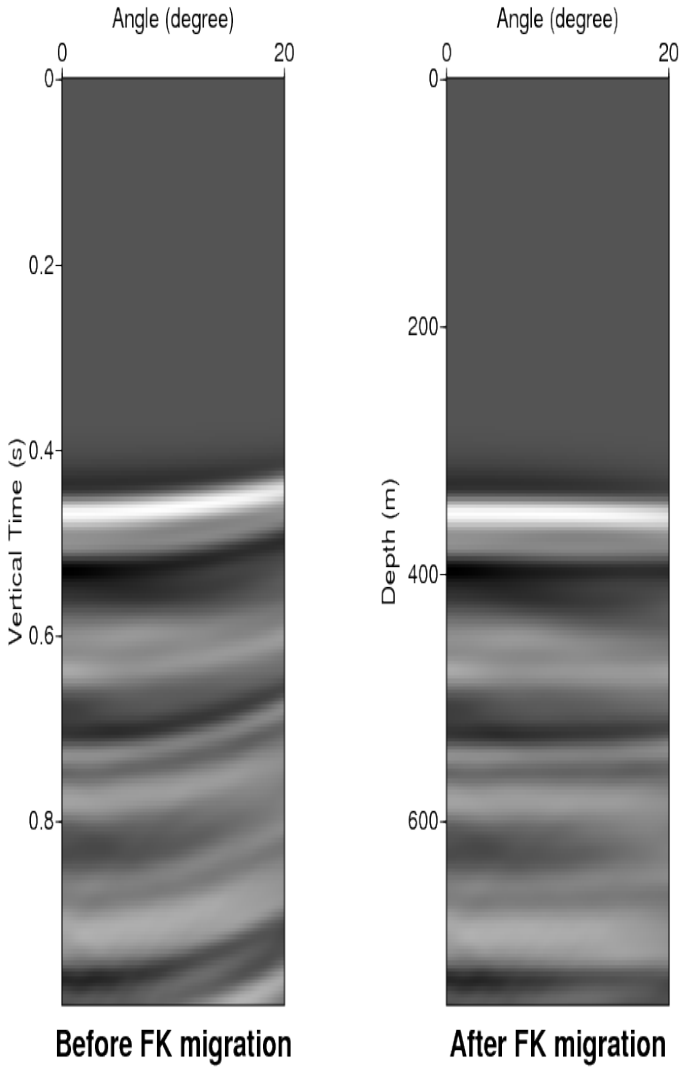

Figure 13: The water bottom becomes flat after water speed migration.

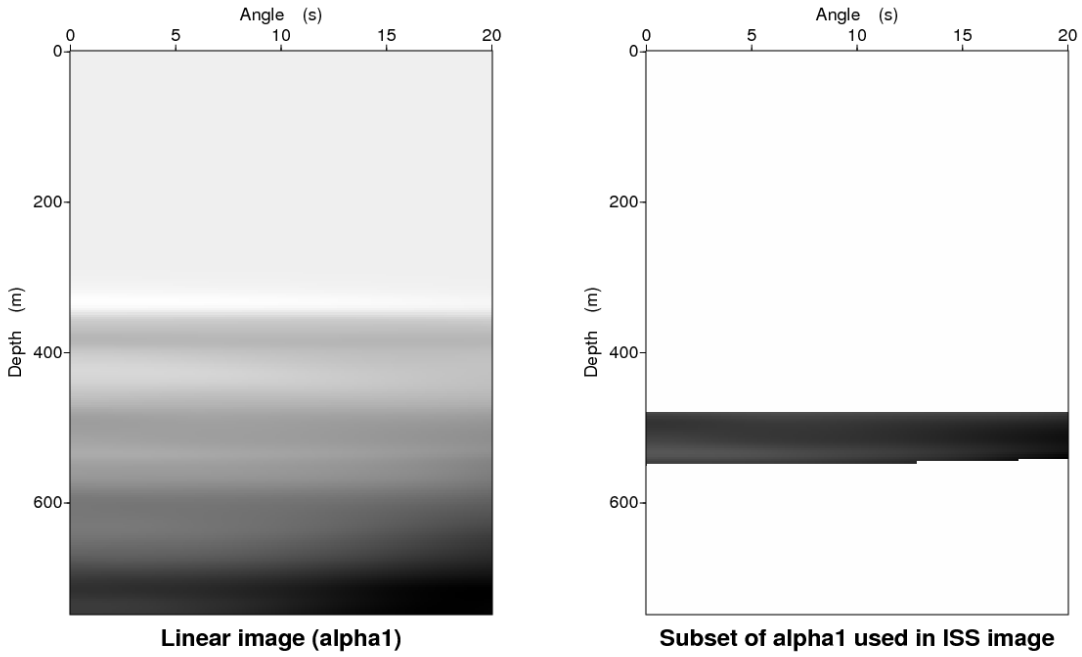

Figure 14: Subset of the linear image (α_1) used in the ISS imaging subseries.

Step	Comments
CDP reorganization	Finished by Terenghi, see Figure 2.
Wavelet estimation	Finished by Tang et. al.
t^{-2} gain	Suggested by Terenghi
Wavelet analysis and regularization	See Figure 3.
Radon transform	See Figure 3.
Deghosting	
Water Speed FK migration	
Multiply the result by a 0.34 factor	Emperical
Extract section to kick out non-velocity contribution	
ISS image subseries	Equation 2.34 from Liu (2006).

Table 2: Data processing flow for the Kristin data set.

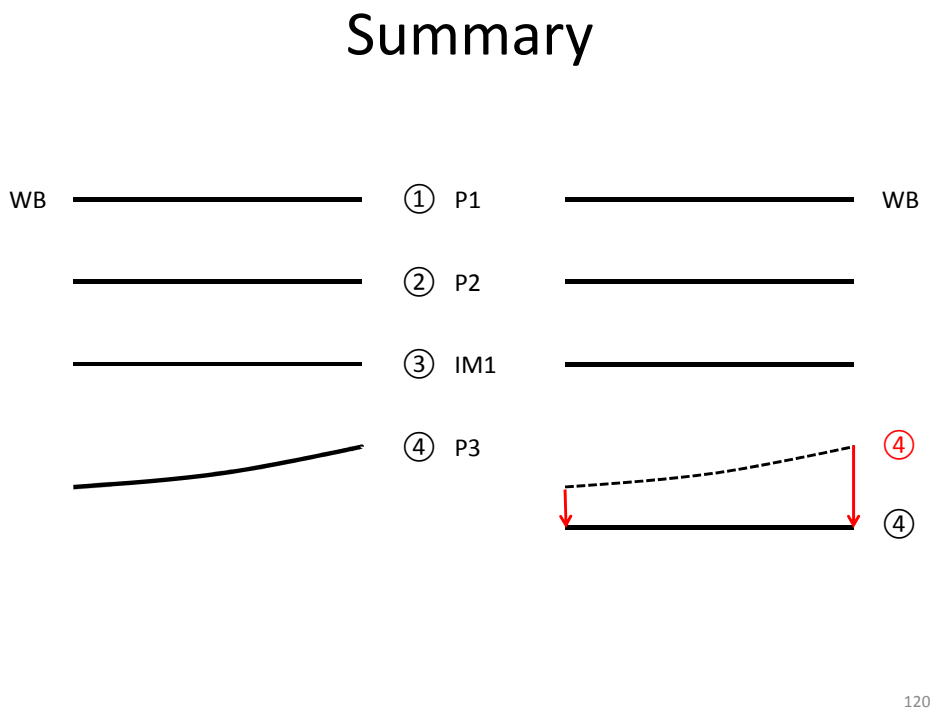

Figure 15: Summary of the results of the initial ISS depth imaging tests on the very shallow, near bottom section of the Kristin data.

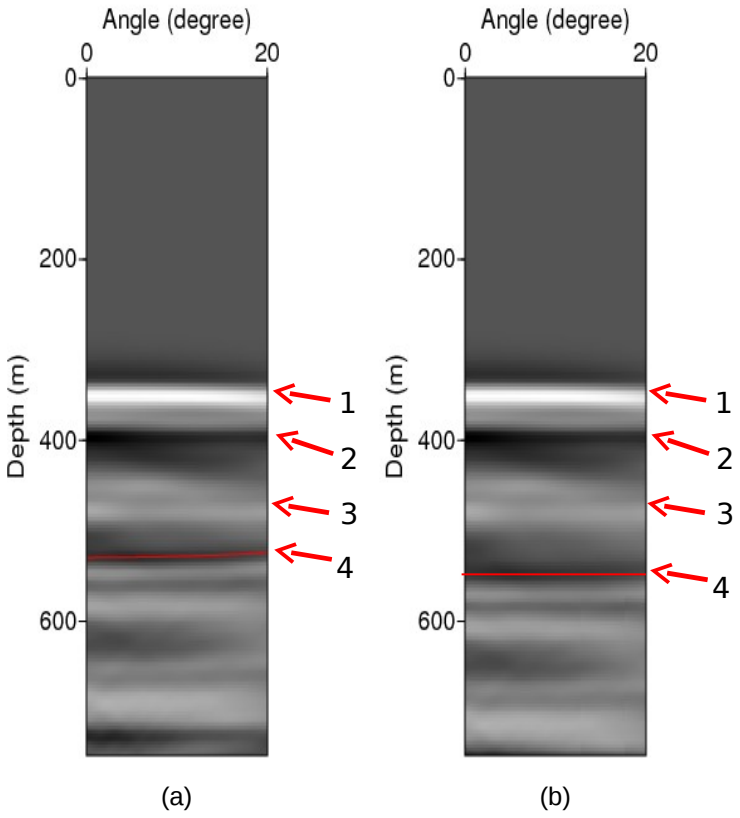

Figure 16: For the Kristin data test: Left panel shows water speed migration. Red line shows water speed migration image for event 4. Right panel shows the ISS imaging result. Red line shows ISS image for event 4.

of the subsurface event does not take advantae of any curvature information. The moving capability of the ISS imaging algorithm is not stopped by the lack of low frequencies in the field data. The viability of the ISS imaging algorithm under current seismic acquisition is established.

Further work, extending the velocity-only framework in the simplest velocity only acoustic world and taking advantage of curvature information of events and cross communication between angles, for example, acoustic model with both velocity and density variation Li et al. (2008); Wang et al. (2010); Liang et al. (2010), with density and lateral variation Chang et al. (2010), had been initiated and provided us with more insights.

8 Acknowledgment

We thank all the sponsors of M-OSRP for their support and encouragement. We have been partially funded by and are grateful for NSFCMG award DMS-0327778 and DOE Basic Sciences award DE-FG02-05ER15697. The M-OSRP group would like to thank Statoil ASA, Petoro, ExxonMobil, Eni, Total and Schlumberger/WesternGeco for granting access to the Kristin data and Ed Kragh, Joachim Mispel, Lasse Amundsen, Mark Thompson, Mariusz Majdanski and Einar Otnes for their assistance and cooperation.

The data and necessary preprocessing were provided by Statoil ASA and Schlumberger/WesternGeco. Tang, Terenghi, and Mayhan provided us with the source signature. Terenghi provided the suggestion of a t^{-2} gain and newly defined CDP gather with a much smaller lateral sampling interval.

References

Abramowitz, Milton and Irene A. Stegun. *Handbook of Mathematical Functions*. New York: Dover, 1965.

Chang, D., A. B. Weglein, and F. Liu. "Developing multidimensional depth imaging with a velocity and density varying earth." *2010 M-OSRP Annual Report* (2010).

Feng, Lianzhong, Jingfeng Zhang, and Arthur B. Weglein. "Initial analysis of the effect of receiver arrays on wavelet estimation based on the Extinction Theorem." *M-OSRP Annual Report* (2002): 149–159.

Fu, Qiang, Yi Luo, Panos G. Kelamis, ShouDong Huo, Ghada Sindi, Shih-Ying Hsu, and Arthur B. Weglein. "The inverse scattering series approach towards the elimination of land internal multiples." *SEG Technical Program Expanded Abstracts* 29 (2010): 3456–3461.

Hsu, S.-Y. and A. B. Weglein. An analysis example examining the reference velocity sensitivity of the elastic internal multiple attenuation algorithm. Technical report, Mission-Oriented Seismic Research Project, University of Houst on, 2009.

Hsu, S.-Y. and A. B. Weglein. Efficacy determination and efficiency advances for the inverse scattering series internal multiple removal: an update, land data testing and evaluation. Technical report, Mission-Oriented Seismic Research Project, University of Houston, 2010.

Innanen, Kristopher. A. *Reflector location using high-order inverse scattering series terms.* PhD thesis, 2004.

Jiang, S. and A. B. Weglein. "Deriving an imaging algorithm for a laterally invariant multi-parameter acoustic medium from the inverse scattering series." *M-OSRP Annual Report* (2007).

Jiang, S., A. B. Weglein, and S. A. Shaw. "Progressing multiparameter imaging using the inverse scattering series: An initial analytic test of the leading order imaging subseries (LOIS) closed form and its extended higher order imaging subseries (HOIS) closed form for a laterally invariant two-parameter acoustic medium." *M-OSRP Annual Report* (2008).

Li, X., F. Liu, S. Jiang, and A. B. Weglein. "Depth imaging without the velocity cares about the phase and amplitude information of events: Focusing on the use of the angle dependent amplitude information of events." *M-OSRP Annual Report* (2008).

Li, X. and A. B. Weglein. "ISS imaging for type 1 and type 2 AVO targets: analysis of forward and inverse series for target identification, part I." *2009 M-OSRP Annual Report* (2010).

Liang, H., A. B. Weglein, , and X. Li. "Initial tests for the impact of matching and mismatching between the earth model and the processing model for the ISS imaging and parameter estimation." *M-OSRP 2009 Annual meeting* (2010): 164–179.

Liang, H., A. B. Weglein, and X. Li. "Initial tests for the impact of matching and mismatching between the earth model and the processing model for ISS imaging and parameter estimation." *2009 M-OSRP Annual Report* (2009).

Liu, F. and A. B. Weglein. "Addressing the bandlimited nature of seismic source and rapid lateral variations of the Earth: source regularization and cascaded imaging operator." *2009 M-OSRP Annual Report* (2010): 72–117.

Liu, F., A. B. Weglein, B. G. Nita, and K. A. Innanen. "Inverse scattering series for vertically and laterally varying media: application to velocity independent depth imaging." *M-OSRP Annual Report* 4 (2005).

Liu, F. and Arthur B. Weglein. "Inverse scattering series with lateral variations in 3D." *M-OSRP Annual Report* 6 (2007).

Liu, Fang. *Multi-dimensional depth imaging without an adequate velocity model.* PhD thesis, University of Houston, 2006.

Matson, K. H., D. C. Corrigan, A. B. Weglein, C. Y. Young, and P. M. Carvalho. "Inverse scattering internal multiple attenuation: results from complex synthetic and field data examples." *69th Annual International Meeting, SEG, Expanded Abstracts* (1999): 1060–1063.

Mayhan, J. D. and A. B. Weglein. "Preprocessing 3D seismic data." *M-OSRP Annual Report* 9 (2010): 10–39.

Mayhan, James D., Paolo Terenghi, Arthur B. Weglein, and Nizar Chemingui. "Green's theorem derived methods for preprocessing seismic data when the pressure P and its normal derivative are measured." *81st Annual International Meeting, SEG, Expanded Abstracts.* . submitted. Soc. Expl. Geophys., 2011.

Morse, Philip M. and Herman Feshbach. *Methods of theoretical physics.* McGraw-Hill Book Co., 1953.

Ramírez, Adriana C. *I.- inverse scattering subseries for removal of internal multiples and depth imaging primaries; II.- green's theorem as the foundation of interferometry and guiding new practical methods and applications.* PhD thesis, University of Houston, 2007.

Ramírez, Adriana C. and Arthur B. Weglein. "An inverse scattering internal multiple elimination method: Beyond attenuation, a new algorithm and initial tests." *M-OSRP Annual Report* 4 (2005).

Shaw, S. A., A. B. Weglein, D. J. Foster, K. H. Matson, and R. G. Keys. "Isolation of a leading order depth imaging series and analysis of its convergence properties." *M-OSRP Annual Report* 2 (2003): 157–195.

Shaw, Simon. A. *An inverse scattering series algorithm for depth imaging of reflection data from a layered acoustic medium with an unknown velocity model.* PhD thesis, University of Houston, 2005.

Stolt, Robert H. and Alvin K. Benson. *Seismic Migration: Theory and Practice*. Ed. Klaus Helbig and Sven Treitel. Volume 5 of Seismic Exploration. Geophysical Press, 1986.

Tang, L., A. B. Weglein, P. Terenghi, and J. D. Mayhan. "Wavelet estimation from the reference wave in the Kristin data set." *M-OSRP Annual Report* 10 (2011).

Wang, Z., A. B. Weglein, and X. Li. "New capture of direct velocity independent depth imaging in a one-dimensional two-parameter acoustic earth." *2009 M-OSRP Annual Report* (2009).

Wang, Z., A. B. Weglein, and X. Li. "New capture of direct velocity independent depth imaging in a one-dimensional two-parameter acoustic earth." *2009 M-OSRP Annual Report* (2010).

Wang, Z., A. B. Weglein, and F. Liu. "Aperture-compensated linear asymptotic imaging and testing as input for the nonlinear velocity independent depth imaging algorithms of the inverse scattering series: analysis and plans." *M-OSRP Annual Report* 7 (2008).

Wapenaar, C. P. A., D. J. Verschuur, and P. Herrmann. "Amplitude preprocessing of single and multicomponent seismic data." *Geophysics* 57 (1992): 1178–1188.

Weglein, A. B., F. V. Araújo, P. M. Carvalho, R. H. Stolt, K. H. Matson, R. T. Coates, D. Corrigan, D. J. Foster, S. A. Shaw, and H. Zhang. "Inverse scattering series and seismic exploration." *Inverse Problems* 19 (2003): R27–R83.

Weglein, A. B., D. J. Foster, K. H. Matson, S. A. Shaw, P. M. Carvalho, and D. Corrigan. "Predicting the correct spatial location of reflectors without knowing or determining the precise medium and wave velocity: initial concept, algorithm and analytic and numerical example." *Journal of Seismic Exploration* 10 (2002): 367–382.

Weglein, A. B., F. A. Gasparotto, P. M. Carvalho, and R. H. Stolt. "An inverse-scattering series method for attenuating multiples in seismic reflection data." *Geophysics* 62 (1997): 1975–1989.

Weglein, A. B., K. H. Matson, D. J. Foster, P. M. Carvalho, D. Corrigan, and S. A. Shaw. "Imaging and inversion at depth without a velocity model: Theory, concepts and initial evaluation." *70th Annual Internat. Mtg., Soc. Expl. Geophys., Expanded Abstracts.* . Soc. Expl. Geophys., 2000. 1016–1019.

Weglein, Arthur B. and William H. Dragoset. *Multiple Attenuation (Geophysics Reprint No. 24).* Soc. Expl. Geophys., 2005.

Zhang, H. *Direct non-linear acoustic and elastic inversion: Towards fundamentally new comprehensive and realistic target identification.* PhD thesis, University of Houston, 2006.

Zhang, H. and A. B. Weglein. "Target identification using the inverse scattering series: data requirements for the direct inversion of large-contrast, inhomogeneous elastic media." *M-OSRP Annual Report* 3 (2004).

Zhang, Jingfeng. *Wave theory based data preparation for inverse scattering multiple removal, depth imaging and parameter estimation: analysis and numerical tests of Green's theorem deghosting theory.* PhD thesis, University of Houston, 2007.

Ziolkowski, A., G. Parkes, L. Hatton, and T. Haugland. "The signature of an air gun array: Computation from near-field measurements including interactions." *Geophysics* 47 (1982): 1413–1421.

Dealing with the wavelet aspect of the low frequency issue: A synthetic example

X. Li, F. Liu and A. B. Weglein

Abstract

The first field data tests of inverse scattering series (ISS) depth imaging are encouraging. A regularization scheme was applied to the Kristin data set to deal with the low frequency issue in favor of imaging tests. In this report, the same regularization scheme is used on a synthetic data example to demonstrate that it will allow the ISS imaging to be effective on field data. The corresponding results show that the further steps to extend these tests to more complex media are achievable.

1 Introduction

Depth imaging produces a structure map of reflectors in the subsurface by processing seismic reflection data. Traditional migration requires an adequate velocity model which is difficult to achieve under some circumstances. Therefore, depth imaging through a complicated geologic overburden has been an important and long standing challenge in exploration seismology. In contrast, the ISS can achieve all seismic processing objectives (including depth imaging) directly using only recorded data and reference medium which is generally considered as the original unperturbed medium.

An imaging subseries of the inverse series has been identified and isolated, which corresponds to a direct multi-dimensional inversion procedure. Imaging algorithms with different degrees of imaging capture and capability are developed first for earth models with only variable velocity. Detailed discussions of the imaging algorithm can be found in Weglein et al. (2000, 2002, 2003); discussions of leading order imaging series (LOIS) in Shaw et al. (2003a,b); Innanen (2003); discussions of higher order imaging series (HOIS) in Liu (2006). Later, Weglein (2009) extended single parameter imaging algorithm to multi-parameter case. Early tests on multi-parameter imaging results (Li et al., 2009; Jiang et al., 2009; Li and Weglein, 2010) were successful and encouraging. However, the effectiveness of imaging algorithms greatly depends on low frequency information in the data. In Shaw (2005), the impact of missing low frequencies on the LOIS was examined, showing that more effectiveness is achieved when lower frequency information is present. So, this is to say that the success of ISS imaging algorithms not only rely on their own capability, but also are affected by low frequency information. Failing to deal with the low frequency issue will stop ISS imaging algorithms from delivering their promise in locating reflectors, even though larger degree of capture and capability is achieved.

The main purpose of this report is to show that a regularization scheme is working in field data tests (Liu et al., 2011). A synthetic data example is provided to show more details. ISS imaging results for data with low frequency information, diminished low frequency information, and regularized low frequency information are shown to demonstrate that the low frequency issue has been addressed in Kristin data.

2 Preparing 1D data

This section briefly introduce how to prepare the data tested in this report. For a detailed derivation, please refer to Liu and Weglein (2010). A layered model with two reflectors located at z_1 and z_2 is considered. Figure 1 shows the velocity and density profile, and Figure 2 shows the corresponding data in (τ, p) domain.

Examining a Gaussian type wavelet as follows:

$$\omega(t) = \frac{\partial}{\partial t}\frac{ae^{-a^2t^2/4}}{2\sqrt{\pi}} = -\frac{a^3t}{4\sqrt{\pi}}e^{-a^2t^2/4}. \tag{1}$$

So the direct wave in (τ, p) domain can be written as:

$$P_0(p,z,\tau) = \int_{-\infty}^{\infty} G_0(p,z,t')\omega(\tau - t')dt' = -\frac{\rho_0}{2\sqrt{c_0^{-2}-p^2}}\int_{-\infty}^{\tau-|z|\sqrt{c_0^{-2}-p^2}} \omega(t')dt'. \tag{2}$$

In this specific case, the wavelet has the form of equation 1, so P_0 is

$$P_0(p,z,\tau) = -\frac{c_0\rho_0 a}{4\cos(\theta)\sqrt{\pi}}e^{-\frac{a^2}{4}(\tau-|z|\sqrt{c_0^{-2}-p^2})^2}. \tag{3}$$

Then the reflected data from this layered model is (for displaying purpose, the polarity of the data is the opposite of what is in the following formula):

$$\hat{D}(\tau,p) = R_0(\theta)P_0(\tau - t_1) + R_1'(\theta)P_0(\tau - t_2). \tag{4}$$

3 Numerical examples

Data prepared from the last section are used in this section for further imaging tests. In Figure 3 the original data has low frequency information. Water speed migration and ISS imaging results for this data are shown in Figure 6. Because the location of the reflectors are the most important information, the section from $400m$ to $1100m$ is enlarged to display the details of the reflectors, and the same section is plotted in the following figures. Then a sine squared taper is applied to the original data from $0Hz$ to $12Hz$. Figure 4 shows the amplitude spectrum for this altered data. It indicates that the low frequency information has been greatly damped. Corresponding water speed migration and ISS imaging result are shown in Figure 7. The mis-located second reflector almost does not move when applying ISS imaging. Next, start from the data with diminished low frequency information, a regularization scheme is applied, which changes the original wavelet to Gaussian type wavelet.

$$D'(\omega,p) = D(\omega,p)\frac{G(\omega)}{A(\omega)}, \tag{5}$$

where $D(\omega,p)$ represents the low frequency diminished data, $A(\omega)$ is the corresponding wavelet, $D'(\omega,p)$ represents the regularized data, and $G(\omega)$ is the Gaussian type wavelet.

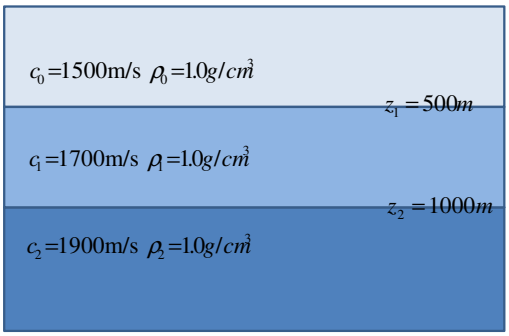

Figure 1: Acoustic model with only velocity variations.

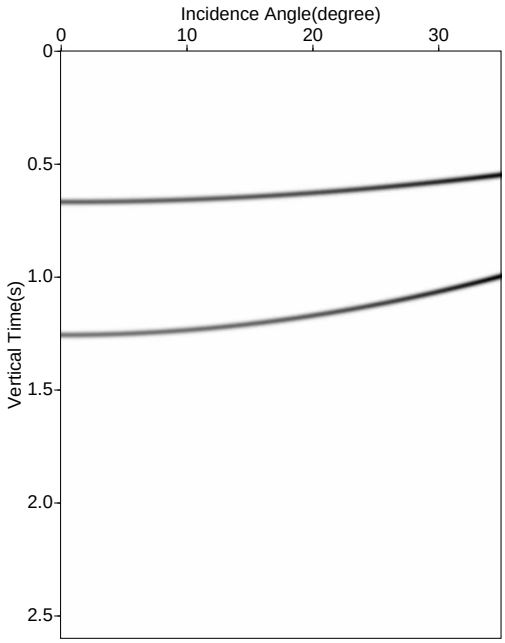

Figure 2: Data after radon transform. Only primary events are shown here.

Figure 5 shows the amplitude spectrum for data after regularization. Figure 8 shows the water speed migration on the left and ISS imaging result on the right. Compared with ideal ISS imaging result on the right of Figure 6, it indicates that with regularization in the data, ISS imaging can produce a flat image gather at the correct location.

4 Conclusions

In this report, the band limited issue for ISS depth imaging algorithm has been studied. It is shown that, with the regularization for low frequency information, ISS imaging algorithm can successfully deal with the low frequency issue. Compared with this synthetic example, the early tests on Kristin data set (Liu et al., 2011) demonstrate that this regularization method allows the ISS imaging algorithms to be effective on field data. These tests also indicate that With the most serious practical limitation been addressed, the further steps to extend these tests to variable density and velocity acoustic and elastic media are achievable.

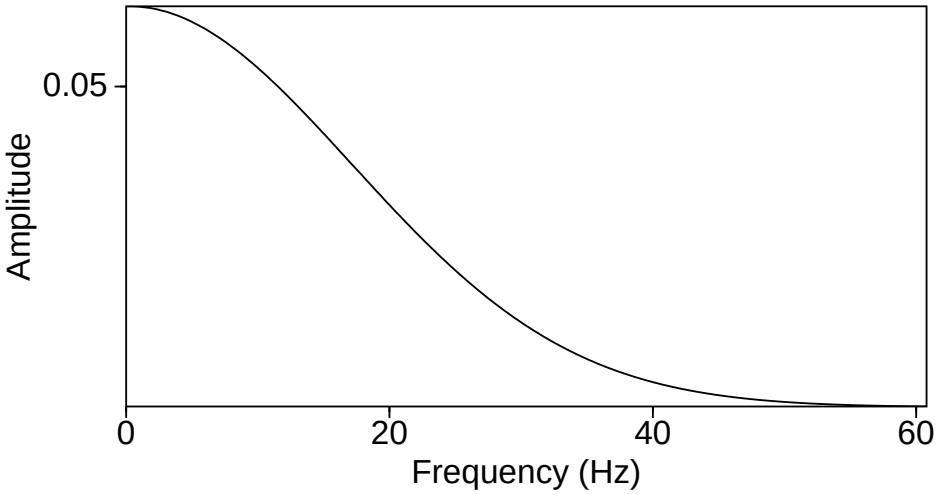

Figure 3: Amplitude spectrum for original data with low frequency information.

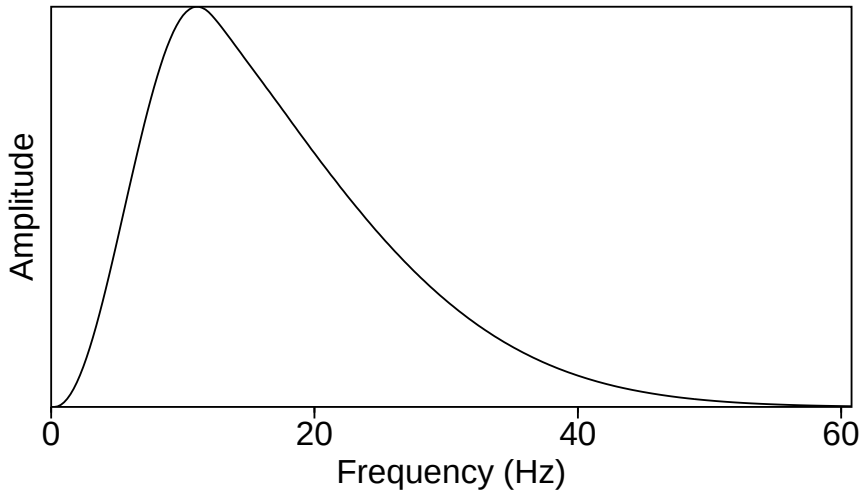

Figure 4: Amplitude spectrum for data altered by a sine squared taper up to $12Hz$.

5 Acknowledgments

We are grateful to all M-OSRP sponsors for their long-term encouragement and support in this research. In particular, Statoil ASA, Petoro, ExxonMobil, Eni, Total and WesternGeco are thanked for granting access to the Kristin data and permission to publish this work.

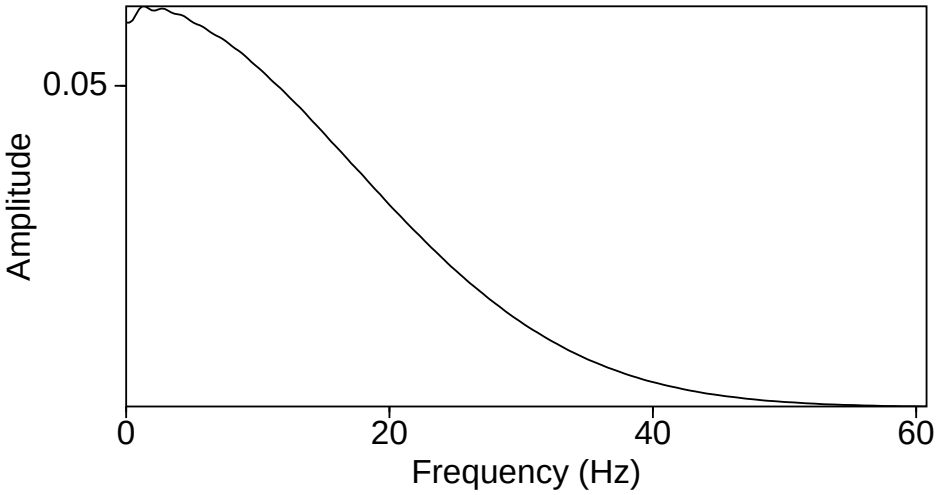

Figure 5: Amplitude spectrum for data after regularization.

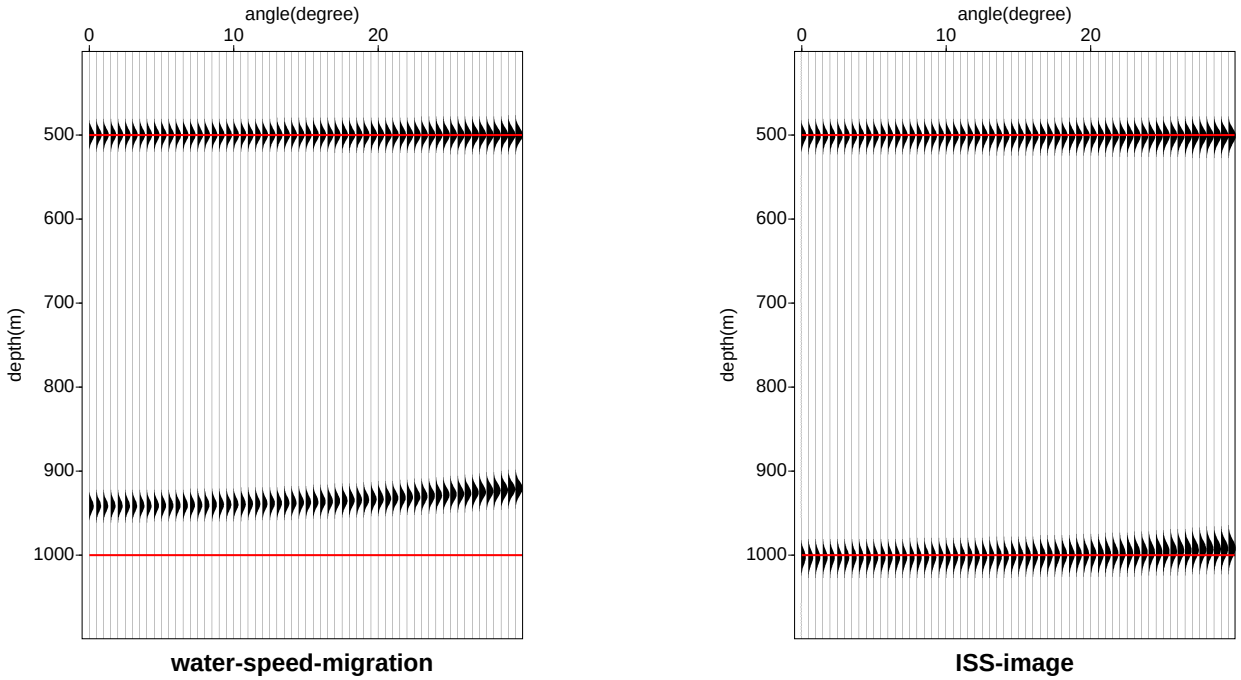

Figure 6: On the left is the water speed migration for data with low frequency information. On the right is the ISS ideal imaging result. The red lines are the actual depth of the two reflectors.

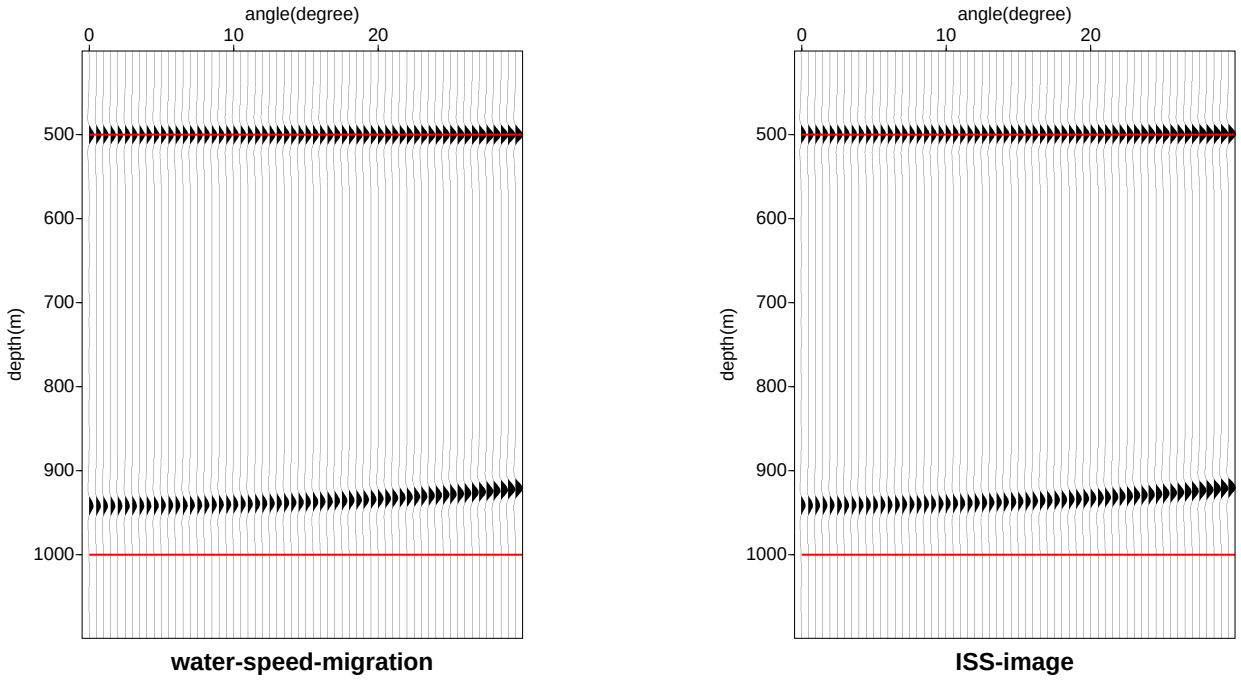

Figure 7: On the left is the water speed migration for data with a sine squared taper applied up to $12Hz$. On the right is the ISS imaging result for data on the left. The red lines are the actual depth of the two reflectors. Note that with low frequency information being diminished, the ISS imaging is ineffective.

Members of M-OSRP are also thanked for their help toward completing this report and valuable discussions in this research program.

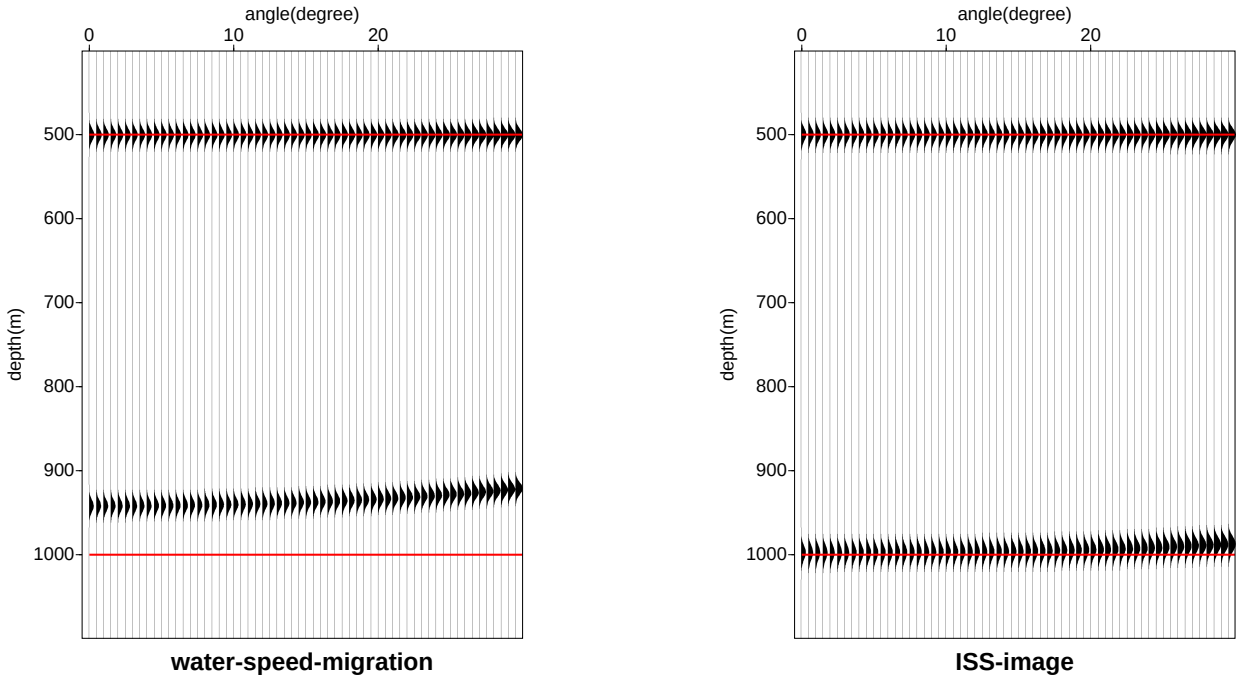

Figure 8: On the left shows the water speed migration for data being regularized. On the right is the corresponding ISS imaging result. The red lines are the actual depth of the two reflectors. With the regularization applied, ISS successfully correct the move-out and place the reflectors to the right location.

References

Innanen, Kristopher. A. *Methods for the treatment of acoustic and absorptive/dispersive wave field measurements.* PhD thesis, University of British Columbia, 2003.

Jiang, S., A. B. Weglein, and S. A. Shaw. "Progressing multiparameter imaging using the inverse scattering series: An initial analytic test of the leading order imaging subseries (LOIS) closed form and its extended higher order imaging subseries (HOIS) closed form for a laterally invariant two-parameter acoustic medium." *2008 M-OSRP Annual Report* (2009): 91–113.

Li, X., F. Liu, S. Jiang, and A. B. Weglein. "Depth imaging without the velocity cares about the phase and amplitude information of events: Focusing on the use of the angle dependent amplitude information of events." *2008 M-OSRP Annual Report* (2009): 114–128.

Li, X. and A. B. Weglein. "An unanticipated and immediate AVO by-product (responding to pressing type 1 and type 2 AVO challenges) delivered within the ISS imaging program." *2009 M-OSRP Annual Report* (2010).

Liu, F. *Multi-dimensional depth imaging without an adequte velocity model.* PhD thesis, University of Houston, 2006.

Liu, F., X. Li, A. B. Weglein, P. Terenghi, E. Kragh, J. Mayhan, S. Hsu, H. Liang, L. Tang, Z. Wang, J. Mispel, and L. Amundsen. "Inverse scattering series depth imaging: First field data examples." *SEG Technical Program Expanded Abstracts* (2011): submitted.

Liu, Fang and Arthur B. Weglein. "Progress in Inverse Scattering Imaging: Source Regularization and Cascaded Structure." *2009 M-OSRP Annual Report* (2010).

Shaw, S. A. *An inverse scattering series algorithm for depth imaging of reflection data from a layered acoustic medium with an unknown velocity model.* PhD thesis, University of Houston, 2005.

Shaw, S. A., A. B. Weglein, D. J. Foster, K. H. Matson, and R. G. Keys. "Convergence properties of a leading order depth imaging series." *73rd Annual Internat. Mtg., Soc. Expl. Geophys., Expanded Abstracts*. . Soc. Expl. Geophys., 2003. 937–940.

Shaw, S. A., A. B. Weglein, D. J. Foster, K. H. Matson, and R. G. Keys. "Isolation of a leading order depth imaging series and analysis of its convergence properties." *2002 M-OSRP Annual Report* 2 (2003): 157–195.

Weglein, A. B. "M-OSRP 2008 Introduction and Preface." *2008 M-OSRP Annual Report* (2009): 1–8.

Weglein, A. B., F. V. Araújo, P. M. Carvalho, R. H. Stolt, K. H. Matson, R. T. Coates, D. Corrigan, D. J. Foster, S. A. Shaw, and H. Zhang. "Inverse scattering series and seismic exploration." *Inverse Problems* 19 (2003): R27–R83.

Weglein, A. B., D. J. Foster, K. H. Matson, S. A. Shaw, P. M. Carvalho, and D. Corrigan. "Predicting the correct spatial location of reflectors without knowing or determining the precise medium and wave velocity: initial concept, algorithm and analytic and numerical example." *Journal of Seismic Exploration* 10 (2002): 367–382.

Weglein, A. B., K. H. Matson, D. J. Foster, P. M. Carvalho, D. Corrigan, and S. A.Shaw. "Imaging and inversion at depth without a velocity model: Theory, concepts and initial evaluation." *70th Annual Internat. Mtg., Soc. Expl. Geophys., Expanded Abstracts*. . Soc. Expl. Geophys., 2000. 1016–1019.

Discussion of the impact of shear waves on the model type assumption for ISS depth imaging: how far below the water bottom might we expect value for a velocity and density varying acoustic ISS imaging algorithm

H. Liang, A. B. Weglein and X. Li, M-OSRP, University of Houston

Abstract

Accurately imaging at depth and identifying targets in the subsurface are both high priority and serious technical challenges for the petroleum industry. The current inverse scattering series (ISS) approaches for both of the tasks depend on the model type assumption (e.g., acoustic, elastic, isotropic, anisotropic), which is defined by the chosen set of parameters to be inverted for. Acoustic medium is characterized by P-wave velocity and density, whereas elastic medium such as the water bottom and below is defined by elastic parameters (e.g., P-wave and S-wave velocity, density). For ISS depth imaging without subsurface information, the more number of parameters are chosen to describe the medium, the more issues have to be addressed. Thus, in this report we evaluate the applicability domain of ISS acoustic imaging for elastic medium to investigate the value of a velocity and density varying acoustic ISS imaging algorithm below the water bottom. Based on a series of numerical tests, we conclude that the ISS acoustic imaging is suitable for elastic medium when both the density and shear modulus variations are small compared to the primary wave velocity change, or when the value of shear wave velocity is small enough.

1 Introduction

The objective of seismic processing is to locate and identify the targets in the subsurface from the measured data. The inverse scattering series could perform all the tasks associated with inversion (free surface multiple removal, internal multiple attenuation, depth imaging and parameter estimation) directly without requiring subsurface information (Weglein et al., 2003). Among all the tasks, both the current ISS depth imaging and parameter estimation algorithms are model type dependent. For these two approaches it is important to assume an adequate model type in the algorithms (Liang et al., 2010). Here, an adequate model type means a minimally complicated model adequate to reach E&P goals, but not too simple to be harmful, nor too complicated to be more than necessary to predict drilling decisions (Weglein et al., 2010).

Within the overall inverse scattering series a certain subseries performs only one specific task and acts as though no other tasks existed. By collecting different imaging subseries and assuming different model types different imaging algorithms are obtained. For a simplest acoustic model with only velocity variation, the leading order imaging subseries (LOIS) (Shaw et al., 2002) and extended higher order imaging subseries (HOIS) (Liu, 2006) can achieve the imaging objective to a certain degree. However, these algorithms would fail if the medium has large density variations. To accommodate both velocity change and density change a multi-parameter imaging conjecture was proposed by Weglein in 2007 which can exclude reflections

due to only density change. The leading order closed form imaging conjecture was validated by Jiang and Weglein (2008) and an extended higher order closed form was tested in the 2008 M-OSRP annual reports (Li et al., 2009; Jiang and Weglein, 2009). This imaging conjecture has also been generalized to accommodate the 1D three-parameter elastic earth model with P wave velocity, S wave velocity, and density all varying (Jiang and Weglein, 2009; Li et al., 2010; Liang et al., 2010).

For ISS depth imaging without velocity the challenges have to be addressed are: the size of velocity contrast, the duration of the contrast, the number of parameters and dimensions chosen to describe the medium (Wang et al., 2010). The two-parameter acoustic imaging conjecture needs the combination of data at two different incident angles (Jiang and Weglein, 2009), whereas the three-parameter elastic imaging conjecture is more complicated and requires the data combination at three different angles. The goal of this study is to evaluate the circumstances that ISS acoustic imaging conjecture is applicable for elastic medium, and the study may give a hint about when the acoustic imaging conjecture could be used below the water bottom.

2 The theory

We start from the inverse scattering theory (Weglein et al., 2003)

$$\begin{aligned} D =& [G_0 V_1 G_0]_{ms} && (1)\\ 0 =& [G_0 V_2 G_0]_{ms} + [G_0 V_1 G_0 V_1 G_0]_{ms} && (2)\\ 0 =& [G_0 V_3 G_0]_{ms} + [G_0 V_1 G_0 V_2 G_0]_{ms} \\ & + [G_0 V_2 G_0 V_1 G_0]_{ms} + [G_0 V_1 G_0 V_1 G_0 V_1 G_0]_{ms} && (3)\\ & \vdots \end{aligned}$$

where D is the measured data, G_0 is Green's function in the reference medium, V is the perturbation operator which characterizes the properties of actual medium, and V_n is the portion of V which is n^{th} order in D. The inverse scattering series provides a direct method to solve the perturbation operator V order by order using only D and G_0.

2.1 Linear parameter estimation

From equation 1 we can obtain the linear estimation of the medium properties using only D and G_0. For 1D two-parameter acoustic medium with both density and velocity changes, the linear term of the perturbation operator, i.e., V_1, has the following form:

$$V_1(z, \bigtriangledown) = \frac{\omega^2 \alpha_1(z)}{K_0} + \frac{1}{\rho_0}\beta_1(z)\frac{\partial^2}{\partial x^2} + \frac{1}{\rho_0}\frac{\partial}{\partial z}\beta_1(z)\frac{\partial}{\partial z} \quad (4)$$

where $K = c\rho^2$, c is P wave velocity and ρ is density. The two parameters to be inverted are $\alpha = 1 - K/K_0$ and $\beta = 1 - \rho/\rho_0$, where the subscript 0 represents the quantities in the reference medium. The corresponding linear terms are α_1 and β_1. Assuming the source and

receiver at depth zero and substituting equation 4 into equation 1, we can obtain the linear equation in frequency domain:

$$\tilde{D}(q_g, \theta, z_g, z_s) = -\frac{\rho_0}{4}\left[\frac{1}{\cos^2\theta}\tilde{\alpha_1}(-2q_g) + (1-\tan^2\theta)\tilde{\beta_1}(-2q_g)\right] \tag{5}$$

where the subscripts s and g denote source and receiver quantities respectively, θ is the incidence angle, and q_g is the receiver vertical wave number given by $q_g = \omega\cos\theta/c$. The linear estimation of the medium parameters α_1 and β_1 can be solved by choosing two different angles. We can also obtain the linear estimation of the relative change in P-wave velocity (Zhang, 2006):

$$\left(\frac{\triangle c}{c}\right)_1 = \frac{1}{2}(\alpha_1 - \beta_1) \tag{6}$$

For 1D three-parameter elastic medium the perturbation is given in the PS domain (Weglein et al., 1997). The three parameters to be inverted are: $a_\rho = \rho/\rho_0 - 1$, $a_\gamma = \gamma/\gamma_0 - 1$ and $a_\mu = \mu/\mu_0 - 1$, where ρ denotes density, α is P-wave velocity, β is S-wave velocity, γ is bulk modulus given by $\gamma = \rho\alpha^2$, and μ is shear modulus given by $\mu = \rho\beta^2$. We consider only PP data in this report. Assuming source and receiver depths are zero, we can obtain the equation that relates the linear components of the three elastic parameters to PP data (Zhang and Weglein, 2006):

$$\tilde{D}^{PP}(\nu_g, \theta) = -\frac{1}{4}(1-\tan^2\theta)\tilde{a}_\rho^{(1)}(-2\nu_g) - \frac{1}{4}(1+\tan^2\theta)\tilde{a}_\gamma^{(1)}(-2\nu_g) + \frac{2\beta_0^2}{\alpha_0^2}\sin^2\theta\tilde{a}_\mu^{(1)}(-2\nu_g) \tag{7}$$

where θ is the incident angle and ν_g is the receiver vertical wave number given by $\nu_g = \omega\cos\theta/\alpha_0$. The linear estimation of the medium parameters $a_\rho^{(1)}$, $a_\gamma^{(1)}$, and $a_\mu^{(1)}$ can be solved by choosing three different angles. We can also obtain the linear estimation of the relative change in P-wave velocity (Zhang, 2006):

$$\left(\frac{\triangle c}{c}\right)_1 = \frac{1}{2}(a_\gamma^{(1)} - a_\rho^{(1)}) \tag{8}$$

Equation 6 and 8 will be used respectively as input to the acoustic and elastic multiparameter imaging conjecture in the next section.

2.2 Multiparameter imaging conjecture

There are different imaging subseries captured within the overall inverse scattering series with different degrees of capability. For 1D one-parameter acoustic medium with only P wave velocity change, the closed form of the higher order imaging series (Liu, 2006) is:

$$\alpha^{HOIS}(z + \frac{1}{2}\int_{-\infty}^{z}\frac{\alpha_1(z')}{\cos^2\theta - 0.25\alpha_1(z')}dz', \theta) = \alpha_1(z, \theta) \tag{9}$$

where α_1 is the linear estimation of P wave velocity change.

By comparing the imaging-only terms in the first nonlinear equation of the inverse scattering series for one-parameter and two-parameter acoustic case (Jiang and Weglein, 2008) we substitute α_1 in equation 9 with $\alpha_1 - \beta_1$, and get the conjectured imaging algorithm for 1D two-parameter acoustic medium:

$$D^{HOIS}(z + \frac{1}{2}\int_{-\infty}^{\infty} \frac{\alpha_1(z') - \beta_1(z')}{\cos^2\theta - 0.25(\alpha_1(z') - \beta_1(z'))} dz', \theta) = D(z, \theta) \tag{10}$$

Similarly, substituting α_1 with $a_\gamma^{(1)} - a_\rho^{(1)}$ in equation 9 we can obtain the imaging conjecture for 1D three-parameter elastic medium:

$$D^{HOIS}(z + \frac{1}{2}\int_{-\infty}^{\infty} \frac{a_\gamma^{(1)}(z') - a_\rho^{(1)}(z')}{\cos^2\theta - 0.25(a_\gamma^{(1)}(z') - a_\rho^{(1)}(z'))} dz', \theta) = D^{PP}(z, \theta) \tag{11}$$

The imaging conjecture has a multiparameter front end, which is $\alpha_1 - \beta_1$ in the acoustic case and $a_\gamma^{(1)} - a_\rho^{(1)}$ in the elastic case. They are prepared by inverting the linear equation of inverse scattering series (equation 5 and equation 7), respectively, and imaged as a composite form by the corresponding imaging conjecture. The imaging front ends are linear combinations of data, and able to exclude reflections due to density change only (Li et al., 2009).

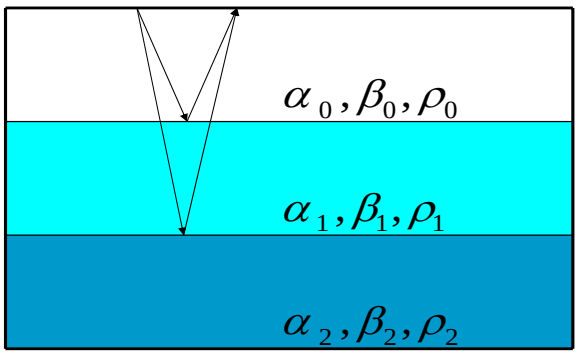

Figure 1: A 1D three-layer elastic model with P-wave velocity, S-wave velocity and density.

3 Numerical tests

Since it is difficult to evaluate the exact valid conditions under which the acoustic imaging would give reasonable results for the elastic medium in theory, we study the problem through a series of numerical tests.

3.1 Analytic data preparation

A three-layer elastic model shown in Figure 1 is used to generate the data. We consider only two primaries reflected from the reflectors and assume all other events (ghosts, free surface multiples, and internal multiples) have been removed. For this three-layer elastic model, the analytic data in the frequency domain can be written as (Weglein et al., 1986):

$$\tilde{D}^{PP}(\nu_g,\theta) = R_{01}^{PP}(\theta)\frac{e^{2i\nu_g a}}{4\pi i\nu_g} + \hat{R}_{12}^{PP}\frac{e^{2i\nu_g a}+e^{2iq_g(b-a)}}{4\pi i\nu_g} \tag{12}$$

where a and b are the exact depths of the two reflectors, ν_g and q_g are vertical wavenumbers for P wave in the first two layers, and θ is the incident angle. R_{01}^{PP} and R_{12}^{PP} are the reflection coefficients at the first and second reflectors, T_{01}^{PP} and T_{10}^{PP} are the transmission coefficients, and $\hat{R}_{12}^{PP} = T_{01}^{PP}R_{12}^{PP}T_{10}^{PP}$. The reflection and transmission coefficients can be calculated by the Zoeppritz equation. Fourier transforming equation 12 over $2\nu_g$, we have:

$$D^{PP}(z,\theta) = R_{01}^{PP}(\theta)H(z-a) + \hat{R}_{12}^{PP}H(z-b') \tag{13}$$

This is the linear imaging result using the velocity in the first layer as the reference velocity, which equals to constant velocity FK migration. Since the reference velocity equals to the actual velocity above the first reflector, the first reflector is located correctly by the linear imaging. For the second reflector the depth is mislocated at a pseudo depth b', where $b'(\theta) = a + (b-a)q_g/\nu_g$ (Jiang and Weglein, 2009).

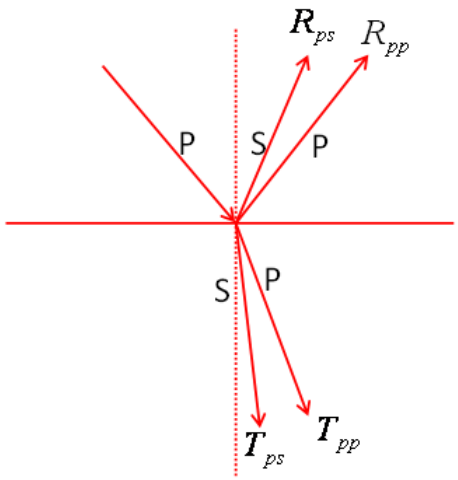

Figure 2: Plane P wave striking a planar interface between two elastic media

3.2 Numerical results

The ISS acoustic and elastic imaging conjectures are tested using the same data modeled in the elastic medium. With the elastic imaging result as a reference, we will evaluate the

applicability of acoustic imaging for elastic data under different conditions. The elastic imaging conjecture would allow P-wave velocity, S-wave velocity and density to all vary, whereas the acoustic imaging conjecture would treat the data as though only P-wave velocity and density varied. Since the same data sets are used by different algorithms, we will investigate the numerical results by examining the modeled data. The imaging conjecture only makes use of the information above the reflector to locate it. Thus, we will only consider the wave scattering across the first reflector to investigate the locating results of the second reflector.

As shown in Figure 2, a plane P wave striking a planar interface between two elastic medium would give rise to four plane waves: transmitted P wave, reflected P wave, transmitted S wave and reflected S wave. The amplitudes for the four plan waves are: T_{pp}, R_{pp}, T_{ps}, R_{ps}. In the analytic data the elastic reflection and transmission coefficients are calculated using Zoeppritz equation (Sheriff and Geldart, 1994). Following Keys (1989), we examine the two special conditions that would cause the elastic reflection and transmission coefficients reduce to the acoustic case. The first case is when both the density and shear modulus change is zero the elastic P-wave reflection and transmission coefficients would reduce to the corresponding acoustic coefficients, and the S-wave reflection and transmission coefficients would be zero (see Appendix A). Under this circumstance the data is actually acoustic. This indicates that if both the density and shear modulus changes are small the elastic medium would be act like an acoustic medium.

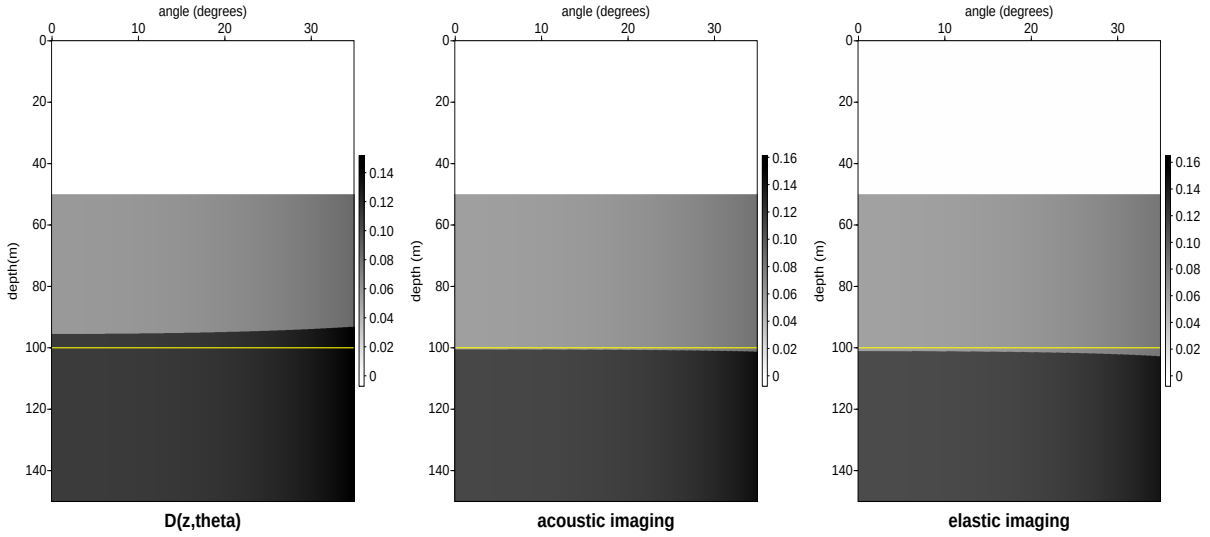

Figure 3: Imaging results for small density change and zero shear modulus changes. Left panel is constant velocity migration, middle panel is acoustic imaging, right panel is elastic imaging, and the yellow line indicates the correct depth of the second reflector. Parameters across the first reflector are: $a_\rho = 0.02, \triangle v_p/v_{p0} = 0.1$, a_μ=0, ρ_0=1.0g/cm^3, v_{p0}=1500m/s, v_{s0}=800m/s.

In the data model of Figure 3 density variation is small and shear modulus change is zero above the second reflector, so we can speculate that the P-wave reflection coefficient across the first reflector would be close to the acoustic reflection coefficient. This is confirmed in Figure 4, which shows the elastic and acoustic reflection coefficients are very close, especially

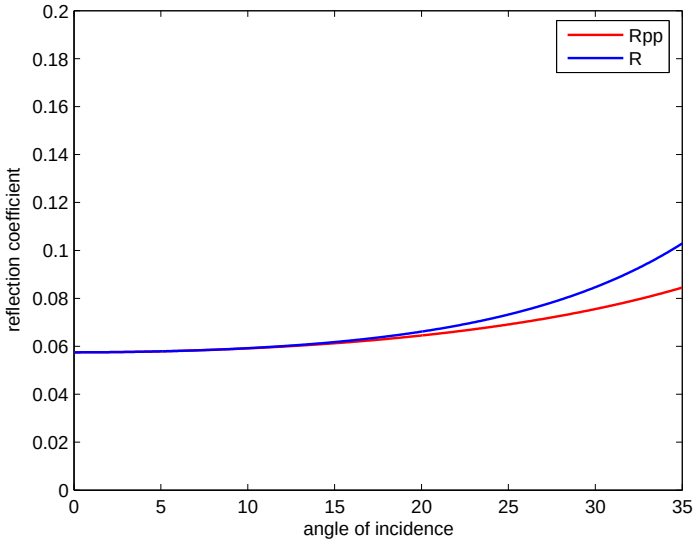

Figure 4: Comparison of elastic and acoustic reflection coefficients as a function of incident angle. R_{pp} represents the elastic reflection coefficient across the first reflector in the data model of Figure 3. R represents the reflection coefficient for the acoustic medium which has the same P-wave velocity and density.

at angles below 25 degrees. Next we examine all the reflection and transmission coefficients across the first reflector. Figure 5 shows the corresponding amplitudes for the four plan waves: T_{pp}, R_{pp}, T_{ps}, R_{ps}. The result shows that the amplitudes of the converted waves (P-S reflected wave and P-S transmitted wave) are extremely small compared to the primary waves (P-P reflected wave and P-P transmitted wave). The above results indicate data above the second reflector in the data model of Figure 3 is like acoustic. This explains why the acoustic imaging is better at locating the deeper reflector than the elastic imaging conjecture in figure 3.

Then we examine the impact of shear modulus variation on the imaging results when the density variation is small. In Figures 6.a and 6.b the value and the changes of both density and P-wave velocity are all the same across the first reflector, and the only difference is the shear modulus change. In Figure 6.a the shear modulus change is about half of the P-wave velocity change, and the acoustic imaging result is almost as good as the elastic imaging result; in Figure 6.b, the shear modulus change is nearly equal to the P-wave velocity change, and the acoustic imaging result is worse than the elastic imaging result. This confirms that when the density variation and shear modulus change are small compared to the P-wave velocity change the acoustic imaging conjecture could well locate the reflector in the elastic medium.

The second case is when the shear wave velocities are zero the medium is actually acoustic. Under this circumstance, the elastic P-wave reflection and transmission coefficients would reduce to the corresponding acoustic coefficients, and the S-wave reflection and transmission coefficients would be zero (see Appendix B). This indicates if the shear wave velocities in the elastic medium are small enough the data generated in the elastic medium would be like acoustic. Next we examine the impact of the shear wave velocity on the imaging results under

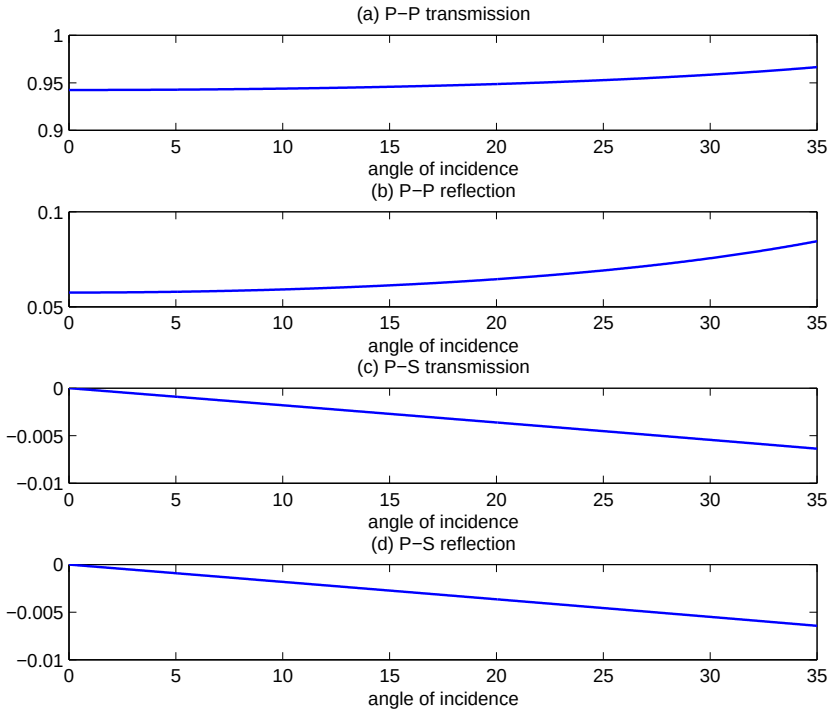

Figure 5: Amplitudes of scattered waves across the first reflector in the data model of Figure 3. (a) Transmitted P wave. (b) Reflected P wave. (c) Transmitted S wave. (d) Reflected S wave.

different conditions.

First consider the case when the shear modulus variation is large. In Figure 7.a and 7.b the value and the changes of both density and P-wave velocity across the first reflector, as well as the shear modulus variation, are all the same. The only difference is the value of shear wave velocities: in Figure 7.a, $v_{s0} = 800m/s$, and $v_{s1} = 830m/s$; in Figure 7.b, $v_{s0} = 400m/s$, and $v_{s1} = 415m/s$. According to the previous example large shear modulus variation in Figure 7.a causes the acoustic imaging fail to locate the deeper reflector, whereas in Figure 7.b acoustic imaging well locate the reflectors in the elastic medium since small shear wave velocities make the elastic data like acoustic.

Then consider the case when the density variation is large. Similar to the previous example, in Figure 8.a and 8.b the only difference is the value of shear wave velocities: in figure 8.a, $v_{s0} = 1600m/s$, and $v_{s1} = 1300m/s$; in Figure 8.b, $v_{s0} = 400m/s$, and $v_{s1} = 325m/s$. The acoustic imaging in Figure 8.a fails to image the elastic medium due to large density variation, whereas in Figure 8.b acoustic imaging well locate the reflectors in elastic medium since small shear wave velocities makes the elastic data like acoustic.

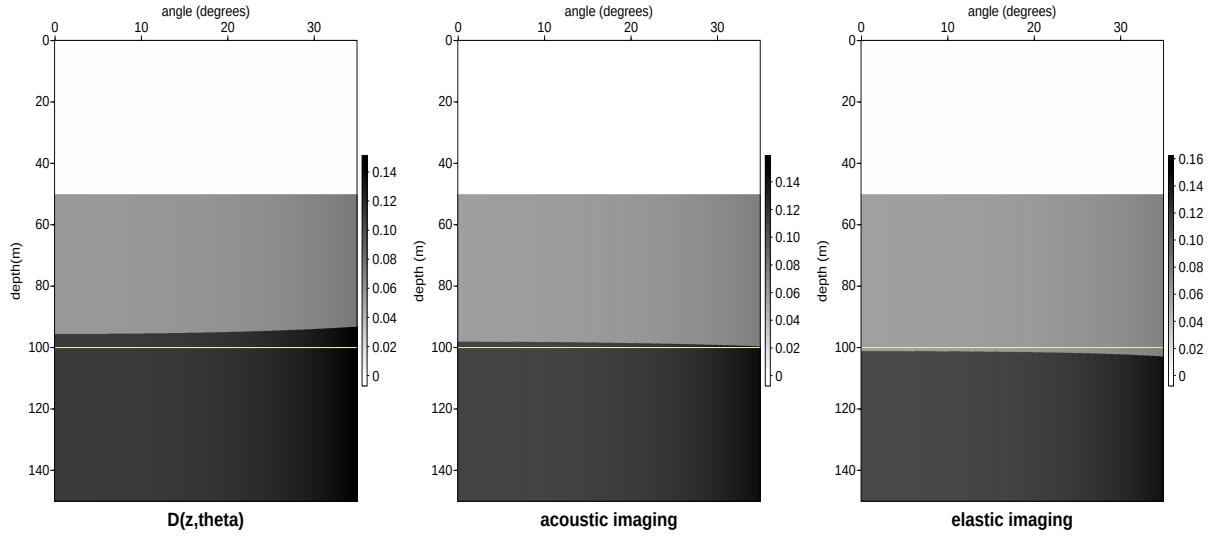

(a)

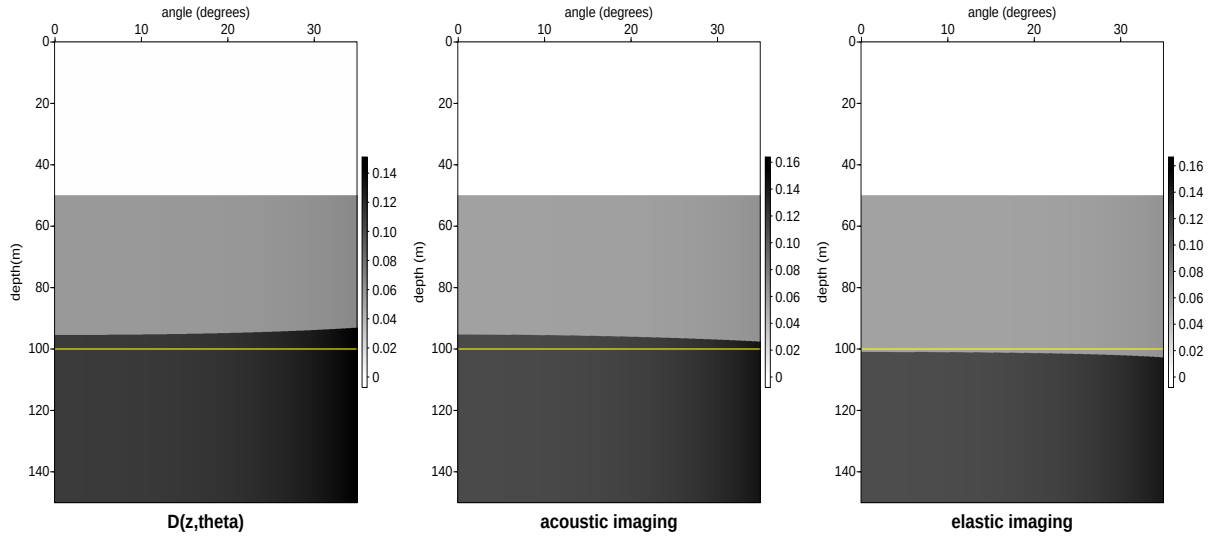

(b)

Figure 6: Comparison of imaging results for different shear modulus changes when density change is small. In both (a) and (b) left panel is constant velocity migration, middle panel is acoustic imaging, right panel is elastic imaging, and the yellow line indicates the correct depth of the second reflector. Parameters across the first reflector in two figures are the same except shear modulus change: $a_\rho = 0.02, \triangle v_p/v_{p0} = 0.1$, ρ_0=1.0g/cm^3, v_{p0}=1500m/s, v_{s0}=800m/s. (a) Case with small shear modulus change: $a_\mu = 0.046$, (b) Case with large shear modulus change: $a_\mu = 0.098$.

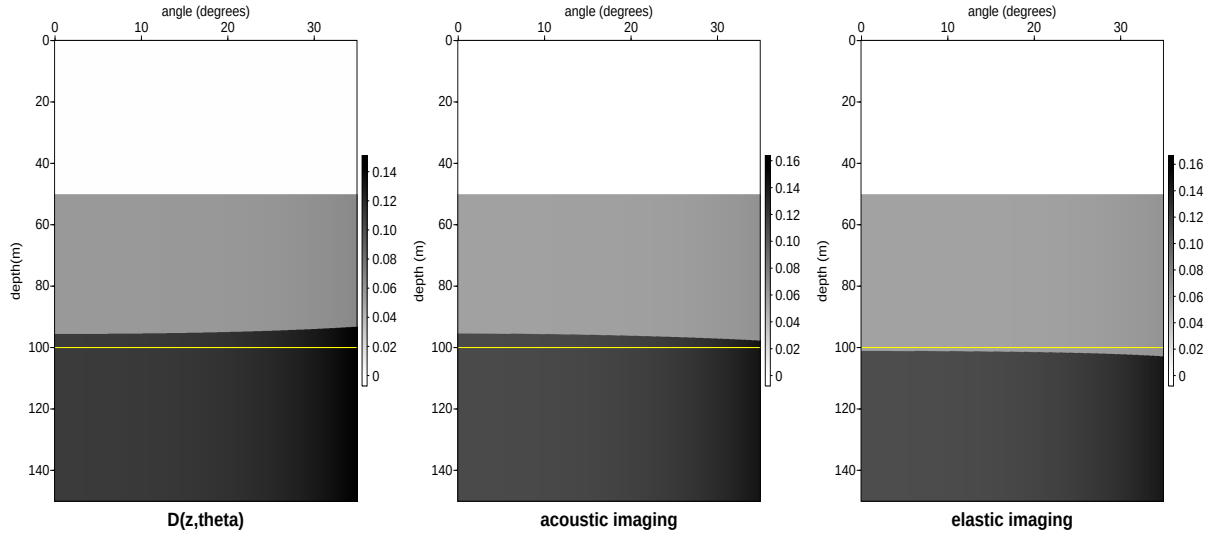

(a)

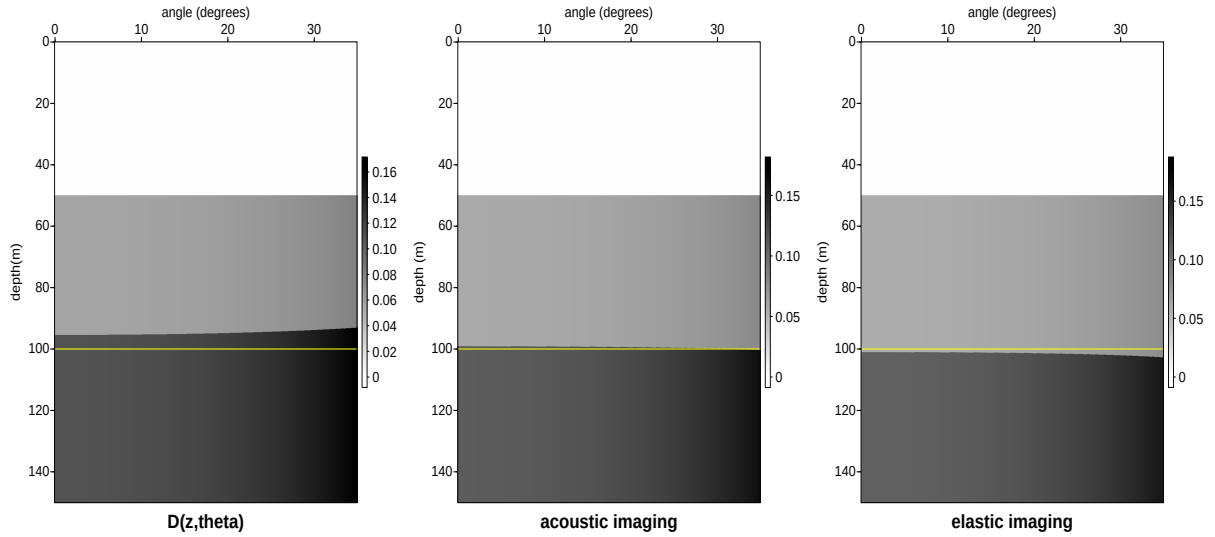

(b)

Figure 7: Comparison of imaging results for different shear wave velocities when shear modulus change is large. In both (a) and (b) left panel is constant velocity migration, middle panel is acoustic imaging, right panel is elastic imaging, and the yellow line indicates the correct depth of the second reflector. Parameters across the first reflector in two figures are the same except shear wave velocities: $a_\rho = 0.02, \triangle v_p/v_{p0} = 0.1$, $a_\mu = 0.098$, ρ_0=1.0g/cm^3, v_{p0}=1500m/s. (a) Case with large shear wave velocities: v_{s0}=800m/s, and v_{s1}=830m/s. (b) Case with small shear wave velocities: v_{s0}=400m/s, and v_{s1}=415m/s.

4 Conclusions

We have studied the applicability domain of inverse scattering series acoustic imaging conjecture for elastic media. Based on the performed numerical tests we conclude that if both

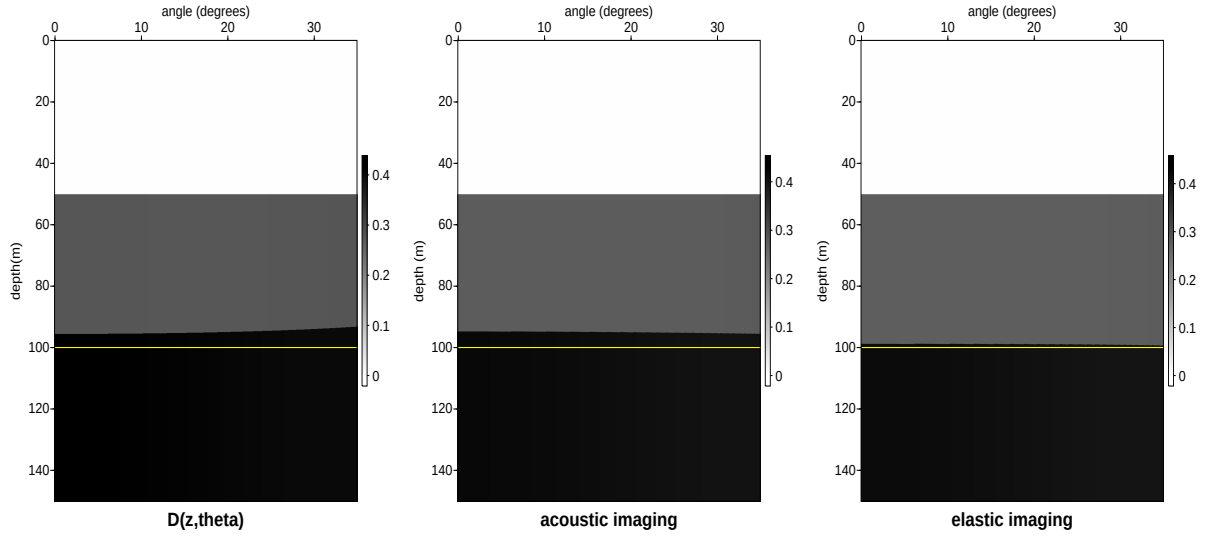

(a)

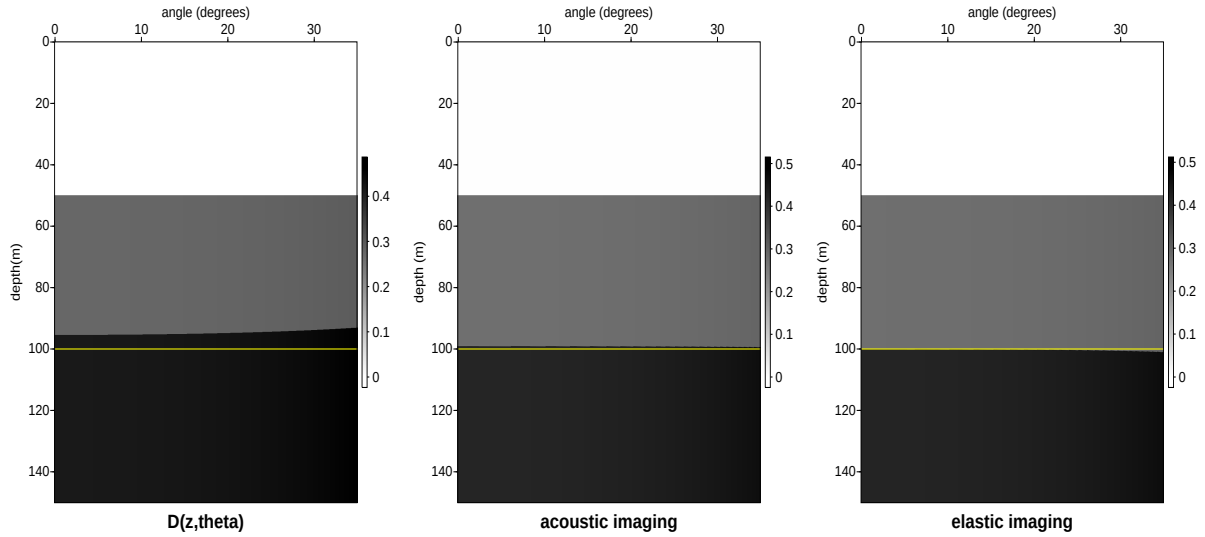

(b)

Figure 8: Comparison of imaging results for different shear wave velocities when density change is large. In both (a) and (b) left panel is constant velocity migration, middle panel is acoustic imaging, right panel is elastic imaging, and the yellow line indicates the correct depth of the second reflector. Parameters across the first reflector in two figures are the same except Shear wave velocities: $a_\rho = 0.6, \triangle v_p/v_{p0} = 0.1$, $a_\mu = 0.056$, ρ_0=1.0g/cm^3, v_{p0}=3000m/s. (a) Case with large shear wave velocities: v_{s0}=1600m/s, and v_{s1}=1300m/s. (b) Case with small shear wave velocities: v_{s0}=400m/s, and v_{s1}=325m/s.

the shear modulus variation and density variation are small enough compared to the P-wave velocity variation, or if the shear wave velocity is small enough compared to the P-wave ve-

locity, the elastic data would be like acoustic. Under these circumstances, the ISS acoustic imaging could give reasonable results for the elastic data. Since the elastic parameters are coupled in the data, it is difficult to provide the exact conditions that the acoustic imaging conjecture is applicable for elastic data. However, the study could give a hint about how far below the water bottom might we expect value for a velocity and density varying acoustic ISS imaging algorithm by checking the data properties.

5 Acknowledgements

We are grateful to all M-OSRP sponsors for the long-term encouragement and support in our research. All members in M-OSRP are appreciated for their help in supporting the content generation of this paper and the valuable discussions presented in this research program.

References

Jiang, S. and A. B. Weglein. "Deriving an imaging algorithm for a laterally invariant multi-parameter acoustic medium from the inverse scattering series." *M-OSRP 2007 Annual meeting* (2008): 125–141.

Jiang, S. and A. B. Weglein. "Progressing multi-parameter imaging using the inverse scattering series: an initial analytic test on the Leading Order Imaging Subseries (LOIS) closed form and its extended Higher Order Imaging Subseries (HOIS) closed form for a laterally invariant two-parameter acoustic medium." *M-OSRP 2008 Annual meeting* (2009): 91–113.

Keys, R. G. "Polarity reversals in reflections from layered media." *Geophysics* (1989): 900–905.

Li, X., F. Liu, S. Jiang, and A. B. Weglein. "Depth imaging without the velocity cares about the phase and amplitude information of events: focusing on the use of angle dependent amplitude information of events." *M-OSRP 2008 Annual meeting* (2009): 114–128.

Li, X., A. B. Weglein, , and H. Liang. "An unanticipated and immediate AVO by-product (responding to pressing type 1 and type 2 AVO chanllenges) delivered within the ISS imaging program." *M-OSRP 2009 Annual meeting* (2010): 153–163.

Liang, H., A. B. Weglein, , and X. Li. "Initial tests for the impact of matching and mismatching between the earth model and the processing model for the ISS imaging and parameter estimation." *M-OSRP 2009 Annual meeting* (2010): 165–180.

Liu, F. *Multi-dimensional depth imaging without an adequte velocity model.* PhD thesis, University of Houston, 2006.

Shaw, S., A. B. Weglein, K. H. Matson, and D. J. Foster. "Cooperation of the leading order terms in an inverse-scattering subseries for imaging: 1-D analysis and evaluation.." *SEG Technical Program Expanded Abstracts* (2002): 2277–2280.

Sheriff, R. E. and L. P. Geldart. *Exploration seismology.* Cambridge University Press, 1994.

Wang, Z., A. B. Weglein, , and X. Li. "New capture of direct velocity independent depth imaging in a one-dimension two-parameter acoustic Earth." *M-OSRP 2009 Annual meeting* (2010): 137–143.

Weglein, A. B., F. V. Araújo, P. M. Carvalho, R. H. Stolt, K. H. Matson, R. T. Coates, D. Corrigan, D. J. Foster, S. A. Shaw, and H. Zhang. "Inverse Scattering Series and Seismic Exploration." *Inverse Problems* (2003): R27–R83.

Weglein, A. B., F. A. Gasparotto, P. M. Carvalho, and R. H. Stolt. "An inverse-scattering series method for attenuating multiples in seismic reflection data." *Geophysics* (1997): 1975–1989.

Weglein, A. B., F. Liu, Z. Wang, X. Li, and H. Liang. "The inverse scattering series depth imaging algorithms: development, tests and progress towards field data application." *SEG Technical Program Expanded Abstracts* (2010): 4133–4138.

Weglein, A. B., P. B. Violette, and T. H. Keho. "Using multiparameter Born theory to obtain certain exact multiparameter inversion goals." *Geophysics* (1986): 1069–1074.

Zhang, H. *Direct nonlinear acoustic and elastic inversion: towards fundamentally new comprehensive and realistic target identification.* PhD thesis, University of Houston, 2006.

Zhang, H. and A. B. Weglein. "Direct non-linear inversion of multi-parameter 1D elastic media using the inverse scattering series." *SEG Technical Program Expanded Abstracts* (2006): 284–311.

A Appendix

Non-normal incidence of P-plane wave on a horizontal interface between two elastic solids would give rise to four plane waves: reflected P-wave (R_{pp}), reflected S-wave (R_{ps}), transmitted P-wave (T_{pp}) and transmitted S-wave (T_{ps}). The amplitudes of these plane waves can be given by the boundary conditions that the normal and tangential components of stress and displacement must be continuous. From the continuity equations, we can derive the reflection and transmission coefficients (see Sheriff and Geldart (1994), Zhang (2006)).

The P-wave reflection coefficient is given by $R_{pp} = N_{R_{pp}}/D$, where

$$\begin{aligned} N_{R_{pp}} = & -(1+2kx^2)^2 b\sqrt{1-c^2x^2}\sqrt{1-d^2x^2} - (1-a+2kx^2)^2 bcdx^2 \\ & + (a-2kx^2)^2 cd\sqrt{1-x^2}\sqrt{1-b^2x^2} \\ & + 4k^2x^2\sqrt{1-x^2}\sqrt{1-b^2x^2}\sqrt{1-c^2x^2}\sqrt{1-d^2x^2} \\ & - ad\sqrt{1-b^2x^2}\sqrt{1-c^2x^2} + abc\sqrt{1-x^2}\sqrt{1-d^2x^2} \end{aligned}$$

$$\begin{aligned} D = & (1+2kx^2)^2 b\sqrt{1-c^2x^2}\sqrt{1-d^2x^2} + (1-a+2kx^2)^2 bcdx^2 \\ & + (a-2kx^2)^2 cd\sqrt{1-x^2}\sqrt{1-b^2x^2} \\ & + 4k^2x^2\sqrt{1-x^2}\sqrt{1-b^2x^2}\sqrt{1-c^2x^2}\sqrt{1-d^2x^2} \end{aligned}$$

$$+ ad\sqrt{1-b^2x^2}\sqrt{1-c^2x^2} + abc\sqrt{1-x^2}\sqrt{1-d^2x^2}$$

The variable x is $sin(\theta)$, where θ is the incident angle. The parameters a, b, c, d, k represent the ratios of various elastic parameters: $a = \rho_2/\rho_1, b = \beta_1/\alpha_1, c = \alpha_2/\alpha_1, d = \beta_2/\alpha_1, k = ad^2 - b^2$, where ρ_i, α_i, β_i are the density, P-wave velocity, S-wave velocity of medium i, respectively. If we set $\rho_1 = \rho_2$, and $\beta_1 = \beta_2$, we can obtain $a = 1, b = d, k = 0$. Then the P-wave reflection coefficient would reduce to

$$R_{pp} = \frac{c\sqrt{1-x^2} - \sqrt{1-c^2x^2}}{c\sqrt{1-x^2} + \sqrt{1-c^2x^2}}$$

which equals to the acoustic reflection coefficient. Similarly, we can prove that the P-wave transmission coefficient would reduce to the acoustic transmission coefficient.

The S-wave reflection coefficient is given by $R_{ps} = N_{R_{ps}}/D$, where

$$N_{R_{ps}} = -4kx(1+2kx^2)\sqrt{1-x^2}\sqrt{1-c^2x^2}\sqrt{1-d^2x^2} - 2cdx(2kx^2-a)(2kx^2-a+1)\sqrt{1-x^2}$$

If we set $\rho_1 = \rho_2$, and $\beta_1 = \beta_2$, then $N_{R_{ps}} = 0$, and $R_{ps} = 0$. Similarly, we can prove that $T_{ps} = 0$.

B Appendix

Consider a two-layer elastic medium as in Appendix A. Following Keys (1989), we first set the shear wave velocity in the first layer equal to zero, which would lead to $b = 0$, and $k = ad^2$. In this case the first layer reduces to an acoustic medium, the Zoeppritz equation gives the correct P-wave reflection coefficient for a fluid-solid interface:

$$\begin{aligned} R_{pp} &= \frac{(a-2ad^2x^2)^2cd\sqrt{1-x^2} + 4a2d^4x^2\sqrt{1-x^2}\sqrt{1-c^2x^2}\sqrt{1-d^2x^2} - ad\sqrt{1-c^2x^2}}{(a-2ad^2x^2)^2cd\sqrt{1-x^2} + 4a^2d^4x^2\sqrt{1-x^2}\sqrt{1-c^2x^2}\sqrt{1-d^2x^2} + ad\sqrt{1-c^2x^2}} \\ &= \frac{(1-2d^2x^2)ac\sqrt{1-x^2} + 4ad^3x^2\sqrt{1-x^2}\sqrt{1-c^2x^2}\sqrt{1-d^2x^2} - \sqrt{1-c^2x^2}}{(1-2d^2x^2)ac\sqrt{1-x^2} + 4ad^3x^2\sqrt{1-x^2}\sqrt{1-c^2x^2}\sqrt{1-d^2x^2} + \sqrt{1-c^2x^2}} \end{aligned}$$

Then we set the shear wave velocity in the second layer also equal to zero, which leads to $d = 0$, and $k = 0$. The P-wave reflection coefficient reduces to the following form:

$$R_{pp} = \frac{ac\sqrt{1-x^2} - \sqrt{1-c^2x^2}}{ac\sqrt{1-x^2} + \sqrt{1-c^2x^2}}$$

which equals to the acoustic reflection coefficient. Similarly, we can prove that the P-wave transmission coefficient would reduce to the acoustic transmission coefficient. With the first solid layer replaced by a fluid layer, the Zoeppritz equation gives the nonphysical shear wave reflection coefficient:

$$R_{ps} = \frac{-4ad^2x(1+2ad^2x^2)\sqrt{1-x^2}\sqrt{1-c^2x^2}\sqrt{1-d^2x^2} - 2cdx(2ad^2x^2-a)(2ad^2x^2-a+1)\sqrt{1-x^2}}{(a-2ad^2x^2)^2cd\sqrt{1-x^2} + 4a^2d^4x^2\sqrt{1-x^2}\sqrt{1-c^2x^2}\sqrt{1-d^2x^2} + ad\sqrt{1-c^2x^2}}$$

$$= \frac{-4dx(1+2ad^2x^2)\sqrt{1-x^2}\sqrt{1-c^2x^2}\sqrt{1-d^2x^2} - 2cx(2d^2x^2-1)(2ad^2x^2-a+1)\sqrt{1-x^2}}{(1-2d^2x^2)^2ac\sqrt{1-x^2}+4a2d^3x^2\sqrt{1-x^2}\sqrt{1-c^2x^2}\sqrt{1-d^2x^2}+\sqrt{1-c^2x^2}}$$

If we set the shear wave velocity in the second layer also equal to zero, which leads to $d = 0$, and $k = 0$. Then the S-wave reflection coefficient would reduce to the following form:

$$R_{ps} = \frac{-4dx(1+2ad^2x^2)\sqrt{1-x^2}\sqrt{1-c^2x^2}\sqrt{1-d^2x^2} - 2cx(2d^2x^2-1)(2ad^2x^2-a+1)\sqrt{1-x^2}}{(1-2d^2x^2)^2ac\sqrt{1-x^2}+4a2d^3x^2\sqrt{1-x^2}\sqrt{1-c^2x^2}\sqrt{1-d^2x^2}+\sqrt{1-c^2x^2}}$$

$$= 0$$

Similarly, we can prove the the S-wave transmission coefficient would also equal to zero.

An investigation of ISS imaging algorithms beyond HOIS, to begin to address exclusively laterally varying imaging challenges

Z. Wang and A. B. Weglein

Abstract

The inverse scattering series (ISS) is wave-equation based and has the potential capability to image a reflector with any dipping angle. The leading-order imaging subseries in closed form (LOIS) and the higher-order imaging subseries in closed form (HOIS) are both subseries of ISS. Many terms related to lateral variations are not captured by them; certain degree of lateral variation can be accommodated.

We tested two ISS direct-depth imaging algorithms beyond HOIS to accommodate larger lateral variations in the medium. The first is the gradient HOIS which migrates along the gradient of every point in the water-speed Stolt migration result. The second is the HOIS plus lateral exclusive (HOISPLE) which migrates every point of the water-speed Stolt migration result into a semicircle and the interference over all angles constructs the desired imaging.

1 Introduction

In exploration seismology, a man-made source of energy on or near the surface of the earth generates waves that propagate into the subsurface. The waves travel through the earth with a finite velocity, which is governed by the material properties of the earth. When the waves reach a rock layer with a different velocity, a portion of the energy is reflected back towards the surface. Finally, the reflected waves arrive at the measurement surface and are recorded by geophones. After many preprocessing steps, a process called seismic imaging is applied, by which seismic events are relocated to where the event occured in the subsurface rather than the location where it was recorded at the measurement surface.

In conventional seismic imaging, the recorded arrival times of the events and a velocity map are used to calculate the locations of the reflectors. In this process, an accurate velocity map, which is generated from a preprocessing step called velocity analysis, is a key factor for the reliability of the imaging result and often is a big challenge, especially when the medium is complex.

The ISS provides a new vision and level of seismic capability and effectiveness. That promise has already been realized for the removal of free surface and internal multiples, while big progress is being made for direct-depth imaging.

In an earth model that allows only variations in velocity, two major closed forms of the inverse scattering imaging subseries with different degrees of imaging capture and capability have been identified and tested in M-OSRP: LOIS (Shaw et al., 2004):

$$\alpha^{LOIS}(x,z) = \alpha_1\left(x, z - \frac{1}{2}\int_{-\infty}^{z}\alpha_1(x,u)du\right) \tag{1}$$

and HOIS (Liu, 2006; Wang et al., 2009):

$$\alpha^{HOIS}\left(x, z + \frac{1}{2}\int_{-\infty}^{z} du\frac{\alpha_1(x,u)}{1-0.25\alpha_1(x,u)}\right) = \alpha_1(x,z). \tag{2}$$

Both of these forms are missing many terms, especially those related to lateral variations, and can accomodate only certain degrees of lateral variation.

In this paper, two ISS direct-depth imaging algorithms beyond HOIS (to accommodate larger lateral variations in the medium) are investigated. The gradient HOIS direct-depth imaging algorithm, which utilizes the gradient of α_1 at each location as the direction for the migration, is discussed and tested. Its results show that dipping reflectors are better located than in the HOIS, while the shadow zones beneath the dipping-reflectors are out of order, because of the disorder of the gradient in those areas (caused by diffraction energy). Then we investigate the HOISPLE direct-depth imaging algorithm. Instead of migrating in a specified direction, it migrates in all directions and the results interfere for different directions. The algorithm attenuates the energy except in the desired direction, which is the same as the one calculated from the gradient. HOISPLE testing results show improvements for dipping reflectors in both the fault model and the salt model.

2 ISS direct-depth imaging algorithm

Scattering theory is a form of perturbation analysis. It considers the original unperturbed medium as the reference medium and the difference between the actual and reference media as the perturbation. The corresponding wavefields are the reference wavefield and the scattered wavefield. Based on the reference medium (already chosen) and the reference wavefield (calculated from the wave equation using the reference velocity), forward scatting constructs the scattered wavefield from the perturbation, while inverse scattering reconstructs the perturbation from the scattered wavefield.

The Lippman-Schwinger equation is the fundamental equation of scattering theory,

$$\Psi = G_0 + G_0 V \Psi \tag{3}$$

where Ψ is the actual wavefield, G_0 is the reference wavefield and V is the perturbation operator. Substituting equation 3 into itself generates the forward scattering series

$$\Psi_s = \Psi - G_0 = G_0 V G_0 + G_0 V G_0 V G_0 + \cdots \tag{4}$$

where Ψ_s is the scattered wavefield.

In the inverse scattering series, the perturbation is expanded as a series

$$V = V_1 + V_2 + V_3 + \cdots \tag{5}$$

where V_n is the portion of V that is nth order in Ψ_s. The series of V_n resides in a series of equations (Weglein et al., 2003),

$$(\Psi_s)_m = (G_0 V_1 G_0)_m, \tag{6}$$

$$0 = (G_0 V_2 G_0)_m + (G_0 V_1 G_0 V_1 G_0)_m, \tag{7}$$

$$0 = (G_0 V_3 G_0)_m + (G_0 V_2 G_0 V_1 G_0)_m + (G_0 V_1 G_0 V_2 G_0)_m + (G_0 V_1 G_0 V_1 G_0 V_1 G_0)_m, \tag{8}$$

$$0 = (G_0 V_n G_0)_m + (G_0 V_1 G_0 V_{n-1} G_0)_m + \cdots + (G_0 V_1 G_0 V_1 G_0 V_1 \cdots G_0 V_1 G_0)_m. \tag{9}$$

V_1 can be solved using equation 6 in terms of the reference wavefield G_0 and the scattered wavefield Ψ_s, and each $V_n (n \geq 2)$ could be solved from the corresponding equation in terms of the reference wavefield G_0 and all $V_i (i < n)$. Thus the total perturbation $V = \sum_{n=1}^{\infty} V_n$ is an explicit direct inversion formalism. Each V_n consists of several terms, some of which are related only to correcting the spatial locations of the reflectors. We call them imaging subseries. Capturing the imaging-only subseries (Weglein et al., 2002; Shaw et al., 2004) is less ambitious but more practical than capturing the whole series.

The imaging-only subseries still consists of an infinite number of terms, and adding them up requires large amounts of calculations and computations. Pulling out a subseries and compacting them into a closed form saves massive computations and makes the subseries more physically meaningful. Until now, only LOIS and HOIS for a one-parameter (only velocity changing) acoustic medium, and the imaging conjecture (Weglein, 2008, pp. 1-8) and beyond conjecture (Wang et al., 2009) for a multi-parameter acoustic medium have been provided and tested in M-OSRP.

Below we will take the HOIS closed form for the two-dimension one-parameter acoustic medium as an example and discuss the beyond direct-depth imaging algorithms. ISS direct-depth imaging algorithm is completed in two steps:

(1). Based on equation 6, inverting the G_0 operator on both sides of V_1 gives the linear (in the data) imaging in terms of the measured data and the reference velocity. It is a Stolt migration using the reference velocity. In the two-dimension one-parameter acoustic medium, it is (Liu, 2006)

$$\tilde{\tilde{\alpha}}_1(k_m, k_z) = -\frac{4 q_g q_s}{\omega^2 / c_0^2} \int_{-\infty}^{\infty} dx_m e^{-i k_m x_m} \int_{-\infty}^{\infty} d\tau e^{i\omega\tau} D^{\tau p}(x_m, \tau), \tag{10}$$

in which,

$$D^{\tau p}(x_m, \tau) = \int_{-\infty}^{\infty} dx_h D(x_m + \frac{x_h}{2}, x_m - \frac{x_h}{2}, \tau + x_h \frac{\sin\theta}{c_0}), \tag{11}$$

and

$$\alpha_1(x, z) = V_1(x, z) / \frac{\omega^2}{c_0^2}. \tag{12}$$

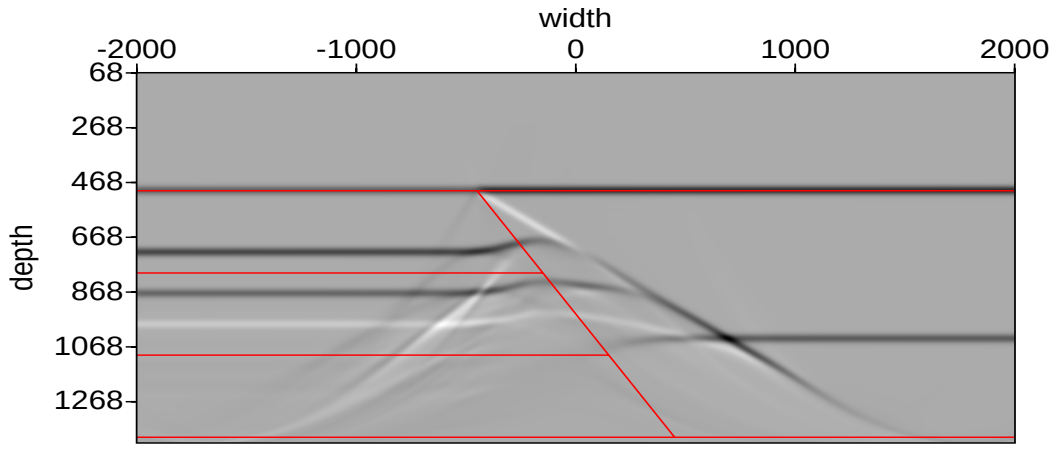

Figure 1: Water-speed Stolt migration for the fault model.

(2). Plug the α_1 result from step 1 into the HOIS closed form

$$\alpha^{HOIS}\left(x, z+\frac{1}{2}\int_{-\infty}^{z} du \frac{\alpha_1(x,u)}{1-0.25\alpha_1(x,u)}\right) = \alpha_1(x,z), \tag{13}$$

and get a remigrated result.

Figure 1 shows the water-speed Stolt migration for the fault model (Liu and Weglein, 2009), and Figure 2 shows the imaging result after applying the HOIS closed form. For the flat reflectors the HOIS imaging result shows improved accuracy, and for the dipping reflectors the accuracy is good but there is still room for improvement. This issue will be addressed by those terms that are not captured by HOIS.

3 ISS imaging algorithms beyond HOIS for lateral variations

3.1 Gradient HOIS

Figure 3 is a scheme of what happens to the dipping reflector when HOIS is applied. The reflector is undermigrated because HOIS does not fully make use of the information from the linear imaging result and only remigrates in the z direction. One reasonable modification is to localize the HOIS imaging algorithm: let the gradient guide the migration direction. The modified gradient HOIS has the following form:

$$\alpha^{HOIS}\left(\vec{r}+\frac{\nabla\alpha_1}{|\nabla\alpha_1|} * \frac{1}{2}\int_{-\infty}^{z} du \frac{\alpha_1(x,u)}{1-0.25\alpha_1(x,u)}\right) = \alpha_1(\vec{r}). \tag{14}$$

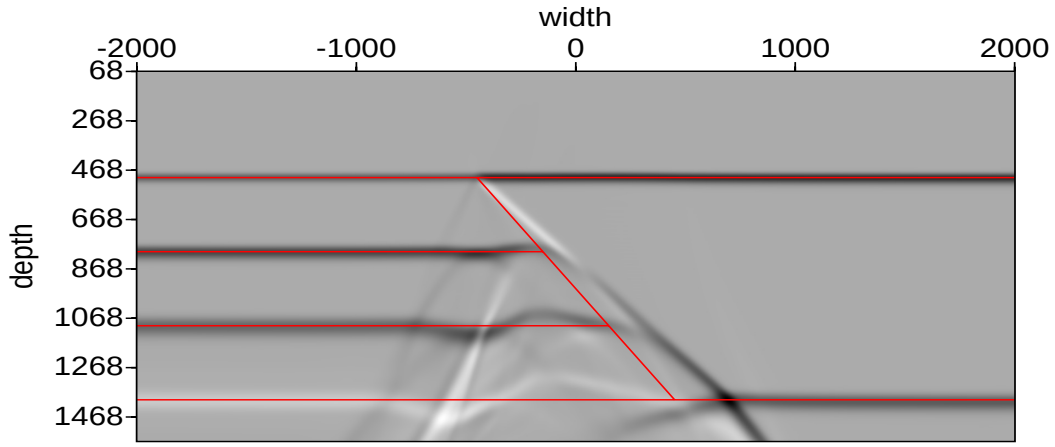

Figure 2: HOIS image for the fault model.

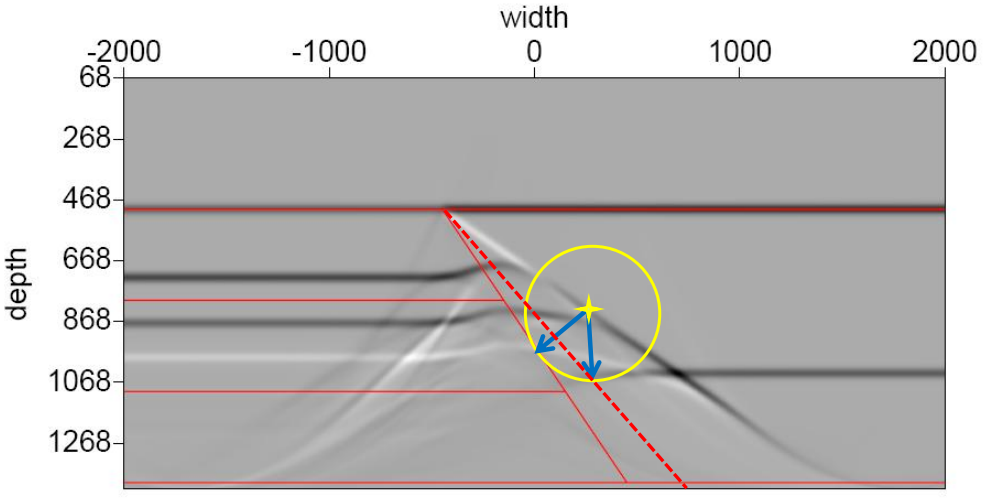

Figure 3: A scheme about the HOIS imaging.

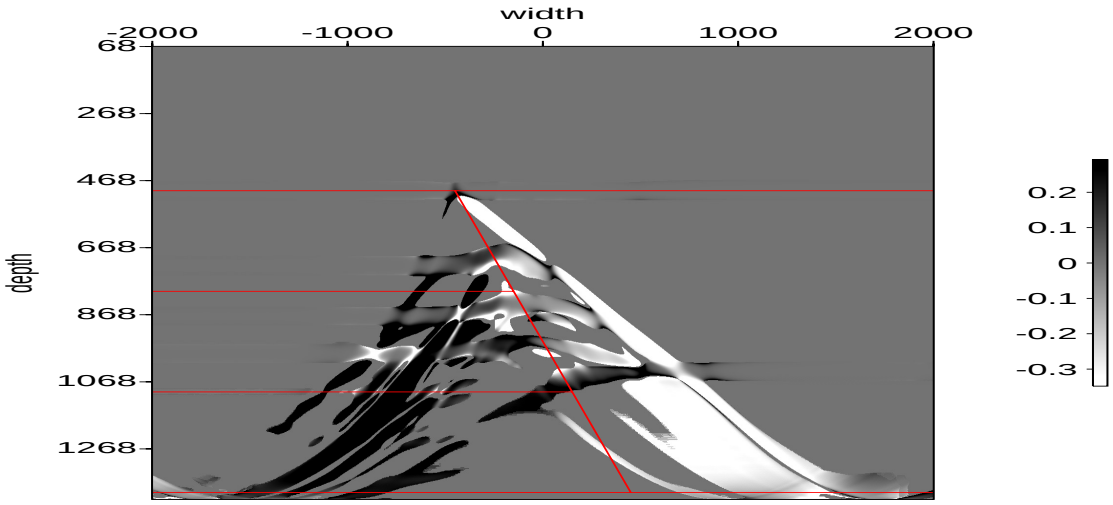

Figure 4: Normalized $\partial\alpha_1/\partial x$ for the fault model.

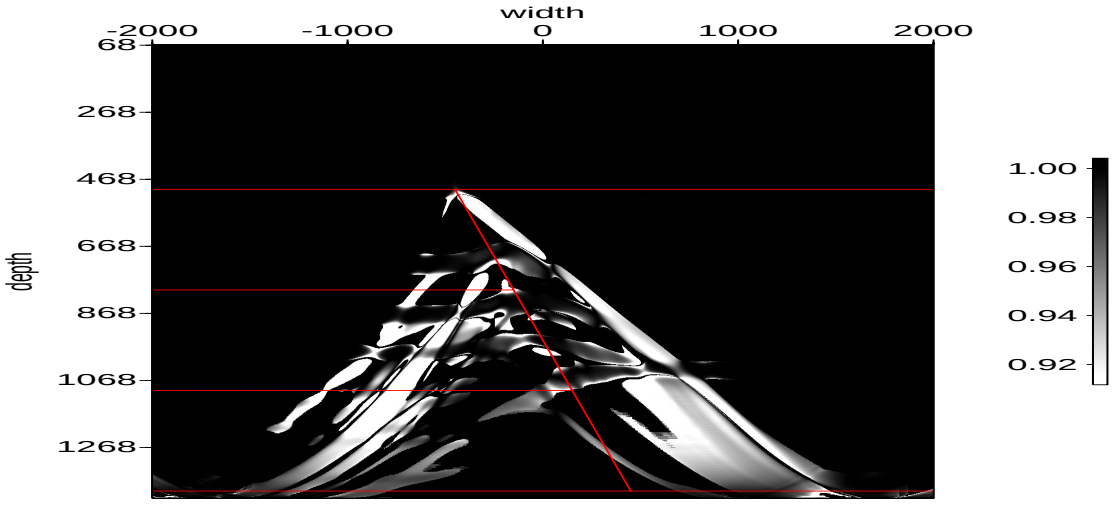

Figure 5: Normalized $\partial\alpha_1/\partial z$ for the fault model.

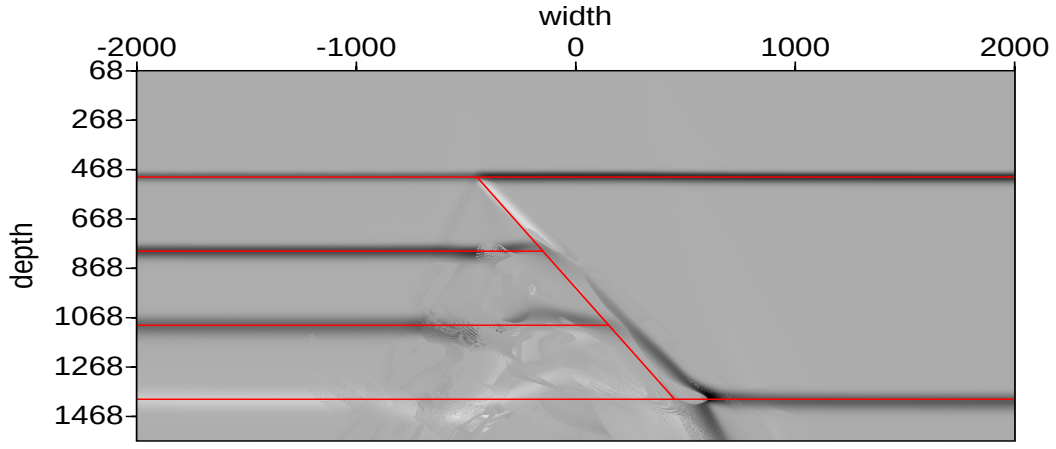

Figure 6: Localized HOIS image for the fault model.

If we take a look at $\alpha_{2,2}$, the first term that is not captured by HOIS (Liu, 2006)

$$\alpha_{2,2}(x,z) = \frac{1}{2}\frac{\partial \alpha_1(x,z)}{\partial x}\int_{-\infty}^{z} dz \int_{-\infty}^{u} dv \frac{\partial \alpha_1(x,z)}{\partial x}, \tag{15}$$

and the imaging term in $\alpha_{2,1}$

$$\alpha_{2,1}^{IM}(x,z) = \frac{1}{2}\frac{\partial \alpha_1(x,z)}{\partial z}\int_{-\infty}^{z} dz \int_{-\infty}^{u} dv \frac{\partial \alpha_1(x,z)}{\partial z}. \tag{16}$$

it does have some quantities related to the gradient, although we are not clear what it is yet.

Figures 4 and 5 show plots of the normalized partial derivatives of α_1 over x, $\frac{\partial \alpha_1/\partial x}{|\nabla \alpha_1|}$, and over z, $\frac{\partial \alpha_1/\partial z}{|\nabla \alpha_1|}$. Figure 6 is the gradient HOIS image result. Compared with the HOIS result in Figure 2, the dipping reflector is located much closer to its actual location, and outside of its shadow zone, the flat reflectors are not affected. When the reflectors are flat, the gradient is in the z direction, but in its shadow zone, the imaging is not clear, and the corresponding area in Figure 4 and 5 is disordered. The energy reflected by those areas take an even more complex path than that reflected by the fault.

3.2 HOIS plus lateral exlusive

In the gradient HOIS, because of the complexity of the energy path, the fault shadow zone area is not well imaged. Here we will try another approach. We do not use the local gradient to guide the migration direction. Instead, similar to Kirchhoff migration, we migrate in every direction and assume that the interfereces over different angles will construct the desired part and destruct the undesired part.

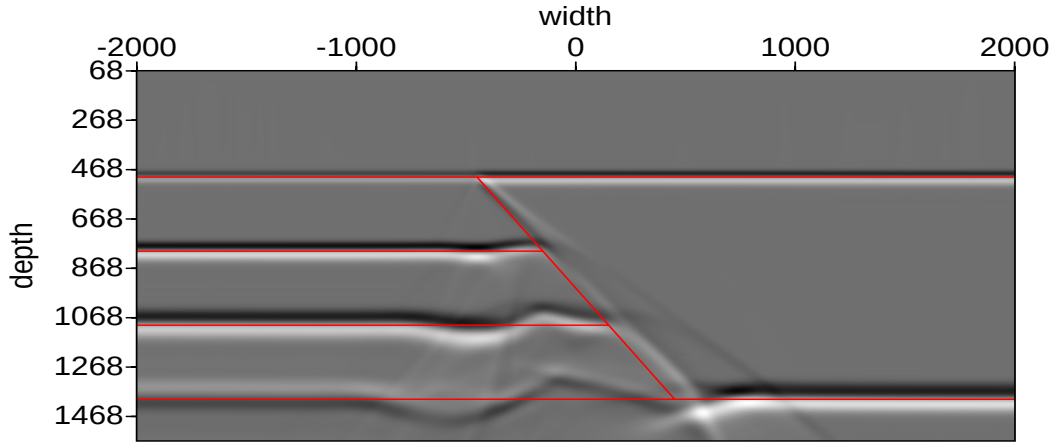

Figure 7: HOISPLE image for the fault model.

We will call the algorithm HOISPLE in the following and mathematically, it has the form,

$$\alpha^{HOIS}\left(\vec{r}+\hat{u}*\frac{1}{2}\int_{-\infty}^{z}du\frac{\alpha_1(x,u)}{1-0.25\alpha_1(x,u)}\right)=\alpha_1(\vec{r}), \tag{17}$$

where

$$\hat{u}=\sin\psi\hat{x}+\cos\psi\hat{z}, \qquad \psi\in[\pi/2,\pi/2] \tag{18}$$

and the final imaging $I(x,z)$ equals to the interference of α over different angles,

$$I(x,z)=\sum_{\psi}\alpha^{''}(x,z,\psi)\,. \tag{19}$$

Here we use α'' instead of α to make the non-wavefront parts cancelled by destructive interference. ψ represents the migration angle with respect to the z direction, which could range in $[\pi/2,\pi/2]$. But for most cases, a subset is chosen to save computational time.

Figure 7 is the HOISPLE imaging result for the fault model. An amplitude gain has been used to bring up the deeper parts in Figure 7. The fault location is similar to the result of gradient HOIS in Figure 6, both being closer to the actual location than the result of the original HOIS in Figure 2. Also, the diffraction effect is attenuated after HOISPLE imaging.

Figures 8 and 9 are the HOIS and KirchhoffPLE imaging results for the salt model (Liu, 2006). An amplitude gain has been used in Figure 9. As in the fault model, the bottom of the salt body after HOISPLE migration is located much closer to the actual location than the HOIS result and the diffractions are largely reduced.

4 Discussion and conclusions

In this paper, we proposed two different beyond HOIS direct-depth imaging algorithms to accommodate large variations within the medium: the gradient HOIS and HOISPLE. The

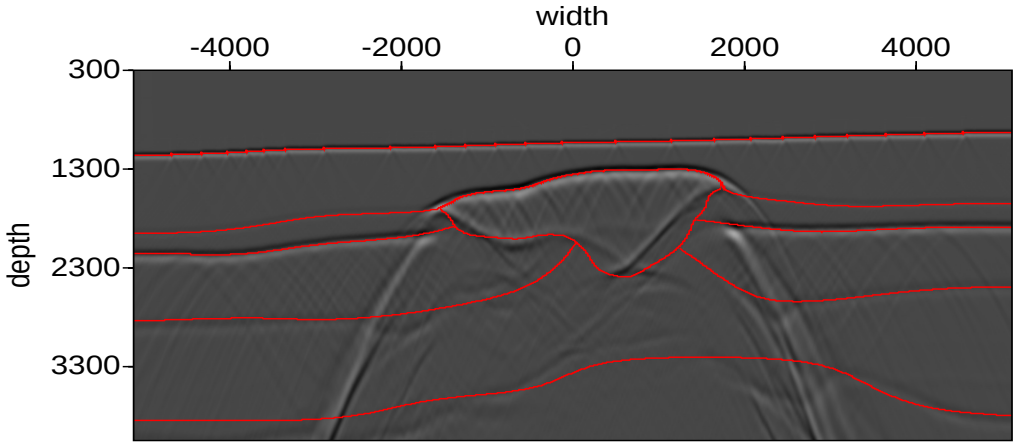

Figure 8: HOIS image for the salt model.

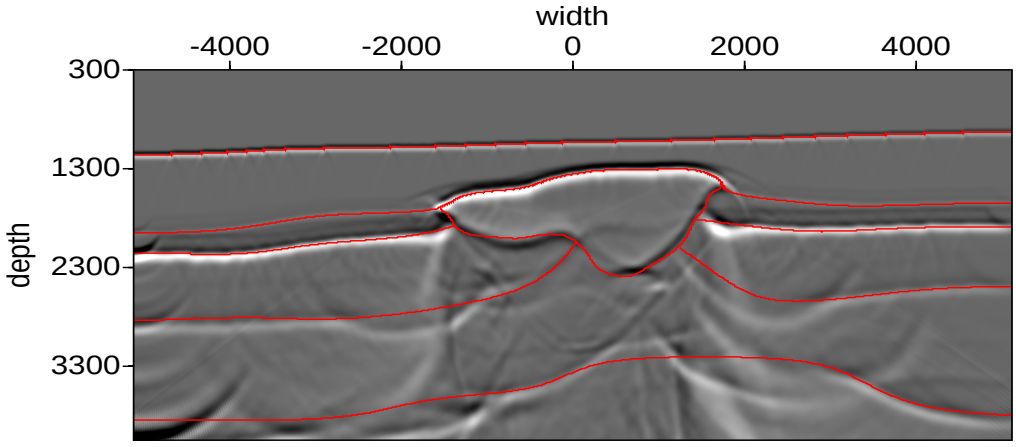

Figure 9: HOISPLE image for the salt model.

gradient HOIS directly uses the gradient of α_1 as the direction guidence for the nonlinear imaging algorithm. The testing result shows that the dipping reflector is better imaged but not those areas beneath it. The HOISPLE migrates in all angles and the interference of its results constructs the desired imaging. Its testing results show improvements in both locating the fault and collapsing diffractions. More research and tests will be done for these new algorithms.

5 Acknowledgements

All M-OSRP sponsors are gratefully appreciated for their support in the research. This work has been partially funded by NSF-CMG (award DMS-0327778) and U.S. DOE-BES (Grant No. DOE-De-FG02-05ER15697). The first author would like to thank Dr. Fang Liu for providing the data and the discussions.

References

Liu, F. *Multi-dimensional depth imaging without an adequate velocity model.* PhD thesis, University of Houston, 2006.

Liu, Fang and Arthur B. Weglein. "Addressing the bandlimited nature of seismic source and rapid lateral variations of the Earth: source regularization and cascaded imaging operator." *M-OSRP Annual Report.* 2009.

Shaw, S. A., A. B. Weglein, D. J. Foster, K. H. Matson, and R. G. Keys. "Isolation of a leading order depth imaging series and analysis of its convergence properties." *Journal of Seismic Exploration* 2 (November 2004): 157–195.

Wang, Z., A. B. Weglein, and X. Li. "New capture of direct velocity independent depth imaging in a one-dimension two-parameter acoustic earth." *M-OSRP Annual Report.* 2009.

Wang, Z., A. B. Weglein, and F. Liu. "Note: Evaluations of the HOIS closed form and its two variations." *M-OSRP Annual Report.* 2009.

Weglein, A. B. "Introduction and preface." *M-OSRP Annual Report.* 2008.

Weglein, A. B., F. V. Araújo, P. M. Carvalho, R. H. Stolt, K. H. Matson, R. T. Coates, D. Corrigan, D. J. Foster, S. A. Shaw, and H. Zhang. "Inverse Scattering Series and Seismic Exploration." *Inverse Problems* (2003): R27–R83.

Weglein, A. B., D. J. Foster, K. H. Matson, S. A. Shaw, P. M. Carvalho, and D. Corrigan. "Predicting the correct spatial location of reflectors without knowing or determining the precise medium and wave velocity: initial concept, algorithm and analytic and numerical example." *Journal of Seismic Exploration* 10 (2002): 367–382.

Developing multidimensional depth imaging for a velocity and density varying earth: An initial imaging study and 2D two-parameter modeling to generate data in the (x, t) domain needed to test ISS imaging algorithms

D. Chang, A. B. Weglein and F. Liu, M-OSRP, University of Houston

Abstract

The inverse scattering series imaging algorithm has been used successfully on multidimensional velocity varying earth. However, in the real case there is always rapid density variation in the medium. We have made progress in the development of multidimensional depth imaging with a velocity and density varying earth. The first step, completed at the time of this writing, is testing the effectiveness of the current ISS imaging algorithm on synthetic data generated by finite difference modeling in the x-t domain. This goes one step further from previous tests using analytic data generated directly in the f-k domain, which is important because numerical data are the only way to multidimensional imaging tests. The ISS multiparameter imaging algorithm requires comparisons between the amplitude of data at different angles, which puts a high bar on the accuracy of numerical data. We show here that ISS imaging results on synthetic data are encouraging. The 2D finite difference modeling for a velocity and density varying earth is documented as a progress in our group. We also discuss the steps we are taking towards multi-D depth imaging research.

1 Introduction

Conventional imaging methods require an adequate velocity model for accurate depth imaging. These methods often fail because of inadequate velocity analysis due to complex subsurface geology. In contrast, the inverse scattering series (ISS) can directly achieve the seismic depth imaging goal without subsurface information. F. Liu's higher order imaging subseries (HOIS) algorithm has produced successful results on multidimensional earth with velocity varying (Liu, 2006). Now, we aim at extending this multidimensional depth imaging algorithm to a velocity and density varying earth.

Reflections from the subsurface can be caused by variations in velocity or density or both. A one-parameter imaging algorithm will misinterpret the imaging results by attributing all the reflections to velocity variation. "Imaging conjecture" was proposed to address this issue in 2007 (Weglein, 2008). It has a front end that excludes the density contribution from data. Solving the front end requires comparisons between data at different angles and this puts a high bar on the quality of data. The form and validity of imaging conjecture has been verified

on 1D analytic data directly generated in the f-k domain (Jiang and Weglein (2009); X. Li and Weglein (2009); H. Liang and Li (2010)). However, there is no analytic data expression in multi-D case, but only numerical data. We tested the capability of excluding density-only reflections for the first time using synthetic data generated in the x-t domain by the finite difference method for a 1D earth with density variations, and outlined the plan and steps towards the multidimensional depth imaging for a multi-parameter earth.

Two additional developments are documented here towards our objective: F. Liu's finite-difference framework for 1D two-parameter acoustic medium has been generalized to 2D to accommodate multi-D depth imaging research within our group. The numerical transformation of data from τ-p domain to pseudodepth angle-gather domain for prestack experiment (water-speed migration) has been demonstrated.

It's important to point out that the generalization of the conjecture in excluding density contribution from its 1D acoustic or elastic form to multi-D medium is still based on intuition rather than a consolidated theory. So, ending up with 2D modeling, we outline the steps towards exploring multi-D depth imaging.

2 The issue of excluding the density contribution from data

2.1 The validity on 1D analytic data

For a 1D acoustic earth with velocity and density varying, ISS imaging algorithm has the following form:

$$D^{HOIS}\left(z+\frac{1}{2}\int_{-\infty}^{z}\frac{\alpha_1(z')-\beta_1(z')}{\cos^2\theta-0.25(\alpha_1(z')-\beta_1(z'))}dz',\theta\right)=D(z,\theta) \tag{1}$$

$D(z,\theta)$ on the right is the result of water-speed migration. The HOIS algorithm corrects the wrong depth in $D(z,\theta)$ and moves the reflectors to their actual depths. θ represents the incident angle. A simple method to solve for the front end $\alpha_1(z)-\beta_1(z)$ from the linear equation 2 is to choose two different angles:

$$D(z,\theta)=-\frac{\rho_0}{4}\left[\frac{1}{\cos^2\theta}\alpha_1(z)+(1-\tan^2\theta)\beta_1(z)\right] \tag{2}$$

$$\alpha_1(z)-\beta_1(z)=-\frac{4}{\rho_0}\frac{D(z,\theta_1)-D(z,\theta_2)}{\tan^2(\theta_1)-\tan^2(\theta_2)} \tag{3}$$

For data directly expressed in the f-k domain as shown in equation 4,

$$\tilde{D}(q_g,\theta)=\rho_0 R(\theta)\frac{e^{2iq_g a}}{4\pi i q_g} \tag{4}$$

it is straightforward to prove (Zhang, 2006) that the linear estimation of the relative change in velocity is related to the front end as the following expression:

$$(\frac{\triangle c}{c})_1 = \frac{1}{2}(\alpha_1 - \beta_1) = 0 \tag{5}$$

when $\triangle c = 0$. This means that if there is no velocity variation across the boundary, $\alpha_1(z) - \beta_1(z)$ is zero.

2.2 The conjecture on 2D numerical data

The research on the challenge of excluding the density contribution from data for a 2D acoustic medium starts with an extension of the front end from its 1D form directly to a 2D form $\alpha_1(x, z) - \beta_1(x, z)$. To evaluate its validity, we have to use numerical data because of the inaccessibility of analytic data expressions for multidimensional medium. In the previous reports, all the multi-parameter imaging tests utilize the perfect analytic data while tests on numerical data have never been tried, which motivates the work in this report. Here, we make one step ahead, testing the current multi-parameter imaging algorithm on numerical data. This serves as a bridge linking our previous 1D analytic data tests and the next 2D numerical data tests by giving us a preliminary estimation that how much will the accuracy of the numerical data affect the imaging results.

3 Numerical tests using synthetic data

3.1 The issue we want to test on synthetic data

From equation 3 we can see that solving the front end needs the communication between data at two different angles and this puts a high bar on the accuracy of numerical data. In this report, we are going to evaluate this accuracy by using numerical data as input rather than perfect analytic data used in the previous tests.

Liu and Weglein (2010) analyzed the effect of using analytic data with a band-limited seismic source within the imaging conjecture and proposed a regularization method to deal with the fact that, for imperfect data, the front end could be nonzero when there is only a density change across the boundary. Here, we use synthetic data generated by finite difference modeling to test the capability of $\alpha_1(z) - \beta_1(z)$ in excluding density-only reflections. Apart from the wavelet issue, other factors such as the intrinsic noise from modeling computation as well as noise from numerical transformations among others might also affect the imaging results.

3.2 Data generation using finite difference modeling

We first review the finite difference modeling for a 2D two-parameter acoustic medium starting with the isotropic acoustic wave equation in Clayton and Stolt (1981):

$$\bigtriangledown \cdot [\frac{1}{\rho(x,z)} \bigtriangledown P(x,z,t)] - \frac{1}{K(x,z)} \frac{\partial^2}{\partial t^2} P(x,z,t) = 0 \tag{6}$$

where $K(x,z) = \rho(x,z)c^2(x,z)$ is the bulk modulus. We apply fourth and second order finite difference schemes for the space and time derivatives respectively. The homogeneous form of equation 6 can be approximated in rectangular coordinates as

$$\begin{aligned} P_{m,n,l+1} = [2 - 5D^2]P_{m,n,l} - P_{m,n,l-1} + \frac{4}{3}D^2(1 + A\rho_{m,n})P_{m+1,n,l} + \\ \frac{4}{3}D^2(1 - A\rho_{m,n})P_{m-1,n,l} - \frac{1}{12}D^2(1 + 2A\rho_{m,n})P_{m+2,n,l} - \\ \frac{1}{12}D^2(1 - 2A\rho_{m,n})P_{m-2,n,l} + \frac{4}{3}D^2(1 + B\rho_{m,n})P_{m,n+1,l} + \\ \frac{4}{3}D^2(1 - B\rho_{m,n})P_{m,n-1,l} - \frac{1}{12}D^2(1 + 2B\rho_{m,n})P_{m,n+2,l} - \\ \frac{1}{12}D^2(1 - 2B\rho_{m,n})P_{m,n-2,l} + \\ 0(h^4 + \triangle t^2) \end{aligned} \tag{7}$$

where $D = \triangle t \cdot c_{m,n}/h$. Our numerical modeling satisfies the stability condition that $D \leq \sqrt{3/8}$. $\triangle x = \triangle z = h$ is the grid size in the x and z directions, respectively; m, n, and l are integers such that $x = m\triangle x$, $z = n\triangle z$, $t = l\triangle t$; the scheme approximates the partial differential equation to the order h^4. Coefficients A and B are determined by densities at different grids as

$$A = -\frac{1}{24}\frac{1}{\rho_{m+2,n}} + \frac{1}{3}\frac{1}{\rho_{m+1,n}} - \frac{1}{3}\frac{1}{\rho_{m-1,n}} + \frac{1}{24}\frac{1}{\rho_{m-2,n}} \tag{8}$$

$$B = -\frac{1}{24}\frac{1}{\rho_{m,n+2}} + \frac{1}{3}\frac{1}{\rho_{m,n+1}} - \frac{1}{3}\frac{1}{\rho_{m,n-1}} + \frac{1}{24}\frac{1}{\rho_{m,n-2}} \tag{9}$$

Liu and Weglein (2005) analyzed the importance of implementing the source signature accurately to the waveform modeling and gave a new method for accurate implementation of the source at arbitrary locations.

Assuming that for a small time interval the wave field propagates in a homogeneous medium around the source location, the energy of the wave outside the circular region can be neglected. Equation 9 in Alford et al. (1974) is used to precalculate the wave fields at two time points. Figure 1 shows two analytic wavefields at $t_0 = 0.0895$ s and $t_0 + \triangle t = 0.0900$ s, which are then straigtforwardly implemented at any location where we want to put the source. The wavelet used here is the Ricker wavelet, one of the most commonly encountered wavelets in the real seismic experiments, with a peak frequency at 28 Hz, as shown in Figure 2. We take the model in Figure 2 as an example. The finite difference data is shown in Figure 3. The parameters in

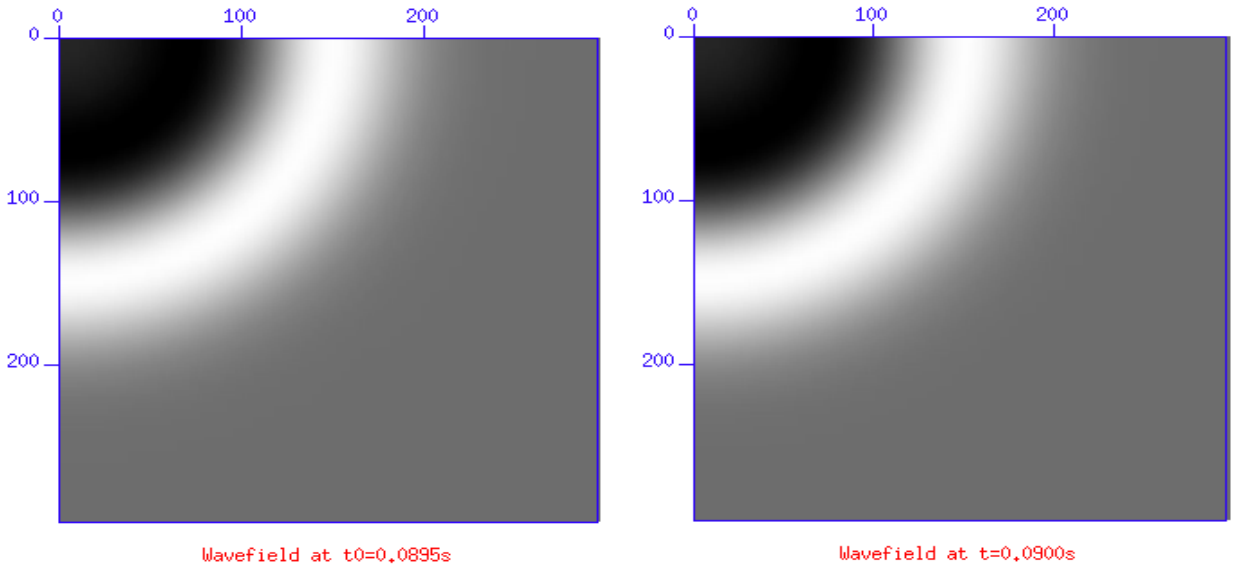

Figure 1: The precalculated wavefields at 0.0895 s and 0.0900 s.

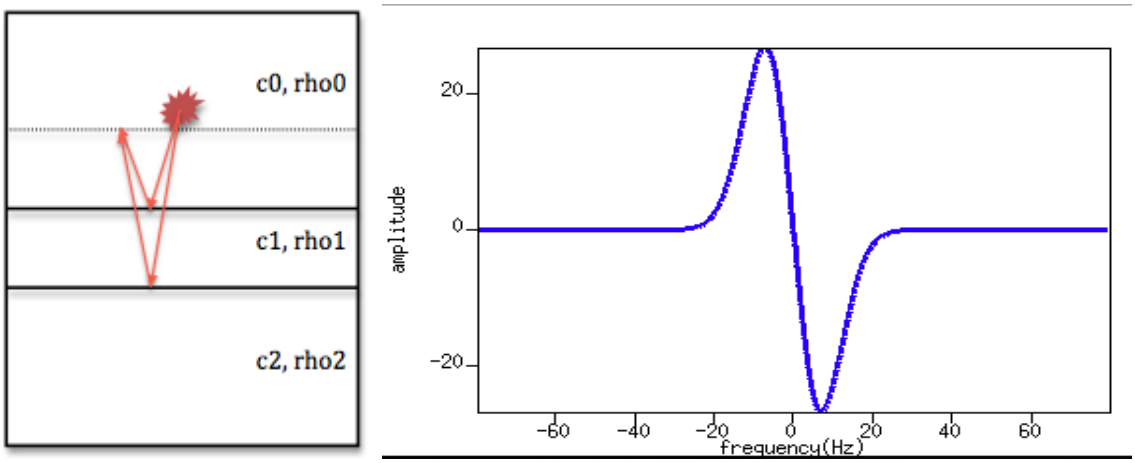

Figure 2: 1D two-parameter acoustic model and the wavelet used for modeling. c_0=1500 m/s, c_1=1600 m/s, c_2=1700 m/s, ρ_0=1.0 g/cm^3, ρ_1=1.1 g/cm^3, and ρ_2=1.2 g/cm^3. The wavelet is the first derivative of Gaussian.

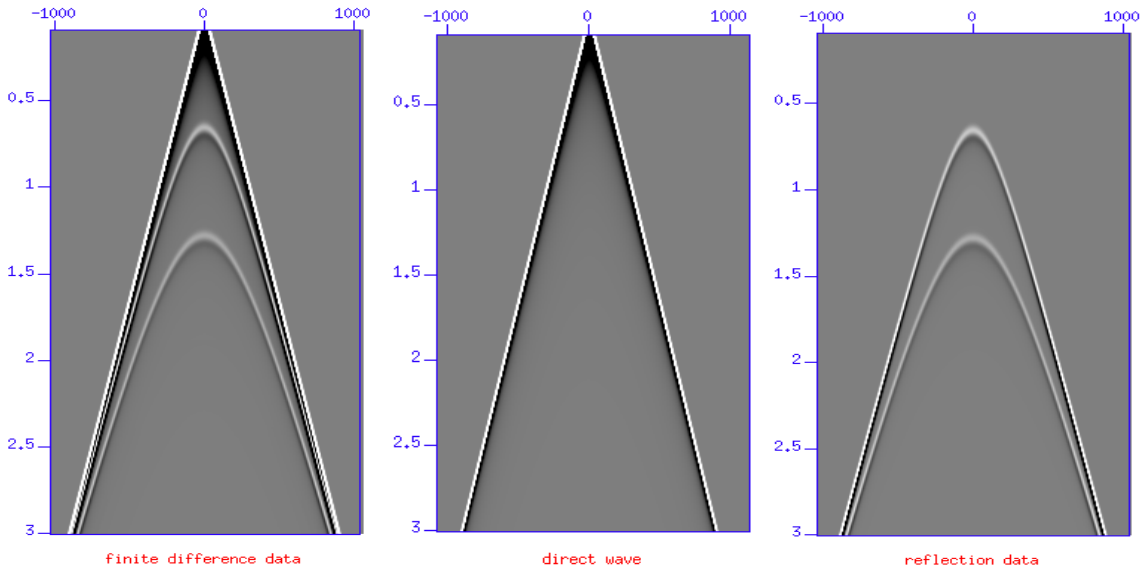

Figure 3: Finite difference modeling results using the source fields at 0.0895 s and 0.0900 s.

Step 1: Source regularization: recovering the wavelet to Gaussian
Step 2: 2D Radon transform (the offset variable is regarded as the x-coordinate)
Step 3: Water speed migration
Step 4: Excluding density contribution
Step 5: ISS imaging subseries

Table 1: Data processing flow.

modeling have been properly adjusted so that there are no ghosts and free-surface multiples in the data. The reflected data contains only primaries and internal multiples.

Before solving the front end for imaging, we need to transform the data to the pseudodepth domain, i.e., $D(z, \theta)$, to accommodate the linear equation 2 for inverting the parameters describing the medium properties. Please note that all the analytic data used in the previous tests are Fourier transformed to this domain for imaging.

3.3 Data processing flow

Our data processing flow starts with the reflected data shown in Figure 3. Table 1 lists all the numerical transformations towards the imaging tests.

The ISS imaging algorithm is written for an ideal source with full bandwidth. Previous tests show that the Gaussian wavelet can offer satisfied imaging results. The source regularization here is to recover the wavelet from the Ricker wavelet to Gaussian. Interested readers can

refer to Fang Liu and Weglein (2011) for more details of source regularization, but for Gussian type wavelets, the operation is just an integral over time. The second step is a 2D Radon transform to this 2D propagation data set. Interested readers can refer to Fang Liu and Weglein (2011) for more details of Radon transform. After this, the data is further migrated to the psudodepth angle-gather domain with water speed. This data set is then used to solve for the front end to exclude density contribution. Finally the water-speed migrated data and the front end are input to the ISS imaging subseries to get the final result. All the tests shown here follow this processing flow.

Liu and Weglein (2010) illustrated how to transform the data from time domain to pseudodepth domain for 1D normal incidence. Here we generalize the analysis to 2D wave propagation. The basic principle that the integration of data in time domain over t should equal the integration of data in pseudodepth domain over z, i.e.,

$$\int d(t)dt = \int D(z)dz \tag{10}$$

results in the conclusion that the data in time domain can be transformed to pseudodepth domain through stretching the argument by a factor $c_0/2$ and squeezing the data amplitude by $2/c_0$.

For 2D wave propagation where data is a function of t and x, the basic idea above should be generalized as follows: The integration of data in τ-p domain over τ equals the integration of data in pseudodepth domain over z, i.e.,

$$\int d(\tau)d\tau = \int D(z)dz \tag{11}$$

because we can think of each trace in x-t domain as a normal incident trace described by its vertical time τ. In Fourier domain the relationship in Liu and Weglein (2010) changes to $\tilde{D}(k_z) = \tilde{D}(2\omega\cos\theta/c_0) = \tilde{d}(\omega)$. Following similar logic and remembering that $z = c_0\tau/2\cos\theta$ or $\tau = 2z\cos\theta/c_0$ for non-normal incidence, we have the transformation described by equation 12.

Thus, the data in τ-p domain can be transformed to pseudodepth domain through stretching the argument by a factor $c_0/2\cos\theta$ and squeezing the data amplitude by $2\cos\theta/c_0$. Figure 4 shows the data transformed to τ-p domain from the data after source regularization and then transformed to pseudodepth domain following the above logic.

$$\begin{aligned} D(z,\theta) &= \frac{1}{2\pi}\int_{-\infty}^{\infty} dk_z e^{-ik_z z}\tilde{D}(k_z,\theta) \\ &= \frac{1}{2\pi}\int_{-\infty}^{\infty} d(\frac{2\omega\cos\theta}{c_0})e^{-i\frac{2\omega\cos\theta}{c_0}z}\tilde{D}(\frac{2\omega\cos\theta}{c_0},\theta) \\ &= \frac{2\cos\theta}{c_0}\frac{1}{2\pi}\int_{-\infty}^{\infty} d\omega e^{-i\omega\frac{2z\cos\theta}{c_0}}\tilde{D}(\frac{2\omega\cos\theta}{c_0},\theta) \end{aligned}$$

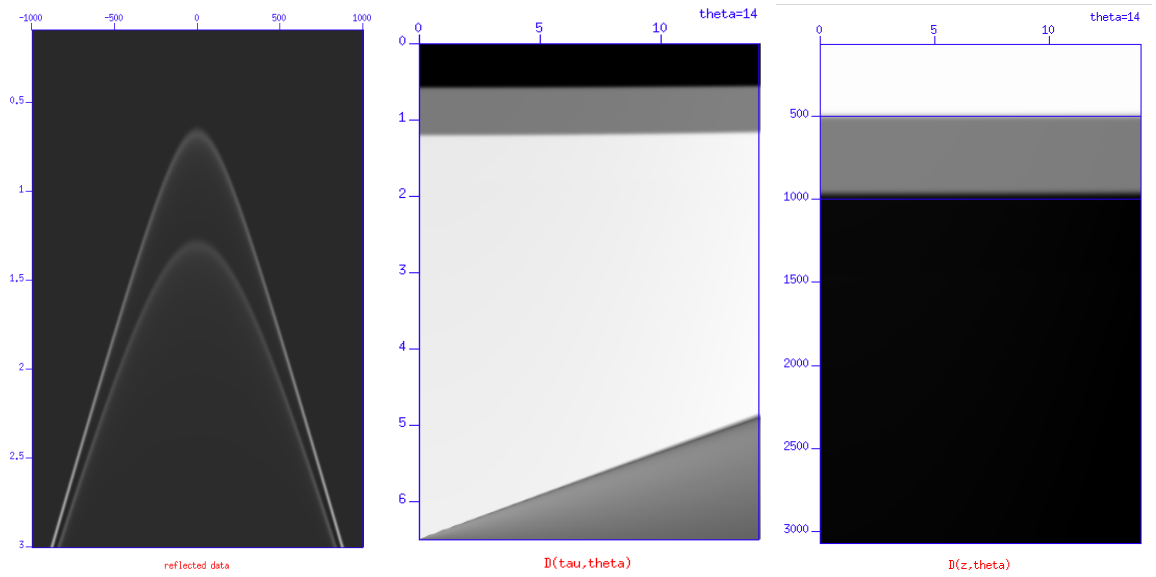

Figure 4: (left) Data after source regularizationin; (middle) Data in the τ-p domain; (right) Data in the pseudodepth domain.

$$
\begin{aligned}
&= \frac{2\cos\theta}{c_0}\frac{1}{2\pi}\int_{-\infty}^{\infty} d\omega e^{-i\omega\frac{2z\cos\theta}{c_0}}\tilde{d}(\omega,\theta) \\
&= \frac{2\cos\theta}{c_0}d(\frac{2z\cos\theta}{c_0},\theta) = \frac{2\cos\theta}{c_0}d(\tau,\theta) \qquad (12)
\end{aligned}
$$

4 Testing results

A series of testing results using imaging conjecture are shown. The models being tested are arranged in increasing order of imaging complexity so that the capability of the ISS imaging conjecture can be clearly seen.

In Figures 5, 6, 7 and 8 the panels represent (left) the earth model, (middle) the data after water-speed migration and (right) the result of ISS imaging algorithm. The first model being tested is a two-interface model with only density change across each reflector (Figure 5). ISS imaging gives the same result as water speed migration by excluding the density contribution.

In the second model we replace the density variation with velocity variation , in which water-speed migration can not give a correct image. ISS imaging algorithm, in this case, reduces to single-parameter imaging algorithm and corrects the image.

In the third example, the density and velocity variations in models 1 and 2 are combined into a two-interface model (Figure 7). ISS imaging algorithm successfully excludes the portion of the reflections due to density change and uses the portion due to velocity change for imaging. The second reflector moves to its correct depth.

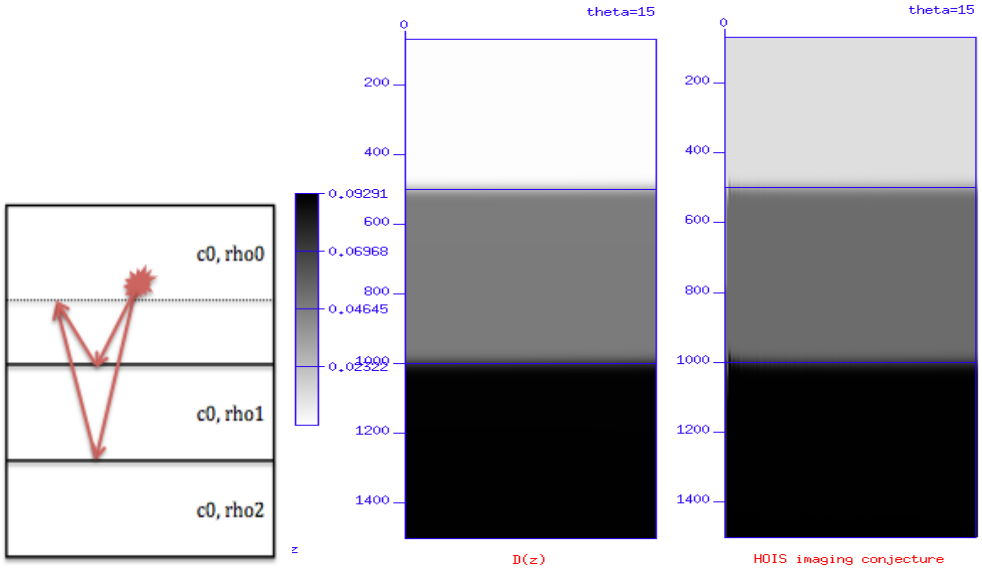

Figure 5: Model-1 c_0=1500 m/s, ρ_0=1.0 g/cm^3, ρ_1=1.1 g/cm^3 and ρ_2=1.2 g/cm^3. Blue lines represent the correct location of the reflectors.

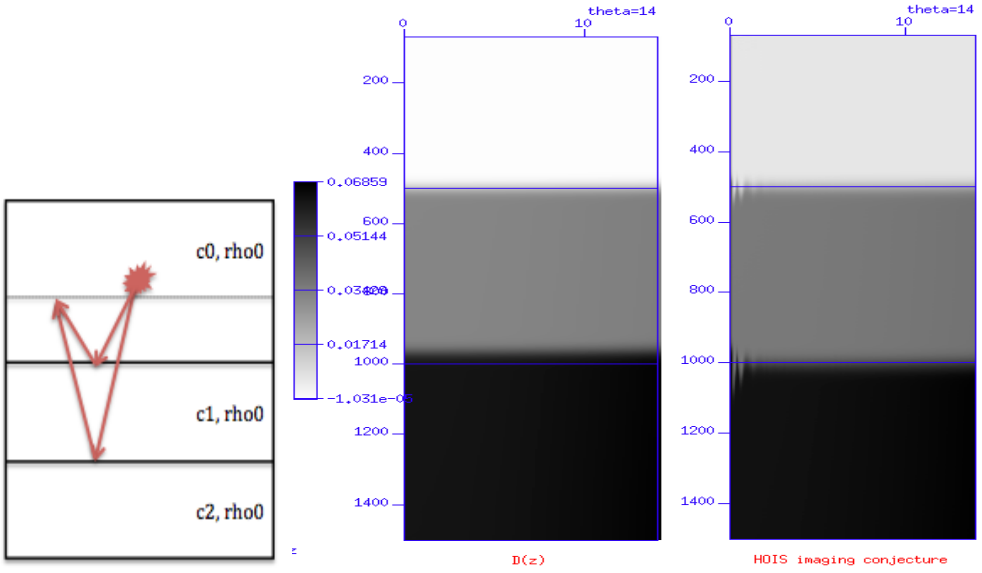

Figure 6: Model-2 c_0=1500 m/s, c_1=1600 m/s, c_2=1700 m/s, and ρ_0=1.0 g/cm^3. Blue lines represent the correct location of the reflectors.

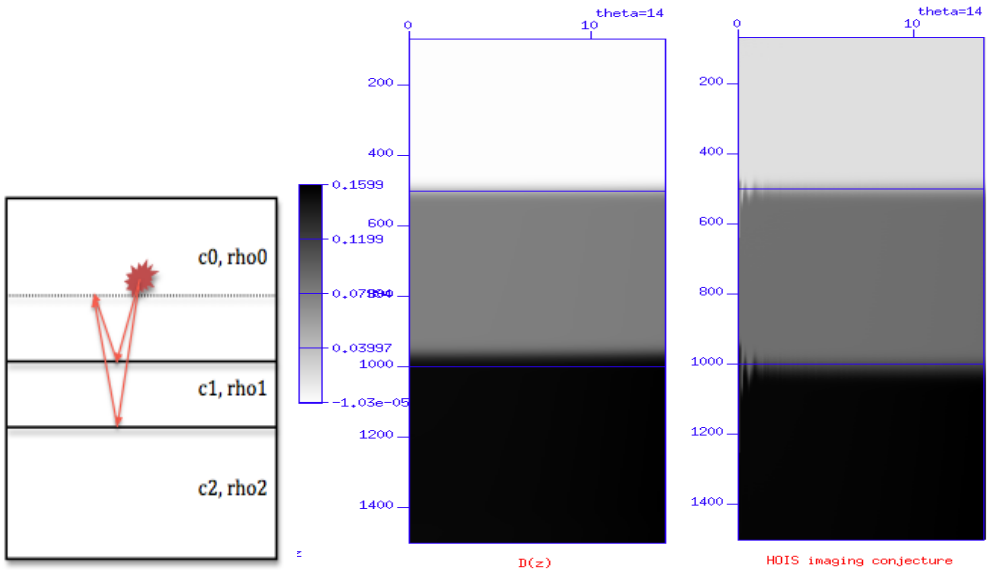

Figure 7: Model-3 c_0=1500 m/s, c_1=1600 m/s, c_2=1700 m/s, ρ_0=1.0 g/cm^3, ρ_1=1.1 g/cm^3, and ρ_2=1.2 g/cm^3. Blue lines represent the correct location of the reflectors.

Figure 8 is the last and most complicated model in which both density and velocity change across three reflectors. Water-speed migration mislocates the second and even worse, third reflectors. However, ISS imaging algorithm deals with this long duration of contrast with satisfactory imaging results.

5 The imaging issue in a multidimensional medium

We first consider a 2D earth model with varying velocity and density, in which the second interface has a dipping angle. We do not have analytic data expressions for this 2D model. The numerical data is generated using the same finite difference modeling and the data is shown in Figure 10. Note that the second primary is not symmetric anymore due to the second dipping reflector.

The first step is to test whether the 2D front end $\alpha_1(x,\, z)-\beta_1(x,\, z)$ goes to zero if velocity does not change across the boundary (Figure 9). The inversion for $\alpha_1(x,\, z)$ and $\beta_1(x,\, z)$ will follow the logic in Clayton and Stolt (1981):

$$D(k_g, k_s, \omega) = \frac{-\rho_0}{4 q_g q_s}\left[\frac{\omega^2}{c_0^2}\alpha_1(k_g - k_s, -q_g - q_s) + (q_g q_s - k_g k_s)\beta_1(k_g - k_s, -q_g - q_s)\right] S(\omega). \quad (13)$$

$$D(k_m, k_h, k_z) = \frac{-\rho_0}{4}\left[\frac{(k_z^2 + k_h^2)(k_z^2 + k_m^2)}{k_z^4 - k_m^2 k_h^2}\alpha_1(k_m, k_z) + \frac{(k_z^2 - k_h^2)(k_z^2 + k_m^2)}{k_z^4 - k_m^2 k_h^2}\beta_1(k_m, k_z)\right] S(\omega). \quad (14)$$

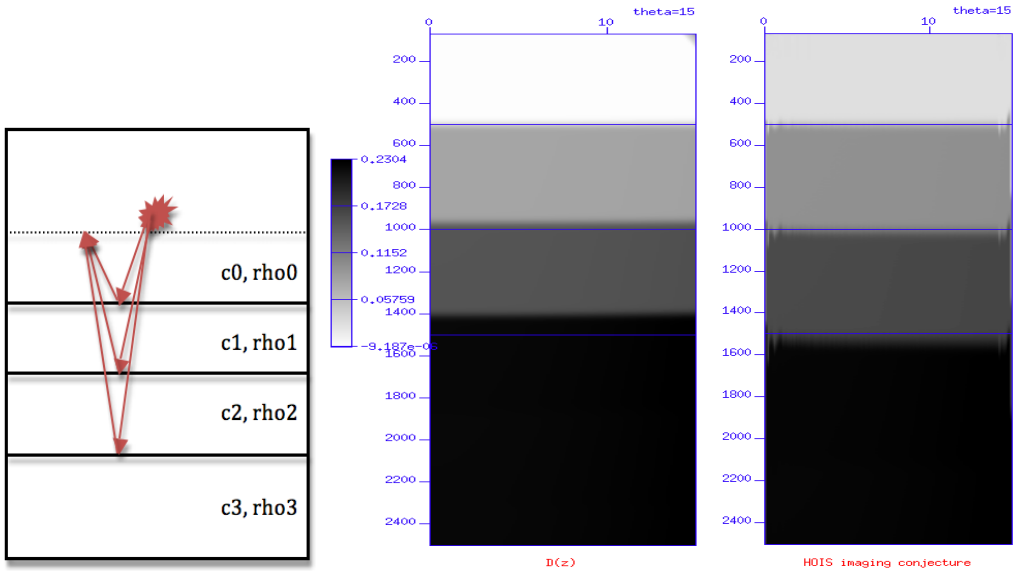

Figure 8: Model-4 c_0=1500 m/s, c_1=1600 m/s, c_2=1700 m/s, c_3=1800 m/s and ρ_0=1.0 g/cm^3, ρ_1=1.1 g/cm^3, ρ_2=1.2 g/cm^3, ρ_3=1.3 g/cm^3. Blue lines represent the correct location of the reflectors.

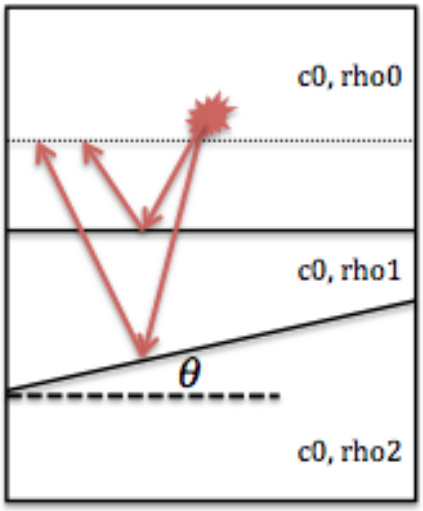

Figure 9: A 2D acoustic earth model with varying velocity and density.

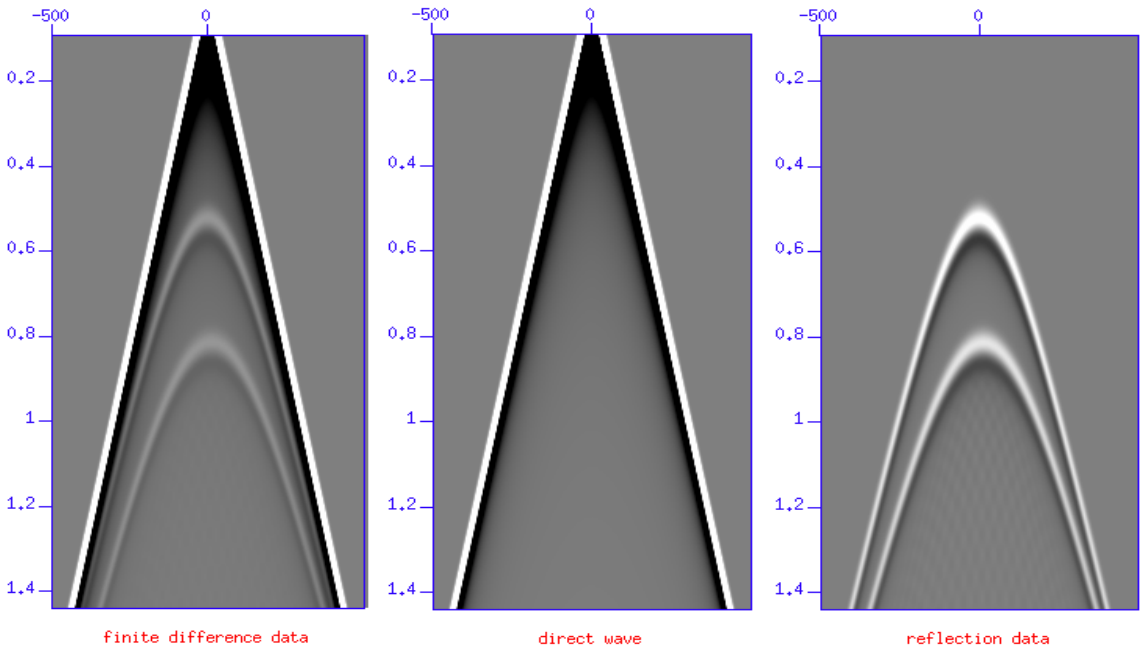

Figure 10: Finite difference modeling results for the 2D model using the same source fields and wavelet.

If the answer is zero, we will further test the conjectured 2D HOIS algorithm:

$$D^{HOIS}\left(x, z + \frac{1}{2}\int_{-\infty}^{z} \frac{\alpha_1(x,z') - \beta_1(x,z')}{\cos^2\theta - 0.25[\alpha_1(x,z') - \beta_1(x,z')]} dz'\right) = D(x,z) \tag{15}$$

However, if the answer is nonzero, we will have to develop a new theory for multi-D depth imaging algorithm to deal with the issue of excluding density contribution.

6 Conclusion and future plan

Starting from finite difference modeling we generated data in the x-t domain for some 1D earth models with variations in velocity and density. After a series of numerical transformations the data was finally prepared in the pseudodepth domain and input to the ISS imaging algorithm. The results showed high capability of imaging conjecture in excluding density contribution. Noise from the finite difference modeling and artifacts from numerical transformations were tolerated by ISS imaging algorithm. Taking the second model as an example, the reflection coefficient at the first interface given by theoretical calculation is around 0.0333. The minimum deviation estimation given by finite difference data is less than 0.05%. This positive message also verifies the fidelity of our finite difference modeling. Next we plan to investigate the removal of density only reflections to a laterally variable earth to allow multidimensional and multi-parameter ISS depth imaging.

7 Acknowledgements

We are grateful to all M-OSRP sponsors for long-term encouragement and support in this research. The author especially thanks F. Liu and X. Li for their valuable discussions in this research program and P. Terenghi for his suggestions in finishing this paper.

References

Alford, R. M., K. R. Kelly, and D. M. Boore. "Accuracy of Finite-Difference Modeling of the Acoustic Wave Equation." *Geophysics* 39 (December 1974): 834–842.

Clayton, R. W. and R. H. Stolt. "A Born-WKBJ inversion method for acoustic reflection data." *Geophysics* 46 (1981): 1559–1567.

Fang Liu, Xu Li and Arthur B. Weglein. "Field data inverse scattering imaging test in Kristin - part I: flattened common image gather in the velocity only framework." (2011): 116–144.

H. Liang, Arthur B. Weglein and X. Li. "Initial tests for the impacts of matching and mismatching between the earth model and the processing model for the ISS imaging and parameter estimation." (2010): 165–180.

Jiang, S. and Arthur B. Weglein. "Progressing multi-parameter imaging using the inverse scattering series: an initial analytic test on the Leading Order Imaging Subseries (LOIS) closed form and its extended Higher Order Imaging Subseries (HOIS) closed form for a laterally invariant two-parameter acoustic medium." (2009): 91–113.

Liu, F. *Multi-dimensional depth imaging without an adeaqute velocity model.* PhD thesis, University of Houston, 2006.

Liu, Fang and Arthur Weglein. "Accurate implementation of the wavelet in finite-difference modeling." (2005): 111–125.

Liu, Fang and Arthur B. Weglein. "Addressing the bandlimited nature of seismic source and rapid lateral variation of the Earth: source regularization and cascaded imaging operator." (2010): 72–117.

Weglein, Arthur B. "Depth imaging and AVO in technical highlights - Preface and Introduction." (2008): 3–5.

X. Li, S. Jiang,F. Liu and Arthur B. Weglein. "Depth imaging without the velocity cares about the phase and amplitude information of events: focusing on the use of angle dependent amplitude information of events." (2009): 114–128.

Zhang, H. *Direct non-linear acoustic and elastic inversion: Towards fundamentally new comprehensive and realistic target identification.* PhD thesis, University of Houston, 2006.

Initial examination of the concept of events in seismic processing: A 2D source single reflector modeling example

L. Tang, A. B. Weglein and P. Terenghi

Abstract

In this report we revisit the meaning of events in seismic physics. In seismic exploration, ray theory is broadly applied because of its simplicity and intuition. However ray theory is strictly valid only on the basis of high frequency assumption, which is often not true in the developing standard for seismic exploration. In this report we use the Cagniard-de Hoop method to model perfect seismic data in time domain, and then observe the differences between the direct wave and the reflected wave generated by a one-reflector acoustic model with a line source. The validation of ray theory is examined and discussed.

1 Introduction

In seismology, ray theory and the convolutional model are extensively used due to their simplicity, intuition and broad applicability. Under ray theory, an event is a sharp arrival, generated by energy traveling through a raypath from source to receiver. The raypath is the stationary path defined by Fermat's Principle. The portions of the model not visited by the ray provide no contributions to the wave-field. A more accurate way of describing wave propagation is using wave theory, where according to the Huygen-Fresnel Principle, each point on the wavefront contributes to the wave-field at the receiver. In the case of high frequency, ray theory well approximates wave theory. However, the seismic industry trend is to extend the use of low frequency to values as low as 2 Hz, in order to have farther propagation and better inversion result (Dragoset and Gabitzsch (2007)). When, as in these cases, ray theory is not sufficiently accurate, then the meanings of events as defined in the convolutional model should be reconsidered carefully.

In this report we testify the validation of ray theory at different frequencies. Using a simple one-reflector acoustic model and a line source, we observe and compare the waves that propagate from the source to the receiver directly and the wave that experiences reflection at the interface. The comparison of the waves' bandwidth and shape requires an accurate modeling method in the space-time domain. For our test, the Cagniard-de Hoop method is a good choice (de Hoop and van der Hijden (1983); Aki and Richards (2002)). First of all, in our simple model case this method can provide an exact analytic solution without doing numerical integrations. Secondly, it can calculate individual wavefield events, so that the direct wave and reflected wave can be obtained directly.

In the following sections, after a brief theoretical introduction, we discuss the two Green's functions defined within the Cagniard-de Hoop method (direct wave and reflected wave).

Then the convolution of the Green's function with source wavelets with different frequencies is performed. Thus the direct wave and reflected wave are compared, followed by a discussion on the validity of the ray theory.

2 Modeling using Cagniard-de Hoop Method

We consider the 2D wavefield excited by a line source in a simple one reflector 1D acoustic medium. For that case the Cagniard-de Hoop method has the ability to provide an exact, perfect solution for the wave-field in time domain. The modeling method was implemented to code by Zhang and Weglein (2006). The wave equation for 2D propagation, in a constant density medium is

$$\nabla^2 P(x,z,t) - \frac{1}{c^2}\frac{\partial^2}{\partial t^2}P(x,z,t) = A(t)\delta(x)\delta(z-z_s), \tag{1}$$

where the line source is located at $(0, z_s)$, with the source signature $A(t)$. In order to have all the frequencies observed, we set $A(t) = \delta(t)$, and thus the solution to this equation is the medium's Green's function, which satisfies

$$\nabla^2 G(x,z,0,z_s,t) - \frac{1}{c^2}\frac{\partial^2}{\partial t^2}G(x,z,0,z_s,t) = \delta(t)\delta(x)\delta(z-z_s). \tag{2}$$

In order to solve equation 2, the Cagniard-de Hoop method performs Laplace transform over t and a Fourier transform over x, which means to apply

$$\int_{-\infty}^{\infty} e^{-ik_x x}dx \int_0^{\infty} e^{-st}dt \tag{3}$$

on both sides of equation 2, where $s > 0$. The new equation becomes

$$\frac{\partial^2}{\partial z^2}G(k_x,z,s) - n^2 G(k_x,z,s) = \delta(z-z_s), \tag{4}$$

where $n^2 = k_x^2 + s^2/c^2$. To solve equation 4, we find that everywhere except at $z = z_s$, $\frac{\partial^2}{\partial z^2}G(k_x,z,s) = n^2 G(k_x,z,s)$, the solution is

$$G(k_x,z,s) = Ae^{n(z-z_s)} + Be^{-n(z-z_s)} \qquad for \quad z \neq z_s, n > 0, \tag{5}$$

where A and B are constants determined by the boundary conditions. Considering $z \to \pm\infty$, we have that $A = 0$ for $z > z_s$ and B=0 for $z < z_s$. Also considering the continuity of G at $z = z_s$ and the step jump of $\partial G/\partial z$ at $z = z_s$ by -1, we solve equation 4 as

$$G(k_x,z,s) = -\frac{1}{2n}e^{-n|z-z_s|}. \tag{6}$$

After solving equation 4, we have

$$G(x,z,s) = \frac{1}{2\pi}\int_{-\infty}^{\infty} G(k_x,z,s)e^{ik_x x}dk_x. \tag{7}$$

We also notice that

$$G(x,z,s)=\int_0^\infty G(x,z,t)e^{-st}dt, \tag{8}$$

so if we can manipulate equation 7 to be in the form of equation 8, then the expression for G(x,z,t) can be solved by just looking at the new form of integrand without carrying out any actual numerical integrals. The details of the derivation can be found in de Hoop (1960), and here we just write the solutions directly.

$$G^d(x,z;0,z_s,t)=-\frac{1}{2\pi}\frac{H(t-R_0/c_0)}{\sqrt{t^2-R_0^2/c_0^2}}, \tag{9}$$

where

$$R_0=\sqrt{x^2+(z-z_s)^2}. \tag{10}$$

For Green's function for the reflected wave, we should also consider the existence of head wave in the region of $x<R_0c_0/c_1$. For a two layer constant density acoustic model with velocities c_0 and c_1, the reflection's Green's function for the pre-critical region ($x<Rc_0/c_1$) is

$$G^{refl}(x,z;0,z_s,t)=-\frac{1}{2\pi}Re\grave{P}\acute{P}\frac{H(t-R/c_0)}{\sqrt{t^2-R^2/c_0^2}}, \tag{11}$$

and for $x<Rc_0/c_1$, the post-critical region, the Green's function is

$$G^{refl}(x,z;0,z_s,t)=-\frac{1}{2\pi}Im\grave{P}\acute{P}\frac{H(t-t_h)-H(t-R/c_0)}{\sqrt{R^2/c_0^2-t^2}}-\frac{1}{2\pi}Re\grave{P}\acute{P}\frac{H(t-R/c_0)}{\sqrt{t^2-R^2/c_0^2}}, \tag{12}$$

where

$$\begin{aligned}
R &= \sqrt{x^2+(z+z_s-2z_d)^2}, && (13)\\
t_h &= \frac{x}{c_1}+|z+z_s-2z_d|\sqrt{c_0^{-2}-c_1^{-2}}, && (14)\\
\grave{P}\acute{P} &= \frac{\eta_0-\eta_1}{\eta_0+\eta_1}, && (15)\\
\eta_i &= \sqrt{c_i^{-2}-p^2}, \quad where \quad i=0,1 && (16)\\
p &= \begin{cases} \frac{xt-|z+z_s-2z_d|\sqrt{R^2/c_0^2-t^2}}{R^2} & t\le R/c_0 \\ \frac{xt+i|z+z_s-2z_d|\sqrt{R^2/c_0^2-t^2}}{R^2} & t\ge R/c_0 \end{cases}. && (17)
\end{aligned}$$

Here $Re\grave{P}\acute{P}(t)$ is the generalized reflection coefficient which relates with all the reflections at each point on the reflector. t_h is the time when the head wave arrives. In our experiment, to simplify the discussion, we choose to compare only the direct wave in the pre-critical reflection region.

3 Analytic Test Result

Before starting to compare the direct wave and the reflected wave, we need to notice from the form of Green's functions that the values of R_0 in G^d and R in G^{refl} should be the same,

so that only the effect due to the reflection at the subsurface contributes to the difference of the two waves. Figure 1 shows two models we used to generate direct wave and reflected wave. Figure 2 shows the two Green's functions in time domain. Since the amplitude of the reflection's Green's function is smaller than that of the direct wave due to the effect of generalized reflection coefficient $Re\grave{P}\acute{P}$, and because we are more interested in their shape than in their absolute amplitude, in the following steps, we choose to normalize these two waves to the same maximum.

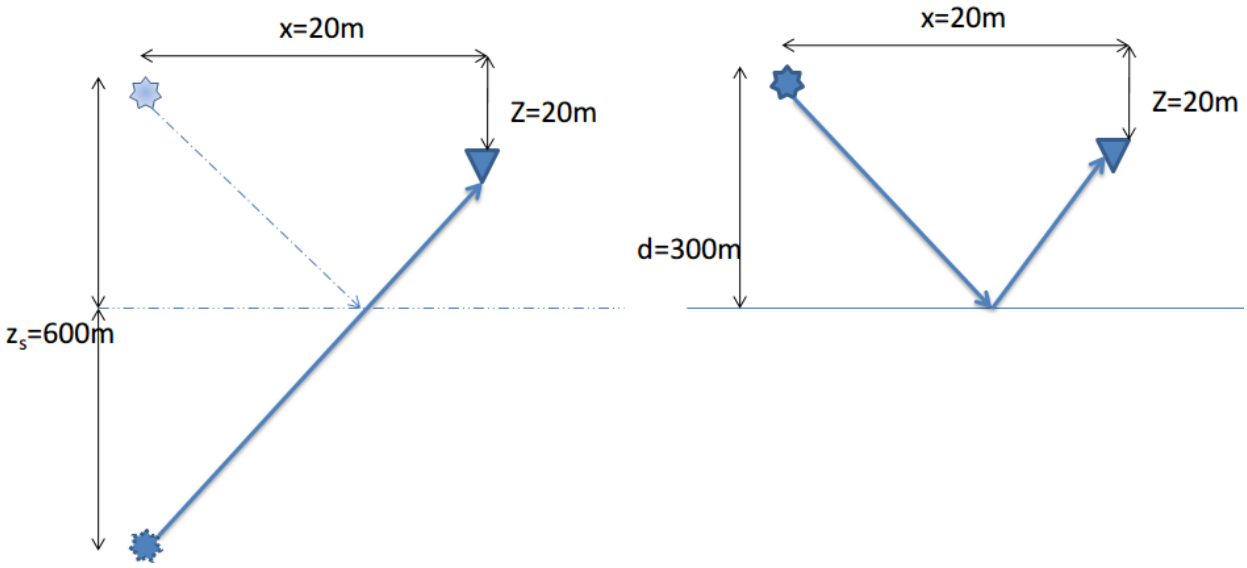

Figure 1: Models used to generate (left) direct wave, (right) reflected wave

Then we use Ricker wavelets at different peak frequencies, and convolve them with the Green's functions, to get the direct wave and reflected wave. An example of Ricker wavelet with a peak frequency of 15 Hz is shown in Figure 3. From the comparison of the shapes of direct wave and reflected wave shown in Figure 4. We can see that in the low-frequency range as shown in Figure 4 (a) and (b), there is an apparent difference between them. As the frequency goes higher the difference decreases, and at 50 Hz the shape of direct and reflected wave almost overlap.

The test result provides an insight into the conditions and assumptions behind the ray theory. In the high frequency range, the exact wavefield solution provided by the Cagniard-de Hoop method shows that the reflected wave cannot be distinguished from a direct wave with the same arrival time. In that case, the wave theoretic result is well approximated by a geometric ray, determined by Snell's law, which only experiences the reflector at one point. When the frequency goes to as low as 6 Hz, the approximation of geometric rays is no longer valid. The reflected wave in this case is contributed by all the reflections at different points on the reflector with different arrival times.

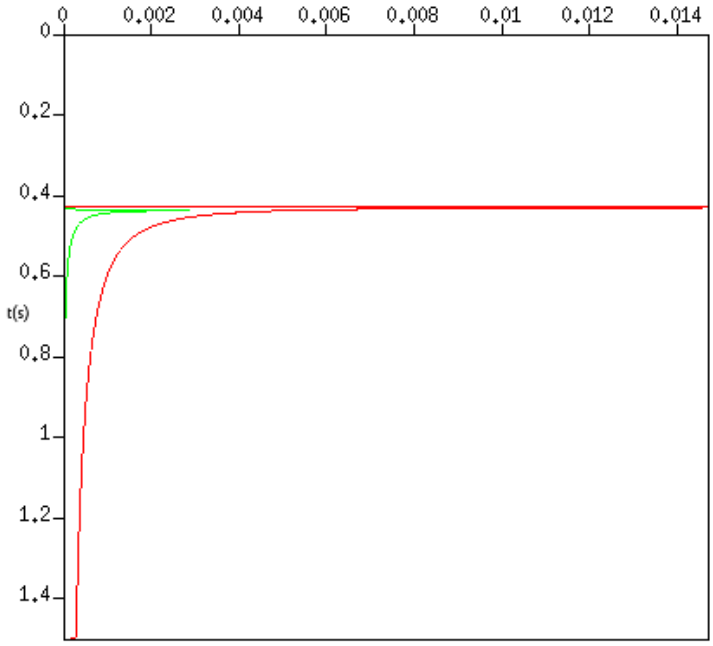

Figure 2: Two Green's functions in time domain. Red: direct Green's function. Green: reflection Green's function.

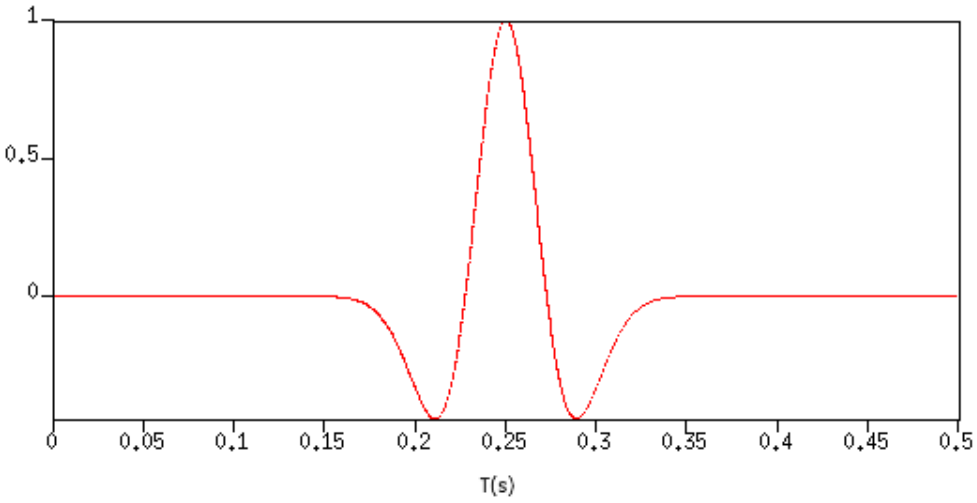

Figure 3: Ricker wavelet, peak frequency 15 Hz.

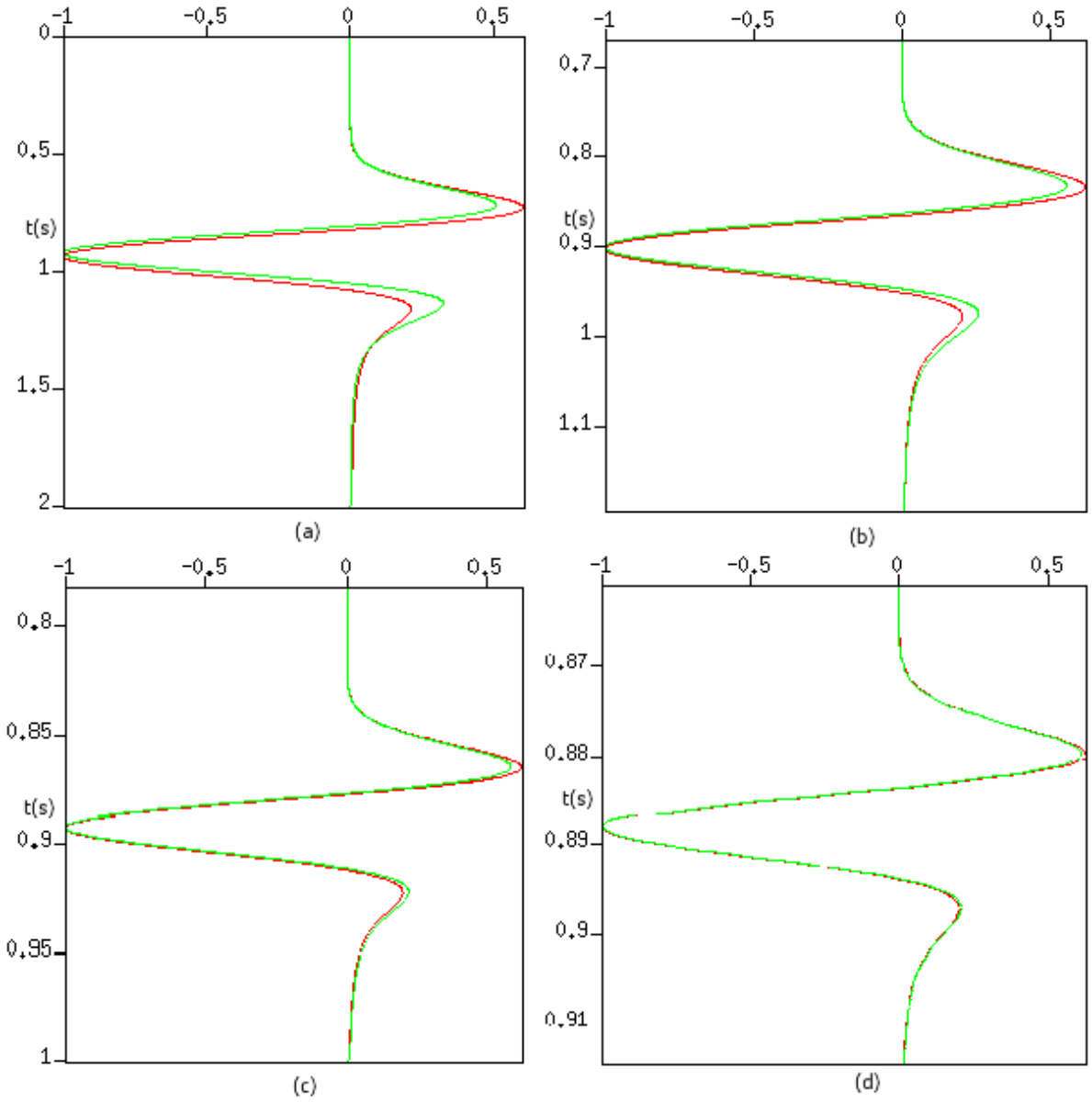

Figure 4: Comparison of direct wave (red) and reflected wave (green). Peak frequency of Ricker wave:(a)2 Hz,(b)6 Hz,(c)15 Hz,(d)50 Hz

4 Conclusion

In this report, the validation of ray theory is studied. With the aid of the Cagniard-de Hoop modeling method, the direct Green's function and the reflection Green's function are computed and examined. The convolution with a Ricker wavelet is performed under different frequencies, so that the shape of direct wave and reflected wave are compared. In doing so we

observed that in the high-frequency range ray theory is valid and the shape of the reflected wave remains the same as the direct wave, while in the low-frequency range, the reflected wave displays a distortion contributed by wave theoretical effects which are not accounted for in the ray theory.

5 Acknowledgements

We are grateful to all M-OSRP sponsors for long-term encouragement and support in this research. The first author would like to thank Dr. Paolo Terenghi, Jim Mayhan, and Xu Li for valuable discussion and generous help in this report, and owes deepest gratitude to Dr. Weglein for his guidance, encouragement, and support.

References

Aki, K. and P. G. Richards. *Quantitative Seismology.* 2nd edition. University Science Books, 2002.

Hoop, A. T.de . "A modification of Cagniard's method for solving seismic pulse problems." *Appl. Sci. Res. B* 8 (1960): 349–356.

Hoop, A. T.de and J. H. M. T. van der Hijden. "Generation of acoustic waves by an impulsive line source in a fluid/solid configuration with a plane boundary." *J. Acoust. Soc. Am.* 74 (1983): 333–342.

Dragoset, Bill and Jozica Gabitzsch. "Introduction to this special section: Low-frequency seismic." *The Leading Edge* 26 (2007): 34–35.

Zhang, J. and A. B. Weglein. "A note on data modeling using the Cagniard-de Hoop method." *Mission-Oriented Seismic Research Program Annual Report* (2006): 132–144.

An inverse scattering approach to free-surface multiple removal from quasi-elastic ocean bottom seismic data

Mozhdeh Niazmand, Paolo Terenghi and Arthur B.Weglein

Abstract

We study the inverse scattering series method for predicting and eliminating multiples from ocean bottom seismic data. In particular, we focus our analysis on non-consolidated ocean floors. This study is inspired by the problem of soft ocean bottoms where poor coupling of receivers makes collecting multi-component data difficult or impossible. In 1997, Ken Matson formulated an inverse scattering based subseries to eliminate elastic ocean bottom multiples for the first time where a solid ocean bottom was considered. We conduct a study to adapt that approach to the problem of soft ocean bottoms. We take a closer look at the reflection coefficients that play a direct role in the ocean bottom multiple removal sub-series. In order to simulate the effect of a muddy unconsolidated ocean bottom, we analyzed the behavior of the reflection coefficient affecting elastic wave propagation for a set of gradually decreased values of shear wave velocity. The P-wave reflection coefficient for an acoustic over elastic half-space can be described as the P-wave reflection coefficient of two acoustic half-spaces plus a correction term, which in the zero shear wave velocity limit will vanish. Thus, at the zero shear wave velocity limit, the two reflection coefficients are equal. We then analyze these reflection coefficients. The analysis shows that for angles less than 10 degrees and for shear wave velocities ranging from zero to 800 m/sec, the P-wave reflection coefficients have a good agreement with one another, regardless of the value for shear wave velocity.

1 Introduction

Ocean bottom seismic (OBS) data acquisition has the potential to provide us with shear wave components in addition to pressure wave components and, in that sense, it could lead to a more complete set of collected data. However, proper placement and coupling of the receivers to the bottom of the ocean can be a challenge; it can be even more difficult if the ocean bottom is not consolidated. An example is the deep water Gulf of Mexico where the ocean floor starts as muddy, gradually gains rigidity, and eventually becomes rock solid. A measure of rigidity in substances is the shear modulus which describes the material's response to shearing strains. The more rigid a substance is, the higher is its shear modulus. For example, the shear modulus of diamond is 478 Gpa. In liquids and gases, on the other hand,

the shear modulus is zero. Shear modulus is denoted by μ and is directly related to the shear wave velocity of the substance. It is described mathematically as

$$v_s = \beta = \sqrt{\frac{\mu}{\rho}}, \tag{1}$$

where v_s or β is the shear wave velocity and ρ is the density of the substance.

2 Background

2.1 An overview of the Inverse Scattering Series

In physics, a theory that enables us to predict the outcome of some measurements, given a complete description of a system, is referred to as the forward description or forward problem. An inverse problem would be to use the actual result of some measurement of an unknown system to infer values of the parameters that characterize that system. Scattering theory is a wave theoretical approach that has been used in many disciplines of physics, engineering, and medical sciences as a tool in studying and investigating the structure of matter. Scattering theory describes the physics of the deviation of any form of radiation (e.g. light, sound or particle beams) from its trajectory in a reference meduim, by colliding to a localized obstacle or a form of perturbation in the medium through which it's propagating. The perturbation can be characterized by a change in the mechanical properties of the medium of propagation(i.e. density and/or velocity) or an inhomogeneity. The deviated wavefield is denoted as the *scattered* wavefield and the change or deviation from the mechanical properties that causes the scattering is known as the *scattering potential*. Forward scattering deals with determining the scattered wave field from a known scattering potential and a known reference medium.

Inverse scattering theory aims to determine the scattering potential from the measurements of the scattered wavefield that satisfies certain boundary conditions. Inverse scattering-based methods were introduced to geophysical sciences and petroleum exploration industry in the early 1980s (Weglein et al., 1981). Recent development presented by Weglein et al. (2003) introduces an new framework that utilizes inverse scattering series that consists of several task-specific subseries for the purposes of multiple removal, imaging and inversion, which does not require any *a priori* information from the subsurface, i.e. it's data-driven.

As a solution to the inverse scattering problem, one can take the physical (actual) medium under the study, and split it into a background or reference and a perturbation. There are many ways to split the actual medium into a reference and a perturbation but for mathematical convenience the background medium can be chosen in way that a Green's function propagating in that medium can be easily obtained either analytically or numerically.

The mathematical description of this process starts with the differential equations that govern the wave propagation in each of the media

$$\mathbf{LG} \quad = \quad -\delta(\mathbf{r} - \mathbf{r_s}), \tag{2}$$

$$\mathbf{L_0 G_0} \quad = \quad -\delta(\mathbf{r} - \mathbf{r_s}), \tag{3}$$

where $\mathbf{L}$, $\mathbf{L_0}$, $\mathbf{G}$ and $\mathbf{G_0}$ are, respectively, the wave equation differential operators and the Green's function operators of the actual and reference media; $\delta(\mathbf{r}-\mathbf{r_s})$ is a Dirac delta function denoting an impulsive point source located at point $\mathbf{r_s}$ and observed at point $\mathbf{r}$. The scattering potential, denoted by $\mathbf{V}$, indicates the difference between the wave equation operators for the actual and reference media

$$\mathbf{V} = \mathbf{L} - \mathbf{L_0}. \tag{4}$$

The data $\mathbf{D}$ is constituted by the difference between the measured wavefield and the reference wavefield at the measurement surface,

$$\mathbf{D} = (\mathbf{G} - \mathbf{G_0})_\mathbf{m}, \tag{5}$$

where m indicates the measurement surface. The relationship between the data and difference in actual and reference media is described by the *Lippmann-Schwinger* equation, the basis equation for scattering techniques,

$$\mathbf{G} - \mathbf{G_0} = \mathbf{G_0 V G}. \tag{6}$$

This is a non-linear relationship in a sense that $\mathbf{G}$ appears on both sides of the equation. A way to isolate $\mathbf{G}$ to one side is to iterate the equation into itself. That results in an infinite series known as the Born (or the forward) series:

$$\mathbf{G} = \mathbf{G_0} + \mathbf{G_0 V G_0} + \mathbf{G_0 V G_0 V G_0} + \dots. \tag{7}$$

Using the scattered wavefield in 5 we can re-write the Born series as,

$$\mathbf{D} = (\mathbf{G_0 V G_0} + \mathbf{G_0 V G_0 V G_0} + \mathbf{G_0 V G_0 V G_0 V G_0} + \dots)_\mathbf{m}, \tag{8}$$

where m refers to measurement surface. Now, assuming the perturbation $\mathbf{V}$ is itself expandable in a power series ($\mathbf{V} = \mathbf{V_1} + \mathbf{V_2} + ...$), such that the i^{th} order term in $\mathbf{V}$, is the i^{th} order term in the data ($i = 1, 2, 3, ...$), we arrive at the inverse scattering series

$$\begin{aligned} \mathbf{G} - \mathbf{G_0} = \quad & \mathbf{G_0}(\mathbf{V_1} + \mathbf{V_2} + \dots)\mathbf{G_0} \\ & + \mathbf{G_0}(\mathbf{V_1} + \mathbf{V_2} + \dots)\mathbf{G_0}(\mathbf{V_1} + \mathbf{V_2} + \dots)\mathbf{G_0} + \dots. \end{aligned} \tag{9}$$

Evaluating both sides of 10 at the measurement surface and equating terms of equal order with each other, we obtain for the first order term

$$\mathbf{D} \quad = (\mathbf{G_0 V_1 G_0})_\mathbf{m}, \tag{10}$$

for the second order term

$$\mathbf{0} \quad = (\mathbf{G_0 V_2 G_0})_\mathbf{m} + (\mathbf{G_0 V_1 G_0 V_1 G_0})_\mathbf{m}, \tag{11}$$

and for third order term,

$$\begin{aligned}\mathbf{0} &= (\mathbf{G_0V_3G_0})_\mathbf{m} + (\mathbf{G_0V_1G_0V_2G_0})_\mathbf{m} \\ &+(\mathbf{G_0V_2G_0V_1G_0})_\mathbf{m} + (\mathbf{G_0V_1G_0V_1G_0V_1G_0})_\mathbf{m} \quad .\end{aligned} \tag{12}$$

$$\vdots$$

Equation 10 is now an exact equation for $\mathbf{V_1}$ and can be inverted. Once $\mathbf{V_1}$ is obtained we can substitute it in equation 11 to determine $\mathbf{V_2}$. Then $\mathbf{V_2}$ itself can be inserted into the third order equation 12 to get $\mathbf{V_3}$ and this trend continues to obtain any order $\mathbf{V_i}$. It's important to understand the symmetry between the forward and inverse scattering series. In the forward series, operator $\mathbf{G_0}$ acts on the perturbation $\mathbf{V}$ to create data $\mathbf{D}$; in the inverse series, that same $\mathbf{G_0}$ operator acts on the data $\mathbf{D}$, to create the perturbation $\mathbf{V}$(eq. 10). The significance of this symmetry is that any Green's operator that is in charge of creating a certain type of event in the forward series, is held accountable for removing that same event in the inverse scattering series. This property can be used to remove multiples. For the case of this report, we are using it to remove ocean bottom multiples from seismic data.

2.2 Previous Works

Carvalho (1992) derived an algorithm for identifying and removing acoustic free surface multiples from marine seismic data using the inverse scattering series. A model for the geometry for the problem is shown in figure 1. The sources and receivers are located in the water below the free surface.

The reference medium of choice is a half-space of water bounded by a free surface on the top. The existence of the free-surface boundary, causes the reference Green's function to consist of two parts: one that directly propagates from the source to the receiver, and another part that propagates upward, impinges on the free surface and then gets reflected back down towards the receivers. These two reference Green's functions are referred to as G_0^d and G_0^{fs} respectively (d for direct and fs for free surface)(Weglein et al., 1997; Carvalho, 1992). If the free surface did not exist, the reference Green's function would consist only of G_0^d. The G_0^{fs} part, exists because of the presence of the free surface, and is creating all the free surface-related events, i.e. ghosts and free surface multiples in the forward series. Hence, it should be in charge of removing those events in the inverse series(Carvalho et al., 1992). Using this, Carvalho formulated the subseries to identify and remove free surface multiples, using the inverse scattering series(ISS) formalism devised by Weglein et al. (1981).

Matson (1997) adapted the ISS-based acoustic free surface multiple removal procedure by Carvalho (1992) to elastic free surface multiple removal for land data, and using that, he devised a procedure for identifying and attenuating multiples associated with an elastic ocean-bottom.

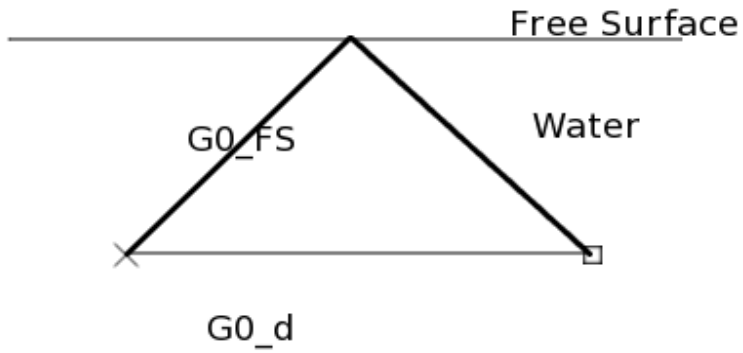

Figure 1: Carvalho's model for the free-surface multiple removal algorithm

The choice of reference for the ocean bottom removal procedure is a layer of water bounded by a free surface on top and a homogenous elastic half-space on the bottom. The sources and receivers are located at or slightly embedded in the ocean bottom (at depths z_s and z_g respectively). The Green's function for the reference medium in this case becomes more complicated compared to the free surface case, since the water layer is now bounded both on top and bottom. The presence of air-water free-surface, and the ocean bottom interface, leads to creation of a host of events: reflections from the top of the water layer, reflections from the bottom of the ocean bottom, and a series of reverberations inside the water column. All those events are referred to as *water column* events. The reference Green's function therefore, similar to the method of Carvalho (1992), splits into two parts: a directly propagating Green's function G_0^d, directly from source to the receiver, and the Green's function associated with the water column events G_0^{wc},

$$\mathbf{G_0} = \mathbf{G_0^d} + \mathbf{G_0^{wc}}, \tag{13}$$

where d indicates direct and wc denotes water column (see figure 2). With the same analogy as the free surface case, G_0^{wc} accounts for all of the events that have at least had one encounter with the water column in the forward series and therefore is in charge of removing those events in the inverse series.

Combining equations 8 and 13, the forward series to model the data is then

$$\mathbf{D} = (\mathbf{G_0^d} + \mathbf{G_0^{wc}})\mathbf{V}(\mathbf{G_0^d} + \mathbf{G_0^{wc}}) + (\mathbf{G_0^d} + \mathbf{G_0^{wc}})\mathbf{V}(\mathbf{G_0^d} + \mathbf{G_0^{wc}})\mathbf{V}(\mathbf{G_0^d} + \mathbf{G_0^{wc}}) + \dots. \tag{14}$$

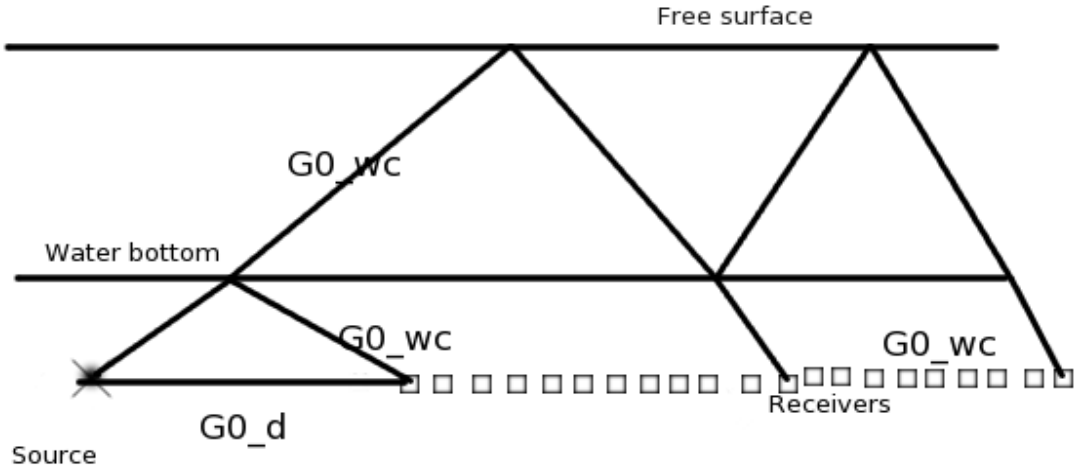

Figure 2: Reference Green's function for the water bottom multiple removal algorithm

Recall that

$$\mathbf{V} = \mathbf{V_1} + \mathbf{V_2} + \mathbf{V_3} + \cdots ; \tag{15}$$

using this series expansion and matching equal orders of the data , we arrive at ,

$$\mathbf{D} = (\mathbf{G_0^d} + \mathbf{G_0^{wc}})\mathbf{V_1}(\mathbf{G_0^d} + \mathbf{G_0^{wc}}), \tag{16}$$

$$\mathbf{0} = (\mathbf{G_0^d} + \mathbf{G_0^{wc}})\mathbf{V_2}(\mathbf{G_0^d} + \mathbf{G_0^{wc}}) + (\mathbf{G_0^d} + \mathbf{G_0^{wc}})\mathbf{V_1}(\mathbf{G_0^d} + \mathbf{G_0^{wc}})\mathbf{V_1}(\mathbf{G_0^d} + \mathbf{G_0^{wc}}), \tag{17}$$

$$\begin{aligned}\mathbf{0} = (\mathbf{G_0^d} + \mathbf{G_0^{wc}})\mathbf{V_3}(\mathbf{G_0^d} + \mathbf{G_0^{wc}}) + (\mathbf{G_0^d} + \mathbf{G_0^{wc}})\mathbf{V_1}(\mathbf{G_0^d} + \mathbf{G_0^{wc}})\mathbf{V_2}(\mathbf{G_0^d} \\ +\mathbf{G_0^{wc}}) + (\mathbf{G_0^d} + \mathbf{G_0^{wc}})\mathbf{V_2}(\mathbf{G_0^d} + \mathbf{G_0^{wc}})\mathbf{V_1}(\mathbf{G_0^d} + \mathbf{G_0^{wc}}),\end{aligned} \tag{18}$$

$$\vdots$$

Selecting from this series, only the terms that contain $\mathbf{G_0^{wc}}$ between all the scatterers, will lead to a subseries that will be used to eliminate multiples that are created because of the

existence of the water column. This new subseries is called $\mathbf{V'}$ and like $\mathbf{V}$, it is also assumed to be expandable in a power series,

$$\mathbf{V'} = \mathbf{V_1} + \mathbf{V'_2} + \mathbf{V'_3} + \ldots, \tag{19}$$

where

$$\mathbf{V_1} = \mathbf{G_0^{-1}DG_0^{-1}}, \tag{20}$$
$$\mathbf{V'_2} = -\mathbf{V_1G_0^{wc}V_1}, \tag{21}$$
$$\mathbf{V'_3} = -\mathbf{V'_2G_0^{wc}V_1} - \mathbf{V_1G_0^{wc}V'_2} - \mathbf{V_1G_0^{wc}V_1G_0^{wc}V_1} \tag{22}$$

$$\vdots$$

Note that the linear term in the $\mathbf{V'}$ subseries is the original linear term inherited from the $\mathbf{V}$ series. From these equations, a recursive relation can be derived that relates the n^{th} order term in the subseries, to its previous order term,

$$\mathbf{V'_n} = -\mathbf{V'_{n-1}G_0^{wc}V_1}. \tag{23}$$

To transform $\mathbf{V'}$ into data, two directly propagating Green's function operators need to act on it from both sides. This creates a series consisting of a range of water column multiples where their order reflects their number of encounters with the water column,

$$\mathbf{D'} = \mathbf{G_0^d V' G_0^d} = \mathbf{D_1} + \mathbf{D'_2} + \mathbf{D'_3} + \ldots, \tag{24}$$

where $\mathbf{D_1}$ is the original data that's already been decomposed into up and down-going P and S waves(down-going from the source and up-going at the reciever), $\mathbf{D'_2}$ represents a modeling of events which propagate up from the scattering region, interact once with the water column, and then propagate back down to the scattering region. When $\mathbf{D'_2}$ is added to $\mathbf{D_1}$, it cancels all first order water column multiples in the data. In general, $\mathbf{D'_n}$ removes all $(n-1)^{th}$ order water column multiples as it gets added to the data.
The n^{th} order term in the multiple removal series is obtained as, (equation 4.24 in Matson (1997))

$$\mathbf{D'_n} = -\mathbf{D_1}(\mathbf{G_0^d})^{-1}\mathbf{G_0^{wc}}(\mathbf{G_0^d})^{-1}\mathbf{D'_{n-1}} = -\mathbf{D'_{n-1}JD_1}, \tag{25}$$

and it represents a modeling of events that undergo $(n-1)$ interactions with the water column. To remove successive orders of water column multiples, these terms need to be added to each other order by order.

3 The analysis

Our objective is to be able to make an effective adaptation of the elastic ocean bottom multiple removal procedure for ocean bottoms that are not rigid. The choice for the reference medium

is, a water column bounded by a free surface on top and a homogeneous quasi-elastic half-space in the bottom. The sources and receivers are located at or slightly embedded into the water bottom. Figure 3 displays a sketch of the geometry of the problem. As mentioned earlier, the motivation for this study lies in the fact that the unconsolidated ocean bottoms are a quite common encounter in the OBS explorations, hence we aim to analyze the behavior of the elastic ocean bottom multiple removal subseries as the water bottom goes through a transition from elastic to acoustic. This leads to an investigation on the tolerance level of the elastic ocean bottom multiple removal procedure for low or zero shear wave velocity and/or missing or partially reliable recordings of shear waves.

Figure 3: A model for the geometry of the ocean bottom multiple removal problem.
The half-space below the water is assumed to be a homogeneous, unconsolidated water bottom.

Similar to the elastic case the Green's function for the reference splits into a direct part and a water column part: $G_0 = G_0^d + G_0^{wc}$

We investigate the J operator containing the reference Green's operator in equation (25). An explicit form of this operator is given by,

$$J(k,\omega) = \frac{i}{\rho_1 \omega^2 \Theta} e^{i\nu_1(z_s - z_{wb})} \begin{pmatrix} \frac{\grave{P}\acute{P} + Z^2 \acute{S}\grave{S}}{\eta_2^2 - k^2} & 2\rho_2 k \nu_1 \eta_2 \beta_2^2 (1+Z^2) \\ \rho_2 \nu_1 \beta_2^2 (k^2 - \eta_2^2)(1+Z^2) & \frac{\grave{P}\acute{P} + Z^2 \acute{S}\grave{S}}{k\nu_2} \end{pmatrix}, \tag{26}$$

where $\Theta = 1 + \grave{P}\acute{P}Z^2$ and $Z = e^{i\nu_1(z_s - z_{wb})}$.

(A complete derivation of the operator $J(k,\omega)$ can be found in Matson (1997) appendix D, equation D.60)

The grave and acute accents are a convention from Aki and Richards (2002) and pertain to the propagation direction of the wavefield. The(´) accent indicates an upward and the (`) denotes a downward propagation. For example, $\acute{P}\grave{P}$ indicates a reflection coefficient for a P-wave that starts propagating up towards a reflector, and after reflecting off from a reflector continues its journey downwards still as a P-wave. Alternatively, in this report we may refer to this type of reflection, as an up-down type.

Table 1 shows each variable in $J(k,\omega)$ and their description. The vertical wave numbers for

Table 1: Elements in the J- matrix

Variable	Description
$\acute{P}\grave{P}$	reflection coefficient for an up-down P-wave
$\grave{P}\acute{P}$	reflection coefficient for a down-up P-wave
$\acute{S}\grave{S}$	reflection coefficient for an up-down S-wave
ν_1	vertical P-wave number for the upper half-space
ν_2	vertical P-wave number for the lower half-space
η_2	vertical S-wave number for the lower half-space
k	horizontal wave number
ω	temporal frequency
β_2	shear wave velocity of the lower-halfspace
ρ_1	density of the upper half-space
ρ_2	density of the lower half-space
z_s	depth of source
z_{wb}	depth of waterbottom

P and S-waves are obtained as follows

$$\nu_1 = sgn(\omega)\sqrt{\frac{\omega^2}{\alpha_1^2} - k^2}, \tag{27}$$

$$\nu_2 = sgn(\omega)\sqrt{\frac{\omega^2}{\alpha_2^2} - k^2}, \tag{28}$$

$$\text{and } \eta_2 = sgn(\omega)\sqrt{\frac{\omega^2}{\beta_2^2} - k^2}, \tag{29}$$

where α and β are P-wave and S-wave velocities respectively.

$$\alpha = \sqrt{\frac{\kappa + 4/3\mu}{\rho}}, \text{and } \beta = \sqrt{\frac{\mu}{\rho}} \tag{30}$$

where κ is the bulk modulus, which is one of the elastic moduli that describe the physical properties of a substance; it describes the ratio of pressure to the change in the volume due to that pressure. μ is the shear modulus (explained in the introduction) and ρ is the density. Indices refer to the orientation of half-spaces in contact: 1 indicates upper and 2 is for lower halfspace; so, for example, α_2 refers the the P-wave velocity of the lower halfspace.
We start our study by taking a closer look at the $\acute{P}\grave{P}$ reflection coefficient that appears directly in the J-matrix and has an explicit dependence on the shear wave velocity of the ocean bottom (β_2),

$$\acute{P}\grave{P} = \frac{\frac{\omega^4\rho_1\nu_2}{\beta_2^2} + \beta_2^2\rho_2\nu_1(-(\eta_2^2-k^2)^2 + 4\eta_2\nu_2k^2)}{\frac{\omega^4\rho_1\nu_2}{\beta_2^2} + \beta_2^2\rho_2\nu_1((\eta_2^2-k^2)^2 + 4\eta_2\nu_2k^2)}. \tag{31}$$

The derivation of this reflection coefficient can be found in Matson (1997). After some algebraic operations, this reflection coefficient (from here on we will refer to this reflection coefficient as $(\acute{P}\grave{P})_{ae}$ to indicate that it pertains to an acoustic halfspace over an elastic halfspace.)can be written as,

$$(\acute{P}\grave{P})_{ae} = \frac{\omega^4(\rho_1\nu_2-\rho_2\nu_1) + 4\beta_2^2\rho_2\nu_1\omega^2k^2 - 4\beta_2^4\rho_2\nu_1k^4 + 4\rho_2\nu_1\nu_2\sqrt{\omega^2k^4\beta_2^6 - k^6\beta_2^8}}{\omega^4(\rho_1\nu_2+\rho_2\nu_1) - 4\beta_2^2\rho_2\nu_1\omega^2k^2 + 4\beta_2^4\rho_2\nu_1k^4 + 4\rho_2\nu_1\nu_2\sqrt{\omega^2k^4\beta_2^6 - k^6\beta_2^8}}, \tag{32}$$

which after some more algebraic manipulations can be re-written as,

$$\begin{aligned}(\acute{P}\grave{P})_{ae} = & \quad \tfrac{\rho_1\nu_2-\rho_2\nu_1}{\rho_1\nu_2+\rho_2\nu_1} \\ & + \tfrac{8\rho_1\nu_1\rho_2\nu_2\beta_2^2k^2(\omega^2-\beta_2^2k^2+\rho_2\nu_1\beta_2\sqrt{\omega^2-\beta_2^2k^2}/\rho_1)}{\omega^4(\rho_1\nu_2+\rho_2\nu_1)^2-(1+\frac{\rho_2\nu_1}{\rho_1\nu_2})(4\rho_1\nu_1\rho_2\nu_2\beta_2^2k^2)(\omega^2-\beta_2^2k^2-\nu_2\beta_2\sqrt{\omega^2-\beta_2^2k^2})} \\ = & \quad \tfrac{\rho_1\nu_2-\rho_2\nu_1}{\rho_1\nu_2+\rho_2\nu_1} + \Delta\acute{P}\grave{P}.\end{aligned} \tag{33}$$

The first term can be instantly recognized as the $\acute{P}\grave{P}$ reflection coefficient of two acoustic half-spaces in contact. We refer to this as $(\acute{P}\grave{P})_{aa}$. The second term could be regarded as a correction term that can be added to the acoustic reflection coefficient to take it to an elastic reflection coefficient. Please observe that in the special case that β_2 is identically zero, this reflection coefficient will shrink down to,

$$(\acute{P}\grave{P})_{ae}|_{(\beta_2=0)} = \frac{\rho_1\nu_2-\rho_2\nu_1}{\rho_1\nu_2+\rho_2\nu_1} = (\acute{P}\grave{P})_{aa}, \tag{34}$$

which is the $\acute{P}\grave{P}$ reflection coefficient for two acoustic halfspaces in contact.

In a similar fashion, the $\grave{P}\acute{P}$ reflection coefficient (Matson, 1997) that is given by,

$$\grave{P}\acute{P} = \frac{\frac{-\omega^4\rho_1\nu_2}{\beta_2^2} + \beta_2^2\rho_2\nu_1((\eta_2^2-k^2)^2 + 4\eta_2\nu_2k^2)}{\frac{\omega^4\rho_1\nu_2}{\beta_2^2} + \beta_2^2\rho_2\nu_1((\eta_2^2-k^2)^2 + 4\eta_2\nu_2k^2)}, \tag{35}$$

can be algebraically manipulated to obtain,

$$(\grave{P}\acute{P})_{ae} = \frac{-\omega^4(\rho_1\nu_2-\rho_2\nu_1) - 4\beta_2^2\rho_2\nu_1\omega^2k^2 + 4\beta_2^4\rho_2\nu_1k^4 + 4\rho_2\nu_1\nu_2\sqrt{\omega^2k^4\beta_2^6 - k^6\beta_2^8}}{\omega^4(\rho_1\nu_2+\rho_2\nu_1) - 4\beta_2^2\rho_2\nu_1\omega^2k^2 + 4\beta_2^4\rho_2\nu_1k^4 + 4\rho_2\nu_1\nu_2\sqrt{\omega^2k^4\beta_2^6 - k^6\beta_2^8}}, \tag{36}$$

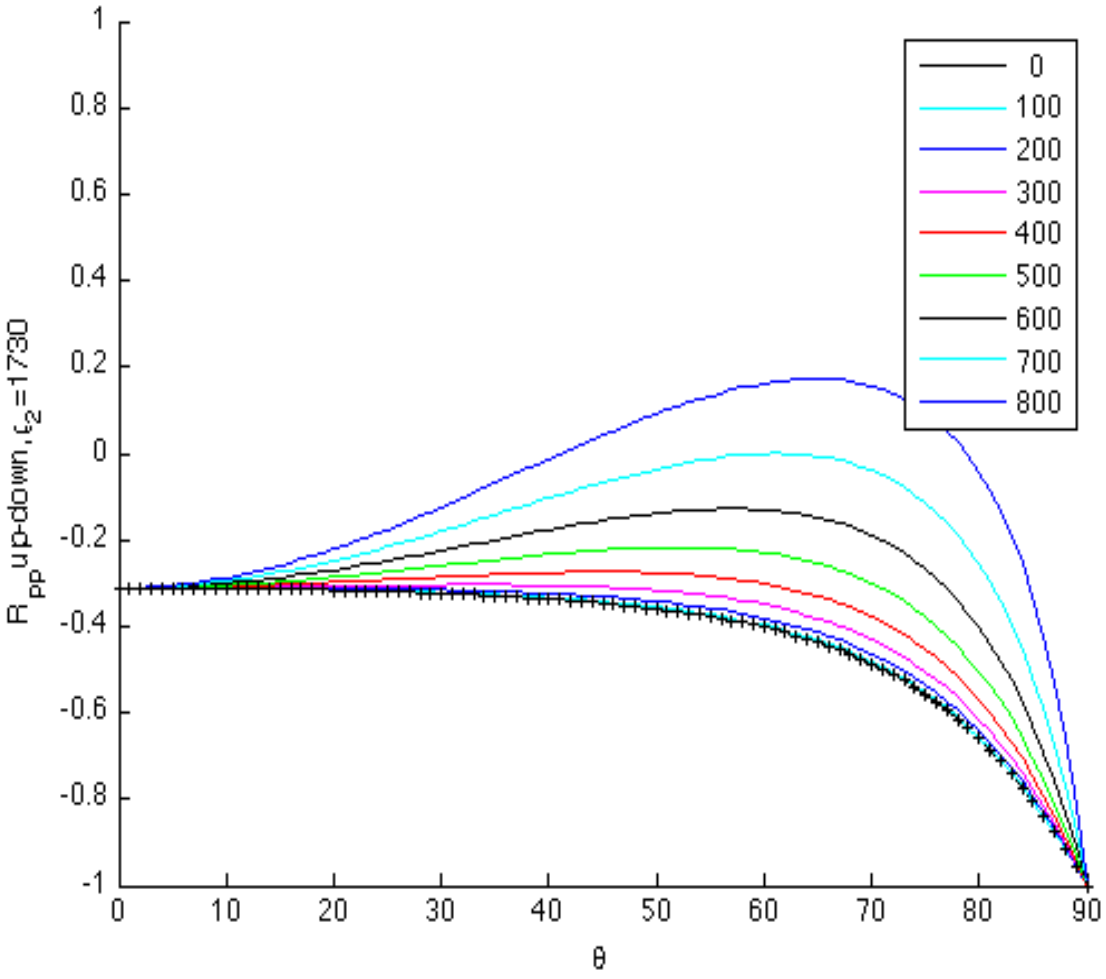

Figure 4: $(\acute{P}\grave{P})_{ae}$ reflection coefficient for two halfspaces in contact.The parametes for the upper(water) and lower halfspaces are: $\rho_1 = 1000kg/m^3$, $\alpha_1 = 1500m/sec$, $\beta_1 = 0m/sec$; $\rho_2 = 1730kg/m^3$ and $\alpha_2 = 1650m/s$ and β_2 is varying between 0 to 800 m/sec (see the legend box). '+' is associated with $\beta_2 = 0$.

or

$$(\grave{P}\acute{P})_{ae} = \frac{-(\rho_1\nu_2-\rho_2\nu_1)}{\rho_1\nu_2+\rho_2\nu_1} + \frac{-8\rho_1\nu_1\rho_2\nu_2\beta_2^2k^2(\omega^2-\beta_2^2k^2+\rho_2\nu_1\beta_2\sqrt{\omega^2-\beta_2^2k^2}/\rho_1)}{\omega^4(\rho_1\nu_2+\rho_2\nu_1)^2-(1+\frac{\rho_2\nu_1}{\rho_1\nu_2})(4\rho_1\nu_1\rho_2\nu_2\beta_2^2k^2)(\omega^2-\beta_2^2k^2-\nu_2\beta_2\sqrt{\omega^2-\beta_2^2k^2})} \tag{37}$$

$$= \frac{-(\rho_1\nu_2-\rho_2\nu_1)}{\rho_1\nu_2+\rho_2\nu_1} + \Delta\grave{P}\acute{P}. \tag{38}$$

Once again, we can recognize the first term as the $\grave{P}\acute{P}$ reflection coefficient of two acoustic

halfspaces in contact,

$$(\grave{P}\acute{P})_{ae}|_{(\beta_2=0)} = \frac{-\rho_1\nu_2 + \rho_2\nu_1}{\rho_1\nu_2 + \rho_2\nu_1} = (\grave{P}\acute{P})_{aa}. \tag{39}$$

4 Numerical results

To better understand the effect of low shear wave velocity in the ocean bottom, we simulated two halfspaces in contact. For the upper halfspace, we used the density and velocites of water($\rho_1 = 1000kg/m^3, v_p = \alpha_1 = 1500m/sec$, and $\beta_1 = 0m/sec$) and for the purpose of this study, for the lower half-space parameters, we used a density of $1730kg/m^3$ which pertains to that of fluid mud. The lower halfspace starting value for the P-wave velocity is $\alpha_2 = 1650m/s$. We then gradually decreased the S-wave velocity β_2 of the lower halfspace from $800m/s$ to $0m/s$ in steps of 100. Finally, we plotted each reflection coefficient as a function of incident angle. The results are shown in figures 4 and 5.

To test the robustness of the results for varying water bottom density(ρ_2) and P-wave velocity(α_2), we repeated the experiment with densities of 1500 kg/m^3 and 1900 kg/m^3 while keeping the P-wave velocity at 1650 m/sec and then another set of tests with P-wave velocities of 1550 m/sec and 1750 m/sec with a fixed density of $1730kg/m^3$ (all the parameters pertain to the lower halfspace)for both the $(\acute{P}\grave{P})_{ae}$ and $(\grave{P}\acute{P})_{ae}$ reflection coefficients. Those results are shown in figures 6 , 7, 8 , 9, 10, 11, 12, and 13.

5 Discussion

The results presented in figures 4 to 13 are the graphs of the $(\acute{P}\grave{P})_{ae}$ and $(\grave{P}\acute{P})_{ae}$ reflection coefficients as a function of incidnet angle. In all of these plots, it can be observed that in a relatively small regime of angles (i.e $\theta < 10degrees$) the $(\acute{P}\grave{P})_{ae}$ and $(\grave{P}\acute{P})_{ae}$ reflection coefficients with different β_2 values, seem to coincide with each other and with their acoustic reflection coefficient counterpart. This could mean that in that vicinity of angles, the elastic reflection coefficient can be approximated as the acoustic reflection coefficient. For larger angles, the correction terms(see equations 34 and 38) need to be taken into account. Also, the reflection coefficients associated with β_2 values of 100 and 200 have the least deviation from the reflection coefficient with zero β_2 value(i.e. the acoustic reflection coefficient). From this, we can argue that the reflection coefficients corresponding to those β_2 values are relatively more accurate approximations to the acoustic reflection coefficient. On the other hand, in the $(\acute{P}\grave{P})_{ae}$ plots, the largest deviations from the acoustic reflection coefficient is observed in the angle interval of $(50 < \theta < 80)$ degrees which implies that in this regime the correction term must be taken into account.

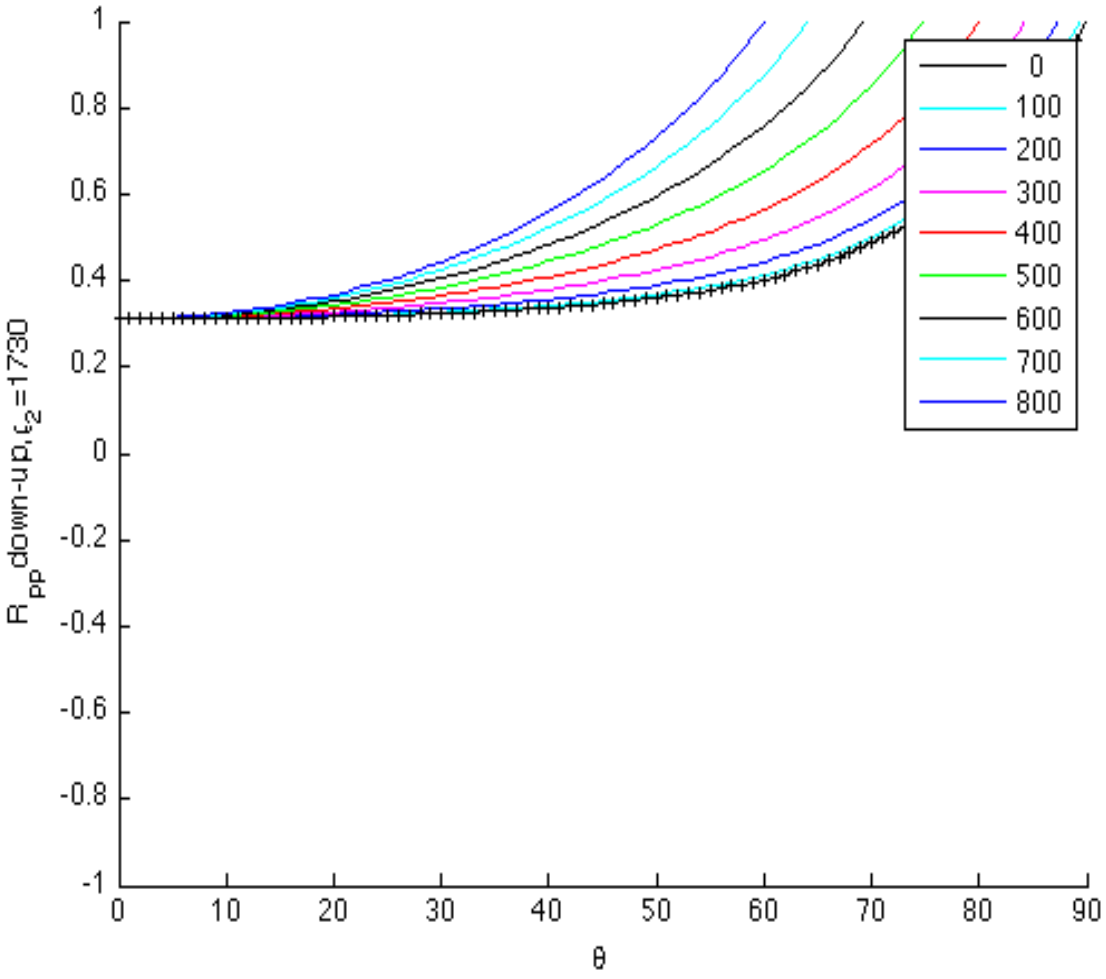

Figure 5: $(\grave{P}\acute{P})_{ae}$ reflection coefficient for two halfspaces in contact, as a function of incident angle.The parametes for the upper(water) and lower halfspaces are: $\rho_1 = 1000kg/m^3$, $\alpha_1 = 1500m/sec$, $\beta_1 = 0m/sec$; $\rho_2 = 1730kg/m^3$ and $\alpha_2 = 1650m/s$ and β_2 is varying between 0 to 800 m/sec (see the legend box). '+' is associated with $\beta_2 = 0$.

6 Conclusions

In this report, we study a quasi-elastic ocean bottom and investigate how its low shear velocity will effect the procedure for elastic ocean bottom multiple removal devised by as the ocean floor goes through a transition from elastic to acoustic. Eliminating ocean bottom multiples can help avoiding misinterpretation of these events as primary reflections. It can also make a difference in AVO analysis, and it is a prerequisite for most imaging and inversion methods. While there exists theories and algorithms based on the inverse scattering series (ISS) to

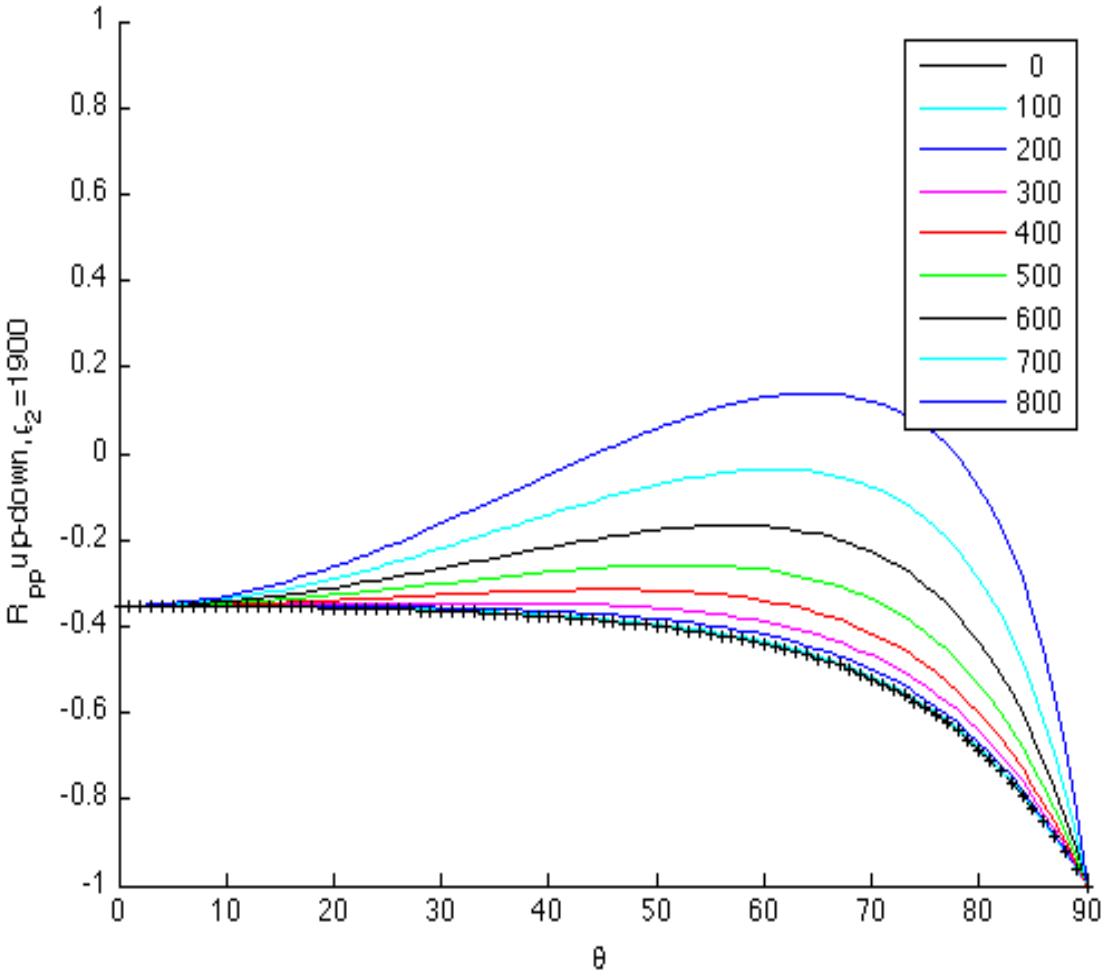

Figure 6: $(\acute{P}\grave{P})_{ae}$ reflection coefficient for two halfspaces in contact, as a function of incident angle. The parametes for the upper(water) and lower halfspaces are: $\rho_1 = 1000kg/m^3$, $\alpha_1 = 1500m/sec$, $\beta_1 = 0m/sec$; $\rho_2 = 1900kg/m^3$ and $\alpha_2 = 1650m/s$ and β_2 is varying between 0 to 800 m/sec (see legend box). '+' is associated with $\beta_2 = 0$.

eliminate, in a data-driven manner, ocean bottom multiples from an elastic ocean bottom, the practical challenge of proper coupling of the receivers to the ocean bottom still remains and it intensifies where the ocean floors are made of substances that are not rigid, e.g. mud, sediments, etc. This leads to shear wave component measurements that are weak or even missing, due to low shear modulus values in unconsolidated ocean floors. To adapt the ISS-based elastic ocean bottom multiple removal procedure for the quasi-elastic ocean bottoms, we focus on the operator $J(k,\omega)$ which is the machinery behind generating n^{th} order ocean bottom multiple from the 1^{st} order data and the $(n-1)^{th}$ order ocean bottom multiple. Among

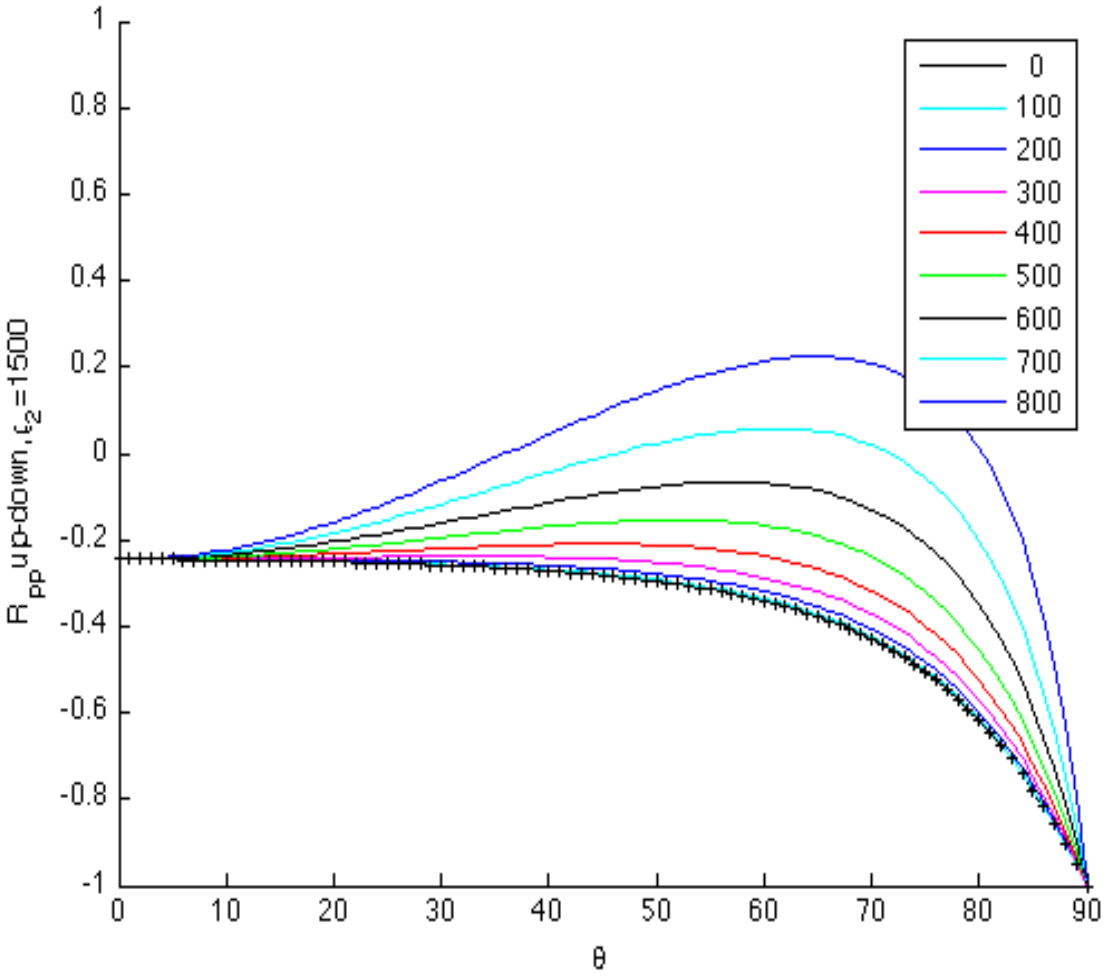

Figure 7: $(\acute{P}\grave{P})_{ae}$ reflection coefficient for two halfspaces in contact, as a function of incident angle. The parametes for the upper(water) and lower halfspaces are: $\rho_1 = 1000kg/m^3$, $\alpha_1 = 1500m/sec$, $\beta_1 = 0m/sec$; $\rho_2 = 1500kg/m^3$ and $\alpha_2 = 1650m/s$ and β_2 is varying between 0 to 800 m/sec(see legend box). '+' is associated with $\beta_2 = 0$.

the elements of $J(k, \omega)$ we focus on two reflection coefficients that have explicit dependence on the shear wave velocity of the ocean bottom, namely $\acute{P}\grave{P}$ and $\grave{P}\acute{P}$. The analytical tests on these reflection coefficients showed that each of these reflection coefficients can be written as an acoustic reflection coefficient plus a correction term that vanishes in the limit of zero ocean bottom shear wave velocity.

Numerical results shows that all the elastic reflection coefficients are in good agreement with each other and with their acoustic reflection counterpart, in an angle interval of zero to 10 degrees, regardless of the given value for the shear wave velocity at the ocean bottom which

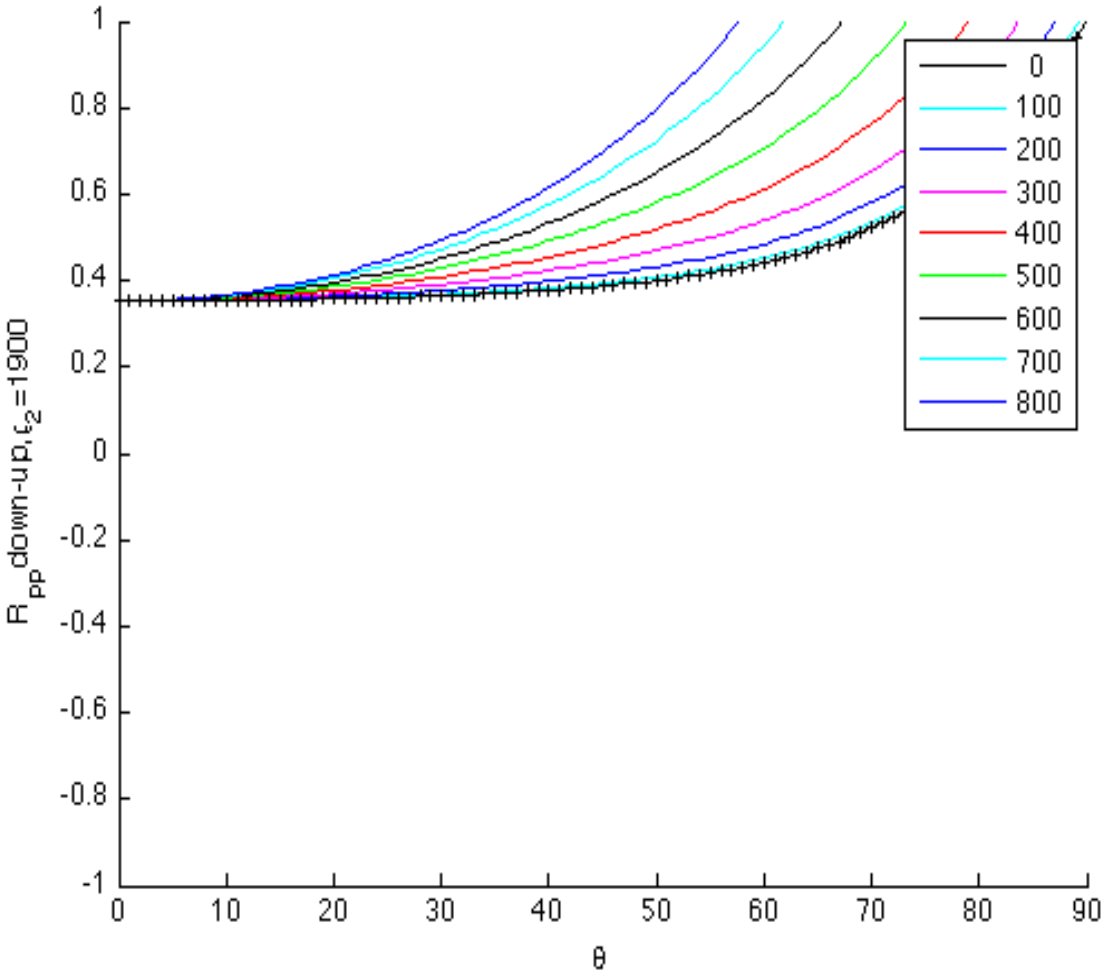

Figure 8: $(\grave{P}\acute{P})_{ae}$ reflection coefficient for two halfspaces in contact, as a function of incident angle. The parametes for the upper(water) and lower halfspaces are: $\rho_1 = 1000kg/m^3$, $\alpha_1 = 1500m/sec$, $\beta_1 = 0m/sec$; $\rho_2 = 1900kg/m^3$ and $\alpha_2 = 1650m/s$ and β_2 is varying between 0 to 800 m/sec(see legend box). '+' is associated with $\beta_2 = 0$.

could imply that in that regime, the acoustic-over-elastic P-wave reflection coefficient can be approximated as the acoustic-over-acoustic P-wave reflection coefficient.

A similar study is being conducted on the $\acute{S}\grave{S}$ reflection coefficient. Numerical tests are in progress to study the correction terms $\Delta\acute{P}\grave{P}$ and $\Delta\grave{P}\acute{P}$, in 34 and 38 in their sensitivity towards the elastic to acoustic transition(i.e. $\beta_2 \to 0$).

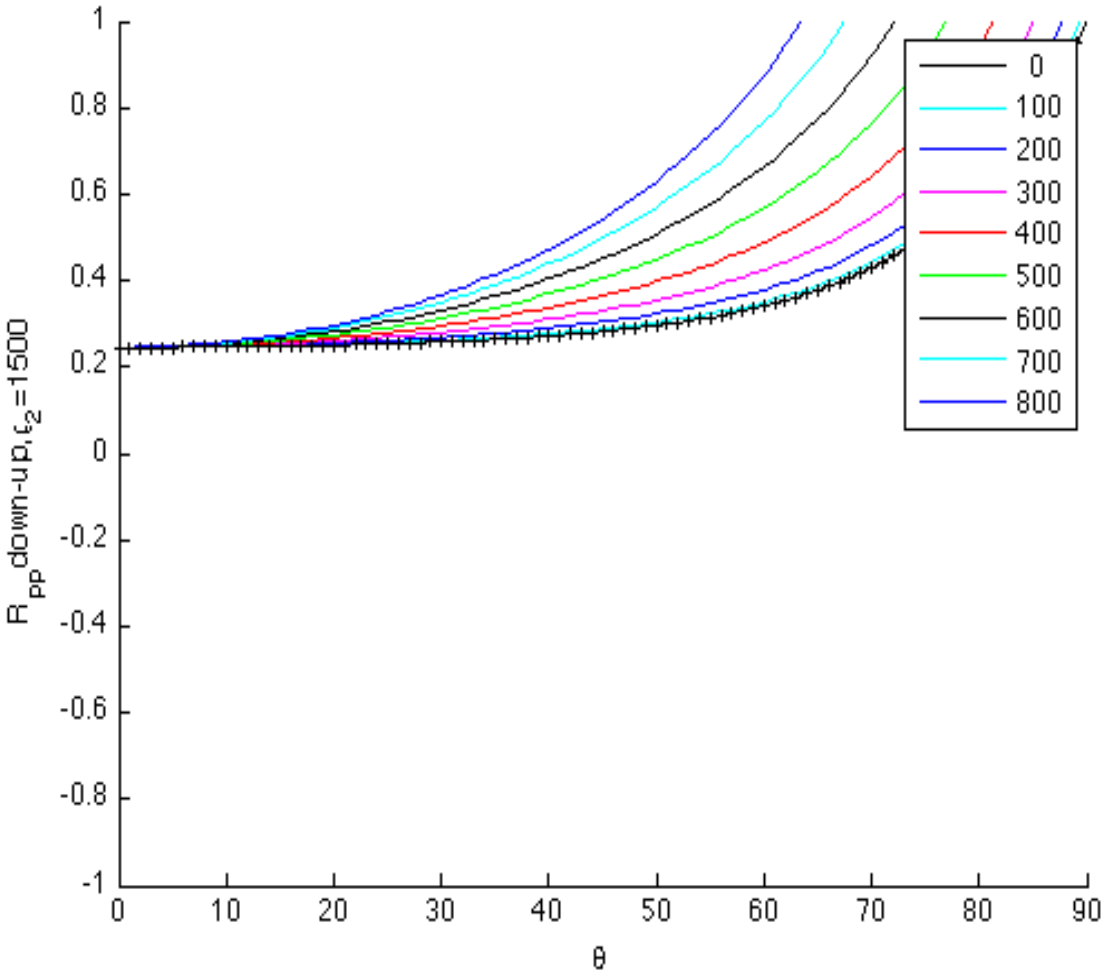

Figure 9: $(\grave{P}\acute{P})_{ae}$ reflection coefficient for two halfspaces in contact, as a function of incident angle . The parametes for the upper(water) and lower halfspaces are: $\rho_1 = 1000kg/m^3$, $\alpha_1 = 1500m/sec$, $\beta_1 = 0m/sec$; $\rho_2 = 1500kg/m^3$ and $\alpha_2 = 1650m/s$ and β_2 is varying between 0 to 800 m/sec(see legend box). '+' is associated with $\beta_2 = 0$.

7 Acknowledgements

We are grateful to all M-OSRP sponsors for long-term encouragement and support in this research. The first author would like to thank long standing friends Adriana C. Ramírez and Einar Otnes for their invaluable comments, questions, suggestions and their constant encouragement. Adriana is acknowledged for help proof-reading the manuscript and providing feedback that improved the quality of this work.

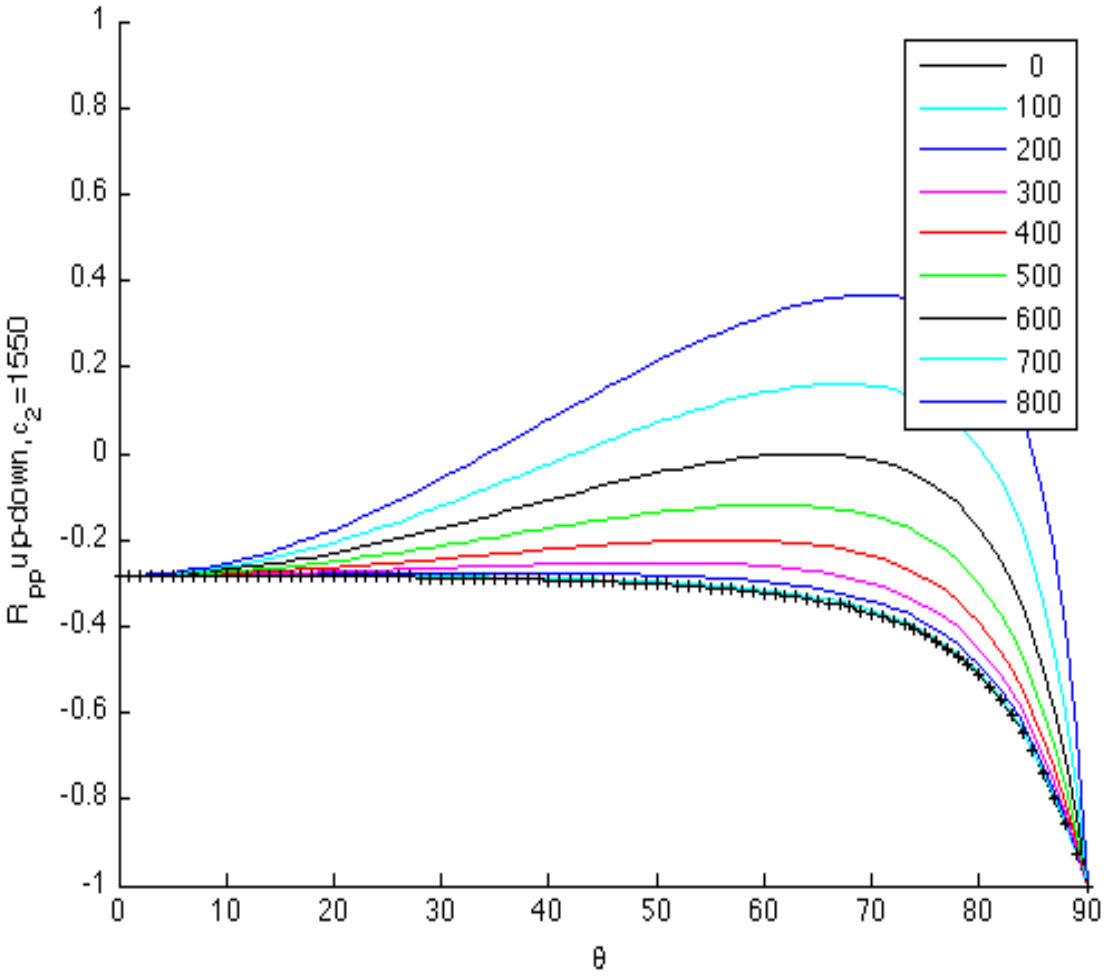

Figure 10: $(\acute{P}\grave{P})_{ae}$ reflection coefficient for two halfspaces in contact, as a function of incident angle. The parametes for the upper(water) and lower halfspaces are: $\rho_1 = 1000kg/m^3$, $\alpha_1 = 1500m/sec$, $\beta_1 = 0m/sec$; $\rho_2 = 1730kg/m^3$ and $\alpha_2 = 1550m/s$ and β_2 is varying between 0 to 800 m/sec(see legend box). '+' is associated with $\beta_2 = 0$.

References

Aki, K. and P.G. Richards, 2002, Quantitative seismology: University Science Books, 2nd edition.

Weglein, A. B., Boyce, W. E., and Anderson, J. E., 1981, Obtaining three-dimensional velocity information directly from reflection seismic data: An inverse scattering formalism: Geophysics, **46**, 1116-1120.

Matson, K. H., 1997, An inverse scattering series method for attenuating elastic multiples from multicomponent land and ocean bottom seismic data: Ph.D thesis, University of British Columbia.

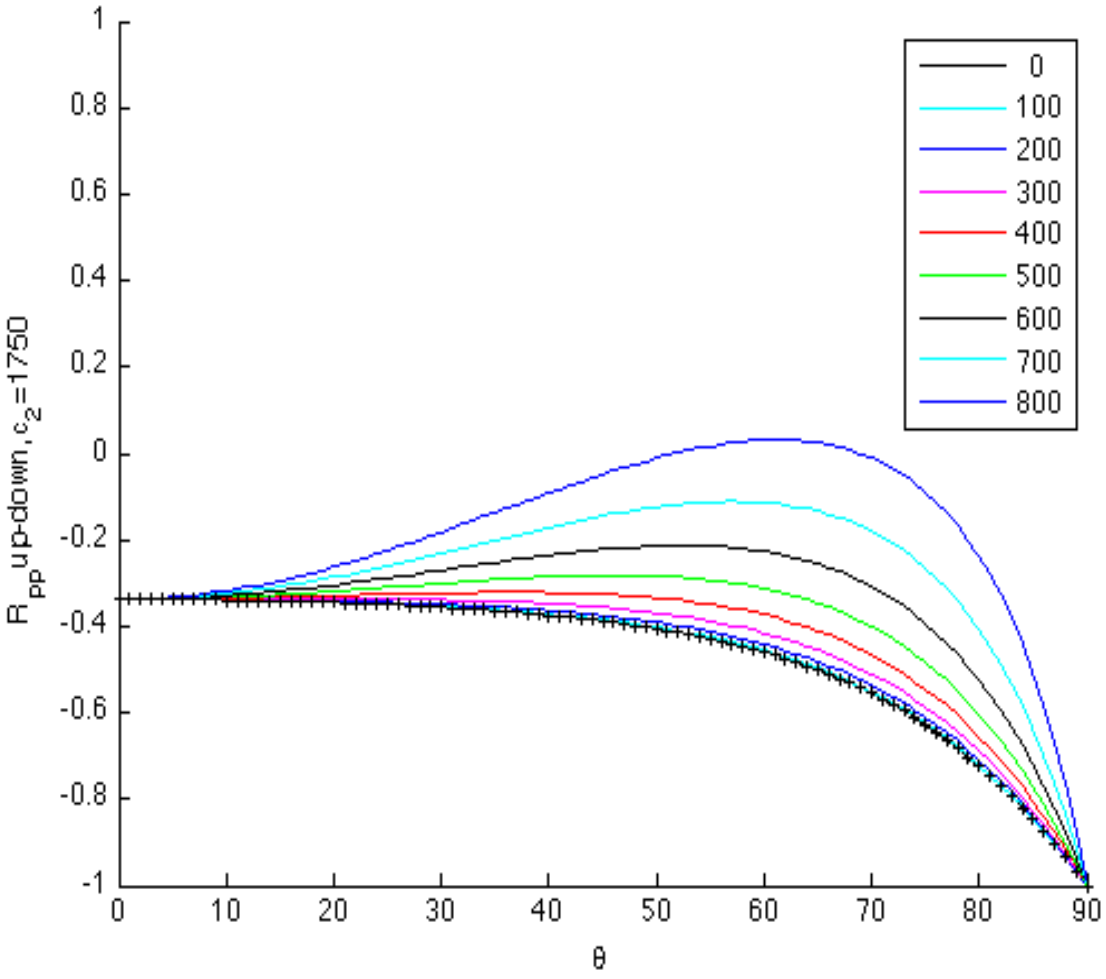

Figure 11: $(\acute{P}\grave{P})_{ae}$ reflection coefficient for two halfspaces in contact. The parametes for the upper(water) and lower halfspaces are: $\rho_1 = 1000kg/m^3$, $\alpha_1 = 1500m/sec$, $\beta_1 = 0m/sec$; $\rho_2 = 1730kg/m^3$ and $\alpha_2 = 1750m/s$ and β_2 is varying between 0 to 800 m/sec(see legend box). '+' is associated with $\beta_2 = 0$.

Carvalho P.M.,1992, Free surface multiple elimination method based on nonlinear inversion of seismic data: Ph.D thesis, Universidade Federal da Bahia, Brazil (in Portuguese).

Carvalho, P. M., Weglein, A. B., and Stolt, R. H., 1992, Nonlinear inverse scattering for multiple suppression: Application to real data. Part i : SEG Technical Program Expanded Abstracts, **11**, 1093-1095.

Weglein, et al., 2003, Inverse scattering series and seismic exploration: Institute of Physics Publishing, Inverse Problems , **19** R27-R83.

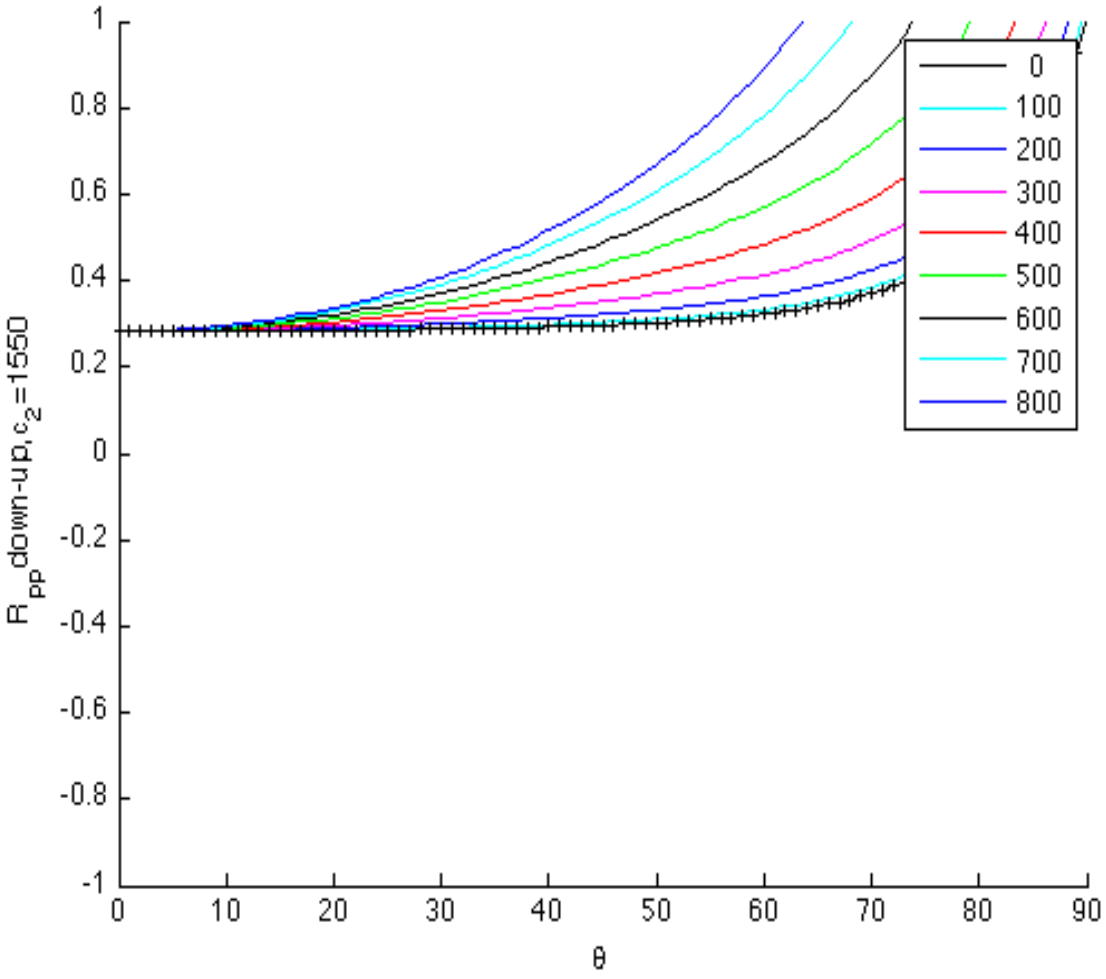

Figure 12: $(\grave{P}\acute{P})_{ae}$ reflection coefficient for two halfspaces in contact, as a function of incident angle. The parametes for the upper(water) and lower halfspaces are: $\rho_1 = 1000kg/m^3$, $\alpha_1 = 1500m/sec$, $\beta_1 = 0m/sec$; $\rho_2 = 1730kg/m^3$ and $\alpha_2 = 1550m/s$ and β_2 is varying between 0 to 800 m/sec(see legend box). '+' is associated with $\beta_2 = 0$.

Keys, Robert G., 1989, Polarity reversals in reflections from layered media: Geophysics, **54**, no. 7, 900-905.

Achenbach, J. D., 1973, Wave propagation in elastic solids: North Holland Publishing Company, Amsterdam-London.

Weglein, A. B., F. V. Araújo Gasparotto, P. M. Carvalho and R. H. Stolt, 1997, An inverse-scattering series method for attenuating multiples in seismic reflection data: Geophysics, **62**, no. 6, 1975–1989.

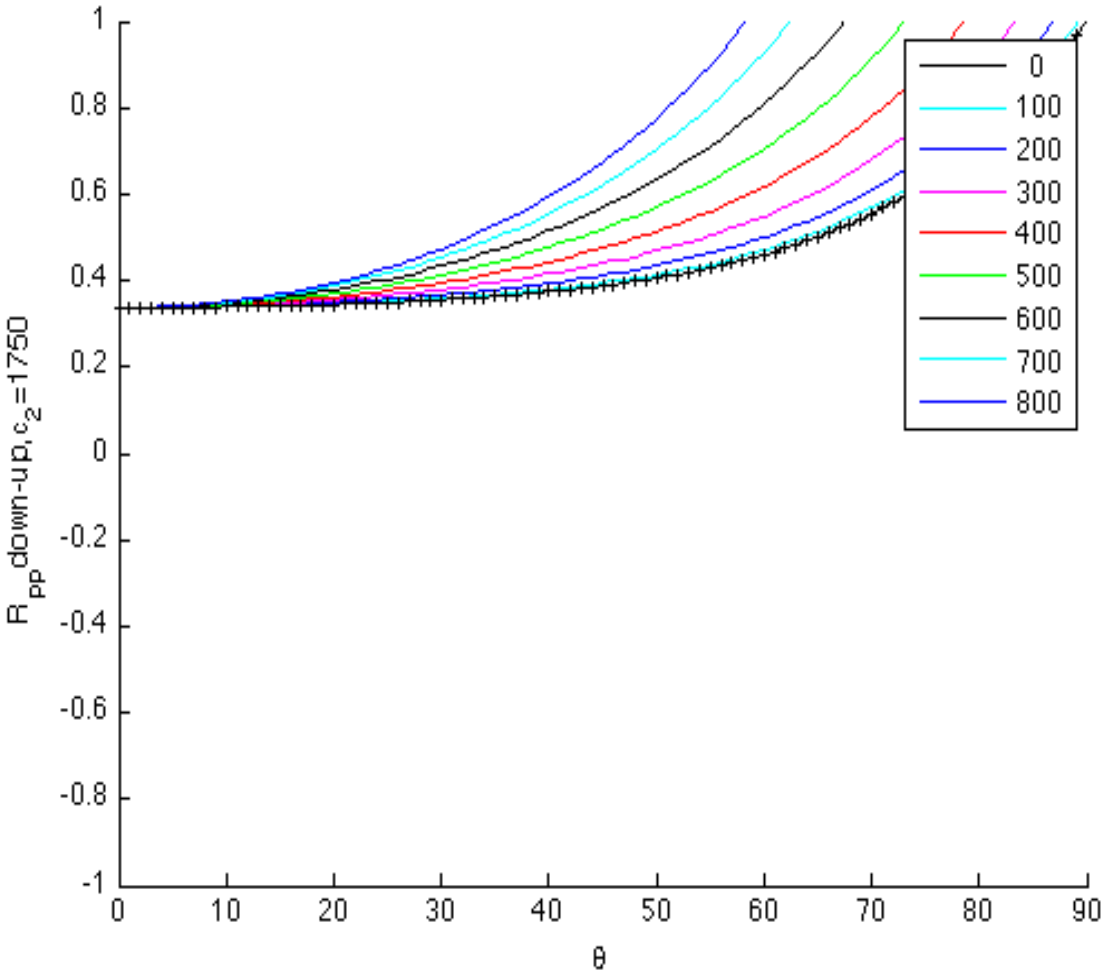

Figure 13: $(\grave{P}\acute{P})_{ae}$ reflection coefficient for two halfspaces in contact, as a function of incident angle. The parametes for the upper(water) and lower halfspaces are: $\rho_1 = 1000kg/m^3$, $\alpha_1 = 1500m/sec$, $\beta_1 = 0m/sec$; $\rho_2 = 1730kg/m^3$ and $\alpha_2 = 1750m/s$ and β_2 is varying between 0 to 800 m/sec(see legend box). '+' is associated with $\beta_2 = 0$.

Weglein, A. B., Zhang, H., Ramírez, A. C., Liu, F., and Lira, J. E. M., 2009, Clarifying the underlying and fundamental meaning of the approximate linear inversion of seismic data: Geophysics, **74**, no. 6, P.WCD1-WCD13.

Incorporating an angle dependent source signature into an Inverse Scattering Series free surface multiple elimination algorithm: Initial analysis and formulation

J. Yang and A. B. Weglein

Abstract

The inverse scattering free-surface multiple elimination algorithm is extended from an isotropic point source to a general source, which is an unknown array of air-guns with radiation pattern. This extended FSME method is a more general multidimensional free-surface multiple elimination method without any subsurface information. It can reduce to the current FSME method as the general source reduces to a point source. This extended FSME algorithm requires the deghosted data D_1' and a general source signature $\rho(k,\omega)$, which is a function of wavenumber k and temporal frequency ω. The source signature can be solved using the reference wavefield P_0 in f-k domain. The wavenumber k represents the amplitude variations with takeoff angle from the source radiation pattern.

1 Introduction

Multiple removal is a classic and long-standing problem in marine exploration seismology. The inability to remove multiples can lead to multiples misinterpreted as or interfering with primaries. Many data processing methods are based on the fundamental assumption that seismic data contains primaries only. Therefore, effective demultiple algorithms are required in marine seismic data processing.

Various methods have been developed in the last three decades to either attenuate or eliminate free-surface multiples which are dominant in marine case, especially in the water bottom with a high velocity contrast. The inverse scattering series (ISS) free-surface multiple elimination method (FSME) is an important multidimensional free-surface demultiple method, that does not require any subsurface information and most importantly it preserves primary energy (e.g., Carvalho, 1992; Araújo, 1994; Weglein et al., 1997). A crucial assumption in this method, however, is that the source is an isotropic point source, *i.e.*, no variation of amplitude or phase with angle. In practice, source array is usually applied in seismic exploration to increase the power of the source, broaden the bandwidth and cancel the random noise. The source array has radiation pattern and the radiation pattern has a profound effect on AVO (Gassaway et al., 1986) and large marine air-gun arrays produce significant variations of the source signature (Loveridge et al., 1984). The variant source signature due to the source array will affect the results of free-surface and internal multiples elimination. Therefore, to extend the

FSME algorithm to a general source with radiation pattern is the goal of this report, which is organized as follows: In the next section, the inverse scattering series is constructed for a general source ρ using the reference wavefield P_0. In the third section, the FSME subseries is derived from the inverse scattering series for removing the free-surface multiples. In the forth section, we formulate and solve the general angle dependent source signature $\rho(k,\omega)$ using the direct reference wavefield P_0^d and then extend the ISS FSME algorithm to source array by incorporating the angle dependent source signature. Finally, we give some analysis on the extended FSME method.

2 Inverse Scattering Series

Starting from the two basic differential equations (Weglein et al., 2003), which govern wave propagation in actual medium and reference medium

$$LP = \rho \tag{1}$$

$$L_0 G_0 = \delta \tag{2}$$

where L, L_0 are respectively the differential operators in actual and reference medium. P is the total wavefield in the actual medium, which is generated by an arbitrary source distribution ρ and G_0 is the Green's function in the reference medium. We define the perturbation as $V = L_0 - L$. The Lippmann-Schwinger equation is given by

$$P = P_0 + G_0 V P \tag{3}$$

where P_0 is the reference wavefield. It is the response of the reference medium to a real source, which is an array of impulsive point sources, while G_0 is an impulse response. Iterating equation 3 back into itself produces the Born series

$$P = P_0 + G_0 V P_0 + G_0 V G_0 V P_0 + \cdots \tag{4}$$

When convergent, the forward scattering series gives a solution to the total wavefield P in terms of the reference wavefield P_0, reference Green's function G_0, and the perturbation operator V. In other words, the forward series predicts the total wavefield P by summing an infinite amount of terms involving interactions between the reference wavefield P_0 and the perturbation V (e.g., Stolt and Weglein, 1985; Weglein et al., 2003).

The scattered wavefield $\psi_s = P - P_0$ is

$$\begin{aligned} \psi_s &= G_0 V P_0 + G_0 V G_0 V P_0 + G_0 V G_0 V G_0 V P_0 + \cdots \\ &= (\psi_s)_1 + (\psi_s)_2 + (\psi_s)_3 + \cdots \end{aligned} \tag{5}$$

where $(\psi_s)_n$ is the portion of ψ_s that is n^{th} order in V. The measured value of ψ_s is the data $D = (\psi_s)_{ms}$, which means the data on the measurement surface. Expanding V as a series in orders of D yields,

$$V = V_1 + V_2 + V_3 + \cdots \tag{6}$$

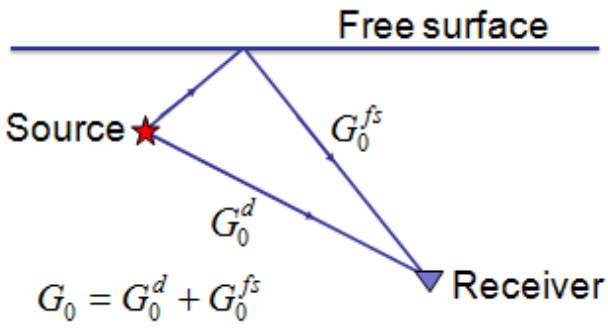

Figure 1: The reference Green's function G_0 consists of two parts, $G_0 = G_0^d + G_0^{fs}$. G_0^d is the direct Greens' function and G_0^{fs} is the additional part of the Greens' function caused by the presence of the free surface.

where V_n is the portion of V that is n^{th} order in the data D. Substituting equation 6 into equation 5 and setting terms of equal order of the data equal yields,

$$D = [G_0 V_1 P_0]_{ms} \tag{7}$$

$$0 = [G_0 V_2 P_0]_{ms} + [G_0 V_1 G_0 V_1 P_0]_{ms} \tag{8}$$

$$0 = [G_0 V_3 P_0]_{ms} + [G_0 V_1 G_0 V_2 P_0]_{ms} + [G_0 V_2 G_0 V_1 P_0]_{ms} + [G_0 V_1 G_0 V_1 G_0 V_1 P_0]_{ms} \tag{9}$$

$$\vdots$$

To solve these equations, the measured data D, the reference Green's function G_0 and the reference wavefield P_0 are required. Following Weglein et al. (1997; 2003), equation 7 is the linear or Born form and allows V_1 to be determined from the data D. V_2 is then calculated from V_1 with equation 8. Equation 9 determines V_3 from V_1 and V_2, and continuing in the same manner to compute V_n. Hence the entire series for the perturbation operator $V = \sum V_n$ is constructed starting with the data D.

3 Free-surface multiple elimination subseries

The free-surface multiple elimination subseries is constructed using the inverse scattering series in Weglein et al. (1997; 2003). As we know, if a given term in the forward scattering series creates a certain type of data, that term in the inverse scattering series removes that type of data, *e.g.*, if there is no free surface, there are no ghosts and free-surface multiples in the data. Hence, the reference Green's function G_0 must consist of two contributions as shown in figure 1: the direct arrival G_0^d and its ghost G_0^{fs}, where G_0^{fs} acts to create (in the forward series) and remove (in the inverse series) ghosts and free-surface multiples. Similarly, the reference wavefield P_0 also consists of two parts in terms of the two parts of G_0, *i.e.*, $P_0 = P_0^d + P_0^{fs}$.

The G_0 and P_0 factors in equation 7 correspond to direct waves and ghosts for the source and the receiver. When they are replaced by G_0^d and P_0^d, the inverse scattering series becomes

$$\begin{aligned} G_0^d V_1 P_0^d &= D_1' && (10)\\ G_0^d V_2 P_0^d &= -G_0^d V_1 G_0 V_1 P_0^d && (11)\\ G_0^d V_3 P_0^d &= -G_0^d V_1 G_0 V_2 P_0^d - G_0^d V_2 G_0 V_1 P_0^d \\ &\quad -G_0^d V_1 G_0 V_1 G_0 V_1 P_0^d && (12)\\ &\vdots \end{aligned}$$

Note: D_1' is the source and receiver deghosted data and also the first term in the series for data without free-surface effects.

The portion of V_2 due to the presence of the free-surface V_2' is determined from V_1 by replacing the inner Green's function G_0 with G_0^{fs} in equation 11,

$$G_0^d V_2' P_0^d = -G_0^d V_1 G_0^{fs} V_1 P_0^d \qquad (13)$$

And then V_3' is determined from V_1 and V_2' in equation 12,

$$\begin{aligned} G_0^d V_3' P_0^d &= -G_0^d V_1 G_0^{fs} V_2' P_0^d - G_0^d V_2' G_0^{fs} V_1 P_0^d \\ &\quad -G_0^d V_1 G_0^{fs} V_1 G_0^{fs} V_1 P_0^d && (14) \end{aligned}$$

Using equation 13, the equation 14 can be rewritten as

$$G_0^d V_3' P_0^d = -G_0^d V_1 G_0^{fs} V_2' P_0^d \qquad (15)$$

In general,

$$G_0^d V_n' P_0^d = -G_0^d V_1 G_0^{fs} V_{n-1}' P_0^d \qquad (16)$$

Consequently, the deghosted reflection data with free-surface multiples eliminated are

$$D' = \sum_{n=1}^{\infty} D_n' = \sum_{n=1}^{\infty} G_0^d V_n' P_0^d \qquad (17)$$

4 Inverse scattering series FSME algorithm for source array

Using the FSME subseries, the FSME algorithm is extended for source array with radiation pattern. The algorithm requires the deghosted data D_1' and the direct reference wavefield P_0^d. The Greens' theorem can give the deghosted data D_1' and the reference wavefield P_0 but not P_0^d when we choose the different reference medium and volume.

Note: The reference wavefield P_0, which is the response of the reference medium to the real general source, also consists of two contributions: the direct reference wavefield P_0^d and its ghost P_0^{fs} propagating from the source up to the free-surface and being reflected down to the receivers: $P_0 = P_0^d + P_0^{fs}$.

When we choose (1) the reference medium is a half space of air over a half space of water, (2) the volume V is below the measurement surface, (3) the source distribution is located between the measurement surface and the free surface (*i.e.*, outside V), and (4) the observation position $\vec{r}$ is in the volume V, the reference wavefield P_0 can be obtained using Green's theorem by measuring the total wavefield P and its normal derivative (Appendix A) as

$$P_0(\vec{r},\vec{r}_s,\omega) = \int_{ms} dS'\,\hat{n}\cdot[P(\vec{r}',\vec{r}_s,\omega)\nabla' G_0(\vec{r}',\vec{r},\omega) - G_0(\vec{r}',\vec{r},\omega)\nabla' P(\vec{r}',\vec{r}_s,\omega)] \tag{18}$$

The direct reference wavefield P_0^d can be obtained generally by deghosting the source side of the reference wavefield P_0. For some special cases, it can be solved directly from P_0 by dividing a factor and we will discuss it later.

When we choose (1) the reference medium is a whole space of water, (2) the volume V is between the measurement surface and the free surface, and (3) the source distribution $\vec{r}'$ and the observation position $\vec{r}$ are in the volume V, the receiver side of the scattered data is deghosted using the deghosting algorithm based on Green's theorem (Zhang, 2007) as

$$P_s'(\vec{r},\vec{r}_s,\omega) = \int_{ms} dS'\,\hat{n}\cdot[P(\vec{r}',\vec{r}_s,\omega)\nabla' G_0(\vec{r}',\vec{r},\omega) - G_0(\vec{r}',\vec{r},\omega)\nabla' P(\vec{r}',\vec{r}_s,\omega)] \tag{19}$$

where P_s' is the receiver side deghosted data and G_0 is the causal Greens' function in the whole space of water. Using the theorem of wavefield reciprocity , exchanging the receiver coordinate with the source coordinate, the source side is also deghosted through applying the same algorithm. Jim Mayhan, a fellow graduate student in our group, can provide the reference wavefield P_0^d and the deghosted D_1' data towards testing this algorithm.

The source array can be described as a superposition of point sources, whose spatial distribution can be described by a function ρ:

$$\rho = \rho(\vec{r}',\vec{r}_s,\omega) \tag{20}$$

Thus, the direct reference wavefield P_0^d can be expressed as the integral of the causal reference Green's function G_0^d over the whole range occupied by the general source ρ (Morse and Feshbach, 1953) as

$$P_0^d(\vec{r},\vec{r}_s,\omega) = \int d\vec{r}'\,\rho(\vec{r}',\vec{r}_s,\omega)G_0^d(\vec{r},\vec{r}',\omega) \tag{21}$$

where $\vec{r}'$, $\vec{r}_s$ and $\vec{r}$ represent respectively the source distribution, the source array locator and the observation position as shown in figure 2.

Due to the translational symmetry of the source array, its geometry is invariant to the source array locator $\vec{r}_s$, and the source distribution ρ only cares about the difference between the source array locator $\vec{r}_s$ and the specific air gun $\vec{r}'$ as shown in figure 3, which means that the source distribution ρ doesn't care about the specific $\vec{r}'$ and $\vec{r}_s$. In other words, for a given source array, the source distribution is the same about the source array locator $\vec{r}_s$. Thus, the source array is only a function of the relative distance to the source array position as $\rho(\vec{r}',\vec{r}_s,\omega) = \rho(\vec{r}'-\vec{r}_s,\omega)$. The direct reference wavefield P_0^d becomes

$$P_0^d(\vec{r},\vec{r}_s,\omega) = \int d\vec{r}'\,\rho(\vec{r}'-\vec{r}_s,\omega)G_0^d(\vec{r},\vec{r}',\omega) \tag{22}$$

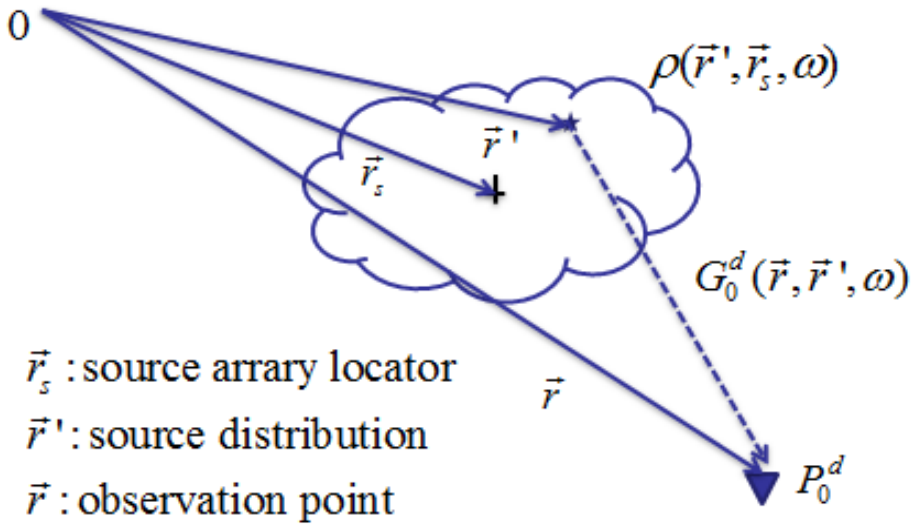

Figure 2: The source array can be described as a function $\rho(\vec{r}', \vec{r}_s, \omega)$.

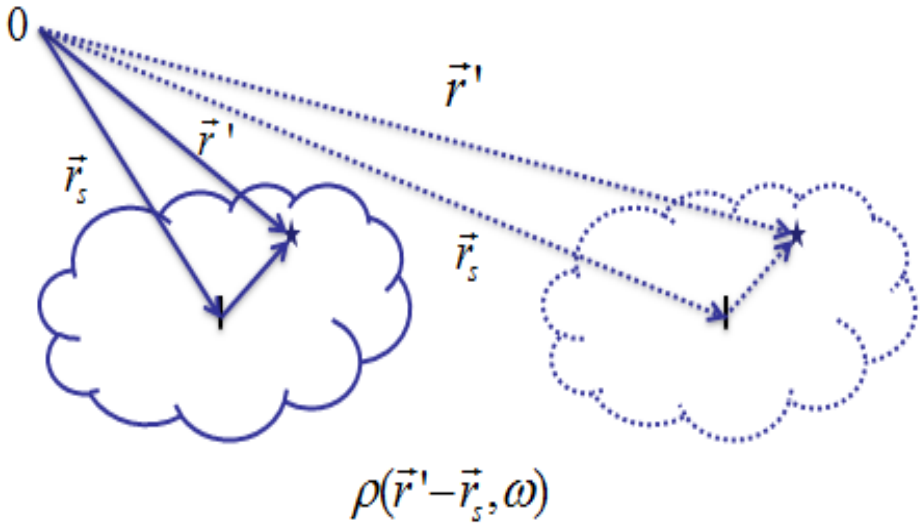

Figure 3: The source array ρ only cares about the difference between the source array locator $\vec{r}_s$ and the specific air gun point $\vec{r}'$ as the source moving.

Note: If the source array reduces to an isotropic point source, the source distribution $\rho(\vec{r}' - \vec{r}_s, \omega)$ becomes $A(\omega)\delta(\vec{r}' - \vec{r}_s)$, where $A(\omega)$ is the point source signature.

When we change the coordinate, let $\vec{r}'' = \vec{r}' - \vec{r}_s$, P_0^d can be rewritten as

$$P_0^d(\vec{r}, \vec{r}_s, \omega) = \int d\vec{r}'' \rho(\vec{r}'', \omega) G_0^d(\vec{r}, \vec{r}'' + \vec{r}_s, \omega)$$

where $\vec{r}''$ describes the source distribution relative to $\vec{r}_s$, and $\vec{r}''$ is invariant as the source moving. Recalling $\vec{r}''$ as $\vec{r}'$, the direct reference wavefield P_0^d becomes

$$P_0^d(\vec{r}, \vec{r}_s, \omega) = \int d\vec{r}' \rho(\vec{r}', \omega) G_0^d(\vec{r}, \vec{r}' + \vec{r}_s, \omega) \tag{23}$$

Consider a simple 2D case, we assume that the source array only distributes laterally and locates at depth ϵ_s below the free surface. In other words, the source array as air guns are only at the x direction. x' gives the distance from the source array locator to the individual air gun. Equation 23 becomes

$$P_0^d(x, z, x_s, \epsilon_s, \omega) = \int dx' \rho(x', \omega) G_0^d(x, z, x' + x_s, \epsilon_s, \omega) \tag{24}$$

For this case, the direct reference wavefield P_0^d can be solved from the reference wavefield P_0 as $P_0^d = P_0/(1 - e^{2iq_s\epsilon_s})$. Using the bilinear form of Green's function and then Fourier transforming over x_s, we obtain the relationship between ρ and P_0^d (Appendix B) as

$$P_0^d(x, z, k_s, \epsilon_s, \omega) = \rho(k_s, \omega) \frac{e^{iq_s|z-\epsilon_s|}}{2iq_s} e^{ik_s x} \tag{25}$$

where $k_s^2 + q_s^2 = \omega^2/c_0^2$ and $z > \epsilon_s$.Thus, the general source signature, in other words, the angle dependent source signature $\rho(k_s, \omega)$ can be calculated in f-k domain using the reference wavefield P_0^d. As we know, in the space domain, a straightforward picture of physics tells us that the general source signature ρ is a function of source distribution $\vec{r}'$ and temporal frequency ω as we discussed in figure 2. After Fourier transformation, the angle dependent source signature ρ becomes a function of horizontal wavenumber k and temporal frequency ω in the f-k domain. The variable k_s represents the amplitude variations of the general source signature with angle due to the source array.

The FSME algorithm is extended to source array with radiation pattern incorporating the angle dependent source signature. The procedure of the extended FSME algorithm is as follows:

(1) The data D is calculated by subtracting the reference wavefield P_0 from the total wavefield P on the measurement surface.

(2) The data D is deghosted for both source and receiver sides using equation 19 (Zhang, 2007).

(3) Using the angle dependent source signature $\rho(k, \omega)$ in equation 25, the projection of V_1 on the measurement surface is expressed from the first-order equation 10 as

$$V_1(k_g, -q_g, -k_s, -q_s, \omega) = \frac{2iq_g}{e^{-iq_g\epsilon_g}} \frac{D_1'(k_g, z_g, k_s, \epsilon_s, \omega)}{\rho(k_s, \omega)} \frac{2iq_s}{e^{-iq_s\epsilon_s}} \tag{26}$$

(4) Substituting V_1 into equation 16, the final expression for the deghosted and free-surface demultipled data D' in terms of the deghosted data D'_1 and the angle dependent source signature $\rho(k,\omega)$ as follows:

$$D'_n(k_g,k_s,\omega)=\frac{1}{i\pi\rho_0}\int\frac{dk}{\rho(k,\omega)}D'_1(k_g,k,\omega)qe^{iq(\epsilon_g+\epsilon_s)}D'_{n-1}(k,k_s,\omega) \tag{27}$$

and

$$D'(k_g,k_s,\omega)=\sum_{n=1}^{\infty}D'_n(k_g,k_s,\omega) \tag{28}$$

with k_g, k_s and ω representing the wave-numbers along the source and receiver axes and the angular frequency, respectively. ρ_0 is the reference density and $\rho(k,\omega)$ is the general source signature, which is a function of wavenumber k and temporal frequency ω in the f-k domain. ϵ_g and ϵ_s are the depth of the receiver and source below the free surface, respectively and q is the obliquity factor given by:

$$q=sgn(\omega)\sqrt{\frac{\omega^2}{c_0^2}-k^2} \tag{29}$$

Using the FSME subseries, the FSME algorithm is extended by incorporating the angle dependent source signature $\rho(k,\omega)$, which includes the effects of the source directivity. The extended FSME method requires the deghosted data D'_1 and the angle dependent source signature $\rho(k,\omega)$ and does not need any subsurface information.

Details of the derivation for equation 27 can be found in Appendix C.

5 Analysis

The extended FSME algorithm should be consistent with the current FSME algorithm as the source array reduces to a point source. Let's consider the simplest case: The source array reduces to an isotropic point source $A(\omega)$, then the source distribution $\rho(\vec{r}'-\vec{r}_s,\omega)$ becomes $A(\omega)\delta(\vec{r}'-\vec{r}_s)$ and the direct reference wavefield P_0^d becomes $A(\omega)G_0^d$. The whole procedure of FSME algorithm is the same as the one we talked in the last section. The difference is that the expression of V_1 in the step 3 becomes

$$V_1(k_g,-q_g,-k_s,-q_s,\omega)=\frac{2iq_g}{e^{-iq_g\epsilon_g}}\frac{D'_1(k_g,z_g,k_s,\epsilon_s,\omega)}{A(\omega)}\frac{2iq_s}{e^{-iq_s\epsilon_s}} \tag{30}$$

Substituting it into equation 16, equation 27 becomes

$$D'_n(k_g,k_s,\omega)=\frac{1}{i\pi\rho_0A(\omega)}\int dkD'_1(k_g,k,\omega)qe^{iq(\epsilon_g+\epsilon_s)}D'_{n-1}(k,k_s,\omega) \tag{31}$$

which is the current FSME algorithm derived in Carvalho (1992).

Second, if all the air guns are the same, which means that they have the same source signature $\rho(\omega)$, the general source signature $\rho(k,\omega)$ in equation 48 becomes

$$\rho(k,\omega) = \rho(\omega)\int_{-a}^{a} dx' e^{-ikx'} = \rho(\omega)\frac{2}{k}\sin(ka) \tag{32}$$

where we assume that the range of the source array is from $-a$ to a. Then equation 27 reduces to

$$D'_n(k_g,k_s,\omega) = \frac{1}{i\pi\rho_0\rho(\omega)}\int \frac{dk}{\frac{2}{k}\sin(ka)} D'_1(k_g,k,\omega) q e^{iq(\epsilon_g+\epsilon_s)} D'_{n-1}(k,k_s,\omega) \tag{33}$$

where ρ_0 is the reference density and $\rho(\omega)$ is the source wavelet for each air gun.

From the above analysis, we can see that the extended FSME algorithm can deal with more general cases of sources with or without radiation pattern.

6 Conclusion

The FSME algorithm is extended by incorporating a more general source signature $\rho(k,\omega)$, which includes the effects of the source directivity. The wavenumber k describes the amplitude variations with angle in f-k domain. The extended FSME method requires the deghosted data D'_1 and the angle dependent source signature $\rho(k,\omega)$, which can be solved from the reference wavefield P_0^d. It doesn't require any subsurface information. One of its special cases is the current FSME algorithm as the source array reduces to an isotropic point source. Therefore, the extended FSME algorithm is a more general and effective multidimensional free-surface multiple elimination method, which can accommodate sources with or without radiation pattern.

7 Acknowledgements

The first author is grateful to all M-OSRP sponsors for their support of this research and to Dr. Paolo Terenghi and Zhiqiang Wang for their helpful and valuable discussions in this research. My special appreciation to my advisor Dr. Arthur Weglein for his teaching, guidance and patience.

Appendices

A Estimation of reference wavefield P_0

The effective source signature or reference wavefield P_0 is derived in Weglein and Secrest (1990), in which they derive two equations: the Lippmann-Schwinger equation and Green's second identity. Comparing the two equations gives an equation for the reference wavefield P_0 as a function of measured data and a reference medium Green function.

The acoustic wave equation with constant density for the total field P created by a general source $\rho(\vec{r}, \vec{r}_s, t)$ at the effective position $\vec{r}_s$ in frequency domain is

$$\left(\nabla^2 + \frac{\omega^2}{c^2(\vec{r})}\right) P(\vec{r}, \vec{r}_s, \omega) = \rho(\vec{r}, \vec{r}_s, \omega) \tag{34}$$

Characterizing $c(\vec{r})$ in terms of c_0 and the variation index of refraction $\alpha(\vec{r})$ gives

$$\frac{1}{c^2(\vec{r})} = \frac{1}{c_0^2}(1 - \alpha(\vec{r})) \tag{35}$$

Substituting equation 35 into equation 34 gives

$$\left(\nabla^2 + \frac{\omega^2}{c_0^2}\right) P(\vec{r}, \vec{r}_s, \omega) = \rho(\vec{r}, \vec{r}_s, \omega) + \frac{\omega^2}{c_0^2}\alpha(\vec{r})P(\vec{r}, \vec{r}_s, \omega) \tag{36}$$

Converting equation 36 from a partial differential equation into an integral equation (the Lippmann-Schwinger equation) gives

$$P(\vec{r}, \vec{r}_s, \omega) = \int d\vec{r}\,'\rho(\vec{r}', \vec{r}_s, \omega)G_0(\vec{r}, \vec{r}\,', \omega) + \int_\infty d\vec{r}\,'G_0(\vec{r}, \vec{r}\,', \omega)\frac{\omega^2}{c_0^2}\alpha(\vec{r}\,')P(\vec{r}\,', \vec{r}_s, \omega) \tag{37}$$

Choosing a causal Green function G_0^+ in the Lippmann-Schwinger equation gives a causal solution $P(\vec{r}, \vec{r}_s, \omega)$:

$$P(\vec{r}, \vec{r}_s, \omega) = \int d\vec{r}\,'\rho(\vec{r}', \vec{r}_s, \omega)G_0^+(\vec{r}, \vec{r}\,', \omega) + \int_\infty d\vec{r}\,'G_0^+(\vec{r}, \vec{r}\,', \omega)\frac{\omega^2}{c_0^2}\alpha(\vec{r}\,')P(\vec{r}\,', \vec{r}_s, \omega) \tag{38}$$

Substituting P and G_0 into Green's theorem gives

$$\begin{aligned}&\int_V d\vec{r}\,'[P(\vec{r}\,', \vec{r}_s, \omega)\nabla'^2 G_0(\vec{r}\,', \vec{r}, \omega) - G_0(\vec{r}\,', \vec{r}, \omega)\nabla'^2 P(\vec{r}\,', \vec{r}_s, \omega)] = \\ &\oint_S dS'\,\hat{n} \cdot [P(\vec{r}\,', \vec{r}_s, \omega)\nabla' G_0(\vec{r}\,', \vec{r}, \omega) - G_0(\vec{r}\,', \vec{r}, \omega)\nabla' P(\vec{r}\,', \vec{r}_s, \omega)]\end{aligned} \tag{39}$$

where V is the hemispheric volume below the measurement surface, and S is the hemisphere's surface. Substituting equation 36 and its corresponding reference medium Green function differential equation into equation 39 gives

$$\oint_S dS'\,\hat{n} \cdot [P(\vec{r}\,', \vec{r}_s, \omega)\nabla' G_0(\vec{r}\,', \vec{r}, \omega) - G_0(\vec{r}\,', \vec{r}, \omega)\nabla' P(\vec{r}\,', \vec{r}_s, \omega)]$$

$$
\begin{aligned}
&= \int_V d\vec{r}'[P(\vec{r}',\vec{r}_s,\omega) \underbrace{\nabla'^2 G_0(\vec{r}',\vec{r},\omega)}_{(-\omega^2/c_0^2)G_0(\vec{r}',\vec{r},\omega)+\delta(\vec{r}'-\vec{r})} \\
&\quad -G_0(\vec{r}',\vec{r},\omega) \underbrace{\nabla'^2 P(\vec{r}',\vec{r}_s,\omega)}_{(-\omega^2/c_0^2)P(\vec{r}',\vec{r}_s,\omega)+\frac{\omega^2}{c_0^2}\alpha(\vec{r}')P(\vec{r}',\vec{r}_s,\omega)+\rho(\vec{r}',\vec{r}_s,\omega)}] \\
&= \int_V d\vec{r}'[\underbrace{-\frac{\omega^2}{c_0^2}G_0(\vec{r}',\vec{r},\omega)P(\vec{r}',\vec{r}_s,\omega)}_{cancels} + \delta(\vec{r}'-\vec{r})P(\vec{r}',\vec{r}_s,\omega) \\
&\quad + \underbrace{\frac{\omega^2}{c_0^2}P(\vec{r}',\vec{r}_s,\omega)G_0(\vec{r}',\vec{r},\omega)}_{cancels} - \frac{\omega^2}{c_0^2}\alpha(\vec{r}')P(\vec{r}',\vec{r}_s,\omega)G_0(\vec{r}',\vec{r},\omega) \\
&\quad -\rho(\vec{r}',\vec{r}_s,\omega)G_0(\vec{r}',\vec{r},\omega)] \\
&= \int_V d\vec{r}'[P(\vec{r}',\vec{r}_s,\omega)\delta(\vec{r}'-\vec{r}) - \frac{\omega^2}{c_0^2}\alpha(\vec{r}')P(\vec{r}',\vec{r}_s,\omega)G_0(\vec{r}',\vec{r},\omega) \\
&\quad -\rho(\vec{r}',\vec{r}_s,\omega)G_0(\vec{r}',\vec{r},\omega)] \qquad (40)
\end{aligned}
$$

If we choose $\vec{r} \in V$, the general source ρ is zero because it is outside of the volume, the equation 40 will be

$$
\begin{aligned}
&\oint_S dS'\,\hat{n}\cdot[P(\vec{r}',\vec{r}_s,\omega)\nabla' G_0(\vec{r}',\vec{r},\omega) - G_0(\vec{r}',\vec{r},\omega)\nabla' P(\vec{r}',\vec{r}_s,\omega)] \\
&= \int_V d\vec{r}'[\underbrace{P(\vec{r}',\vec{r}_s,\omega)\delta(\vec{r}'-\vec{r})}_{P(\vec{r},\vec{r}_s,\omega)} - \frac{\omega^2}{c_0^2}\alpha(\vec{r}')P(\vec{r}',\vec{r}_s,\omega)G_0(\vec{r}',\vec{r},\omega) \\
&\quad - \underbrace{\rho(\vec{r}',\vec{r}_s,\omega)}_{0} G_0(\vec{r}',\vec{r},\omega)] \\
&= P(\vec{r},\vec{r}_s,\omega) - \int_V d\vec{r}'\frac{\omega^2}{c_0^2}\alpha(\vec{r}')P(\vec{r}',\vec{r}_s,\omega)G_0(\vec{r}',\vec{r},\omega) \qquad (41)
\end{aligned}
$$

If the support for $\alpha \in V$, rearranging equation 41 gives

$$
\begin{aligned}
P(\vec{r},\vec{r}_s,\omega) &= \int_V d\vec{r}' G_0(\vec{r}',\vec{r},\omega)\frac{\omega^2}{c_0^2}\alpha(\vec{r}')P(\vec{r}',\vec{r}_s,\omega) \\
&\quad + \oint_S dS', \hat{n}\cdot[P(\vec{r}',\vec{r}_s,\omega)\nabla' G_0(\vec{r}',\vec{r},\omega) - G_0(\vec{r}',\vec{r},\omega)\nabla' P(\vec{r}',\vec{r}_s,\omega)] \\
&= \int_\infty d\vec{r}' G_0(\vec{r}',\vec{r},\omega)\frac{\omega^2}{c_0^2}\alpha(\vec{r}')P(\vec{r}',\vec{r}_s,\omega) \\
&\quad + \oint_S dS'\,\hat{n}\cdot[P(\vec{r}',\vec{r}_s,\omega)\nabla' G_0(\vec{r}',\vec{r},\omega) - G_0(\vec{r}',\vec{r},\omega)\nabla' P(\vec{r}',\vec{r}_s,\omega)] \qquad (42)
\end{aligned}
$$

In equation 42 the surface integral involves actual pressure measurements and their vertical derivatives. For consistency with equation 38 choose a causal Green function which gives

$$
P(\vec{r},\vec{r}_s,\omega) = \int_\infty d\vec{r}' G_0^+(\vec{r}',\vec{r},\omega)\frac{\omega^2}{c_0^2}\alpha(\vec{r}')P(\vec{r}',\vec{r}_s,\omega)
$$

$$+\oint_S dS'\,\hat{n}\cdot[P(\vec{r}',\vec{r}_s,\omega)\nabla' G_0^+(\vec{r}',\vec{r},\omega)-G_0^+(\vec{r}',\vec{r},\omega)\nabla' P(\vec{r}',\vec{r}_s,\omega)] \quad (43)$$

Comparing the Lippmann-Schwinger equation (38) and Green's theroem (43) gives an equation for the effective source signature or reference wavefield P_0:

$$\begin{aligned} P_0(\vec{r},\vec{r}_s,\omega) &= \int_V d\vec{r}'\rho(\vec{r}',\vec{r}_s,\omega)G_0(\vec{r}',\vec{r},\omega) \\ &= \oint_S dS'\,\hat{n}\cdot[P(\vec{r}',\vec{r}_s,\omega)\nabla' G_0^+(\vec{r}',\vec{r},\omega) \\ &\quad -G_0^+(\vec{r}',\vec{r},\omega)\nabla' P(\vec{r}',\vec{r}_s,\omega)] \end{aligned} \quad (44)$$

equation 44 is one form of the "triangle relation" relating the pressure wavefield $P(\vec{r}',\vec{r}_s,\omega)$, its vertical derivative $\nabla' P(\vec{r}',\vec{r}_s,\omega)$, and the effective source signature or reference wavefield $P_0(\vec{r}\,\vec{r}_s,\omega)$.

B Derivation of Equation 25

Here, the angle dependent source signature $\rho(k,\omega)$ is solved from the reference wavefield P_0^d. We assume that (1) the distribution of the source array is invariant for each experiment, which means that the source distribution doesn't depend on the source array locator $\vec{r}_s$, and (2) the source array only distributes laterally along the horizontal variable x'. Since the translational symmetry of the source array, the source distribution ρ only cares about the distance between the source array locator x_s and each individual air gun x', P_0^d can be rewritten as

$$P_0^d(x,z,x_s,\epsilon_s,\omega)=\int dx'\rho(x',\epsilon_s,\omega)G_0^d(x,z,x'+x_s,\epsilon_s,\omega) \quad (45)$$

where x' is the source distribution relative to the source array locator x_s. Using the bilinear form of Green's function, it becomes

$$P_0^d(x,z,x_s,\epsilon_s,\omega)=\int dx'\rho(x',\omega)\int dk_x dk_z \frac{e^{ik_x(x-x'-x_s)}e^{ik_z(z-\epsilon_s)}}{-k_x^2-k_z^2+\frac{\omega^2}{c_0^2}} \quad (46)$$

Fourier transforming with respect to x_s gives

$$\begin{aligned} P_0^d(x,z,k_s,\epsilon_s,\omega) &= \int dx'\rho(x',\omega)\int dk_x dk_z \frac{e^{ik_x(x-x'-x_s)}e^{ik_z(z-\epsilon_s)}}{-k_x^2-k_z^2+\frac{\omega^2}{c_0^2}}e^{ik_s x_s}dx_s \\ &= \int dx'\rho(x',\omega)\int dk_x dk_z \frac{e^{ik_x(x-x')}e^{ik_z(z-\epsilon_s)}}{-k_x^2-k_z^2+\frac{\omega^2}{c_0^2}}\delta(k_s-k_x) \\ &= \int dx'\rho(x',\omega)e^{ik_s(x-x')}\int dk_z \frac{e^{ik_z(z-\epsilon_s)}}{-k_z^2\underbrace{-k_s^2+\frac{\omega^2}{c_0^2}}_{+q_s^2}} \end{aligned}$$

$$
\begin{aligned}
&= \int dx' \rho(x', \omega) e^{ik_s(x-x')} \int dk_z \frac{e^{ik_z(z-\epsilon_s)}}{-k_z^2 + q_s^2} \\
&= \int dx' \rho(x', \omega) e^{ik_s(x-x')} \frac{e^{iq_s|z-\epsilon_s|}}{2iq_s} \\
&= \rho(k_s, \omega) e^{ik_s x} \frac{e^{iq_s|z-\epsilon_s|}}{2iq_s} \\
&= \rho(k_s, \omega) \frac{e^{-iq_s\epsilon_s}}{2iq_s} e^{ik_s x} e^{iq_s z} \qquad (47)
\end{aligned}
$$

Here $z > \epsilon_s$ is used.

For this special case, source array only distributes laterally, we can similarly obtain the total reference wavefield as

$$
\begin{aligned}
P_0(x, z, k_s, \epsilon_s, \omega) \qquad &= \rho(k_s, \omega) \frac{e^{iq_s|z-\epsilon_s|} - e^{iq_s|z+\epsilon_s|}}{2iq_s} \\
&= \rho(k_s, \omega) \frac{e^{-iq_s\epsilon_s}(1 - e^{2iq_s\epsilon_s})}{2iq_s} e^{iq_s z} \\
&= P_0^d(x, z, k_s, \epsilon_s, \omega)(1 - e^{2iq_s\epsilon_s}) \qquad (48)
\end{aligned}
$$

C Derivation of Equation 27

The n^{th} order free-surface demultipled data

$$
\begin{aligned}
&D_n'(x_g, \epsilon_g, x_s, \epsilon_s, \omega) = -\int dx_1 dz_1 dx_2 dz_2 G_0^d(x_g, \epsilon_g, x_1, z_1, \omega) V_1(x_1, z_1, x_2, z_2, \omega) \\
&* G_0^{fs}(x_2, z_2, x_3, z_3, \omega) V_{n-1}(x_3, z_3, x_4, z_4, \omega) P_0^d(x_4, z_4, x_s, \epsilon_s, \omega) dx_3 dz_3 dx_4 dz_4 \qquad (49)
\end{aligned}
$$

Substituting the bilinear form of the Green's function

$$
G_0^d(x, z, x', z', \omega) = \int dk_x dk_z \frac{e^{ik_x(x-x')} e^{ik_z(z-z')}}{-k_x^2 - k_z^2 + \frac{\omega^2}{c_0^2}} \qquad (50)
$$

into equation 49, gives

$$
\begin{aligned}
&D_n'(x_g, \epsilon_g, x_s, \epsilon_s, \omega) = -\int dx_1 dz_1 dx_2 dz_2 \int dk_x' dk_z' \frac{e^{ik_x'(x_g - x_1)} e^{ik_z'(\epsilon_g - z_1)}}{-k_x'^2 - k_z'^2 + \frac{\omega^2}{c_0^2}} V_1(x_1, z_1, x_2, z_2, \omega) \\
&* \int dk dk_z \frac{e^{ik(x_2 - x_3)} e^{ik_z(z_2 + z_3)}}{-k^2 - k_z^2 + \frac{\omega^2}{c_0^2}} V_{n-1}(x_3, z_3, x_4, z_4, \omega) P_0^d(x_4, z_4, x_s, \epsilon_s, \omega) dx_3 dz_3 dx_4 dz_4 \qquad (51)
\end{aligned}
$$

Fourier transforming with respect to x_g and x_s gives

$$
D_n'(k_g, \epsilon_g, k_s, \epsilon_s, \omega) = -\int dx_1 dz_1 dx_2 dz_2 \int dk_x' dk_z' \frac{e^{ik_x'(x_g - x_1)} e^{ik_z'(\epsilon_g - z_1)}}{-k_x'^2 - k_z'^2 + \frac{\omega^2}{c_0^2}} e^{-ik_g x_g} dx_g
$$

$$*V_1(x_1,z_1,x_2,z_2,\omega)\int dkdk_z\frac{e^{ik(x_2-x_3)}e^{ik_z(z_2+z_3)}}{-k^2-k_z^2+\frac{\omega^2}{c_0^2}}V_{n-1}(x_3,z_3,x_4,z_4,\omega)$$

$$*P_0^d(x_4,z_4,x_s,\epsilon_s,\omega)e^{ik_sx_s}dx_sdx_3dz_3dx_4dz_4$$

$$=-\int dx_1dz_1dx_2dz_2\int dk_x'dk_z'\frac{e^{-ik_x'x_1}e^{ik_z'(\epsilon_g-z_1)}}{-k_x'^2-k_z'^2+\frac{\omega^2}{c_0^2}}2\pi\delta(k_x'-k_g)V_1(x_1,z_1,x_2,z_2,\omega)$$

$$*\int dkdk_z\frac{e^{ik(x_2-x_3)}e^{ik_z(z_2+z_3)}}{-k^2-k_z^2+\frac{\omega^2}{c_0^2}}V_{n-1}(x_3,z_3,x_4,z_4,\omega)P_0^d(x_4,z_4,k_s,\epsilon_s,\omega)dx_3dz_3dx_4dz_4 \quad (52)$$

Integrating over k_x' gives

$$D_n'(k_g,\epsilon_g,k_s,\epsilon_s,\omega)=-\int dx_1dz_1dx_2dz_2dz_2 2\pi\int dk_z'\frac{e^{-ik_gx_1}e^{ik_z'(\epsilon_g-z_1)}}{-k_z'^2\underbrace{-k_g^2+\frac{\omega^2}{c_0^2}}_{+q_g^2}}V_1(x_1,z_1,x_2,z_2,\omega)$$

$$*\int dkdk_z\frac{e^{ik(x_2-x_3)}e^{ik_z(z_2+z_3)}}{\underbrace{-k_z^2-k^2+\frac{\omega^2}{c_0^2}}_{+q^2}}V_{n-1}(x_3,z_3,x_4,z_4,\omega)P_0^d(x_4,z_4,k_s,\epsilon_s,\omega)dx_3dz_3dx_4dz_4$$

$$=-\int dx_1dz_1dx_2dz_2e^{-ik_gx_1}2\pi\int dk_z'\frac{e^{ik_z'(\epsilon_g-z_1)}}{-k_z'^2+q_g^2}V_1(x_1,z_1,x_2,z_2,\omega)$$

$$*\int dkdk_z\frac{e^{ik(x_2-x_3)}e^{ik_z(z_2+z_3)}}{-k_z^2+q^2}V_{n-1}(x_3,z_3,x_4,z_4,\omega)P_0^d(x_4,z_4,k_s,\epsilon_s,\omega)dx_3dz_3dx_4dz_4$$

$$=-\int dx_1dz_1dx_2dz_2e^{-ik_gx_1}\frac{e^{iq_g|\epsilon_g-z_1|}}{2iq_g}V_1(x_1,z_1,x_2,z_2,\omega)\frac{1}{2\pi}\int dke^{ik(x_2-x_3)}\frac{e^{iq|z_2+z_3|}}{2iq}$$

$$*V_{n-1}(x_3,z_3,x_4,z_4,\omega)P_0^d(x_4,z_4,k_s,\epsilon_s,\omega)dx_3dz_3dx_4dz_4 \quad (53)$$

Since $\epsilon_g<z_1$ and $z_2,z_3>0$, equation 53 becomes

$$D_n'(k_g,\epsilon_g,k_s,\epsilon_s,\omega)=-\int dx_1dz_1dx_2dz_2e^{-ik_gx_1}\frac{e^{iq_g(\epsilon_g-z_1)}}{2iq_g}V_1(x_1,z_1,x_2,z_2,\omega)$$

$$*\frac{1}{2\pi}\int dke^{ik(x_2-x_3)}\frac{e^{iq(z_2+z_3)}}{2iq}V_{n-1}(x_3,z_3,x_4,z_4,\omega)P_0^d(x_4,z_4,k_s,\epsilon_s,\omega)dx_3dz_3dx_4dz_4$$

$$=-\frac{1}{2\pi}\int dk\frac{e^{-iq_g\epsilon_g}}{2iq_g}\int dx_1dz_1dx_2dz_2e^{-ik_gx_1}e^{iq_gx_1}V_1(x_1,z_1,x_2,z_2,\omega)e^{ikx_2}e^{iqz_2}\frac{1}{2iq}$$

$$*e^{-ikx_3}e^{iqz_3}V_{n-1}(x_3,z_3,x_4,z_4,\omega)P_0^d(x_4,z_4,k_s,\epsilon_s,\omega)dx_3dz_3dx_4dz_4$$

$$=-\frac{1}{2\pi}\int dk\frac{e^{-iq_g\epsilon_g}}{2iq_g}V_1(k_g,-q_g,-k,-q,\omega)\frac{1}{2iq}V_{n-1}(k,-q,x_4,z_4,\omega)$$

$$*P_0^d(x_4,z_4,k_s,\epsilon_s,\omega)dx_4dz_4 \quad (54)$$

Inserting two identities into equation 54 gives

$$D'_n(k_g,\epsilon_g,k_s,\epsilon_s,\omega) = -\frac{1}{2\pi}\int dk \frac{e^{-iq_g\epsilon_g}}{2iq_g} V_1(k_g,-q_g,-k,-q,\omega) \underbrace{\frac{e^{-iq\epsilon_s}}{2iq}\frac{2iq}{e^{-iq\epsilon_s}}}_{1}\frac{1}{2iq}$$

$$* \underbrace{\frac{2iq}{e^{-iq\epsilon_g}}\frac{e^{-iq\epsilon_g}}{2iq}}_{1} V_{n-1}(k,-q,x_4,z_4,\omega)P_0^d(x_4,z_4,k_s,\epsilon_s,\omega)dx_4dz_4$$

$$= -\frac{1}{2\pi}\int dk \underbrace{\frac{e^{-iq_g\epsilon_g}}{2iq_g}V_1(k_g,-q_g,-k,-q,\omega)\frac{e^{-iq\epsilon_s}}{2iq}}_{\frac{D'_1(k_g,\epsilon_g,k,\epsilon_s,\omega)}{\rho(k,\omega)}} \underbrace{\frac{2iq}{e^{-iq\epsilon_s}}\frac{1}{2iq}\frac{2iq}{e^{-iq\epsilon_g}}}_{2iqe^{iq(\epsilon_s+\epsilon_g)}}$$

$$* \underbrace{\frac{e^{-iq\epsilon_g}}{2iq}V_{n-1}(k,-q,x_4,z_4,\omega)P_0^d(x_4,z_4,k_s,\epsilon_s,\omega)dx_4dz_4}_{D'_{n-1}(k,\epsilon_g,k_s,\epsilon_s,\omega)}$$

$$= \frac{1}{i\pi}\int \frac{dk}{\rho(k,\omega)} D'_1(k_g,\epsilon_g,k,\epsilon_s,\omega)qe^{iq(\epsilon_s+\epsilon_g)}D'_{n-1}(k,\epsilon_g,k_s,\epsilon_s,\omega) \tag{55}$$

If the constant reference density ρ_0 is considered, equation 55 becomes

$$D'_n(k_g,\epsilon_g,k_s,\epsilon_s,\omega) = \frac{1}{i\pi\rho_0}\int \frac{dk}{\rho(k,\omega)} D'_1(k_g,\epsilon_g,k,\epsilon_s,\omega)qe^{iq(\epsilon_s+\epsilon_g)}D'_{n-1}(k,\epsilon_g,k_s,\epsilon_s,\omega) \tag{56}$$

where ρ_0 is the reference density, $\rho(k,\omega)$ is the angle dependent source signature. ϵ_s and ϵ_g are the depth of sources and receivers below the free surface. k_g, k_s and k are the Fourier conjugates of x_g, x_s and x, respectively. q is the obliquity factor $\sqrt{(\omega/c_0)^2 - k^2}$.

References

Araújo, F. V. *Linear and non-linear methods derived from scattering theory: backscattered tomography and internal multiple attenuation.* PhD thesis, Universidade Federal da Bahia, 1994.

Carvalho, P. M. *Free-surface multiple reflection elimination method based on nonlinear inversion of seismic data.* PhD thesis, Universidade Federal da Bahia, 1992.

Gassaway, G.S., R.A. Brown, and L.E. Bennett. "Pitfalls in seismic amplitude versus offset analysis: Case histories." *56th Annual SEG Meeting* (1986).

Loveridge, M.M., G.E. Parkes, L. Hatton, and M.H. Worthington. "Effects of marine source array directivity on seismic data and source signature deconvolution." *First Break* 2 (1984): 16–22.

Morse, P. M. and H. Feshbach. *Methods of theoretical physics.* McGraw-Hill Book Co., 1953.

Stolt, R. H. and A. B. Weglein. "Migration and inversion of seismic data." *Geophysics* 50 (1985): 2458–2472.

Weglein, A. B., F. V. Araújo, P. M. Carvalho, R. H. Stolt, K. H. Matson, R. T. Coates, D. Corrigan, D. J. Foster, S. A. Shaw, and H. Zhang. "Inverse Scattering Series and Seismic Exploration." *Inverse Problems* (2003): R27–R83.

Weglein, A. B., F. A. Gasparotto, P. M. Carvalho, and R. H. Stolt. "An Inverse-Scattering Series Method for Attenuating Multiples in Seismic Reflection Data." *Geophysics* 62 (November-December 1997): 1975–1989.

Weglein, Arthur B. and Bruce G. Secrest. "Wavelet estimation for a multidimensional acoustic earth model." *Geophysics* 55 (July 1990): 902–913.

Zhang, Jingfeng. *Wave theory based data preparation for inverse scattering multiple removal, depth imaging and parameter estimation: analysis and numerical tests of Green's theorem deghosting theory.* PhD thesis, University of Houston, 2007.

Short documentation on comparison of finite difference modeling and reflectivity modeling

X. Li, F. Liu and P. Terenghi

This is a short documentation for the group.

1 Background and motivation

Depth imaging using inverse scattering series for multi-parameter is a very important and challenging issue. Not only the imaging algorithm needs to include more terms to increase its capability and accommodate larger contrast, the AVO front end for imaging also needs attention. In previous reports, Li et al. (2009); Li and Weglein (2010) and Jiang et al. (2009) studied 1D multi-parameter depth imaging and showed results on acoustic and elastic case for analytic data. In this year's reports, Chang et al. (2011) discuss about the 1D two-parameter finite difference data test showing encouraging results. Because the calculation of AVO front end, $\alpha_1 - \beta_1$, is sensitive to the amplitude information of the events, it is important to estimate the quality of the modeled data for initial study. In this short note, data generated by the finite difference method and the reflectivity method (from D. Corrigan code) are qualitatively compared. The results show that data generated by the finite difference code does not correctly preserve polarity reversal information in reflection coefficient, while the reflectivity code generates more accurate data. This study is important to understand and to isolate issues produced from different steps in the perspective of the imaging goal.

2 Results

Reflectivity modeling (from D. Corrigan code) and finite difference modeling are compared on the same model. A simple three-layered model with two interfaces and no free surface is considered. The parameters are as follows: $\rho_0 = 1.0\ g/cm^3$, $c_0 = 1500\ m/s$, $\rho_1 = 1.1\ g/cm^3$, $c_1 = 1600\ m/s$, $\rho_2 = 1.5\ g/cm^3$, and $c_2 = 1200\ m/s$. The parameters are designed so that polarity reversal of the reflection coefficient from the second reflector is observable. A wavelet whose amplitude spectrum is a trapezoid with characteristic frequencies 0, 10, 60, 100 Hz is used in both cases. Modeling results using two-dimensional propagation ares chosen for comparison. For the reflectivity modeling code, the choice corresponding to use the appropriate entry in the parameter card. For the finite difference modeling code, a 2D Green's function must be used to generate the starting wavefields which are further propagated using a 2D discretization scheme.

2.1 Reflectivity modeling

Figure 1 shows data generated from reflectivity code in (x,t) domain. The polarity reversal information of the second primary is what should be observed in the data. In Figure 2 we can see that at some point the polarity changes sign (at about $x \approx 500$ m). Figure 3 and 4 show the corresponding reflectivity data in (τ, θ) domain. Again the polarity reversal information shows up clearly.

2.2 Finite difference modeling

Figure 3 shows data generated from finite difference code in (x,t) domain for the same model. As mentioned previously, polarity reversal in the second primary is expected. However, from the enlarged Figure 4, it is not as clear as in the reflectivity data. The wave form has smoothly changed around the point of polarity reversal without ever reaching a zero. Figure 7 and Figure 8 show the corresponding finite difference data in (τ, θ) domain.

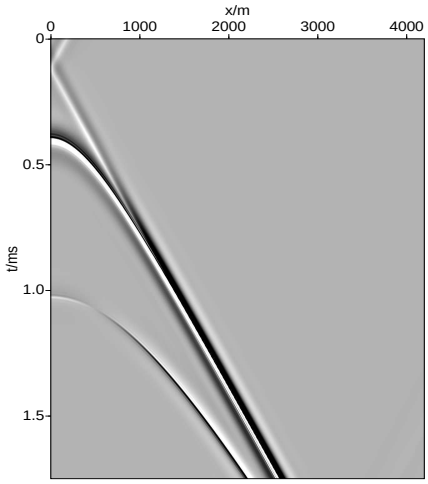

Figure 1: Reflectivity data in (x,t) domain.

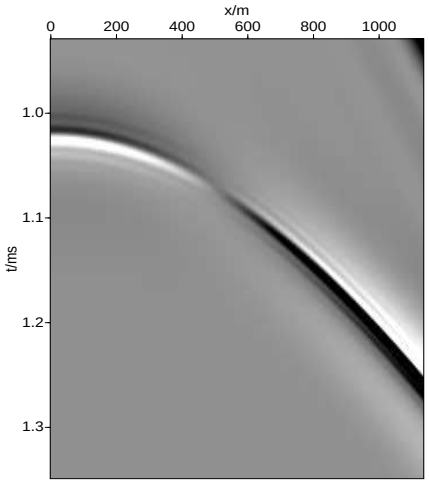

Figure 2: Enlarged second event from Figure 1.

3 Conclusions

This short note mainly focused on comparing the data generated by finite difference modeling and reflectivity modeling. In terms of modeling the polarity reversal information, finite difference modeling is not as accurate as reflectivity modeling.

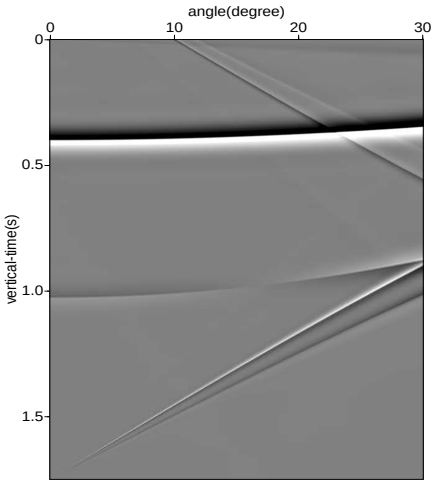

Figure 3: Reflectivity data in (τ, θ) domain.

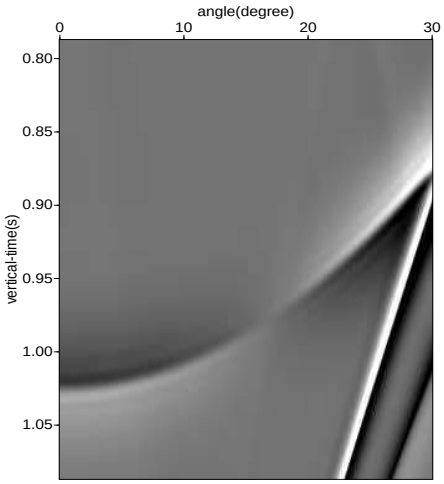

Figure 4: Enlarged second event from Figure 3.

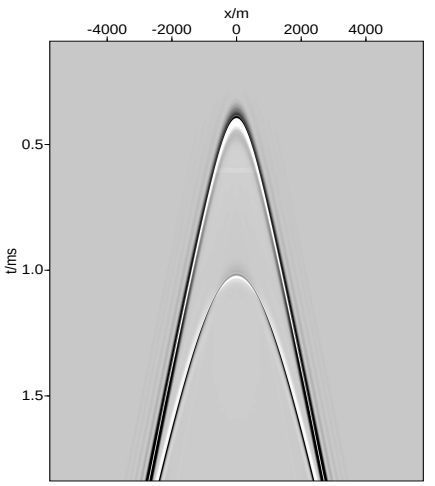

Figure 5: Finite difference data in (x,t) domain

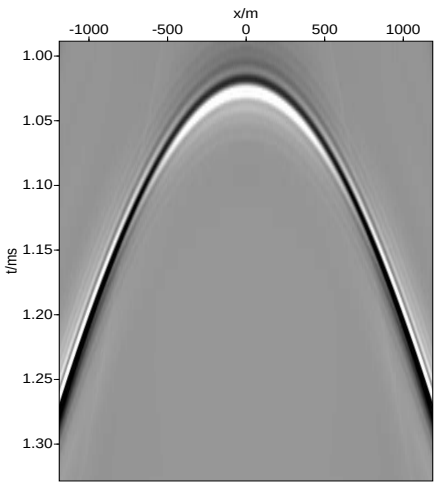

Figure 6: Enlarged second event from Figure 3

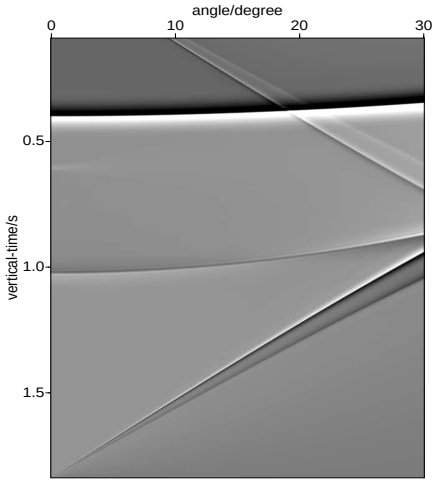

Figure 7: Finite difference data in (τ, θ) domain.

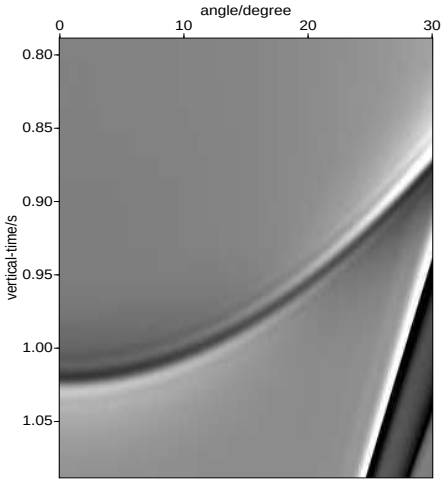

Figure 8: Enlarged second event from Figure 7.

References

Chang, D., A. B. Weglein, and F. Liu. "Developing multi-dimensional depth imaging with a velocity and density varying earth." *2010 M-OSRP Annual Report* (2011).

Jiang, S., A. B. Weglein, and S. A. Shaw. "Progressing multiparameter imaging using the inverse scattering series: An initial analytic test of the leading order imaging subseries (LOIS) closed form and its extended higher order imaging subseries (HOIS) closed form for a laterally invariant two-parameter acoustic medium." *2008 M-OSRP Annual Report* (2009): 91–113.

Li, X., F. Liu, S. Jiang, and A. B. Weglein. "Depth imaging without the velocity cares about the phase and amplitude information of events: Focusing on the use of the angle dependent amplitude information of events." *2008 M-OSRP Annual Report* (2009): 114–128.

Li, X. and A. B. Weglein. "An unanticipated and immediate AVO by-product (responding to pressing type 1 and type 2 AVO challenges) delivered within the ISS imaging program." *2009 M-OSRP Annual Report* (2010).

Short documentation on true-amplitude reflectivity modeling

X. Li

This short note explains how the D. Corrigan reflectivity modeling code should be used for the purpose of testing and analyzing the inverse scattering series (ISS) imaging algorithm. Starting from perfect analytic data make it possible to understand and isolate issues produced by different processing steps. Since the reflectivity method can provide true amplitude synthetic data, it is important to use it correctly to serve the ISS imaging tests. This short note documents items that are crucial for getting accurate synthetic data in the (τ, p) domain. An example illustrates how missing low frequencies make the true-amplitude information less accessible to immediate interpretation.

1 How to compile the code

Under the directory of /home/xli12/pdcorrigan, there are five folders: bin (which has the executable programs), models (which has the parameter input card where you can set up your own model, and there is detailed documentation on each of the choices), obj, lib (the utility libraries) and src (the source codes). There are several *makefiles* for compiling the code (look up the command *make* for more detailed description). First, compile those that generate utility libraries (under src folder, there are four folders: mathadv, segylib, slib and ulib, and each of them has a *makefile*). After the utility libraries are ready, go to the main code folder (src/acoustic or src/acoustic-taup) to compile it. Keep in mind that this code is supposed to be compiled using g77, or else there will be some errors. (For example, when compiling on isis machine, we need to first type the following command: export F77=gfortran.)

2 Remarks on using the parameter card

There are some key items when using acoustic-taup code to generate data. (Refer to Figure 6 for an example of the parameter card. Detailed description of every item is in the original documentation).

- On card #4, which defines the frequency range, when putting a low cut frequency=0, the code will give us NAN values. If a full bandwidth box-like dataset is desired, experience shows that the low cut value has to be smaller than $0.01Hz$.
- On card #7, which defines parameters for each layer, the velocity of the last layer in the model should always be $1500m/s$[1].

[1] This has no physical meaning, just a remark for the code to run correctly.

- According to the documentation titled *Calibrated acoustic modeling*, the output data $O(\tau, p)$ generated from this program is $O(\tau, p) = \frac{[R.C.]}{2*\sqrt{1-c_0^2 p^2}}$, where $[R.C.]$ represents the reflection coefficient. In order to have the reflection coefficient for ISS imaging tests, a rescaling process is needed.

  Taking the above items into consideration, let's look at an example. The model features: a four-layered earth with a constant density profile $\rho = 1.0 g/cm^3$, and a variable velocity profile $c_0 = 1500 m/s$, $c_1 = 1800 m/s$, $c_2 = 2000 m/s$ and $c_3 = 1500 m/s$. First, choose a frequency range (in the 4th row of the parameter card) as $(F_1, F_2, F_3, F_4) = (0.0001, 0.0001, 60, 85) Hz$.

- A closer look at the output data $O(\tau, p)$, e.g., in Figure 1, shows that the trace for $p = 0$ is plotted, above the first reflector (in this case, $z = 400m$), and the amplitude of the data should be zero. This figure reveals that there is a non-zero value in the data above the first reflector. A simple calculation proves that the amplitude has shifted away from its true value by that amount. So when outputting reflection coefficients, it is necessary to compensate for this error by subtracting the bias given by the computed amplitude above the first reflector.

  Keeping this correction in mind, the next step is to compare data generated for different frequency range to get an approximate idea of how the data will be affected.

- The frequency range is $(F_1, F_2, F_3, F_4) = (0.0001, 0.0001, 60, 85) Hz$ for data in Figure 2 and $(F_1, F_2, F_3, F_4) = (0.1, 0.1, 60, 85) Hz$ for data in Figure 3. The low cut and low pass frequencies are the only difference. Figure 4 and 5 shows the corresponding traces in each case for $p = 0$. Here is where the amplitude issues mentioned above are corrected. From these two detailed traces, notice that amplitude of the generated data is greatly affected by missing the low frequency information.

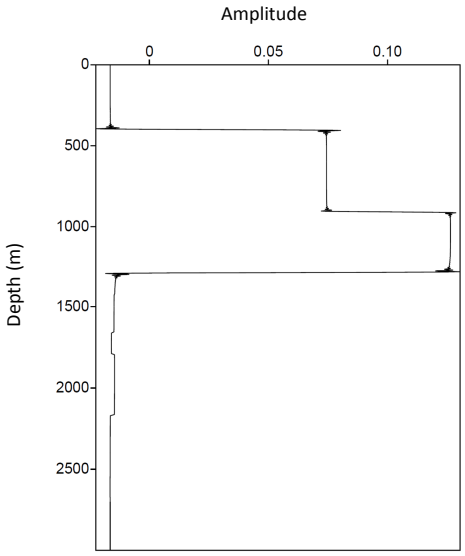

Figure 1: Data generated for the four-layered model using reflectivity data. Full bandwidth box-like data are obtained. The trace for $p = 0$ is plotted in this Figure. Note that there is a bias in the amplitude.

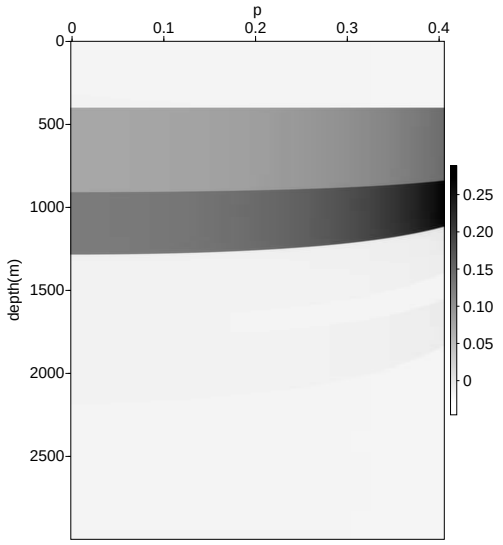

Figure 2: Reflectivity data for frequency range in $(F_1, F_2, F_3, F_4) = (0.0001, 0.0001, 60, 85)Hz$.

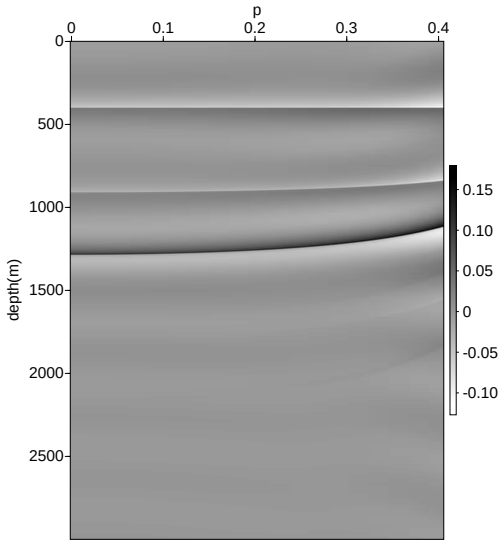

Figure 3: Reflectivity data for frequency range in $(F_1, F_2, F_3, F_4) = (0.1, 0.1, 60, 85)Hz$.

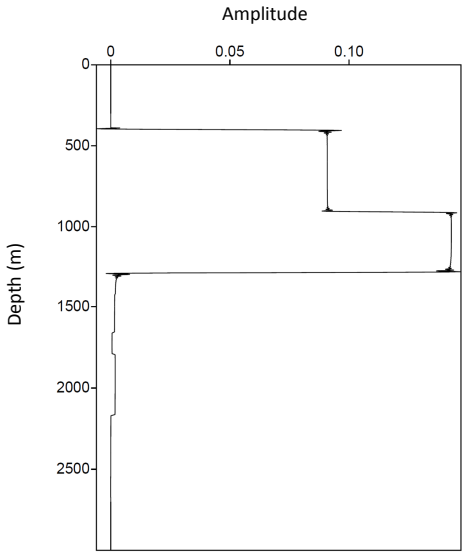

Figure 4: A trace for $p = 0$ is plotted from Figure 2.

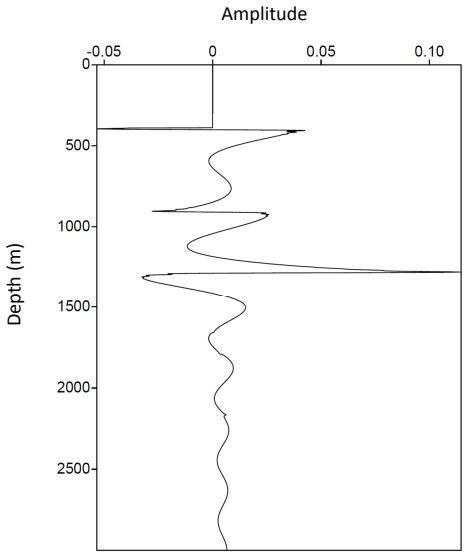

Figure 5: A trace for $p = 0$ is plotted from Figure 3. Compared with Figure 4, notice the significant change in the amplitude.

```
U          N     /home/xli12/pdcorrigan/models/acoustic_taup/xuli01.trc
ustic model for Xu
      0         1        10        10         0         3
0.00001   0.00001        60        85
      1      5000         0        20        51
      4      1480       250         5
   1500                    1      1200                 410
   1800                    1      1200                 610
   2000                    1      1200                 500
   1500                    1      1200
-+----1----+----2----+----3----+----4----+----5----+----6
```

Figure 6: Example of the parameter card. Refer to the original documentation for detailed parameter description.

REVERSE TIME MIGRATION AND GREEN'S THEOREM: PART I - THE EVOLUTION OF CONCEPTS, AND SETTING THE STAGE FOR THE NEW RTM METHOD

A.B. WEGLEIN[1], R.H. STOLT[2] and J.D. MAYHAN[1]

[1] *M-OSRP, University of Houston, 617 Science & Research Bldg. 1, Houston, TX 77004, U.S.A.*
[2] *ConocoPhillips, 600 North Dairy Ashford Road, Houston, TX 77079, U.S.A.*

(Received June 23, 2010; revised version accepted December 17, 2010)

ABSTRACT

Weglein, A.B., Stolt, R.H. and Mayhan, J.D., 2011. Reverse time migration and Green's theorem: Part I - the evolution of concepts, and setting the stage for the new RTM method. *Journal of Seismic Exploration*, 20: 73-90.

In this paper, part I of a two paper set, we describe the evolution of Green's theorem based concepts and methods for downward continuation and migration. This forms the foundation and context for developing Green's theorem reverse time migration (RTM), in part II. We present the evolution of seismic exploration wave-field prediction models, as steps towards more completeness, consistency, realism and predictive effectiveness. Using simple and accessible analytic examples, we describe the difference between the need for subsurface information when the goal is a structure map, and contrast that with the case when the goal is both an accurate depth image and subsequent amplitude analysis at depth, that is, between migration and migration-inversion. The relationship between Green's theorem and the Lippmann Schwinger equation of scattering theory is used to help define the need behind the evolution of Green's theorem concepts and developments in seismic imaging, as well as to provide a new insight for classic results like, e.g., the Sommerfeld radiation condition. This paper provides a platform and detailed background for the second of this two paper set, where part II provides a new and consistent theory and method for RTM.

KEY WORDS: reverse time migration, Green's theorem, two way wave-field prediction.

0963-0651/11/$5.00

INTRODUCTION

An important and central concept resides behind all current seismic processing methods that seek to extract useful subsurface information from recorded seismic data. That concept has two ingredients: (1) from the recorded surface seismic experiment and data, to predict what an experiment with a source and receiver at depth would record, and (2) exploiting the fact that a coincident source receiver experiment at depth, would, for small recording times, be an indicator of only local property changes at the coincident source-receiver position. These two ingredients, a wave-field prediction, and an imaging condition, reside behind all current leading edge seismic migration algorithms. The ultimate purpose of this two paper set is to advance our understanding, and provide concepts and new algorithms for the first of these two components: subsurface wave-field prediction from surface wave-field measurements. An accurate velocity model is required for this procedure to deliver an accurate structure map of boundaries in the subsurface where rapid changes in physical properties occur.

OVERBURDEN INFORMATION FOR MIGRATION AND MIGRATION-INVERSION

In this paper, we show how to formulate and apply Green's theorem in an appropriate manner for one-way propagating waves. We begin with a simple discussion of back propagating waves and imaging to illustrate how the type of a-priori information needed *above* a target reflector depends on our goal and level of information extraction, e.g., about the location of and changes in physical properties across the target reflector. We show that only the velocity model above the reflector is needed to simply locate the reflector; whereas, *all* properties above the reflector are required if we want to determine both where any property has changed (structure imaging or migration) and *what* specific property has changed at the imaged reflector and by what amount (migration-inversion).

We begin by exemplifying how all traditional linear backpropagation methods for predicting waves at depth from surface reflection data need different types and degrees of a-priori overburden subsurface information for different levels of ambition for subsurface target information extraction: migration versus migration-inversion. In traditional seismic processing, the spatial location of reflectors (migration) is determined by the velocity above the reflector while parameter estimation requires all properties above the depth image where changes in earth mechanical properties are to be determined. A very simple illustration of this idea can be obtained by using a 1D normal incidence experiment using the model shown in Fig. 1, where z_{ms} represents the depth of the source and receiver, and the depth of the first reflector is z_1, and

the second reflector's depth is z_2, and z_2 is the location to be determined. The recorded data, D(t), the wave-field at the coincident source and receiver position chosen as $z_{ms} = 0$, is given by

$$D(t,z_m=0) = R_1\delta(t - 2t_1) + R_2'\delta(t - 2t_2) \quad , \tag{1}$$

where $R_1 = R_{01}$ represents the reflection coefficient at the boundary between the first and second media, and $R_2' = T_{01}R_{12}T_{10}$ represents the amplitude of the second event and is the composite transmission and reflection coefficient in the second medium. The two-way travel times for the first and second events are given by $2t_1$ and $2t_2$, respectively. Fourier transforming (1) gives

$$D(\omega,z_m=0) = R_1e^{2i\omega t_1} + R_2'e^{2i\omega t_2} \quad , \tag{2}$$

where the first term on the right hand side is the primary from the first reflector (at $z = z_1$) and the second term is the primary from the second reflector (at $z = z_2$).

The next step is to locate the depth of the second reflector using the recorded data. To do so, we will call upon the simple solutions to the wave equation governing wave propagation in homogeneous media. In this example, that allows us to backpropagate separately the source and the receiver down reversing the actual propagation paths of the recorded upgoing waves. This step is known as downward continuation. Because, in traditional migration we assume that we know the velocity model above each reflector to be imaged, we will treat each primary separately, thus we write (2) as

$$D(\omega,z_{ms}=0) = D_1(\omega,z_{ms}=0) + D_2(\omega,z_{ms}=0) \quad . \tag{3}$$

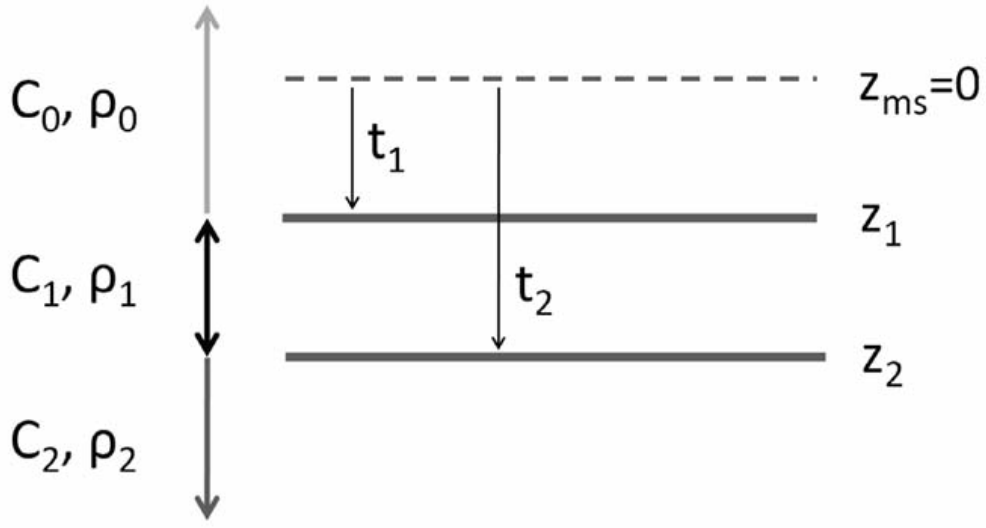

Fig. 1. Zero-offset model. The velocity is denoted by c, and the density by ρ.

The source and receiver corresponding to the first primary,

$$D_1(\omega,z_{ms}=0) = R_1 e^{2i\omega t_1} \quad , \tag{4}$$

are downward continued in the first medium (above the shallower reflector at z_1), giving

$$D_1(\omega,z) = R_1 e^{2i\omega t_1} e^{-2i(\omega/c_0)t} \quad . \tag{5}$$

In the downward continuation for the first primary, we use the medium properties (c_0,ρ_0) above that first reflector and the equation

$$[(d^2/dz^2) + (\omega^2/c_0^2)]D(\omega,z) = 0 \quad , \tag{6}$$

and, hence, the receiver and the source each contribute a factor of $e^{-i(\omega/c_0)z}$.

The solution in (5) simulates a coincident source and receiver reflection experiment at depth z. A non zero value of this coincident source and receiver experiment at depth at $t = 0^+$ indicates a reflector just below the coincident point in the medium. Hence, the next step in our example locates the reflectors by applying the imaging condition at $t = 0$ to the downward continued data. The latter is realized by integrating over all frequencies $\int d\omega D_1(\omega,z)$; in other words, we do an inverse Fourier transform evaluating the time in the exponential of the Fourier kernel with $t = 0$. Thus, we obtain

$$D_1(t=0,z) = R_1\delta(2t_1 - 2z/c_0) \quad , \tag{7}$$

corresponding to an image at $z = c_0t_1$ at the depth of the first reflector. The second primary,

$$D_2(\omega,z_{ms}=0) = R_2' e^{2i\omega t_2} \quad , \tag{8}$$

is downward continued in the medium above the first reflector using the path of an upgoing wave satisfying the differential equation (6) and for the medium between the first and second reflector the equation used is

$$[(d^2/dz^2) + (\omega^2/c_1^2)]D(\omega,z) = 0 \quad , \tag{9}$$

which relates to the properties of the medium between z_1 and z_2. Therefore, taking the source and receiver to depth z in the medium below the first reflector

$$\begin{aligned} D_2(\omega,z) &= D_2(\omega,z_{ms}=0)e^{-i(2\omega/c_0)z_1} e^{-i(2\omega/c_1)(z-z_1)} \\ &= R_2' e^{2i\omega t_2} e^{-i(2\omega/c_0)z_1} e^{-i(2\omega/c_1)(z-z_1)} \quad , \end{aligned} \tag{10}$$

and applying the imaging condition gives

$$D_2(t=0,z) = R_2'\delta[2t_2 - (2z_1/c_0) - (2/c_1)(z - z_1)] \quad . \tag{11}$$

The second primary images at $z = z_1 + c_1(t_2 - t_1)$, the depth of the second reflector, z_2. Therefore the location depends only on the velocity above each reflector (and not on the density).

However, to determine changes in mechanical properties across each reflector requires the reflection coefficients R_1 and R_{12} and the removal of $T_{01}T_{10}$ from R_2' to determine R_{12} where $R_2' = T_{01}R_{12}T_{10}$. To remove T_{01} and T_{10} we must know the changes in velocity and density at the first reflector. In other words, determining material property changes across each reflector requires the velocity and density (and absorption and all other property changes) above these two reflectors. The latter amplitude issue can be viewed as a consequence of the properties of the R's and T's which come from continuity conditions (note: the pressure and its normal derivative are not continuous when the density *and* velocity change across a boundary). If the latter continuity of pressure and its normal derivative were the case, then amplitude would only care about velocity changes, in this simple acoustic example. To determine the amplitude of a reflection coefficient at depth requires knowledge of *all* material properties above the reflector and not only velocity. That's worth keeping in mind for those pursuing/promoting 'true amplitude' migration, especially if non linear target identification is the ultimate goal. The general property of wave-field amplitude at depth from surface measurements follows from Green's theorem, where all medium properties are needed to provide the Green's functions in the medium, and necessary for determining the wave-field at depth.

OVERVIEW ON THE EVOLUTION OF MIGRATION CONCEPTS AND GOALS: FROM NMO-STACK TO AVO AND MIGRATION TO MIGRATION-INVERSION, THE UNCOLLAPSED MIGRATION CONCEPT

As with all useful concepts, seismic migration has evolved and adapted to deal with ever more realistic and complex media and to allow higher and more ambitious goals for the imaged amplitudes. In seismic processing history the 'determine where anything changed' structure/migration people and their ideas/methods typically progressed totally independent from the 'what specifically changed' AVO people and their theories and methods. The AVO theorists and practitioners were never too concerned with locating the position in the earth of earth boundary changes, but rather focused on what specifically in detail was changing somewhere, and the migration people were not too interested in what was actually changing, after it was determined that something was changing at a point in the subsurface. Further, AVO people assumed a simple 1D earth and asked difficult, complex, detailed questions; while the

structure seeking migration people assumed a complex multi-D earth and asked a less ambitious structure question 'where did anything change?' In the 1D world, NMO-stack evolved into AVO and multi-D migration evolved and was generalized into migration-inversion.

The two ingredients within wave equation migration are a backpropagation of waves and an imaging condition, where the latter imaging condition enables the backpropagated waves to be used to locate and delineate reflectors. The uncollapsed migration imaging principle introduced by Stolt, Clayton, and Weglein in the mid-1980's (Clayton and Stolt, 1981; Stolt and Weglein, 1985; Weglein and Stolt, 1999) extended and generalized the earlier Claerbout coincident source and receiver at depth at time equals zero imaging condition. That earlier Claerbout principle imaging condition was aimed at producing a structure map. This paper advances the propagation component theory of the propagation-imaging principle duet and incorporates the Stolt-Clayton-Weglein uncollapsed migration imaging condition. That uncollapsed imaging condition remains the high water mark of imaging conditions today, allowing automatic amplitude analysis at depth with respect to the normal of the imaged reflector, or imaging and inverting a point diffractor. We will not progress the imaging condition in this two paper set. That uncollapsed migration time equals zero but non-coincident, (but proximal, by causality) source and receiver imaging condition has been reinvented (and sometimes relabeled), by among others Berkhout and Wapenaar (1988), de Bruin et al. (1990a,b), Sava and Fomel (2006), and Sava and Vasconcelos (2009). Among recent contributions that have progressed seismic imaging conditions are: Vasconcelos et al. (2010), Sava and Vasconcelos (2010), and Douma et al. (2010).

We begin by discussing the history and evolution of models for the volume beneath the measurement surface within which we backpropagate surface reflection data.

THE INFINITE HEMISPHERICAL MIGRATION MODEL

The earliest wave equation migration pioneers viewed the backpropagation region as an infinite hemispherical half space with known mechanical properties, whose upper plane surface corresponded to the measurement surface, as in, e.g., Schneider (1978) and Stolt (1978). See Fig. 2.

There are several problems with the infinite hemispherical migration model. That model assumes: (1) that all subsurface properties beneath the measurement surface (MS) are known, and (2) that an anticausal Green's function (e.g., Schneider, 1978), with a Dirichlet boundary condition on the measurement surface, would allow measurements (MS) of the wave-field, P, on the upper plane surface of the hemisphere to determine the value of P within the

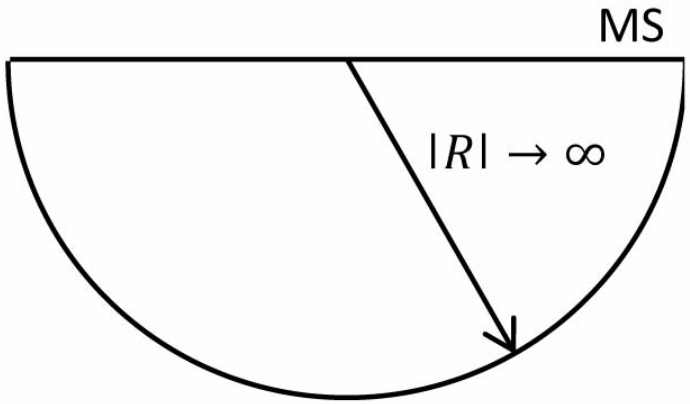

Fig. 2. The infinite hemispherical migration model. The measurement surface is denoted by MS.

hemispherical volume, V. The first assumption leads to the contradiction that we have not allowed for anything that is unknown to be determined in our model, since everything within the closed and infinite hemisphere is assumed to be known. Within the infinite hemispherical model there is nothing and/or nowhere below the measurement surface where an unknown scattering point or reflection surface can serve to produce reflection data whose generating reflectors are initially unknown and being sought by the migration process.

The second assumption, in early infinite hemispherical wave equation migration, assumes that Green's theorem with wave-field measurements on the upper plane surface and using an anticausal Green's function satisfying a Dirichlet boundary condition can determine the wave-field within V.

That conclusion assumes that the contribution from the lower hemispherical surface of S vanishes as the radius of the hemisphere goes to infinity. That is not the case, as we explicitly demonstrate below. To examine the various large radius hemispherical surface contributions to Green's theorem wave prediction in a volume, it is instructive to review the relationship between Green's theorem and the Lippmann-Schwinger scattering equation.

GREEN'S THEOREM REVIEW (THE LIPPMANN-SCHWINGER EQUATION AND GREEN'S THEOREM)

We begin with a space and time domain Green's theorem. Consider two wave-fields P and G_0 that satisfy

$$[\nabla^2 - (1/c^2)\partial_t^2]P(\mathbf{r},t) = \rho(\mathbf{r},t) \quad , \tag{12}$$

and

$$[\nabla^2 - (1/c^2)\partial_t^2]G_0(\mathbf{r},t,\mathbf{r}',t') = \delta(\mathbf{r} - \mathbf{r}')\delta(t - t') \quad , \tag{13}$$

where we assume 3D wave propagation and the wave-field velocity c is a constant. ρ is a general source, i.e., it represents both active sources (air guns, dynamite, vibrator trucks) and passive sources (heterogeneities in the earth). The causal solution to (12) can be written as

$$P(\mathbf{r},t) = \int_{-\infty}^{t^+} dt' \int_{\infty} d\mathbf{r}'\rho(\mathbf{r}',t')G_0^+(\mathbf{r},t,\mathbf{r}',t') \quad , \tag{14}$$

where G_0^+ is the causal whole space solution to (13). The integral from t^+ to ∞ is zero due to the causality of G_0^+. Eq. (14) represents the linear superposition of causal solutions G_0^+ with weights $\rho(\mathbf{r}',t')$ summing to produce the physical causal wave-field solution to (12). Eq. (14) is called the scattering equation and represents an all space and all time causal solution for $P(\mathbf{r},t)$. It explicitly includes all sources and produces the field at all points of space and time. No additional boundary or initial conditions are required in (14).

Now consider the integral

$$\int_0^{t^+} dt' \int_V d\mathbf{r}'(P\nabla'^2G_0 - G_0\nabla'^2P) = \int_0^{t^+} dt' \int_V d\mathbf{r}'\nabla'\cdot(P\nabla'G_0 - G_0\nabla'P) \quad , \tag{15}$$

and we rewrite (15) using Green's theorem

$$\int_0^{t^+} dt' \int_V d\mathbf{r}'\nabla'\cdot(P\nabla'G_0 - G_0\nabla'P) = \int_0^{t^+} dt' \int_S dS'\hat{n}\cdot(P\nabla'G_0 - G_0\nabla'P) \quad . \tag{16}$$

This is essentially an identity, within the assumptions on functions and surfaces, needed to derive Green's theorem. Now choose $P = P(\mathbf{r}',t')$ and $G_0 = G_0(\mathbf{r},t,\mathbf{r}',t')$ from (12) and (13). Then replace ∇'^2P and ∇'^2G_0 from the differential eqs. (12) and (13).

$$\nabla'^2G_0 = (1/c^2)\partial_t'^2G_0 + \delta(\mathbf{r} - \mathbf{r}')\delta(t - t') \quad , \tag{17}$$

$$\nabla'^2P = (1/c^2)\partial_t'^2P + \rho(\mathbf{r}',t') \quad , \tag{18}$$

and assume that the out variables $(\mathbf{r},t)$ are in the intervals of integration: $\mathbf{r}$ in V, $t > 0$. The left hand side of (15) becomes:

$$\int_0^{t^+} dt' \int_V d\mathbf{r}'(1/c^2)(P\partial_{t'}^2G_0 - G_0\partial_{t'}^2P) + P(\mathbf{r},t)$$

$$- \int_0^{t^+} dt' \int_V d\mathbf{r}'\rho(\mathbf{r},t)G_0(\mathbf{r},t,\mathbf{r}',t') \ . \tag{19}$$

The expression inside the first set of parentheses is a perfect derivative $\partial_{t'}(P\partial_{t'}G_0 - G_0\partial_{t'}P)$ integrated over t'. The result is (for $\mathbf{r}$ in V and $t > 0$)

$$\begin{aligned} P(\mathbf{r},t) = & \int_V d\mathbf{r}' \int_0^{t^+} dt'\rho(\mathbf{r}',t')G_0(\mathbf{r},t,\mathbf{r}',t') \\ & - (1/c^2)\Big|_{t'=0}^{t^+} \int_V d\mathbf{r}'(P\partial_{t'}G_0 - G_0\partial_{t'}P) \\ & + \int_0^{t^+} dt' \int_S dS'\hat{n}\cdot(P\nabla'G_0 - G_0\nabla'P) \ . \end{aligned} \tag{20}$$

We assumed differential eqs. (17) and (18) in deriving (20) and G_0 can be *any* solution of (17) in the space and time integrals in (15), causal, anticausal, or neither. Each term on the right hand side of (20) will differ with different choices of G_0, but the sum of the three terms will always be the same, $P(\mathbf{r},t)$.

If we now choose G_0 to be causal ($= G_0^+$) in (20), then in the second term on the right hand side the upper limit gives zero because G_0^+ and $\partial_{t'}G_0^+$ are zero at $t' = t^+$. The causality of G_0^+ and $\partial_{t'}G_0^+$ causes only the lower limit $t' = 0$ to contribute in

$$- (1/c^2)\Big|_{t'=0}^{t^+} \int_V d\mathbf{r}'(P\partial_{t'}G_0^+ - G_0^+\partial_{t'}P) \ . \tag{21}$$

If we let the space and time limits in (20) both become unbounded, i.e., $V \to \infty$ and the t' interval becomes $[-\infty,0]$, and choose $G_0 = G_0^+$, the whole space causal Green's function, then by comparing (14) and (20) we see that for $\mathbf{r}$ in V and $t > 0$ that

$$\begin{aligned} & \int_{-\infty}^{t^+} dt' \int_S dS'\hat{n}\cdot(P\nabla'G_0^+ - G_0^+\nabla'P) \\ & - (1/c^2)\Big|_{-\infty}^{t^+} \int_\infty d\mathbf{r}'(P\partial_{t'}G_0^+ - G_0^+\partial_{t'}P) = 0 \ . \end{aligned} \tag{22}$$

$V = \infty$ means a volume that spans all space, and $\infty - V$ means all points in ∞ that are outside the volume V . For $\mathbf{r}$ in ∞ and any time t from (14) we get

$$P(\mathbf{r},t) = \int_V d\mathbf{r}' \int_0^{t^+} dt' \rho(\mathbf{r}',t') G_0^+(\mathbf{r},t,\mathbf{r}',t')$$

$$+ \int_{\infty - V} d\mathbf{r}' \int_0^{t^+} dt' \rho(\mathbf{r}',t') G_0^+(\mathbf{r},t,\mathbf{r}',t')$$

$$+ \int_V d\mathbf{r}' \int_{-\infty}^{0} dt' \rho(\mathbf{r}',t') G_0^+(\mathbf{r},t,\mathbf{r}',t')$$

$$+ \int_{\infty - V} d\mathbf{r}' \int_{-\infty}^{0} dt' \rho(\mathbf{r}',t') G_0^+(\mathbf{r},t,\mathbf{r}',t') \quad . \tag{23}$$

This equation holds for any $\mathbf{r}$ and any t.

For $\mathbf{r}$ in V and $t > 0$ (23) and (20) must agree and

$$- (1/c^2) \Big|_0^{t^+} \int_V d\mathbf{r}' (P \partial_{t'} G_0^+ - G_0^+ \partial_{t'} P)$$

$$= \int_V d\mathbf{r}' \int_{-\infty}^{0} dt' \rho(\mathbf{r}',t') G_0^+(\mathbf{r},t,\mathbf{r}',t')$$

$$+ \int_{\infty - V} d\mathbf{r}' \int_{-\infty}^{0} dt' \rho(\mathbf{r}',t') G_0^+(\mathbf{r},t,\mathbf{r}',t') \quad , \tag{24}$$

and

$$\int_0^{t^+} dt' \int_S dS' \hat{n} \cdot (P \nabla' G_0 - G_0 \nabla' P)$$

$$= \int_{\infty - V} d\mathbf{r}' \int_0^{t^+} dt' \rho(\mathbf{r}',t') G_0^+(\mathbf{r},t,\mathbf{r}',t') \quad . \tag{25}$$

The solution for $P(\mathbf{r},t)$ in (20) expresses the fact that if all of the factors that both create the wave-field (active sources) and that subsequently influence the wave-field (passive sources, e.g., heterogeneities in the medium) are explicitly included in the solution as in (20), then the causal solution is provided explicitly and linearly in terms of those sources, as a weighted sum of causal solutions, and no surface, boundary or initial conditions are necessary or required.

From (24) and (25) the role of boundary and initial conditions are clear. The contributions to the wave-field, P, at a point $\mathbf{r}$ in V and at a time, t in $[0,t^+]$ derives from three contributions: (1) a causal superposition over the

sources within the volume V during the interval of time, say $[0,t^+]$ and (2) initial conditions of P and P_t over the volume V, providing all contributions due to sources earlier than time $t' = 0$, both inside and outside V, to the solution in V during [0,t] and (3) a surface integral, enclosing V, integrated from $t' = 0$ to t^+ that gives the contribution from sources outside V during the time $[0,t^+]$ to the field, P, in V for times $[0,t^+]$. Succinctly stated, initial conditions provide contributions from sources at earlier times and surface/boundary conditions provide contributions from outside the spatial volume to the field in the volume during the [0,t] time interval. If all sources for all space and all time are explicitly included as in (14), then there is no need for boundary or initial conditions to produce the physical/causal solution derived from a linear superposition of elementary causal solutions.

On the other hand, if we seek to find a physical causal solution for P in terms of a linear superposition of anticausal solutions, as we can arrange by choosing $G_0 = G_0^-$ in (20), then the initial and surface integrals do *not* vanish when we let $V \to \infty$ and $[0,t] \to [-\infty,t]$. The vanishing of the surface integral contribution (as the radius of the surface $\to \infty$) to P with the choice $G_0 = G_0^+$ is called the Sommerfeld radiation condition, and is readily understood by the comparison with (14).

In the $(\mathbf{r},\omega)$ domain (12) and (13) become

$$(\nabla^2 + k^2)P(\mathbf{r},\omega) = \rho(\mathbf{r},\omega) \quad , \tag{26}$$

$$(\nabla^2 + k^2)G_0(\mathbf{r},\mathbf{r}',\omega) = \delta(\mathbf{r} - \mathbf{r}') \quad , \tag{27}$$

and the causal all space and time solution analogous to (14) is

$$P(\mathbf{r},\omega) = \int_\infty d\mathbf{r}'\rho(\mathbf{r}',\omega)G_0^+(\mathbf{r},\mathbf{r}',\omega) \quad , \tag{28}$$

and Green's second identity is

$$\int_V d\mathbf{r}'(P\nabla'^2G_0 - G_0\nabla'^2P) = \oint_S dS'\hat{n}\cdot(P\nabla'G_0 - G_0\nabla'P) \quad . \tag{29}$$

Substituting $\nabla^2G_0 = -k^2G_0 + \delta$ and $\nabla^2P = -k^2P + \rho$ in Green's theorem where $\int_{-\infty}^{\infty} P(\mathbf{r},t)e^{i\omega t}dt = P(\mathbf{r},\omega)$ we find

$$\int_V d\mathbf{r}'P(\mathbf{r}',\omega)\delta(\mathbf{r} - \mathbf{r}') = \int_V d\mathbf{r}'\rho(\mathbf{r}',\omega)G_0(\mathbf{r},\mathbf{r}',\omega) + \oint_S dS'\hat{n}\cdot(P\nabla'G_0 - G_0\nabla'P) \quad , \tag{30}$$

if $\mathbf{r}$ in V. There are no initial conditions, since in $\mathbf{r},\omega$ we have already explicitly included *all* time in Fourier transforming from t to ω. All times of sources are included in the $(\mathbf{r},\omega)$ domain. In $\mathbf{r},\omega$ the issue is whether sources are inside or outside V. The Lippmann-Schwinger equation (28) provides the causal physical P for all $\mathbf{r}$. Eq. (28) is the $\mathbf{r},\omega$ version of (14) and must choose $G_0 = G_0^+$ (causal) to have P as the physical solution built from superposition and linearity. In contrast, (30) [as in (20)] will produce the physical solution, P, with *any* solution for G_0 that satisfies (27).

Eq. (28) can be written as:

$$\int_V \rho G_0^+ + \int_{\infty - V} \rho G_0^+ \quad . \tag{31}$$

For $\mathbf{r}$ in V the second term on the right hand side of (30) (with $G_0 = G_0^+$) equals the second term in (31), i.e.,

$$\int_{\infty - V} d\mathbf{r}' \rho G_0^+ = \oint_S dS' \hat{n} \cdot (P \nabla' G_0^+ - G_0^+ \nabla' P) \quad . \tag{32}$$

Thus, the first term in (31) gives contribution to P, for $\mathbf{r}$ in V due to sources in V, and the second term in (31) gives contribution to P, for $\mathbf{r}$ in V due to sources not in V. With $G_0 = G_0^+$

$$\oint_S dS' \hat{n} \cdot (P \nabla' G_0^+ - G_0^+ \nabla' P) \quad , \tag{33}$$

provides the contribution to the field, P, inside V due to sources outside the volume V.

What about the large $|\mathbf{r}|$ contribution of the surface integral to the field inside the volume? We use Green's theorem to predict that the contribution to the physical/causal solution P in V from the surface integral in Green's theorem, in general, and also

$$\oint_S \{P(\partial G_0^+ / \partial n) - G_0^+ (\partial P / \partial n)\} dS \quad , \tag{34}$$

vanishes as $|\mathbf{r}| \to \infty$ and in contrast the contribution to P in V from

$$\oint_S \{P(\partial G_0^- / \partial n) - G_0^- (\partial P / \partial n)\} dS \quad , \tag{35}$$

does not vanish as $|\mathbf{r}| \to \infty$.

We begin with (30)

$$P(\mathbf{r},\omega) = \int_V d\mathbf{r}'\rho(\mathbf{r}',\omega)G_0^{\pm}(\mathbf{r},\mathbf{r}',\omega)$$

$$+ \oint_S dS'\{P(\partial G_0^{\pm}/\partial n) - G_0^{\pm}(\partial P/\partial n)\} \quad , \quad \mathbf{r} \text{ in } V \tag{36}$$

with G_0 either causal G_0^+ or anticausal G_0^-. When $|\mathbf{r}| \to \infty$, the contribution from the second term on the right hand side of (36) to P in V must go to 0 since

$$P(\mathbf{r},\omega) = \int_\infty d\mathbf{r}'\rho(\mathbf{r}',\omega)G_0^+(\mathbf{r},\mathbf{r}',\omega) \quad , \tag{37}$$

(the Lippmann-Schwinger equation). However, as $|\mathbf{r}| \to \infty$, with $G_0 - G_0^-$,

$$\oint_{S\to\infty} dS'\{P(\partial G_0^-/\partial n) - G_0^-(\partial P/\partial n)\} + \int_{V\to\infty} d\mathbf{r}'\rho(\mathbf{r}',\omega)G_0^-(\mathbf{r},\mathbf{r}',\omega)$$

$$= \int_{V\to\infty} d\mathbf{r}'\rho(\mathbf{r}',\omega)G_0^+(\mathbf{r},\mathbf{r}',\omega) + 0 \quad , \tag{38}$$

so

$$\oint_{S\to\infty} \{P(\partial G_0^-/\partial n) - G_0^-(\partial P/\partial n)\}dS$$

$$= \int_\infty [G_0^+(\mathbf{r},\mathbf{r}',\omega) - G_0^-(\mathbf{r},\mathbf{r}',\omega)]\rho(\mathbf{r}',\omega)d\mathbf{r}' \neq 0 \text{ for all time.} \tag{39}$$

Hence, the large distance surface contribution to the physical field, P, within V with the physical field P and P_n and an anticausal Green's function G_0^- will not vanish as $|\mathbf{r}| \to \infty$. As we mentioned earlier, this is one of the two problems with the infinite hemisphere model of seismic migration.

Although

$$P(\mathbf{r},\omega) = \int_\infty d\mathbf{r}'\rho(\mathbf{r}',\omega)G_0^-(\mathbf{r},\mathbf{r}',\omega) \quad , \tag{40}$$

would be a solution to (12) and (26) for all $\mathbf{r}$, it would not be the

causal/physical solution to (12) and (26). And hence, in summary the contribution to the causal/physical solution for $P(\mathbf{r},\omega)$ for $\mathbf{r}$ in V from

$$\int_S dS'[P(dG_0^+/dn) - G_0^+(dP/dn)] \quad , \tag{41}$$

goes to zero as $|R| \rightarrow \infty$ where P and dP/dn corresponds to physical/causal boundary values of P and dP/dn, respectively. Physical measurements of P and dP/dn on S are always causal/physical values. The integral

$$\int_S dS'[P(dG_0^-/dn) - G_0^-(dP/dn)] \quad , \tag{42}$$

does *not* go to zero for anti-causal, G_0^- and causal/physical P and dP/dn. The latter fact bumps up against a key assumption in the infinite hemisphere models of migration. That combined with the fact the infinite hemisphere model assumes the entire subsurface, down to 'infinite' depth is known, suggests the need for a different model. That model is the finite volume model.

FINITE VOLUME MODEL FOR MIGRATION

The finite model for migration assumes that we know or can adequately estimate earth medium properties (velocity) down to the reflector we seek to image. The finite volume model assumes that beneath the sought after reflector the medium properties are and remain unknown. The 'finite volume model' corresponds to the volume within which we assume the earth properties are known and within which we predict the wave-field from surface measurements. We have moved away from the two issues of the infinite hemisphere model, i.e., (1) the assumption we know the subsurface to all depths and (2) that the surface integral with an anticausal Green's function has no contribution to the field being predicted in the earth.

The finite volume model takes away both assumptions. However, we are now dealing with a finite volume V, and with a surface S, consisting of upper surface S_U, lower surface S_L and walls, S_W (Fig. 3). We only have measurements on S_U. In the following sections on: (1) Green's theorem for one-way propagation; and (2) Green's theorem for two-way propagation we show how the choice of Green's function allows the finite volume migration model to be realized. The construction of the Green's function that allows for two-way propagation in V is the new and significant contribution of this two paper set. It puts RTM on a firm wave theoretical Green's theorem basis, for the first time, with algorithmic consequence and consistent and realizable methods for RTM. The new Green's function is neither causal, anticausal, nor

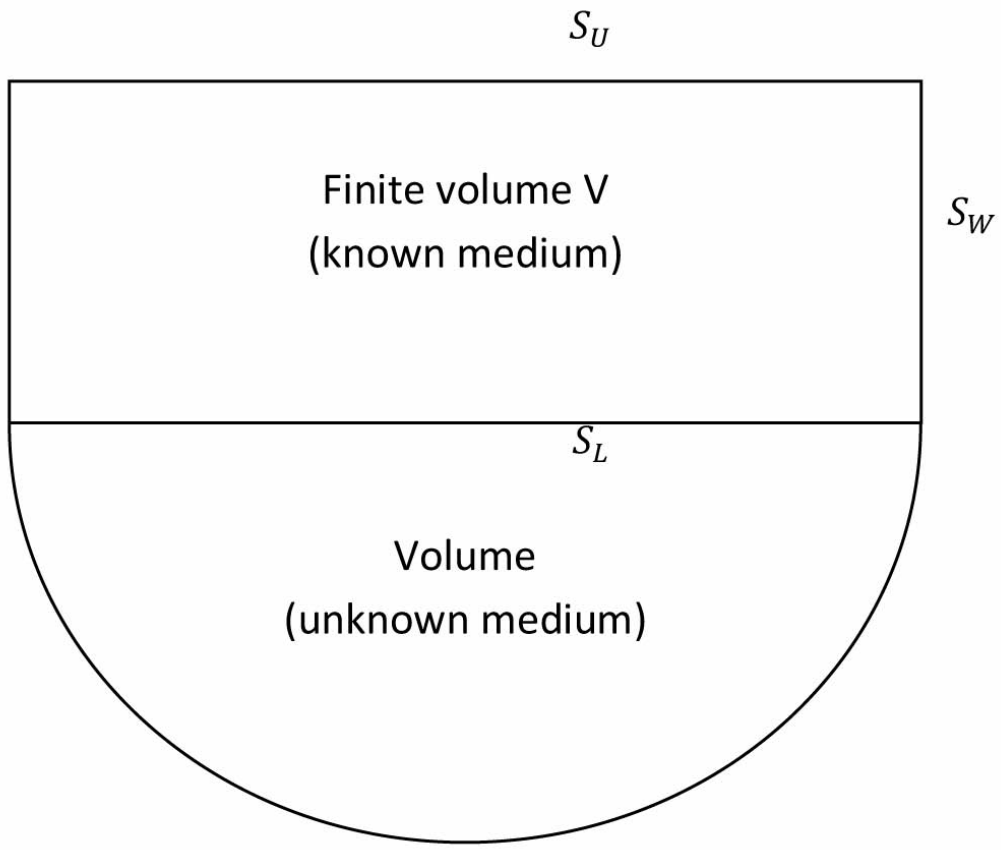

Fig. 3. A finite volume model.

a combination of causal and/or anticausal, Green's functions. In the important paper by Amundsen (1994), a finite volume model for wave-field prediction is developed which requires knowing (i.e., predicting through solving an integral equation) the wave-field at the lower surface. In parts I and II we show that for one and two-way propagation, respectively, that with a proper and distinct choice of Green's function, in each case, that absolutely no wave-field measurement information on the lower surface is required or needs to be estimated/predicted. A major goal and contribution of this two paper set, is to show how to properly choose the Green's functions that allow for two-way propagation (for RTM application) without the need for measurements on the lower boundary of the closed surface in Green's theorem.

FINITE VOLUME: ONE-WAY WAVE GREEN'S THEOREM DOWNWARD CONTINUATION

Consider a 1D up-going plane wave-field $P = Re^{-ikz}$ propagating upward through the 1D homogeneous volume without sources between $z = a$ and $z = b$ (Fig. 4). The wave P inside V can be predicted from

$$P(z,\omega) = \left|_{z'=a}^{b}\{P(z',\omega)(dG_0/dz')(z,z',\omega) - G_0(z,z',\omega)(dP/dz')(z',\omega)\}\right. \quad , \tag{43}$$

with the Green's function, G_0, that satisfies

$$[(d^2/dz'^2) + k^2]G_0(z,z',\omega) = \delta(z - z') \quad , \tag{44}$$

for z and z′ in V. We can easily show that for an upgoing wave, $P = Re^{-ikz}$, that if one chooses $G_0 = G_0^+$ [causal, $e^{ik|z-z'|}/(2ik)$], the lower surface (i.e., $z' = b$) constructs P in V and the contribution from the upper surface vanishes. On the other hand, if we choose $G_0 = G_0^-$ [anticausal solution $e^{-ik|z-z'|}/(-2ik)$], then the upper surface $z = a$ constructs $P = Re^{-ikz}$ in V and there is no contribution from the lower surface $z' = b$. This makes sense since information on the lower surface $z' = b$ will move with the upwave into the region between a and b, with a forward propagating causal Green's function, G_0^+. At the upper surface $z' = a$, the anticausal G_0^- will predict from an upgoing wave measured at $z' = a$, what the wave was previously and when it was moving up and deeper than $z' = a$.

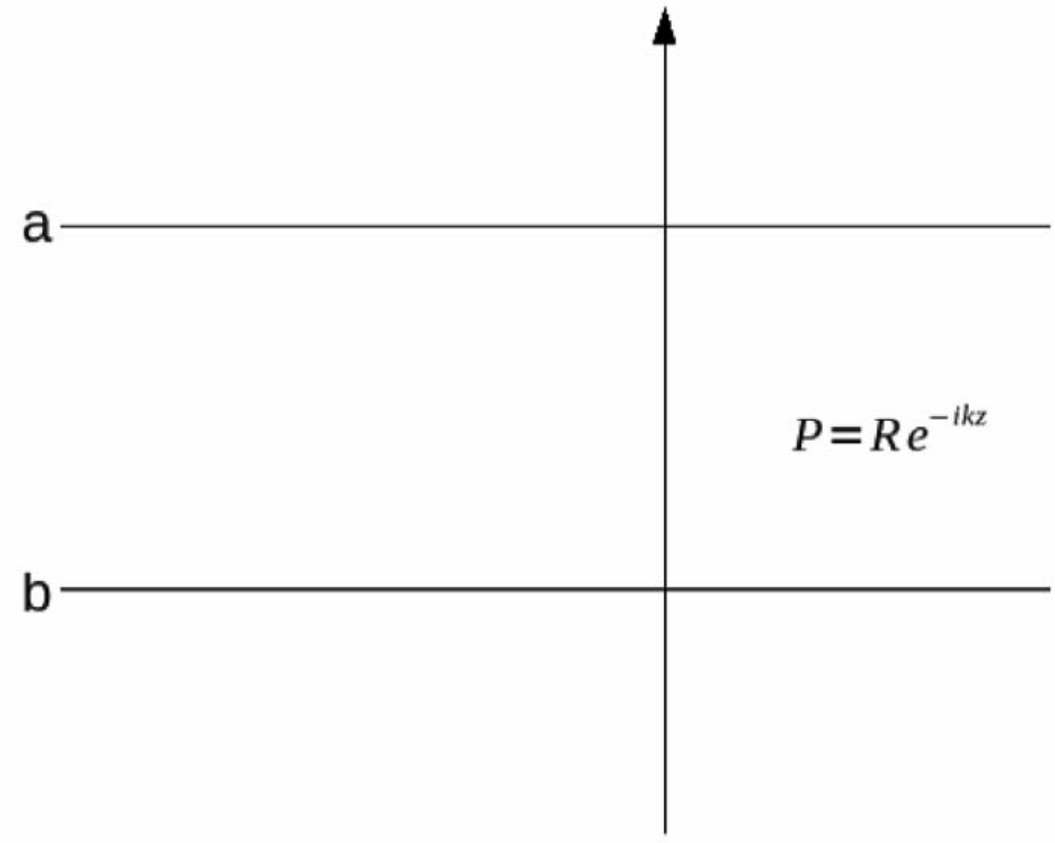

Fig. 4. 1D up-going plane wave-field.

Since in exploration seismology the reflection data is typically upgoing, once it is generated at the reflector, and we only have measurements at the upper surface $z' = a$, we choose an anticausal Green's function G_0^- in one-way wave back propagation in the finite volume model. If in addition we want to rid ourselves of the need for dP/dz' at $z' = a$ we can impose a Dirichlet boundary condition on G_0^-, to vanish at $z' = a$. The latter Green's function is labeled G_0^{-D}.

$$G_0^{-D} = -[e^{-ik|z-z'|}/2ik] - [-e \qquad /2ik] \ , \tag{45}$$

where z_I is the image of z through $z' = a$. It is easy to see that $z_I = 2a - z$ and that

$$P(z) = -(dG_0^{-D}/dz')(z,z',\omega)\big|_{z'=a} P(a) = e^{-ik(z-a)}P(a) \ , \tag{46}$$

in agreement with a simple Stolt FK phase shift for back propagating an up-field. Please note that $P(z,\omega) = -(dG_0^{-D}/dz')(z,z',\omega)\big|_{z'=a} P(a,\omega)$ back propagates $P(z' = a,\omega)$, not G_0^{-D}. The latter thinking that G_0^{-D} back propagates data is a fundamental mistake/flaw in many seismic back propagation migration and inversion theories.

The multidimensional 3D generalization for downward continuing both sources and receivers for an upgoing wave-field is as follows:

$$\int (dG_0^{-D}/dz_s)(x_s',y_s',z_s',x_s,y_s,z_s;\omega)$$

$$\times [\int (dG_0^{-D}/dz_g)(x_g',y_g',z_g',x_g,y_g,z_g;\omega)D(x_g',y_g',z_g',x_s',y_s',z_s';\omega)dx_g'dy_g']dx_s'dy_s'$$

$$= M(x_s,y_s,z_s,x_g,y_g,z_g;\omega)$$

$$= M(x_m,y_m,z_m,x_h,y_h,z_h;\omega) \ , \tag{47}$$

where $x_g + x_s = x_m$, $y_g + y_s = y_m$, $z_g + z_s = z_m$, $x_g - x_s = x_h$, $y_g - y_s = y_h$, and $z_g - z_s = z_h$. The uncollapsed migration is $M(x_m',y_m',z_m',x_h',y_h',z_h'=0;t=0)$ and is ready for subsequent AVO analysis in a multi-D subsurface (see e.g., Clayton and Stolt, 1981; Stolt and Weglein, 1985; Weglein and Stolt, 1999).

In part II of this paper we examine Green's theorem for two-way RTM in a 1D and multi-D earth.

COMMENTS/SUMMARY

In this paper, we have provided an overview of the evolution of migration models for one-way wave propagation, viewed as a progression of wave-field prediction from the perspective of Green's theorem concepts and methods. This provides a platform, background and context for wave-field prediction for RTM, the subject of part II of this two paper set.

ACKNOWLEDGEMENTS

We thank the M-OSRP sponsors, NSF-CMG award DMS-0327778 and DOE Basic Sciences award DE-FG02-05ER15697 for supporting this research. R.H. Stolt thanks ConocoPhillips for permission to publish. We thank Lasse Amundsen of Statoil and Adriana Ramirez and Einar Otnes of WesternGeco for useful discussions and suggestions regarding RTM. We thank Xu Li, Shih-Ying Hsu, Zhiqiang Wang and Paolo Terenghi of M-OSRP for useful comments and assistance in typing the manuscript.

REFERENCES

Amundsen, L., 1994. The propagator matrix related to the Kirchhoff-Helmholtz integral in inverse wavefield extrapolation. Geophysics, 59: 1902-1910.

Berkhout, A.J. and Wapenaar, C.P.A., 1988. Delft philosophy on inversion of elastic data. Expanded Abstr., 58th Ann. Internat. SEG Mtg., Anaheim, 7: 831-833.

Clayton, R.W. and Stolt, R.H., 1981. A Born-WKBJ inversion method for acoustic reflection data. Geophysics, 46: 1559-1567.

de Bruin, C.G.M., Wapenaar, C.P.A. and Berkhout, A.J., 1990a. Angle-dependent reflectivity by means of prestack migration. Geophysics, 55: 1223-1234.

de Bruin, C.G.M., Wapenaar, C.P.A. and Berkhout, A.J., 1990b. Imaging for angle-dependent reflectivity in the presence of dip. Expanded Abstr., 60th Ann. Internat.SEG Mtg., San Francisco, 9: 1503-1506.

Douma, H., Yingst, D., Vasconcelos, I. and Tromp, J., 2010. On the connection between artifact filtering in reverse-time migration and adjoint tomography. Geophysics, 75: S219-S223.

Sava, P. and Fomel, S., 2006. Time-shift imaging condition in seismic migration. Geophysics, 71: S209-S217.

Sava, P. and Vasconcelos, I., 2009. Efficient computation of extended images by wavefield-based migration. Expanded Abstr., 79th Ann. Internat. SEG Mtg., Houston, 28: 2824-2828.

Sava, P. and Vasconcelos, I., 2010. Extended imaging conditions for wave-equation migration. Geophys. Prosp. (in press).

Schneider, W.A., 1978. Integral formulation for migration in two and three dimensions. Geophysics, 43: 49-76.

Stolt, R.H., 1978. Migration by Fourier transform. Geophysics, 43: 23-48.

Stolt, R.H. and Weglein, A.B., 1985. Migration and inversion of seismic data. Geophysics, 50: 2458-2472.

Vasconcelos, I., Sava, P. and Douma, H., 2010. Nonlinear extended images via image-domain interferometry. Geophysics, 75: SA105-SA115.

Weglein, A.B. and Stolt, R.H., 1999. Migration-inversion revisited (1999). The Leading Edge, 18: 950-952, 975.

Reverse time migration and Green's theorem: Part II-A new and consistent theory that progresses and corrects current RTM concepts and methods

A. B. Weglein[*], **R. H. Stolt**[†] **and J. D. Mayhan**[*]

[*] *M-OSRP, University of Houston,*
617 Science & Research Bldg. 1, Houston, TX, 77004.

[†] *ConocoPhillips,*
600 North Dairy Ashford Road, Houston, TX 77079.

(May 17, 2011)
For Journal of Seismic Exploration
Running head: **Wave-field representations using Green's theorem**

ABSTRACT

In this paper, part II of a two paper set, we place Green's theorem based reverse time migration (RTM), for the first time on a firm footing and technically consistent math-physics foundation. The required new Green's function for RTM application is developed and provided, and is neither causal, anticausal, nor a linear combination of these prototype Green's functions, nor these functions with imposed boundary conditions. We describe resulting fundamentally new RTM theory and algorithms, and provide a step-by-step prescription for application in 1D, 2D and 3D, the latter for an arbitrary laterally and vertically varying velocity field. The original RTM method of running the wave equation backwards with surface reflection data as a boundary condition is not a wave theory method for wave-field prediction, neither in depth nor in reversed time. In fact, the latter idea corresponds to Huygens Principle which evolved and was corrected and became a wave theory predictor by George Green in 1826. The original RTM method, where (1) 'running the wave equation backward in time', and then (2) employing a zero lag cross-correlation imaging condition, is in both of these ingredients less accurate and effective than the Green's theorem RTM method of this two paper set. Furthermore, *all* currently available Green's theorem methods for RTM make fundamental conceptual and algorithmic errors in their Green's theorem formulations. Consequently, even with an accurate velocity model, current Green's theorem RTM formulations can lead to image location errors and other reported artifacts. Addressing the latter problems is a principal goal of the new Green's theorem RTM method of this paper. Several simple analytic 1D examples illustrate the new RTM method. We also compare the general RTM methodology and philosophy, as the high water mark of current imaging concepts and application, with the next generation and emerging Inverse Scattering Series imaging concepts and methods.

INTRODUCTION

An important and central concept resides behind all current seismic processing imaging methods that seek to extract useful subsurface information from recorded seismic data. That concept has two ingredients: (1) from the actual recorded surface seismic experiment and data, to predict what an experiment with a source and receiver at depth would record, and (2) exploiting the fact that a coincident source receiver experiment at depth, would, for small recording times, be an indicator of only local earth mechanical property changes at the coincident source-receiver position. These two ingredients, a wave-field prediction, and an imaging condition, reside behind all current leading edge seismic migration algorithms. The purpose of this two paper set is to advance our understanding, and provide concepts and new algorithms for the first of these two ingredients: subsurface wave-field prediction from surface wave-field measurements, when the wave propagation between source and target and/or target and receiver is not a one-way propagating wave in terms of depth..

As with all current migration methods, an accurate velocity model is required for this procedure to deliver an accurate structure map, that is, the spatial configuration of boundaries in the subsurface that correspond to reflectors where rapid changes in physical properties occur.

In this paper, we for the first time place Reverse Time Migration (RTM) on a firm theoretical footing derived from Green's theorem. Green's theorem provides a useful framework for deriving algorithms to predict the wave-field at depth from surface measurements. There is much current interest and activity with RTM in exploration seismology.

The original RTM was pioneered, developed and applied by Dan Whitmore and his AMOCO colleagues in the 1980's (Whitmore (1983)), for exploration in the overthrust belt. The traditional seismic thinking that used a wave traveling from source down to the reflector and then up from the reflector to the receiver was extended to allow, e.g., waves to move down and up from source to a reflector and down and then up from reflector to the receiver. For one-way wave propagation, a single step in depth corresponds to one step in time, with a fixed sign in the relationship between change in depth and change in time. Hence, for one-way waves, we can equivalently go down the up wave in space or take a step backwards in time. For two-way wave propagation, reversing time or extrapolating down an upcoming wave are *not* equivalent. And to image a reflector that reflected a turning wave requires a non-one-way wave model that reversed time can satisfy. In wave theoretic downward continuation migration, the source wave-field and receiver wave-fields are each extrapolated to the subsurface using one-way wave equations to obtain an experiment with coincident sources and receivers at depth.

The idea behind the two-way wave extrapolators (Whitmore (1983), McMechan (1983), Baysal et al. (1983)) is to handle waves propagating in any direction, including overturning waves and prismatic waves. The most common implementation uses finite-difference techniques to solve the wave equation, which in the acoustic case is given by

$$\left(\nabla^2 - \frac{1}{c^2}\partial_t^2\right) P(\mathbf{r}, t) = 0 \quad , \tag{1}$$

where P can be either the source or receiver wave-field. To calculate the source wave-field, standard forward modeling injecting a user defined source signature into the model at the actual source position is done. For the receiver wave-field, the wave equation is run backwards in time and the

recorded wave-field is injected into the model at the receiver positions as a boundary condition. The injection of the recorded wave-field is done starting with later times and finishing with the early times. That idea of using the measured values of the wave-field as the boundary conditions for a wave equation run backwards in time corresponds to Huygens' principle (Huygens, 1690). The image, $I(\mathbf{x})$ is generated using a zero lag cross-correlation imaging condition,

$$I(\mathbf{x}) = \int_0^{t_{max}} dt\, S(\mathbf{x}, t) R(\mathbf{x}, t_{max} - t), \tag{2}$$

where the maximum recording time is t_{max}, $S(\mathbf{x}, t)$ is the modeled source wave-field and $R(\mathbf{x}, t_{max} - t)$ is the receiver wave-field (Fletcher et al., 2006). There are other imaging conditions cited in the literature, among them the deconvolution imaging condition (Zhang et al., 2007) but at this point in time it seems that the cross-correlation imaging condition is often employed. The latter imaging principle is not equivalent to the downward continuation of sources and receivers at depth and seeking a zero time result from a coincident source-receiver experiment.

One of the disadvantages of RTM is that it requires the availability of a large amount of memory which increases with respect to the frequencies we want to migrate (Liu et al., 2009). As a consequence, memory availability has been a limitation to the application of this technology, especially to high resolution data from large 3D acquisitions. Nevertheless, recent improvements in computer hardware have enabled different implementations of RTM throughout the energy industry and there is a renewed interest in this technology due to its ability to accommodate and image in media where waves turn, as e.g. can occur in subsalt plays. Several efforts have been aimed at improving the efficiency of the algorithm and dealing with the high storage cost for 3D implementation. For example, Toselli and Widlund (2000) used domain deconvolution which splits the computations across multiple nodes to improve the efficiency of the algorithm, and Symes (2007) introduced optimal checkpointing techniques to deal with the storage requirements, although, this type of technique can increase the computation cost. These are examples of improvements directly related to the numerical implementation of the RTM algorithm. Other efforts to deal with the practical requirements of RTM are based on changes in the theoretical approach to the problem. One example is the work of Luo and Schuster (2004) where a target oriented reverse time datuming (RTD) technique based on Green's theorem is proposed. RTD can also be seen as a bottom-up shooting approach for RTM. Using RTD's formulation, only the velocity model above the datum is used to calculate the Green's function. No velocity under the datum is required, making the modeling more efficient. This formulation also allows for target oriented RTM and/or inversion. In target oriented RTM, the idea is to redatum the data into a mathematical surface (referred to as the datum surface) within the earth's subsurface and use RTM below the datum surface to obtain a local RTM image of a given target area below the datum (Dong et al., 2009). In target oriented inversion, the inversion is carried out only for a target area below the datum. Target oriented inversion has also been proposed using the CFP domain.

The current formulation of RTD or bottom-up shooting for RTM, uses a high frequency approximation to Green's theorem (interferometry equation) and measurements at the measurement surface. This formulation presents several approximations which can impact the quality of the redatuming or the migration (if an imaging condition is applied after RTD).

1. The first approximation is related to the measurement surface. Green's theorem based al-

gorithms, in principle, require measurements over a closed surface. The fact that we only measure the wave-field in a limited surface has an effect on the quality of the redatuming and can create artifacts in both the redatumed data and the migration. Directly addressing that issue is one of the principle aims of this paper. These measurements can be interchanged for sources at the surface using reciprocity principles.

2. The second approximation is the high frequency, one-way wave approximation commonly used in interferometry. This approximation allows us to remove the need for the normal derivative of the pressure field at the measurement surface. The normal derivative is required by Green's theorem in its most common form, which is the one used by (Luo and Schuster, 2004) in their RTD formulation. As an analogy to interferometry, when used with two-way waves, this high frequency, one-way wave approximation will create spurious multiples in the redatumed wave-field within the earth's subsurface (see e.g. Ramírez and Weglein (2009)).

Dong et al. (2009) deal with the effect of these approximations by smoothing the model, and, hence, reducing the effect of the one-way wave approximation. However, smoothing the model does not solve completely the problems created by the use of approximations. The redatumed wave-field will contain artifacts. Some of these artifacts will be imaged and stacking will not remove these artifacts completely.

Some indication of the level of current interest in RTM can be gleaned by: (1) the number of papers devoted to that subject in recent SEG and EAGE meetings, and subsalt workshops and (2) the November 2010 Special Section of The Leading Edge on Reversed Time Migration with an Introduction by Etgen and Michelena (2010) and papers by Zhang et al. (2010), Jin and Xu (2010), Crawley et al. (2010), and Higginbotham et al. (2010).

PROPAGATION FOR RTM IN A ONE DIMENSIONAL EARTH: USING GREEN'S FUNCTIONS TO AVOID THE NEED FOR DATA AT DEPTH, NEW NONCAUSAL OR CAUSAL GREEN'S FUNCTIONS

Green's theorem in 3D in the $(\mathbf{r},\omega)$ domain to determine a wave-field, $P(\mathbf{r},\omega)$ for $\mathbf{r}$ in V is given by

$$\begin{aligned} P(\mathbf{r},\omega) &= \int_V d\mathbf{r}'\,\rho(\mathbf{r}',\omega)G_0(\mathbf{r},\mathbf{r}',\omega) \\ &+ \oint_S dS'\,\mathbf{n}\cdot(P(\mathbf{r}',\omega)\nabla' G_0(\mathbf{r},\mathbf{r}',\omega) - G_0(\mathbf{r},\mathbf{r}',\omega)\nabla' P(\mathbf{r}',\omega)) \quad . \end{aligned} \tag{3}$$

In 1D in the slab $a \le z \le b$, (3) becomes

$$\begin{aligned} P(z,\omega) &= \int_a^b dz'\,\rho(z',\omega)G_0(z,z',\omega) \\ &+ \Big|_a^b \left(P(z',\omega)\frac{dG_0}{dz'}(z,z',\omega) - G_0(z,z',\omega)\frac{dP}{dz'}(z',\omega)\right) \quad . \end{aligned} \tag{4}$$

Assuming no sources in the slab, the 1D homogeneous wave equation is

$$\left(\frac{d^2}{dz'^2} + k^2\right) P(z',\omega) = 0 \quad , \text{ for } z < z' < b \tag{5}$$

with general solution

$$P(z',\omega) \quad = \quad Ae^{ikz'} + Be^{-ikz'} \text{ for } z < z' < b \tag{6}$$

where $k = \omega/c$. Given the conventions positive z' increasing downward and time dependence $e^{-i\omega t}$ in Fourier transforming from ω to t, the first term in (6) is a downgoing wave and the second term is an upgoing wave.

The equation for the corresponding Green's function is

$$\left(\frac{d^2}{dz'^2} + k^2\right) G_0(z,z',\omega) \quad = \quad \delta(z-z') \quad , \tag{7}$$

with causal and anticausal solutions

$$G_0^+(z,z',\omega) \quad = \quad \frac{1}{2ik} e^{ik|z-z'|} \quad , \tag{8}$$

$$G_0^-(z,z',\omega) \quad = \quad -\frac{1}{2ik} e^{-ik|z-z'|} \quad . \tag{9}$$

Eq. (4) suggests that the Green's function we need is such that it and its derivative vanish at $z' = b$. Such a Green's function removes the need for measurements at $z' = b$. Eq. (7) is an inhomogeneous differential equation with general solution $A_1 e^{ikz'} + B_1 e^{-ikz'} + G_0(z,z',\omega)$ where the first two terms are the general solution to the homogeneous differential equation and the third term is any particular solution to the inhomogeneous differential equation. The choice $G_0(z,z',\omega) = G_0^+(z,z',\omega)$ gives the following general solution of (7):

$$G_0(z,z',\omega) \quad = \quad A_1 e^{ikz'} + B_1 e^{-ikz'} + \frac{1}{2ik} e^{ik|z-z'|} \quad . \tag{10}$$

Its derivative is

$$\begin{aligned} \frac{dG_0}{dz'}(z,z',\omega) \quad &= \quad A_1 e^{ikz'} ik + B_1 e^{-ikz'}(-ik) \\ &+ \quad \frac{1}{2ik} e^{ik|z-z'|} ik \ \text{sgn}(z-z')(-1) \quad . \end{aligned} \tag{11}$$

Now we impose boundary conditions in order to find A_1 and B_1. The requirement that (10) and (11) vanish at $z' = b$ gives

$$\begin{aligned} 0 \quad &= \quad A_1 e^{ikb} + B_1 e^{-ikb} + \frac{1}{2ik} e^{ik\underbrace{|z-b|}_{b-z}} \\ 0 \quad &= \quad A_1 e^{ikb} ik + B_1 e^{-ikb}(-ik) + \frac{1}{2ik} e^{ik\underbrace{|z-b|}_{b-z}} ik \underbrace{\text{sgn}(z-b)}_{-1}(-1) \\ A_1 e^{ikb} + B_1 e^{-ikb} \quad &= \quad -\frac{1}{2ik} e^{ik(b-z)} \\ A_1 e^{ikb} - B_1 e^{-ikb} \quad &= \quad -\frac{1}{2ik} e^{ik(b-z)} \\ 2A_1 e^{ikb} \quad &= \quad -2\frac{1}{2ik} e^{ik(b-z)} \\ A_1 \quad &= \quad -\frac{1}{2ik} e^{-ikz} \quad , \end{aligned} \tag{12}$$

$$\begin{aligned} 2B_1 e^{-ikb} \quad &= \quad 0 \\ B_1 \quad &= \quad 0 \quad . \end{aligned} \tag{13}$$

Substituting (12) and (13) into (10) gives

$$\begin{aligned} G_0(z,z',\omega) &= -\frac{1}{2ik}e^{-ikz}e^{ikz'} + \frac{1}{2ik}e^{ik|z-z'|} \\ &= -\frac{1}{2ik}(e^{-ik(z-z')} - e^{ik|z-z'|}) \quad . \end{aligned} \tag{14}$$

Note the following about (14):

1. When $z' = b$, $G_0(z,b,\omega)$ vanishes:

$$G_0(z,b,\omega) = -\frac{1}{2ik}(e^{-ik(z-b)} - e^{ik\underbrace{|z-b|}_{b-z}}) = -\frac{1}{2ik}(\underbrace{e^{-ik(z-b)} - e^{-ik(z-b)}}_{0}) \quad . \tag{15}$$

2. When $a < z' < b$, $G_0(z,z',\omega)$ is neither causal nor anticausal due to the presence of the term $-1/(2ik)\, e^{-ik(z-z')}$.

3. When $z' = a$, $G_0(z,a,\omega)$ is the sum of anticausal and causal terms, but not in general or at any other depth.

$$G_0(z,a,\omega) = -\frac{1}{2ik}(e^{-ik\underbrace{(z-a)}_{|z-a|}} - e^{ik|z-a|}) = \underbrace{-\frac{1}{2ik}e^{-ik|z-a|}}_{anticausal} + \underbrace{\frac{1}{2ik}e^{ik(z-a)}}_{causal} \quad . \tag{16}$$

4. Normally one uses Dirichlet or Neumann or Robin boundary conditions on the surface S (in our 1D case at both a and b). Constructing the Green's function (14) has enabled us to use both Dirichlet and Neumann boundary conditions on part of the surface S (in our 1D case only at a).

The Green's function for two-way propagation that will eliminate the need for data at the lower surface of the closed Green's theorem surface is found by finding a general solution to the Green's function for the medium in the finite volume model and imposing both Dirichlet and Neumann boundary conditions at the lower surface. We confirm that the Green's function (14), when used in Green's theorem, will produce a two-way wave for $a < z < b$ with only measurements on the upper surface. Substituting (6), (14), and their derivatives into (4) gives $P(z,\omega) = Ae^{ikz} + Be^{-ikz}$, i.e., we recover the original two-way wave-field. The details are in Appendix A.

A and B can be derived from the measured data $P(a)$ and $P'(a)$:

$$\begin{aligned} P(a) &= Ae^{ika} + Be^{-ika} \\ P'(a) &= Ae^{ika}ik + Be^{-ika}(-ik) \\ \frac{P'(a)}{ik} &= Ae^{ika} - Be^{-ika} \\ 2Ae^{ika} &= P(a) + \frac{P'(a)}{ik} \\ A &= e^{-ika}\frac{ikP(a) + P'(a)}{2ik} \quad , \end{aligned} \tag{17}$$

$$\begin{aligned} 2Be^{-ika} &= P(a) - \frac{P'(a)}{ik} \\ B &= e^{ika}\frac{ikP(a) - P'(a)}{2ik} \quad . \end{aligned} \tag{18}$$

In a homogeneous medium the 3D equivalent of (5) is

$$(\nabla^{'\,2} + k^2)P(x', y', z', \omega) \quad = \quad 0 \quad , \tag{19}$$

where $k = \omega/c$. Fourier transforming over x' and y' gives

$$\left(\frac{d^2}{dz'^{\,2}} \underbrace{-k_{x'}^2 - k_{y'}^2 + \frac{\omega^2}{c^2}}_{\equiv k_{z'}^2} \right) P(k_{x'}, k_{y'}, z', \omega) \quad = \quad 0 \quad , \tag{20}$$

which looks like the 1D problem

$$\left(\frac{d^2}{dz'^{\,2}} + k_{z'}^2 \right) P(k_{x'}, k_{y'}, z', \omega) \quad = \quad 0 \quad , \tag{21}$$

with general solution

$$P(k_{x'}, k_{y'}, z', \omega) \quad = \quad A e^{ik_{z'}z'} + B e^{-ik_{z'}z'} \quad . \tag{22}$$

We illustrate, in the next section, a more complicated 1D example, where the finite volume contains a reflector.

RTM AND GREEN'S THEOREM: TWO-WAY WAVE PROPAGATION IN A 1D FINITE VOLUME THAT CONTAINS A REFLECTOR

Consider a single reflector example with the following properties: z increases downward, the source is located at depth z_s (where $0 < z_s < a$), the receiver is located at depth z_g (where $z_s < z_g < a$), for $0 \le z \le a$ the medium is characterized by c_0, for $z > a$ the medium is characterized by c_1, and the reflection coefficient R and transmission coefficient T at the interface ($z = a$) are given by

$$R \quad = \quad \frac{c_1 - c_0}{c_0 + c_1} \quad , \tag{23}$$

$$T \quad = \quad \frac{2c_1}{c_0 + c_1} \quad . \tag{24}$$

Assume the source goes off at $t = 0$. Then the wave-field P for $z < a$, i.e., above a, is given by

$$P \quad = \quad \frac{e^{ik|z - z_s|}}{2ik} + R\,\frac{e^{-ik(z-a)}}{2ik} e^{ik(a - z_s)} \quad . \tag{25}$$

In the time domain, the front of the plane wave travels with $\delta(t - |z - z_s|/c_0)$ out from the source. Hence, the first term in (25) for P is the incident wave-field (an impulse) and for the second term in P

$$\delta \left(t - \underbrace{\frac{|a - z_s|}{c_0}}_{\text{from source to reflector}} - \underbrace{\frac{|z - a|}{c_0}}_{\text{from reflector to field point } z} \right) . \tag{26}$$

Fourier transforming gives:

$$\begin{aligned} \int_{-\infty}^{\infty} e^{i\omega t} \delta \left(t - \frac{|a - z_s|}{c_0} - \frac{|z - a|}{c_0} \right) dt \quad &= \quad e^{\left(i\omega \left(\frac{|a - z_s|}{c_0} + \frac{|z - a|}{c_0} \right) \right)} \\ \text{for } z < a \quad &= \quad e^{ik(a - z_s) - ik(z - a)} = e^{-ik(z - (2a - z_s))} \quad . \end{aligned} \tag{27}$$

Therefore $2a - z_s - z$ is the travel path from the source to the reflector and up to the field point z. If instead of an incident Green's function we choose a plane wave, we drop the $1/(2ik)$ and set $z_s = 0$, and then the incident plane wave passes the origin $z = 0$ at $t = 0$.

The transmitted wave field is for $z > a$

$$P = \frac{1}{2ik} T e^{ik|a-z_s|} e^{ik_1(z-a)} \quad , \tag{28}$$

with R and T given by (23); then (25) and (28) provide the solution for the total wave field everywhere.

Now we introduce Green's theorem. The total wave-field P satisfies

$$\left\{ \frac{d^2}{dz'^2} + \frac{\omega^2}{c^2(z')} \right\} P = \delta(z' - z_s) \quad , \tag{29}$$

and the Green's function G will satisfy

$$\left\{ \frac{d^2}{dz'^2} + \frac{\omega^2}{c^2(z')} \right\} G = \delta(z - z') \quad , \tag{30}$$

where

$$c(z') = \begin{cases} c_0 & z' < a \\ c_1 & z' > a \end{cases} \quad . \tag{31}$$

The solution for P is given in (25) and (28). The solution for G will be determined below. G_H and G_P are a homogeneous solution and particular solution, respectively, of the following differential equations:

$$\left\{ \frac{d^2}{dz^2} + \frac{\omega^2}{c^2(z)} \right\} G_H = 0 \quad , \tag{32}$$

$$\left\{ \frac{d^2}{dz^2} + \frac{\omega^2}{c^2(z)} \right\} G_P = \delta \quad . \tag{33}$$

A particular solution, G_P, can be given by (25) and (28) and with z' replacing z_s, we find

$$P(z, z_s, \omega) = \Big|_A^B \{ P(z', z_s, \omega) \frac{dG}{dz'}(z, z', \omega) - G(z, z', \omega) \frac{dP}{dz'}(z', z_s, \omega) \} \quad , \tag{34}$$

where $A = z_g$, the depth of the MS, and $B > a$ is the lower surface of Green's theorem.

The 'source' at depth z is within $[A, B]$ and either above or below the reflector at $z = a$; conditions will be placed on the solution, G, (for a source within the volume) for the field point of G at depth z' to satisfy at B. That is

$$(G(z, z', \omega))_{z'=B} = 0 \quad , \tag{35}$$

$$\text{and} \qquad \left(\frac{dG}{dz'}(z, z', \omega) \right)_{z'=B} = 0 \quad . \tag{36}$$

First pick the 'source' in the Green's function to be above the reflector, then (25) and (28) provide a specific solution when we substitute for z_s in P, the parameter, z, and for z in P the parameter, z'. The latter allows a particular solution for G for the case that z in G is within $[A, B]$ but above $z = a$. Please note: The physical source is *outside* the volume, but the 'source' in the Green's

function is inside the volume. Also, note that for the case of the (output point, z) 'source' in the Green's function to be below the reflector and within $[A, B]$ that a different solution for P other than what is given in (25) and (28), would be needed for a particular solution of G. The latter would require a solution for P where the source is in the lower half space.

What about the general solution for G_H?

$$\left\{ \frac{d^2}{dz'^2} + \frac{\omega^2}{c^2(z')} \right\} G_H = 0 \quad . \tag{37}$$

The general solution to (37) is, for *any* incident plane wave, $A(k)$ for $[A, B]$

$$G_H = \begin{cases} A_1 e^{ikz'} + B_1 e^{-ikz'} & z' < a \\ C_1 e^{ik_1 z'} + D_1 e^{-ik_1 z'} & z' > a \end{cases} \quad . \tag{38}$$

The general solution to (37) has to allow the possibility of an incident wave from either direction, *that's what general solution means!* The general solution for G for the single reflector problem and the source, z, above the reflector is given by

$$G(z, z', \omega) = \begin{cases} \frac{e^{ik|z'-z|}}{2ik} + R\,\frac{e^{-ik(z'-a)}}{2ik} e^{ik(a-z)} + A_1 e^{ikz'} + B_1 e^{-ikz'} & z' < a \\ \frac{T}{2ik} e^{ik|a-z|} e^{ik_1(z'-a)} + C_1 e^{ik_1 z'} + D_1 e^{-ik_1 z'} & z' > a \end{cases} \tag{39}$$

for the source z being above the reflector and we choose C_1 and D_1 such that

$$G(z, B, \omega) = 0 \quad , \text{ and} \tag{40}$$

$$\left[\frac{dG}{dz'}(z, z', \omega) \right]_{z'=B} = 0 \quad , \tag{41}$$

where, for $z' > a$, G_P is $T/(2ik) e^{ik|a-z|} e^{ik_1(z'-a)}$. Eq. (39) will be the Green's function needed in Green's theorem to propagate/predict above the reflector at $z' = a$ where P is given by (25) and (28). To determine A_1 and B_1, make the solutions for $z' < a$ and $z' > a$ and their derivatives match at $z' = a$ (conditions of continuity across the reflector). The details are in Appendix B. In practice, the deghosted scattered wave is *upgoing* (one-way) and finding its vertical derivative is simply $ik_z \times P$. Deghosting precedes migration.

For downward continuing past the reflector, as previously stated, the P solution needed for the particular solution of the Green's function starts with a source in the lower half space where $k_1 = \omega/c_1$. That's how it works. In practice for a $v(x, y, z)$ medium a modeling will be required that *imposes* a double vanishing boundary condition at depth to produce the Green's function for RTM.

MULTIDIMENSIONAL RTM

Consider a volume V inside a homogeneous medium; V is bounded on the left by $x' = A$, on the right by $x' = L_1$, on the top by $z' = B$, and on the bottom by $z' = L_2$ (Fig. 1). We want to use Green's theorem to estimate the wave-field P in V which requires we measure P and $\partial P/\partial n$ on the boundary S of V. However, we can place receivers only at $z' = B$. Can we construct a Green's function G such that it and its normal derivative $\partial G/\partial n$ vanish on three sides of V so that P can be estimated in V using only the measurements on $z' = B$?

G can be written as the sum of a homogeneous solution G_H and a particular solution G_P where G satisfies the partial differential equation $(\nabla^{'2} + k^2)G = \delta(\mathbf{r} - \mathbf{r}^{'})$ and G_H satisfies the partial differential equation $(\nabla^{'2} + k^2)G_H = 0$. We try solutions of the form:

$$G(\mathbf{r}^{'}, \mathbf{r}, \omega) = \sum_{m,n} A_{m,n}(\mathbf{r}) X_m(x') Z_n(z') + G_P(\mathbf{r}^{'}, \mathbf{r}, \omega) \quad , \tag{42}$$

$$G_H(\mathbf{r}^{'}, \mathbf{r}, \omega) = \sum_{m,n} A_{m,n}(\mathbf{r}) X_m(x') Z_n(z') \quad , \tag{43}$$

with the boundary conditions that G and $\partial G/\partial n$ vanish at $x' = A$, $z' = L_2$, and $x' = L_1$, i.e.,

$$\text{at } x' = A \; G = 0 \text{ and } -\frac{\partial G}{\partial x'} = 0, \tag{44}$$

$$\text{at } z' = L_2 \; G = 0 \text{ and } \frac{\partial G}{\partial z'} = 0, \text{ and} \tag{45}$$

$$\text{at } x' = L_1 \; G = 0 \text{ and } \frac{\partial G}{\partial x'} = 0. \tag{46}$$

Substituting (43) into $(\nabla^{'2} + k^2)G_H = 0$ gives:

$$\begin{aligned}
0 &= \left(\frac{\partial^2}{\partial x^{'2}} + \frac{\partial^2}{\partial z^{'2}} + k^2 \right) X_m(x') Z_n(z') \\
&= X_m''(x') Z_n(z') + X_m(x') Z_n''(z') + k^2 X_m(x') Z_n(z') \\
&= \frac{X_m''(x')}{X_m(x')} + \frac{Z_n''(z')}{Z_n(z')} + k^2 \\
\Longrightarrow \quad & \frac{Z_n''(z')}{Z_n(z')} = -\lambda^2 \\
0 &= Z_n''(z') + \lambda^2 Z_n(z') \\
Z_n(z') &= C_1 e^{i\lambda_n z'} + C_2 e^{-i\lambda_n z'} \qquad (47) \\
0 &= X_m''(x') + (\underbrace{k^2 - \lambda^2}_{\equiv \mu^2}) X_m(x') \\
X_m(x') &= C_3 e^{i\mu_m x'} + C_4 e^{-i\mu_m x'} \quad , \qquad (48)
\end{aligned}$$

where $\mu_m^2 \longrightarrow X_m(x')$ and $\lambda_n^2 \longrightarrow Z_n(z')$. We assume $X_m(x')$ and $Z_n(z')$ are orthonormal and complete.

The boundary conditions on the left are $G(A, z') = 0$ and $G_{x'}(A, z') = 0$, on the right $G(L_1, z') = 0$ and $G_{x'}(L_1, z') = 0$, and on the bottom $G(x', L_2) = 0$ and $G_{z'}(x', L_2) = 0$. Substituting these

boundary conditions into (42) gives:

$$0 = G(A,z',x,z) = \sum_{m,n} A_{m,n}(\mathbf{r}) X_m(A) Z_n(z') + G_P(A,z',x,z) \quad , \tag{49}$$

$$0 = G_{x'}(A,z',x,z) = \sum_{m,n} A_{m,n}(\mathbf{r}) X'_m(A) Z_n(z') + \frac{d}{dx'} G_P(A,z',x,z) \quad , \tag{50}$$

$$0 = G(L_1,z',x,z) = \sum_{m,n} A_{m,n}(\mathbf{r}) X_m(L_1) Z_n(z') + G_P(L_1,z',x,z) \quad , \tag{51}$$

$$0 = G_{x'}(L_1,z',x,z) = \sum_{m,n} A_{m,n}(\mathbf{r}) X'_m(L_1) Z_n(z') + \frac{d}{dx'} G_P(L_1,z',x,z) \quad , \tag{52}$$

$$0 = G(x',L_2,x,z) = \sum_{m,n} A_{m,n}(\mathbf{r}) X_m(x') Z_n(L_2) + G_P(x',L_2,x,z) \quad , \tag{53}$$

$$0 = G_{z'}(x',L_2,x,z) = \sum_{m,n} A_{m,n}(\mathbf{r}) X_m(x') Z'_n(L_2) + \frac{d}{dz'} G_P(x',L_2,x,z) \quad . \tag{54}$$

Eq. (49) is:

$$-G_P(A,z',x,z) = \sum_{m,n} A_{m,n}(\mathbf{r}) X_m(A) Z_n(z') \quad . \tag{55}$$

Multiplying by $Z_s(z')$, integrating, and substituting (47) and (48) give:

$$\begin{aligned} - & \int_{L_2}^{B} G_P(A,z',x,z) Z_s(z')\, dz' = \sum_m A_{m,s}(\mathbf{r}) X_m(A) \\ - & \int_{L_2}^{B} G_P(A,z',x,z)(C_1 e^{i\lambda_s z'} + C_2 e^{-i\lambda_s z'})\, dz' \\ = & \sum_m A_{m,s}(\mathbf{r})(C_3 e^{i\mu_m A} + C_4 e^{-i\mu_m A}) \quad . \end{aligned} \tag{56}$$

In similar fashion we get:

$$
\begin{aligned}
- & \int_{L_2}^{B} \frac{d}{dx'} G_P(A, z', x, z)(C_1 e^{i\lambda_s z'} + C_2 e^{-i\lambda_s z'})\, dz' \\
= & \sum_m A_{m,s}(\mathbf{r}) i\mu_m (C_3 e^{i\mu_m A} - C_4 e^{-i\mu_m A}) \quad , \qquad (57) \\
- & \int_{L_2}^{B} G_P(L_1, z', x, z)(C_1 e^{i\lambda_s z'} + C_2 e^{-i\lambda_s z'})\, dz' \\
= & \sum_m A_{m,s}(\mathbf{r}) (C_3 e^{i\mu_m L_1} + C_4 e^{-i\mu_m L_1}) \quad , \qquad (58) \\
- & \int_{L_2}^{B} \frac{d}{dx'} G_P(L_1, z', x, z)(C_1 e^{i\lambda_s z'} + C_2 e^{-i\lambda_s z'})\, dz' \\
= & \sum_m A_{m,s}(\mathbf{r}) i\mu_m (C_3 e^{i\mu_m L_1} - C_4 e^{-i\mu_m L_1}) \quad , \qquad (59) \\
- & \int_{A}^{L_1} G_P(x', L_2, x, z)(C_3 e^{i\mu_s x'} + C_4 e^{-i\mu_s x'})\, dz' \\
= & \sum_m A_{m,s}(\mathbf{r}) (C_1 e^{i\lambda_n L_2} + C_2 e^{-i\lambda_n L_2}) \quad , \qquad (60) \\
- & \int_{A}^{L_1} \frac{d}{dz'} G_P(x, L_2, x, z)(C_3 e^{i\mu_s x'} + C_4 e^{-i\mu_s x'})\, dz' \\
= & \sum_m A_{m,s}(\mathbf{r}) i\lambda_n (C_1 e^{i\lambda_n L_2} - C_2 e^{-i\lambda_n L_2}) \quad . \qquad (61)
\end{aligned}
$$

The $A_{m,s}$ coefficients are determined by the imposed Dirichlet and Neumann boundary conditions on the base and walls of the finite volume.

GENERAL STEP-BY-STEP PRESCRIPTION FOR RTM IN A FINITE VOLUME WHERE THE VELOCITY CONFIGURATION IS $C(X, Y, Z)$

Step (1) For a desired downward continued/migration output point (x, y, z) for determining $P(x, y, z, \omega)$

$$
\left\{ \nabla^2 + \frac{\omega^2}{c^2(x', y', z')} \right\} G_0(x', y', z', x, y, z, \omega) = \delta(x - x')\delta(y - y')\delta(z - z') \quad , \qquad (62)
$$

for a source at (x, y, z) and P is the physical/causal solution satisfying

$$
\left\{ \nabla'^{\,2} + \frac{\omega^2}{c^2(x', y', z')} \right\} P(x', y', z', x_s, y_s, z_s, \omega) = A(\omega)\delta(x' - x_s)\delta(y' - y_s)\delta(z' - z_s). \qquad (63)
$$

G_0 is the auxiliary or Green's function satisfying

$$
\left\{ \nabla'^{\,2} + \frac{\omega^2}{c^2(x', y', z')} \right\} G_0(x, y, z, x', y', z', \omega) = \delta(x - x')\delta(y - y')\delta(z - z') \quad , \qquad (64)
$$

for (x, y, z) in V *and* G_0 and $\nabla' G_0 \cdot \hat{n}'$ are both zero for (x', y', z') on the lower surface S_L and the walls S_W of the finite volume. The solution for G_0 in V and on S can be found by a numerical modeling algorithm where the 'source' is at (x, y, z) and the field, G_0, at (x', y', z') and $\nabla G_0 \cdot \hat{n}$ are both imposed to be zero on S_L and S_W. Once that model is run for a source at (x, y, z) for $G_0(x', y', z', x, y, z, \omega)$ [for every eventual wave prediction point, (x, y, z), for P] where G_0 satisfies

Dirichlet and Neumann conditions for (x', y', z') on S_L and S_W we output $G_0(x', y', z', x, y, z, \omega)$ for (x', y', z') on S_U (the measurement surface).

Step (2) Downward continue the receiver

$$\begin{aligned} P(x, y, z, x_s, y_s, z_s, \omega) &= \int \left\{ \frac{\partial G_0^{DN}}{\partial z'}(x, y, z, x', y', z', \omega) P(x', y', z', x_s, y_s, z_s, \omega) \right. \\ &- \left. \frac{\partial P}{\partial z'}(x', y', z', x_s, y_s, z_s, \omega) G_0^{DN}(x, y, z, x', y', z', \omega) \right\} dx' dy' \quad , \quad (65) \end{aligned}$$

where z' = fixed depth of the cable and (x_s, y_s, z_s) = fixed location of the source. This brings the receiver down to (x, y, z), a point below the measurement surface in the volume V.

Step (3) Now downward continue the source

$$\begin{aligned} P(x_g, y_g, z, x, y, z, \omega) &= \int \left\{ \frac{\partial G_0^{DN}}{\partial z_s}(x, y, z, x_s, y_s, z_s, \omega) P(x_g, y_g, z, x_s, y_s, z_s, \omega) \right. \\ &- \left. \frac{\partial P}{\partial z_s}(x_g, y_g, z, x_s, y_s, z_s, \omega) G_0^{DN}(x, y, z, x_s, y_s, z_s, \omega) \right\} dx_s dy_s. \quad (66) \end{aligned}$$

$P(x_g, y_g, z, x, y, z, \omega)$ is a downward continued receiver to (x_g, y_g, z) and the source to (x, y, z) and change to midpoint offset $P(x_m, x_h, y_m, y_h, z_m, z_h = 0, \omega)$ and

$$\begin{aligned} &\int d\omega \left\{ \frac{\partial G_0^{DN}}{\partial z_s}(x, y, z, x_s, y_s, z_s, \omega) P(x_g, y_g, z, x_s, y_s, z_s, \omega) \right. \\ &- \left. \frac{\partial P}{\partial z_s}(x_g, y_g, z, x_s, y_s, z_s, \omega) G_0^{DN}(x, y, z, x_s, y_s, z_s, \omega) \right\} \quad , \quad (67) \end{aligned}$$

and Fourier transform over x_m, x_h, y_m, y_h to find $\widetilde{P}(k_{x_m}, k_{x_h}, k_{y_m}, k_{y_h}, k_{z_m}, z_h = 0, t = 0)$ the RTM uncollapsed migration for a general $v(x, y, z)$ velocity configuration.

RTM AND INVERSE SCATTERING SERIES (ISS) IMAGING: NOW AND THE FUTURE

In practice, RTM is often applied using a wave equation that avoids reflections at reflectors above the target. Impedance matching at boundaries in the modeling, allows density and velocity to both have rapid variation at a reflector, but are arranged so that the normal incidence reflection coefficient will be zero. The result ia a smooth 'apparent velocity' that can support diving waves, but seeks to avoid the discontinuous velocity model commitment that including reflections would require. In RTM, including those reflections above the reflector to be imaged, drives a need for an accurate and discontinuous velocity model. The ISS imaging methods welcome (and require) all the reflectors above the one reflector being imaged, *without* implying a concomitant need for an accurate discontinuous velocity model.

One way to view the RTM to Inverse Scattering Series (ISS) (Weglein et al., 2003) imaging step is as removing reflectionless reflectors by an 'impedance matching' differential equation in RTM to avoid the need for a commitment to an accurate and discontinuous velocity. With ISS imaging we have the opposite situation: the welcome of *all* reflections to the imaging of any reflector, and without the need to know or determine the discontinuous velocity model. That is the next step, and our first

field data tests with ISS imaging are underway. In the interim, we thought it useful to provide an assist to current best imaging RTM practice. We will be returning reflections to reflectors thereby turning the problem, observation, and obstacle in current RTM into the instrument of significant imaging progress, and without the need for a velocity model, discontinuous or otherwise.

SUMMARY

Migration and migration-inversion require velocity information for location and beyond velocity only for amplitude analyses at depth. So when we say the medium is 'known,' the meaning of known depends on the goal: migration or migration-inversion. Backpropagation and imaging each evolved and then extended/generalized and merged into migration-inversion (Fig. 2).

For one-way wave propagation the double downward continued data, D is

$$D(\text{at depth}) = \int_{S_s} \frac{\partial G_0^{-D}}{\partial z_s} \int_{S_g} \frac{\partial G_0^{-D}}{\partial z_g} \, D \, dS_g \, dS_s \quad , \tag{68}$$

where D in the integrand = D(on measurement surface), $\partial G_0^{-D}/\partial z_s$ = anticausal Green's function with Dirichlet boundary condition on the measurement surface, s = shot, and g = receiver. For two-way wave double downward continuation:

$$\begin{aligned} D(\text{at depth}) \quad &= \quad \int_{S_s} \left[\frac{\partial G_0^{DN}}{\partial z_s} \int_{S_g} \left\{ \frac{\partial G_0^{DN}}{\partial z_g} \, D + \frac{\partial D}{\partial z_g} G_0^{DN} \right\} dS_g \right. \\ &+ \quad \left. G_0^{DN} \frac{\partial}{\partial z_s} \int_{S_g} \left\{ \frac{\partial G_0^{DN}}{\partial z_g} \, D + \frac{\partial D}{\partial z_g} G_0^{DN} \right\} dS_g \right] dS_s \quad , \end{aligned} \tag{69}$$

where D in the integrands = D(on measurement surface). G_0^{DN} is *neither* causal nor anticausal. G_0^{DN} is not an *anti*causal Green's function; it is not the inverse or adjoint of any physical propagating Green's function. It is the Green's function needed for RTM. G_0^{DN} is the Green's function for the model of the finite volume that vanishes along with its normal derivative on the lower surface and the walls. If we want to use the anticausal Green's function of the two-way propagation with Dirichlet boundary conditions at the measurement surface then we can do that, but we will need measurements at depth and on the vertical walls. To have the Green's function for two-way propagation that doesn't need data at depth and on the vertical sides/walls, that requires a non-physical Green's function that vanishes along with its derivative on the lower surface and walls.

In the Inverse Scattering Series (ISS) model (sketch 4 in Fig. 2) the Lippmann-Schwinger (LS) equation over all space, rather than Green's theorem, is called upon and the Lippmann-Schwinger equation requires no imposed boundary conditions on S since all boundary conditions are already incorporated in LS from linearity/superposition and causality. See, e.g., Weglein et al. (2003), Stolt and Jacobs (1980), Weglein et al. (2009), and Weglein et al. (2006).

The appropriate Green's function, for a closed surface integral in Green's theorem, with an arbitrary and known medium within the volume can be satisfied with *any* Green's function satisfying the propagation properties within the volume and with Dirichlet, Neumann, or Robin boundary conditions on the closed surface. The issue and/or problem in exploration reflection seismology is the measurements are only on the upper surface.

Why Green's theorem for migration algorithms?

1. Allows a wave theoretical platform/framework for wave-field prediction from surface measurements that builds on quantitative and potential field theory history and evolution.

2. Allows $(\mathbf{x},\omega)$ processing without transform artifacts and yet is wave theoretic in a $(\mathbf{x},\omega)$ world where up-down is not so simple to define as in $(\mathbf{k},\omega)$. Deghosting (Zhang (2007)) and wavelet estimation (Weglein and Secrest (1990)) are other examples where Green's theorem provides $(\mathbf{x},\omega)$ advantage.

3. Allows avoidance of very common pitfalls and erroneous algorithm derivations based on qualitative (at best) methods launched from Huygens' principle or discrete matrix inverses and it allows the wave theoretic imaging conditions introduced by Clayton and Stolt (1981) and Stolt and Weglein (1985) to be used rather than the lesser cross-correlation of wave-field imaging concepts.

Backpropagation is quantitative from Green's theorem rather than these G_0^{-1}, G_0^*, less wave theoretic more generalized inverse, discrete matrix thinking approaches for backpropagation. For RTM and Green's theorem the data, D, at depth is definitely *not*

$$D \neq \int G_{0S}^{-1} \int G_{0R}^{-1} D \qquad \text{(Huygens)} \quad , \tag{70}$$

where G_0^- indicates an anticausal Green's function. This is OK with Huygens but *violates Green's theorem* and the equation is not dimensionally consistent with the right hand side not having the dimension of data, D. The data, D, at depth for *one-way* waves is

$$D = \int_{S_s} \frac{\partial G_0^{-D}}{\partial z_s} \int_{S_g} \frac{\partial G_0^{-D}}{\partial z_g} D \, dS_g \, dS_s \qquad \text{(Green)} \quad , \tag{71}$$

where D = Dirichlet boundary condition on top and G_0^- anticausal. This is OK with Green but not for two-way RTM propagation. The data, D, at depth for *two-way* waves is

$$\begin{aligned} D &= \int_{S_s} \left[\frac{\partial G_0^{DN}}{\partial z_s} \int_{S_g} \left\{ \frac{\partial G_0^{DN}}{\partial z_g} D + \frac{\partial D}{\partial z_g} G_0^{DN} \right\} dS_g \right. \\ &+ \left. G_0^{DN} \frac{\partial}{\partial z_s} \int_{S_g} \left\{ \frac{\partial G_0^{DN}}{\partial z_g} D + \frac{\partial D}{\partial z_g} G_0^{DN} \right\} dS_g \right] dS_s \qquad \text{(Green)} \quad , \end{aligned} \tag{72}$$

where DN = Dirichlet and Neumann boundary conditions to be imposed on bottom and walls and G_0^{DN} is neither causal nor anticausal nor a combination. Please see Fig. 3.

COMMENTS AND FUTURE DEVELOPMENTS

In this manuscript, we provide a firm foundation for RTM based on Green's theorem. As in the case of interferometry (Ramírez and Weglein (2009)) misuse, abuse and/or misunderstanding of Green's theorem in RTM has also led to strange and curious interpretations, and to opinions being offered about the cause of artifacts and observed problems and communicating 'deep new insights' that are neither new nor accurate. We communicate here to simply understand and stick with

Green's theorem as the guide and solution in both cases, interferometry and RTM. The original RTM methods of running the wave equation backwards with surface reflection data as a boundary condition is not a wave theory method for wave-field prediction, neither in depth nor in reversed time. In Huygens' principle the wave-field prediction doesn't have the dimension of a wave-field. In fact that idea corresponds to the Huygens' principle idea (Huygens (1690)) which was made into a wave theory predictor by George Green in 1826.

ACKNOWLEDGEMENTS

We thank the M-OSRP sponsors, NSF-CMG award DMS-0327778 and DOE Basic Sciences award DE-FG02-05ER15697 for supporting this research. R. H. Stolt thanks ConocoPhillips for permission to publish. We thank Lasse Amundsen of Statoil and Adriana Ramírez and Einar Otnes of WesternGeco for useful discussions and suggestions regarding RTM. We thank Xu Li, Shih-Ying Hsu, Zhiqiang Wang and Paolo Terenghi of M-OSRP for useful comments and assistance in typing the manuscript.

APPENDIX A: CONFIRMATION THAT THE GREEN'S FUNCTION EQ. (14), WHEN USED IN GREEN'S THEOREM, WILL PRODUCE A TWO-WAY WAVE FOR $A < Z < B$ WITH ONLY MEASUREMENTS ON THE UPPER SURFACE.

$$
\begin{aligned}
& P(z,\omega) \\
= & \int_a^b dz' \left(\underbrace{\frac{-1}{2ik} e^{-ikz} e^{ikz'} + \frac{1}{2ik} e^{ik|z-z'|}}_{G_0(z,z',\omega)} \right) \underbrace{\rho(z',\omega)}_{0} \\
& + |_a^b \left((\underbrace{Ae^{ikz'} + Be^{-ikz'}}_{P(z',\omega)}) \left(\underbrace{\frac{-1}{2ik} e^{-ikz} e^{ikz'} ik + \frac{1}{2ik} e^{ik|z-z'|} ik \ \operatorname{sgn}(z-z')(-1)}_{\frac{dG_0(z,z',\omega)}{dz'}} \right) \right. \\
& \left. - \left(\underbrace{\frac{-1}{2ik} e^{-ikz} e^{ikz'} + \frac{1}{2ik} e^{ik|z-z'|}}_{G_0(z,z',\omega)} \right) (\underbrace{Ae^{ikz'} ik + Be^{-ikz'}(-ik)}_{\frac{dP(z',\omega)}{dz'}}) \right) \\
= & \frac{-1}{2} |_a^b (\cancel{Ae^{ik(2z'-z)}} + A \ \operatorname{sgn}(z-z') e^{ikz'} e^{ik|z-z'|} \\
& + Be^{-ikz} + B \ \operatorname{sgn}(z-z') e^{-ikz'} e^{ik|z-z'|} \\
& - \cancel{Ae^{ik(2z'-z)}} + Ae^{ikz'} e^{ik|z-z'|} + Be^{-ikz} - Be^{-ikz'} e^{ik|z-z'|}) \\
= & \frac{-1}{2} (A \underbrace{\operatorname{sgn}(z-b)}_{-1} e^{ikb} e^{ik\underbrace{|z-b|}_{b-z}} \\
& + \cancel{Be^{-ikz}} + B \underbrace{\operatorname{sgn}(z-b)}_{-1} e^{-ikb} e^{ik\underbrace{|z-b|}_{b-z}} \\
& + Ae^{ikb} e^{ik\underbrace{|z-b|}_{b-z}} + \cancel{Be^{-ikz}} - Be^{-ikb} e^{ik\underbrace{|z-b|}_{b-z}} \\
& - A \underbrace{\operatorname{sgn}(z-a)}_{1} e^{ika} e^{ik\underbrace{|z-a|}_{z-a}} \\
& - \cancel{Be^{-ikz}} - B \underbrace{\operatorname{sgn}(z-a)}_{1} e^{-ika} e^{ik\underbrace{|z-a|}_{z-a}} \\
& - Ae^{ika} e^{ik\underbrace{|z-a|}_{z-a}} - \cancel{Be^{-ikz}} + Be^{-ika} e^{ik\underbrace{|z-a|}_{z-a}}) \\
= & \frac{-1}{2} (-\cancel{Ae^{ik(2b-z)}} - Be^{-ikz} + \cancel{Ae^{ik(2b-z)}} - Be^{-ikz} \\
& - Ae^{ikz} - \cancel{Be^{-ik(2a-z)}} - Ae^{ikz} + \cancel{Be^{-ik(2a-z)}}) \\
= & \frac{-1}{2} (-2Ae^{ikz} - 2Be^{-ikz}) \\
= & Ae^{ikz} + Be^{-ikz}
\end{aligned}
$$

APPENDIX B: EVALUATING A_1, B_1, C_1, AND D_1 IN EQ. (39).

For $z' > a$ choose C_1 and D_1 such that

$$\begin{aligned}
G(z,B,\omega) &= 0 \quad \text{and} \\
\left[\frac{dG}{dz'}(z,z',\omega)\right]_{z'=B} &= 0 \\
\implies \frac{T}{2ik}e^{ik|a-z|}e^{ik_1(B-a)} + C_1e^{ik_1B} + D_1e^{-ik_1B} &= 0 \\
\frac{T}{2ik}e^{ik|a-z|}e^{ik_1(B-a)}ik_1 + C_1e^{ik_1B}ik_1 + D_1e^{-ik_1B}(-ik_1) &= 0 \\
\implies C_1e^{ik_1B} + D_1e^{-ik_1B} &= -\frac{T}{2ik}e^{ik|a-z|}e^{ik_1(B-a)} \\
C_1e^{ik_1B} - D_1e^{-ik_1B} &= -\frac{T}{2ik}e^{ik|a-z|}e^{ik_1(B-a)}
\end{aligned}$$

Adding and subtracting give

$$\begin{aligned}
2C_1e^{ik_1B} &= -\frac{2T}{2ik}e^{ik|a-z|}e^{ik_1(B-a)} \\
C_1 &= -\frac{T}{2ik}e^{ik|a-z|}e^{-ik_1a} \\
2D_1e^{-ik_1B} &= 0 \\
D_1 &= 0
\end{aligned}$$

For $z' = a$ choose A_1 and B_1 such that

$$\begin{aligned}
G(z,a,\omega)|_{z'<a} &= G(z,a,\omega)|_{z'>a} \quad \text{and} \\
\left[\frac{dG}{dz'}(z,z',\omega)\right]_{z'<a \text{ at } z'=a} &= \left[\frac{dG}{dz'}(z,z',\omega)\right]_{z'>a \text{ at } z'=a} \\
\implies \frac{e^{ik|a-z|}}{2ik} + R\frac{\overbrace{e^{-ik(a-a)}}^{1}}{2ik}e^{ik(a-z)} + A_1e^{ika} + B_1e^{-ika} &= \\
\frac{T}{2ik}e^{ik|a-z|}\underbrace{e^{ik_1(a-a)}}_{1} + \underbrace{C_1}_{-(T/2ik)e^{ik|a-z|}e^{-ik_1a}}e^{ik_1a} + \underbrace{D_1}_{0}e^{-ik_1a} & \\
\frac{e^{ik|a-z|}}{2ik}ik\,sgn(a-z) + R\frac{\overbrace{e^{-ik(a-a)}}^{1}}{2ik}(-ik)e^{ik(a-z)} + A_1e^{ika}ik + B_1e^{-ika}(-ik) & \\
\frac{T}{2ik}e^{ik|a-z|}\underbrace{e^{ik_1(a-a)}}_{1}ik_1 & \\
+ \underbrace{C_1}_{-(T/2ik)e^{ik|a-z|}e^{-ik_1a}}e^{ik_1a}ik_1 + \underbrace{D_1}_{0}e^{-ik_1a}(-ik_1) &
\end{aligned}$$

$$\implies \frac{e^{ik|a-z|}}{2ik} + \frac{R}{2ik}e^{ik(a-z)} + A_1 e^{ika} + B_1 e^{-ika} = \frac{T}{2ik}e^{ik|a-z|} - \frac{T}{2ik}e^{ik|a-z|} = 0$$

$$\frac{1}{2}\,sgn(a-z)e^{ik|a-z|} - \frac{R}{2}e^{ik(a-z)} + A_1 ike^{ika} - B_1 ike^{-ika} = \frac{Tik_1}{2ik}e^{ik|a-z|} - \frac{Tik_1}{2ik}e^{ik|a-z|} = 0$$

$$\implies A_1 e^{ika} + B_1 e^{-ika} = -\frac{e^{ik|a-z|}}{2ik} - \frac{R}{2ik}e^{ik(a-z)}$$

$$A_1 e^{ika} - B_1 e^{-ika} = -\frac{1}{2ik}\,sgn(a-z)e^{ik|a-z|} + \frac{R}{2ik}e^{ik(a-z)}$$

Adding and subtracting give

$$2A_1 e^{ika} = -\frac{1}{2ik}e^{ik|a-z|}(1+sgn(a-z))$$

$$A_1 = -\frac{1}{4ik}e^{-ika}e^{ik|a-z|}(1+sgn(a-z))$$

$$2B_1 e^{-ika} = -\frac{1}{2ik}e^{ik|a-z|}(1-sgn(a-z)) - \frac{2R}{2ik}e^{ik(a-z)}$$

$$B_1 = -\frac{1}{4ik}e^{ika}e^{ik|a-z|}(1-sgn(a-z)) - \frac{2R}{4ik}e^{ik(2a-z)} = -\frac{1}{4ik}(e^{ika}e^{ik|a-z|}(1-sgn(a-z)) + 2Re^{ik(2a-z)})$$

Check:

$$\begin{aligned}
&G(z,a,\omega)|_{z'<a} - G(z,a,\omega)|_{z'>a} \\
=&\frac{e^{ik|a-z|}}{2ik} + \frac{R}{2ik}e^{ik(a-z)} + \left(-\frac{1}{4ik}e^{-ika}e^{ik|a-z|}(1+sgn(a-z))\right)e^{ika} \\
&+ \left(-\frac{1}{4ik}(e^{ika}e^{ik|a-z|}(1-sgn(a-z)) + 2Re^{ik(2a-z)})\right)e^{-ika} \\
&- \frac{T}{2ik}e^{ik|a-z|} - \left(-\frac{T}{2ik}e^{ik|a-z|}e^{-ik_1 a}\right)e^{ik_1 a} - (0)e^{-ik_1 a} \\
=&\underbrace{\frac{1}{2ik}e^{ik|a-z|}}_{\text{cancels 1}}\underbrace{+\frac{R}{2ik}e^{ik(a-z)}}_{\text{cancels 2}}\underbrace{-\frac{1}{4ik}e^{ik|a-z|}}_{\text{cancels 1}}\underbrace{-\frac{1}{4ik}e^{ik|a-z|}sgn(a-z)}_{\text{cancels 3}} \\
&\underbrace{-\frac{1}{4ik}e^{ik|a-z|}}_{\text{cancels 1}}\underbrace{+\frac{1}{4ik}e^{ik|a-z|}sgn(a-z)}_{\text{cancels 3}}\underbrace{-\frac{2R}{4ik}e^{ik(a-z)}}_{\text{cancels 2}} \\
&\underbrace{-\frac{T}{2ik}e^{ik|a-z|}}_{\text{cancels 4}}\underbrace{+\frac{T}{2ik}e^{ik|a-z|}}_{\text{cancels 4}} \\
=&0 \quad \text{as desired}
\end{aligned}$$

REFERENCES

Baysal, E., D. D. Kosloff, and J. W. C. Sherwood, 1983, Reverse time migration: Geophysics, **48**, 1514–1524.

Berkhout, A. J., 1997, Pushing the limits of seismic imaging, Part II: integration of prestack migration, velocity estimation, and AVO analysis: Geophysics, **62**, 954–969.

Born, M., and E. Wolf, 1999, Principles of Optics: Electromagnetic Theory of Propagation, Interference, and Diffraction of Light, 7th ed.: Cambridge University Press.

Claerbout, J. F., 1992, Earth soundings analysis: Processing versus inversion: Blackwell Scientific Publications, Inc.

Clayton, R. W., and R. H. Stolt, 1981, A Born-WKBJ inversion method for acoustic reflection data: Geophysics, **46**, 1559–1567.

Crawley, S., S. Brandsberg-Dahl, J. McClean, and N. Chemingui, 2010, Tti reverse time migration using the pseudo-analytic method: The Leading Edge, **29**, 1378–1384.

Dong, S., Y. Luo, X. Xiao, S. Chávez-Pérez, and G. T. Schuster, 2009, Fast 3D target-oriented reverse-time datuming: Geophysics, **74**, WCA141–WCA151.

Esmersoy, C., and M. Oristaglio, 1988, Reverse-time wave-field extrapolation, imaging, and inversion: Geophysics, **53**, 920–931.

Etgen, J. T., and R. J. Michelena, 2010, Introduction to this special section: Reverse time migration: The Leading Edge, **29**, 1363–1363.

Fletcher, R., P. Fowler, P. Kitchenside, and U. Albertin, 2006, Suppressing unwanted internal reflections in prestack reverse-time migration: Geophysics, **71**, E79–E82.

Green, G., 1828, An essay on the application of mathematical analysis to the theories of electricity and magnetism: Privately published.

Higginbotham, J., M. Brown, C. Macesanu, and O. Ramirez, 2010, Onshore wave-equation depth imaging and velocity model building: The Leading Edge, **29**, 1386–1392.

Huygens, C., 1690, Traité de la lumiere: Pieter van der Aa.

Jin, S., and S. Xu, 2010, Visibility analysis for target-oriented reverse time migration and optimizing acquisition parameters: The Leading Edge, **29**, 1372–1377.

Liu, F., A. Weglein, K. Innanen, and B. G. Nita, 2006, Multi-dimensional seismic imaging using the inverse scattering series, *in* 76th Annual International Meeting, SEG, Expanded Abstracts: Soc. Expl. Geophys., **25**, 3026–3030.

Liu, F., G. Zhang, S. A. Morton, and J. P. Leveille, 2009, An optimized wave equation for seismic modeling and reverse time migration: Geophysics, **74**, WCA153–WCA158.

Luo, Y., and G. T. Schuster, 2004, Bottom-up target-oriented reverse-time datuming: CPS/SEG Geophysics Conference and Exhibition, F55.

McMechan, G. A., 1983, Migration by extrapolation of time dependent boundary values: Geophysical Prospecting, **31**, 413–420.

Morse, P. M., and H. Feshbach, 1953, Methods of theoretical physics: McGraw-Hill Book Co.

Ramírez, A. C., and A. B. Weglein, 2009, Green's theorem as a comprehensive framework for data reconstruction, regularization, wavefield separation, seismic interferometry, and wavelet estimation: a tutorial: Geophysics, **74**, W35–W62.

Schneider, W. A., 1978, Integral formulation for migration in two and three dimensions: Geophysics, **43**, 49–76.

Stolt, R. H., 1978, Migration by Fourier transform: Geophysics, **43**, 23–48.

Stolt, R. H., and B. Jacobs, 1980, Inversion of seismic data in a laterally heterogenous medium: Technical Report 24, SEP, Tulsa, OK.

Stolt, R. H., and A. B. Weglein, 1985, Migration and inversion of seismic data: Geophysics, **50**, 2458–2472.

Symes, W. W., 2007, Reverse-time migration with optimal checkpinting: Geophysics, **72**, SM213–SM221.

Toselli, A., and O. Widlund, 2000, Domain Decomposition Methods –Algorithms and Theory: Springer-Verlag.

Weglein, A. B., F. V. Araújo, P. M. Carvalho, R. H. Stolt, K. H. Matson, R. T. Coates, D. Corrigan, D. J. Foster, S. A. Shaw, and H. Zhang, 2003, Inverse scattering series and seismic exploration: Inverse Problems, **19**, R27–R83.

Weglein, A. B., F. A. Gasparotto, P. M. Carvalho, and R. H. Stolt, 1997, An inverse-scattering series method for attenuating multiples in seismic reflection data: Geophysics, **62**, 1975–1989.

Weglein, A. B., B. G. Nita, K. A. Innanen, E. Otnes, S. A. Shaw, F. Liu, H. Zhang, A. C. Ramírez, J. Zhang, G. L. Pavlis, and C. Fan, 2006, Using the inverse scattering series to predict the wavefield at depth and the transmitted wavefield without an assumption about the phase of the measured reflection data or back propagation in the overburden: Geophysics, **71**, SI125–SI137.

Weglein, A. B., and B. G. Secrest, 1990, Wavelet estimation for a multidimensional acoustic earth model: Geophysics, **55**, 902–913.

Weglein, A. B., R. H. Stolt, and J. D. Mayhan, 2011, Reverse-time migration and green's theorem: Part i — the evolution of concepts, and setting the stage for the new rtm method: Journal of Seismic Exploration.

Weglein, A. B., H. Zhang, A. C. Ramírez, F. Liu, and J. E. M. Lira, 2009, Clarifying the underlying and fundamental meaning of the approximate linear inversion of seismic data: Geophysics, **74**, WCD1–WCD13.

Whitmore, D. N., 1983, Iterative depth imaging by back time propagation, *in* 53^{rd} Annual International Meeting, SEG, Expanded Abstracts: Soc. Expl. Geophys., 382–385.

Zhang, J., 2007, Wave theory based data preparation for inverse scattering multiple removal, depth imaging and parameter estimation: analysis and numerical tests of green's theorem deghosting theory: PhD thesis, University of Houston.

Zhang, Y., J. Sun, and S. Gray, 2007, Reverse-time migration: amplitude and implementation issues, *in* 77th Annual International Meeting, SEG, Expanded Abstracts: Soc. Expl. Geophys., **25**, 2145–2149.

Zhang, Y., S. Xu, B. Tang, B. Bai, Y. Huang, and T. Huang, 2010, Angle gathers from reverse time migration: The Leading Edge, **29**, 1364–1371.

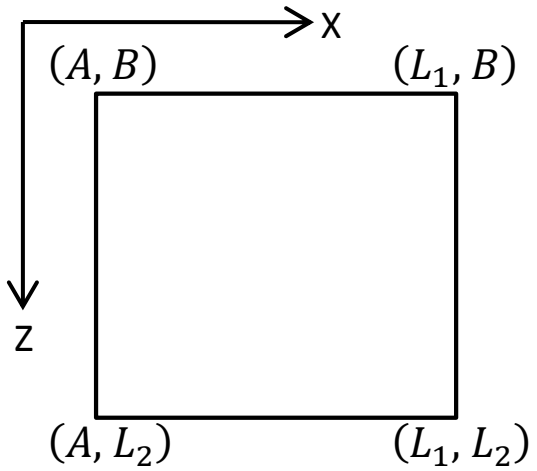

Figure 1: *Two dimensional finite volume model*

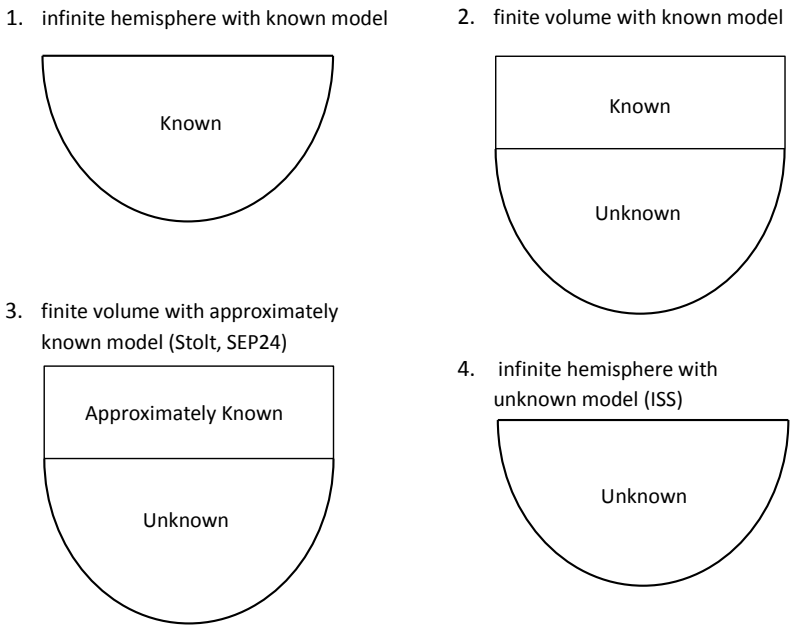

Figure 2: *Backpropagation model evolution*

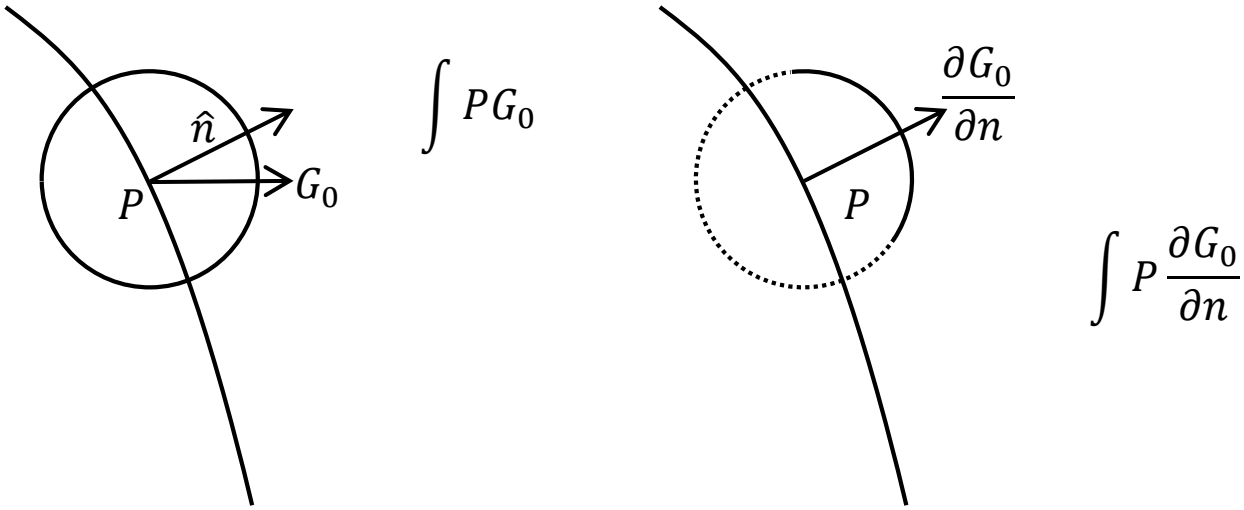

Figure 3: *Qualitative vs. quantitative wave propagation:*
(Left) Huygens (1690), and e.g., Whitmore (1983), McMechan (1983), Fletcher et al. (2006), Berkhout (1997), Claerbout (1992), Dong et al. (2009), Luo and Schuster (2004)
(Right) Green (1828), and e.g., Morse and Feshbach (1953), Born and Wolf (1999), Stolt (1978), Schneider (1978), Esmersoy and Oristaglio (1988), Weglein and Secrest (1990), Weglein et al. (1997), Liu et al. (2006), Ramírez and Weglein (2009), and Weglein et al. (2011)

Green's theorem derived methods for preprocessing seismic data when the pressure P and its normal derivative are measured

James D. Mayhan[*], *Paolo Terenghi*[*], *Arthur B. Weglein*[*], *and Nizar Chemingui*[†], *M-OSRP/Physics Dept./UH*[*] *and PGS*[†]

Summary

We discuss deghosting of marine seismic data using Green's theorem. Deghosting is put into context in the complete M-OSRP processing chain, Green's theorem derived theory is presented, and an algorithm implementing the theory is discussed. The algorithm has been tested on field data and several kinds of synthetic data with positive and encouraging results.

Introduction

The inverse scattering series (ISS) can perform certain tasks (e.g., free surface multiple elimination) without a priori estimates of the spatial distribution of velocity. The Mission-Oriented Seismic Research Program (M-OSRP) has generated algorithms to accomplish seismic data processing goals based on the ISS (free surface multiple elimination, internal multiple removal, depth imaging, nonlinear direct AVO, and Q compensation) and Green's theorem (deghosting, source signature estimation, and data reconstruction). While the ISS is independent of subsurface velocity (and in fact of all subsurface properties), it is data dependent and makes certain assumptions about its input data. Weglein et al. (2003) describe how every ISS isolated task subseries requires (1) the removal of the reference wavefield, (2) an estimate of the source signature and radiation pattern, and (3) source and receiver deghosting and how the ISS has a nonlinear dependence on these preprocessing steps. Therefore, the Green's theorem deghosting methods are critically important to the success of the inverse series methods since they may be used to bring seismic data in line with the assumptions of inverse scattering. The fact that the ISS is nonlinear places a higher bar on preprocessing. An error in the input to a linear process creates a linear error in its output, but the same error in ISS input creates linear, quadratic, cubic, etc. errors in its output.

A brief aside on terminology. The total wavefield P consists of the reference wavefield P_0 (which doesn't experience the earth) and the scattered wavefield P_s (which does experience the earth). Ghosts begin their propagation moving upward from the source (source ghosts) or end their propagation moving downward to the receiver (receiver ghosts) or both (source/receiver ghosts) and have at least one upward reflection from the earth. Free surface multiples have at least one downward reflection from the free surface (air-water interface) and at least one upward reflection from the earth. Internal multiples have no downward reflections from the free surface, more than one upward reflection from the earth, and at least one downward reflection from inside the earth. An nth order internal multiple has n downward reflections from the earth. Primaries have only one upward reflection from the earth.

The freedom of choosing a convenient reference medium means Green's theorem offers a flexible framework for defining a number of useful algorithms — wavefield separation (reference and scattered), wavelet estimation, ghost removal, and two way wavefield continuation (RTM). Green's theorem methods are exact (fully consistent with the wave equation), multidimensional, make no assumptions about the earth, and work in the $(\omega, \mathbf{r})$ data space (and hence are simple to apply to irregularly spaced data). Therefore, Green's theorem preprocessing methods and ISS isolated task subseries are fully consistent.

This paper is focused on the deghosting prerequisite. Deghosting is important because (1) it is a prerequisite for many processing algorithms including data driven multiple elimination (ISS free surface multiples and internal multiples and SRME) and imaging (wavefield continuation often assumes one way waves), and (2) removing the downward component of the field enhances seismic resolution and boosts the low frequencies. Deghosting has benefit for both traditional seismic processing as well as providing an important role in all ISS based isolated task processing. For a discussion of the ISS see Liu et al. (2011).

Theory

The ISS is based on perturbation theory, and Green's theorem based preprocessing utilizes perturbation theory. A reference medium (and its associated Green's function) is chosen to facilitate solving the problem at hand, and the perturbation is the real world properties minus the reference medium. Within that framework, Green's theorem based preprocessing is remarkably wide ranging. For example, Fig. 1 shows the configuration chosen for Green's theorem deghosting. Choosing a reference medium consisting of a whole space of water, a hemispherical surface of integration bounded below by the measurement surface, and the prediction/observation point inside the surface of integration gives deghosted data $P^{deghosted}$. A different choice of a reference medium (a half space of air and a half space of water and the prediction/observation point outside/inside the surface of integration) gives wavefield separation in which the total wavefield P is separated into the reference

wavefield P_0 and scattered wavefield P_s. It should be noted that several processing algorithms for multiple elimination (including the ISS) assume deghosting has been performed on the data and that an accurate estimate of the source wavelet is available.

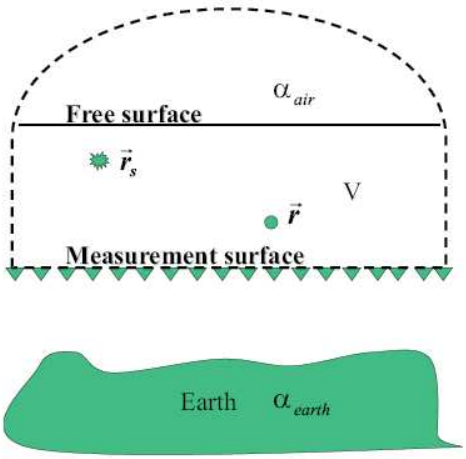

Fig. 1: *Configuration for deghosting using Green's theorem (Zhang, 2007). α_{air} and α_{earth} are perturbations, the differences between the actual medium (air, water, earth) and reference medium (water).*

Deghosting (both receiver and source side) is based on Zhang and Weglein (2005), Zhang and Weglein (2006), and Zhang (2007). The theory assumes measurement of the pressure wavefield P and its normal derivative $\partial P/\partial n \equiv \nabla P(\mathbf{r}', \mathbf{r}_s, \omega) \cdot \hat{n}$ where $\mathbf{r}'$ is the measurement point, $\mathbf{r}_s$ is the location of the air gun array, and $\hat{n}$ is the normal to the measurement surface. The reference medium is a whole space of water (where a causal, analytic solution exists for the acoustic wave equation) and the prediction point is between the free surface and the measurement surface, i.e., inside the volume V bounded by the closed surface of integration consisting of the measurement surface and dashed line in Fig. 1.

Using the above configuration and Green's theorem gives the key equation

$$P^{deghosted}(\mathbf{r}, \mathbf{r}_s, \omega) = \oint_S dS\, \hat{n} \cdot \qquad (1)$$
$$[P(\mathbf{r}', \mathbf{r}_s, \omega)\nabla' G_0^d(\mathbf{r}, \mathbf{r}', \omega) - G_0^d(\mathbf{r}, \mathbf{r}', \omega)\nabla' P(\mathbf{r}', \mathbf{r}_s, \omega)],$$

(Zhang, 2007, Eq. (2.23)) where $\mathbf{r}$ is the prediction point, $\mathbf{r}_s$ is the location of the air gun array, S is the closed surface consisting of the measurement surface and dashed line in Fig. 1, $\hat{n}$ is the normal to S (pointing away from the enclosed volume V), $\mathbf{r}'$ is the measurement point, and G_0^d is a whole space Green's function. Extending the radius of the hemisphere to infinity, invoking the Sommerfeld radiation condition, and assuming a horizontal measurement surface, the integral over the closed surface becomes an integral over the measurement surface:

$$P^{deghosted}(\mathbf{r}, \mathbf{r}_s, \omega) = \int_{m.s.} dS \qquad (2)$$
$$[P(\mathbf{r}', \mathbf{r}_s, \omega)\frac{\partial}{\partial z'} G_0^d(\mathbf{r}, \mathbf{r}', \omega) - G_0^d(\mathbf{r}, \mathbf{r}', \omega)\frac{\partial}{\partial z'} P(\mathbf{r}', \mathbf{r}_s, \omega)]$$

(Zhang, 2007, Eq. (2.24)). In 3D $G_0^d(\mathbf{r}, \mathbf{r}', \omega) = -1/(4\pi)\exp(ikR_+)/R_+$ where $k = \omega/c_0$, c_0 is the speed of sound in the reference medium, and $R_+ = |\mathbf{r} - \mathbf{r}'|$. In 2D $G_0^d(\mathbf{r}, \mathbf{r}', \omega) = -i/4\, H_0^{(1)}(kR_+)$ where $H_0^{(1)}$ is the zeroth order Hankel function of the first kind (Morse and Feshbach, 1953, pp. 810-811).

The implementation of the above theory is done in a straightforward manner. The Green's theorem algorithm computes the surface integral in Eq. (2). The method requires two wavefields as input, the pressure measurements P and their normal derivatives $\partial P/\partial z'$. The latter requires dual sensor cables or dual streamer cables. Source side deghosting is straightforward and amounts to applying reciprocity to exchange sources and receivers. Our illustrations will focus on receiver side deghosting.

Example: Flat layer model

The left panel of Fig. 2 shows synthetic data (produced using ray tracing in a flat layer model) designed so that deghosting is easy to demonstrate. The depth of the receivers is chosen such that primaries and ghosts appear as distinct seismic events. The right panel of Fig. 2 shows Green's theorem output using Eq. (2; note the primary's receiver side ghost at 0.45s and the free surface multiple's receiver side ghost at 0.85s are suppressed. Fig. 3 shows the spectra of the input data (blue) and receiver side deghosted output (red). As expected, the receiver side deghosted data fills in notches related to receiver ghosts.

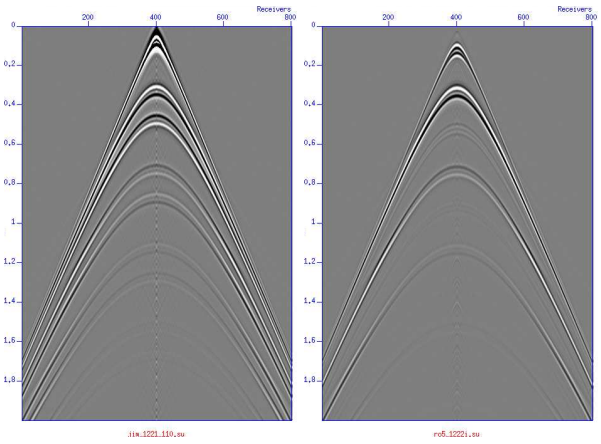

Fig. 2: *Flat layer model (source at 30m, cable at 140m, water bottom at 300m): input data at 110m (left), receiver side deghosted at 100m (right).*

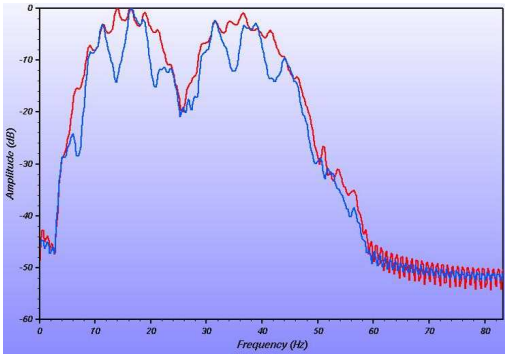

Fig. 3: *Flat layer model: muted input data (blue), receiver side deghosted (red). The receiver notches (at intervals of 5.4Hz) have been filled in; the notch at 25Hz is a source notch.*

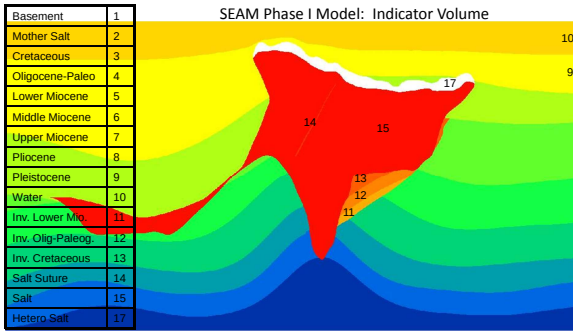

Fig. 4: *SEAM deepwater Gulf of Mexico model: inline section from the middle of the model. Figure courtesy of SEAM.*

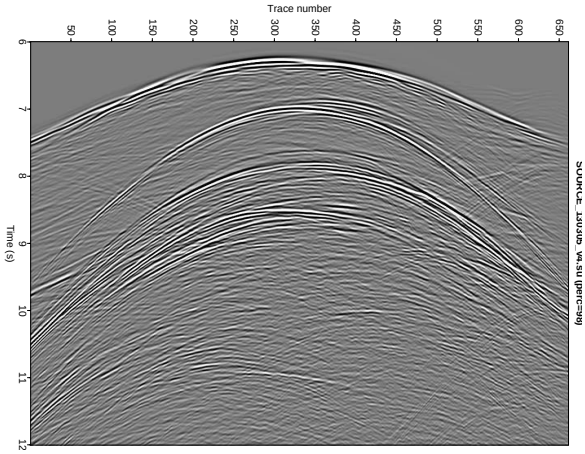

Fig. 5: *SEAM data, shot 130305 (located at sx=16975m, sy=20000m, sz=15m near center of shot grid).*

Example: SEAM application

We applied Green's theorem to the SEAM dataset generated based on a deepwater Gulf of Mexico earth model (Fig. 4) (Society of Exploration Geophysicists, 2011). We used the special SEAM classic dataset modeled to simulate dual sensor acquisition by recording the pressure wavefield at two different depths, 15 and 17m respectively. This dual sensor data consisted of nine sail lines for an equivalent wide azimuth towed streamer survey. The source interval is 150m by 150m while the receiver interval is 30m in both inline and crossline directions. Fig. 5 displays a typical shot gather from the SEAM model. Given the low frequency of the data (less than 30Hz) and the source and receiver depths of 15m and 17m, the ghost reflections are not as separable as in the previous flat layer model. In this situation, successful deghosting would correspond to a change in the wavelet shape. Fig. 6 shows SEAM input (a window of Fig. 5) and receiver side deghosted output computed by the Green's theorem approach. In the right panel of Fig. 6, note the collapsed wavelet. In Fig. 7, note the increased amplitude in lower frequencies and decreased amplitude in higher frequencies, i.e., the shift of the amplitude spectrum towards low frequencies. This is supported by the integral formulation in Eq. (2) which acts like a low pass filter.

Example: Field data

We also applied the deghosting approach to a field survey from the deep water Gulf of Mexico. The data were acquired using dual sensor streamers comprised of hydrophones and vertical geophones. The left panel in Fig. 8 shows a close up on an input shot record while the right panel displays the same traces after receiver side deghosting. Note the collapsed wavelet in the output image. This is also demonstrated in Fig. 9 that compares the amplitude spectra before and after deghosting. As expected, the deghosting solution successfully removed the notches from the spectrum that are associated with the receiver ghost.

Conclusions

We have implemented deghosting based on Green's theorem and have tested the algorithm on field data and several kinds of synthetic data. Testing to date has shown the algorithm works as expected.

ACKNOWLEDGMENTS

We are grateful to the M-OSRP sponsors for their support of this research. The first author (JDM) is grateful to Arthur B. Weglein for his mentoring, Fang Liu and Paolo Terenghi for their teaching, and ExxonMobil and PGS for internships.

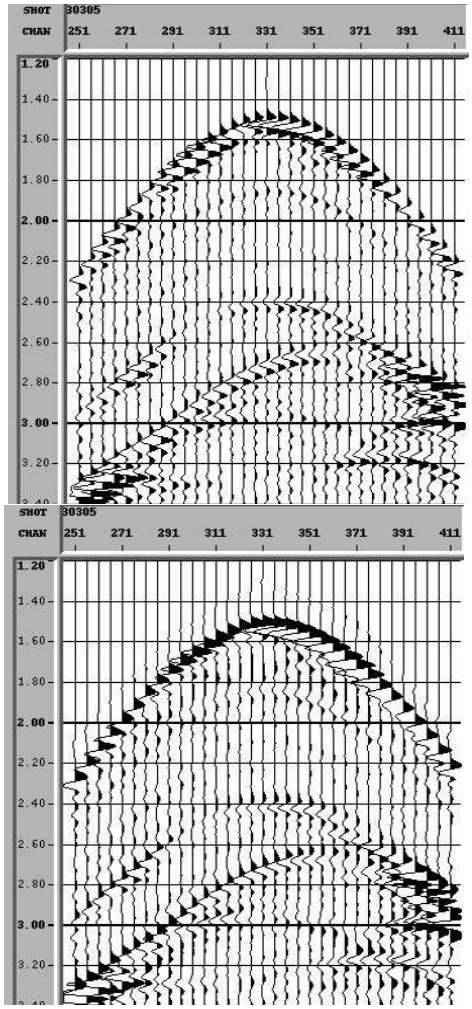

Fig. 6: *SEAM data, shot 130305: recorded data (top), receiver side deghosted at free surface (bottom). Note the collapsed wavelet in the bottom panel.*

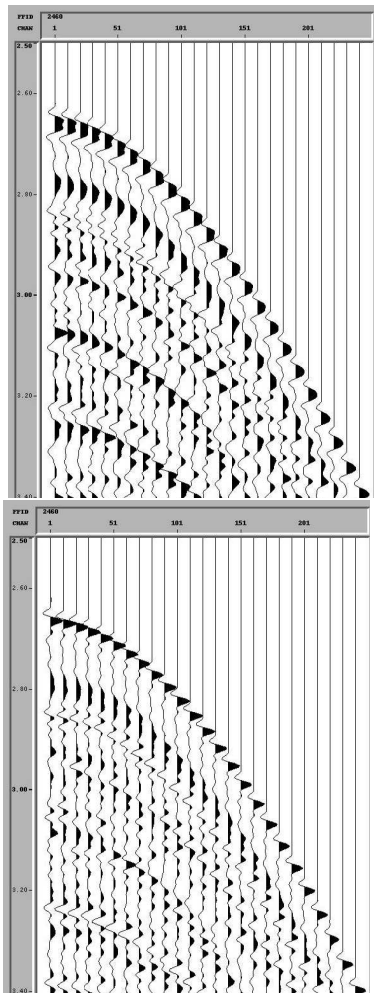

Fig. 8: *Field data: hydrophones (top), receiver side deghosted at free surface (bottom). Note the collapsed wavelet in the bottom panel. Input data courtesy of PGS.*

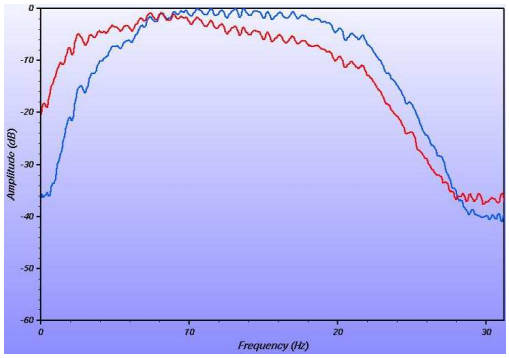

Fig. 7: *SEAM data: shot 130305: recorded data (blue), receiver side deghosted (red). Note the shift of the spectrum towards lower frequencies (first receiver notch is at 50 Hz).*

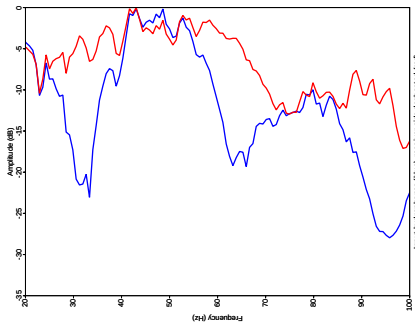

Fig. 9: *Field data: muted hydrophones (blue), receiver side deghosted (red). The receiver notches around 30 Hz, 60 Hz, and 90 Hz have been filled in. Input data courtesy of PGS.*

References

Liu, F., X. Li, A. B. Weglein, P. Terenghi, E. Kragh, H. Liang, J. D. Mayhan, L. Tang, S.-Y. Hsu, Z. Wang, J. Mispel, and L. Amundsen, 2011, Inverse scattering series depth imaging: First field data examples, *in* 81st Annual International Meeting, SEG, Expanded Abstracts: Soc. Expl. Geophys. (submitted).

Morse, P. M., and H. Feshbach, 1953, Methods of theoretical physics: McGraw-Hill Book Co.

Society of Exploration Geophysicists, 2011, The seg advanced modeling corporation. (`http://www.seg.org/resources/research/seam`).

Weglein, A. B., F. V. Araújo, P. M. Carvalho, R. H. Stolt, K. H. Matson, R. T. Coates, D. Corrigan, D. J. Foster, S. A. Shaw, and H. Zhang, 2003, Inverse scattering series and seismic exploration: Inverse Problems, R27–R83.

Zhang, J., 2007, Wave theory based data preparation for inverse scattering multiple removal, depth imaging and parameter estimation: analysis and numerical tests of green's theorem deghosting theory: PhD thesis, University of Houston.

Zhang, J., and A. B. Weglein, 2005, Extinction theorem deghosting method using towed streamer pressure data: analysis of the receiver array effect on deghosting and subsequent free surface multiple removal, *in* 75th Annual International Meeting, SEG, Expanded Abstracts: Soc. Expl. Geophys., **24**, 2095–2098.

———, 2006, Application of extinction theorem deghosting method on ocean bottom data, *in* 76th Annual International Meeting, SEG, Expanded Abstracts: Soc. Expl. Geophys., **25**, 2674–2678.

The inverse scattering series approach to removing internal multiples: delineating and defining its current stand-alone capability, and proposing a plan for additional added value for land application

Arthur B. Weglein[*]*, Paolo Terenghi* [*]*, Shih-Ying Hsu*[*]*, Yi Luo*[†]*, and Panos G. Kelamis*[†]*, M-OSRP, University of Houston*[*] *and Saudi Aramco*[†]

SUMMARY

This paper is a follow-up to Fu et al. (2010). In the latter paper, the capability of the inverse scattering series (ISS) internal multiple attenuation method was demonstrated on complex synthetic and land field data. In this paper, we further delineate and exemplify what is behind the ISS internal multiple capability and offer a strategy and plan for addressing open and outstanding issues.

INTRODUCTION

The industry trend to explore in deep water with plays that involved targets beneath or at complex and rapid varying boundaries caused many traditional multiple removal methods to bump up against their assumptions and to breakdown and fail. In addition, the estimation and removal of land internal multiples can make the toughest marine multiple problem pale in comparison. In Kelamis et al. (2006) the basic cause of that land multiple removal challenge was identified as a series of complex thin layers encountered in the near surface. New methods were needed to respond to these challenges. These methods need to satisfy the following criteria: (1) operate in multi-D, (2) have absolutely no need for subsurface properties, including no multiple generators, no layer properties, nor in any way partially or entirely determine those properties, i.e., not in stages through, e.g., stripping; (3) have no need for picking and interpretive intervention, (4) accommodate the broadest set of multiples of all orders with model type independent algorithms; (5) the meaning of primaries and multiples themselves can be extended to a multi-D earth (Weglein and Dragoset, 2005), and (6) multiples are surgically removed by predicting their amplitudes and phases, and thus do not harm primaries, even if they are proximal and overlapping. The efficacy/responsiveness to complex land and marine multiple removal challenges depends on how well the method under consideration satisfies (1)-(6).

Several different methods were developed for internal multiple attenuation/removal. The first group requires the user to identify the primaries as internal multiple sub-events or the portion of the earth responsible for the internal multiple's downward reflection. The internal multiple reflects off different reflectors which are defined as the 'generator' of the internal multiple. In this first set of methods the interpretation and picking of travel-times is central and paramount and it makes use of only total travel times and produces a kinematic estimate of an internal multiple's phase (but not the amplitude) (pioneered by Keydar et al. (1997) and then promulgated by Jakubowicz (1998)). Within that group reside the DELPHI feedback loop methods, which use the picked travel-times to downward continue the wave-field towards the generator (Berkhout and Verschuur, 2005) [boundary approach] or towards a chosen reference level (Berkhout and Verschuur, 2005; Kelamis et al., 2002) [layer approach]. In the DELPHI layer approach, 'a layer' is chosen, and the prediction operator for first order internal multiples will only allow the downward generator to be within the layer and all upward generators must be below the layer, thus not accommodating the removal of internal multiples whose up and down generators are both within the layer. The chosen phantom layer is fixed or 'static'. The vision behind the latter important methodology is that the complete removal of internal multiples requires a stripping feedback procedure, exactly mimicking and extending the free surface multiple case. This requires complete knowledge of the medium down to, and detailed determination at, the imaged reflector in depth, that would allow each reflector in turn to be removed (transformed away) along with those internal multiples that have their shallowest downward reflection at that reflector. The DELPHI reference level/boundary approach or the layer approach never capture the same set of first order internal multiples as the ISS methods; see e.g., Matson (2003), Fu et al. (2010) and the examples in this paper. Furthermore, the fundamental DELPHI theoretical feedback framework remains, that is, if you want to move beyond attenuate and towards eliminate, for all internal multiples, excluding none, one returns to a layer stripping prescription which requires a layer by layer determination of all the earth mechanical properties, i.e. velocity, density, and Q. Under certain circumstances, when the generators are simple and few and easy to identify, the DELPHI boundary or phantom layer methods can be the appropriate method of choice, due to its relative speed that may offset any need for picking and other compromises.

The second approach and group of algorithms derive as task specific subseries of the inverse scattering series (ISS). The distinct ISS free surface and internal multiple removal algorithms are not only independent of subsurface information, they are independent of earth model type (Weglein et al., 2003, pp R46-R62). In Fu et al. (2010) and Weglein et al. (2003) the background, history and contributors to the distinct ISS algorithms are provided for removing free surface and internal multiples. The conclusion of Fu et al. (2010) was that "the ISS internal multiple attenuator method, demonstrated effectiveness on synthetic and field data, where other internal multiple methods were unable to demonstrate similar effectiveness". That was the first land field data test of ISS internal multiple attenuation. That internal multiple capability fits in the toolbox alongside ISS free-surface complex synthetic and marine field data tests for amplitude and phase fidelity (Carvalho, 1992; Carvalho et al., 1992; Weglein et al., 1997; Matson et al., 1999; Weglein et al., 2003; Weglein and Dragoset, 2005; Zhang and Weglein, 2005, 2006). The ISS multiple removal methods satisfy all of the 'wish list' criteria (1-6) required to address the

challenges described in the introduction, and it is the only candidate with those properties. That explains its efficacy and stand-alone capability. The important paper on internal multiples by ten Kroode (2002) proposes a derivation of the Weglein et al. (1997) paper. ten Kroode (2002) keeps the lower-higher-lower thinking of Weglein et al. (1997), is automatic and without interpretive intervention, but shares with Keydar et al. (1997) the use of total travel time. The use of total travel time is a shortcoming that will ignore and miss certain internal multiples that the vertical time relationship of Weglein et al. (1997) will automatically accommodate and remove. That difference and omission is explicitly pointed out in the examples section of this paper. This paper further defines and illustrates these ISS properties and characteristics for removing internal multiples.

METHOD

The ISS internal multiple attenuation algorithm for first order internal multiple prediction in a 2D earth is given by Araújo (1994); Araújo et al. (1994); Weglein et al. (1997),

$$b_3(k_g,k_s,\omega) = \frac{1}{(2\pi)^2}\int_{-\infty}^{\infty}\int_{-\infty}^{\infty} dk_1 e^{-iq_1(z_g-z_s)} dk_2 e^{iq_2(z_g-z_s)} \times \int_{-\infty}^{\infty} dz_1 b_1(k_g,k_1,z_1) e^{i(q_g+q_1)z_1} \times \int_{-\infty}^{z_1-\varepsilon} dz_2 b_1(k_1,k_2,z_2) e^{-i(q_1+q_2)z_2} \times \int_{z_2+\varepsilon}^{\infty} dz_3 b_1(k_2,k_s,z_3) e^{i(q_2+q_s)z_3},$$

where ω is temporal frequency; k_g and k_s are the horizontal wavenumbers for source and receiver coordinates, respectively; the vertical source and receiver wavenumbers, q_g and q_s, are given by $q_i = sgn(\omega)\sqrt{\omega^2/c_0^2 - k_i^2}$ for $i = (g,s)$; c_0 is the constant background velocity; z_s and z_g are source and receiver depths; and z_i $(i = 1,2,3)$ represents pseudodepth (depth location given by migration with background velocity). The quantity $b_1(k_g,k_s,z)$ corresponds to an uncollapsed prestack Stolt migration (Weglein et al., 1997) of an effective plane-wave incident data (data scaled by an obliquity factor), $b_1(k_g,k_s,q_g+q_s) = -2iq_sD(k_g,k_s,\omega)$, where $D(k_g,k_s,\omega)$ is the Fourier transformed prestack data.

Properties of the first order term - uncollapsed FK migration

Stolt uncollapsed migration resolves many complicated wave phenomena within a constant velocity overburden such as diffractions and multi-pathing. One example of such phenomena is the bow-tie pattern generated by reflections over a sufficiently curved boundary. These effects are common in seismic exploration data and can occur in a variety of geological features, including salt domes, faults, layer terminations, pinch-outs, fractured and/or irregular volcanic layers and for a rough sea-bottom. As we mentioned, several internal multiple removal algorithms require picking of events and travel times. In some of those methods (Keydar et al., 1997) the picked travel-times are directly used to mute the wave-field at earlier or later times with respect

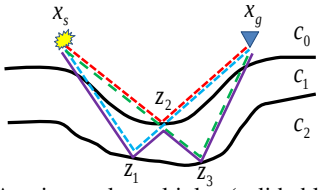

Figure 1: An internal multiple (solid blue) satisfying monotonicity in vertical time but not in total travel time. If wave-speed c_1 is much greater than c_0, the (dashed blue) and (dashed green) primaries arrive at the surface earlier than the (dashed red) primary. The multiple is removed by the ISS method, but not by methods based on total travel time monotonicity.

to the generator, and internal multiples are predicted using auto and cross-correlation operations between traces from the resulting fields. In others, e.g the feedback methods, the travel times are used to determine approximated re-datuming operators. However, all these approaches are based on the implicit assumption that a one-to-one relationship exists between seismic events (their travel-time) and the earth features that create them (such as layer boundaries). In the presence of diffractions and/or multi-pathing, a one-to-one relationship does not exist, as e.g. a single curved interface can produce several seismic arrivals. Picking events, travel times and generators is generally not recommendable even in a normal incidence experiment in a 1D earth, since destructively interfering primary and multiple events are possible and even prevalent in land field data tests (see, e.g., Kelamis et al., 2006; Fu et al., 2010). The ISS method, with its automatic amplitude and phase prediction, and no picking of events nor generators, has no problem and surgically removes multiples that are isolated or interfering with other events.

Example1: internal multiples from curved or rugose surfaces

We present an example based on a simple 3-layer earth model where the shallowest interface is sine-shaped. The model in Figure 3(a) produces the data in Figure 3(b) where all seismic events except the second primary at $2.2s$ can be traced back to their origin at the shallow reflector. Clearly, in this example it is an issue to pick a unique travel-time to represent the curved reflector, as many events are generated, which interfere among themselves and even with the second primary. The ISS method provides a natural solution to that problem by using as input the uncollapsed prestack FK water speed migration (Figure 3(c)). The sketch in Figure 1 describes the case of an internal multiple which would not be predicted if total travel-times were the basis of the method. The multiple can be shown to trace back to an earth feature where the relationship between total travel-times and vertical travel-times (pseudo-depth) is inverted due to the presence of a high velocity layer at depth.

Properties of the leading (third) order term

Let z_1, z_2 and z_3 be the pseudo-depths of three generic points in the first order term of the internal multiples series (un-collapsed constant-velocity pre-stack migration). As those points span the entire data volume, the leading order attenuation algorithm (which is third order in the imaged

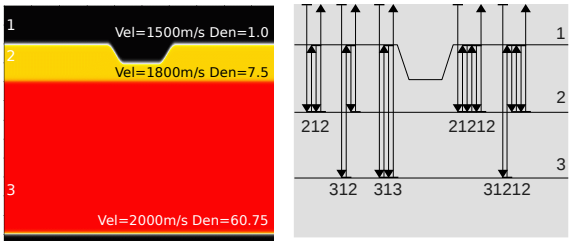

(a) (b)

Figure 2: Earth model (a) and event labeling (b) used in Example2. Densities are chosen to yield a vertical-incidence reflection coefficient of 0.8 at all layer boundaries.

data) allows any combination such that $z_1 > z_2$ and $z_3 > z_2$ to contribute the prediction (lower-higher-lower constraint). In contrast with the methods based on the convolution and correlation of wave-fields, where the definition of the generator is static, the ISS algorithm's lower-higher-lower constraint does not refer to any particular interface or event in the data. On the contrary, it applies to all of their water-speed images and therefore allows the simultaneous prediction of all first order internal multiples from all depths at once without requiring interpretation and travel-time picking of the data or knowledge of the medium.

Example2: a complete one-step prediction

We demonstrate the properties of the ISS internal multiple prediction algorithm and its difference with the phantom layer approach (Berkhout and Verschuur, 2005; Kelamis et al., 2002) using a set of acoustic 3D finite-difference data. The model (shown in Figure 2) is composed of four layers delimited by three interfaces, the first of which has a gap approximately 1.5km long and 100m deep. In Figure 2(b), the travel paths of several internal multiples are drawn schematically using up and down-going arrows representing wave propagation. In a zero offset section of the data (Figure 4(a)) a first train of closely spaced internal multiples (characterized by the pattern $2[12]_n$) can be shown to originate from the energy reflected between the two shallow reflectors (1) and (2). A deeper reflector (3) causes the entire train to begin again at around $1.4s$ ($3[12]_n$ trend) and once more at $2.1s$ ($313[12]_n$ and $323[12]_n$ trends). In general, even in a simple three-interface earth model, the number of reverberations recorded at the surface is extremely large as a result of the various ways three reflectors can be combined to form internal multiples. The ISS internal multiple algorithm predicts all of them at once, without any interpretation required on the data, as shown in Figure 4(b) and 4(c). It is useful to observe that the feedback phantom layer approach and algorithms cannot achieve the same result for any choice of 'layer', even when two or more primaries such as events (1) and (2) form a layer of downward reflecting generators. Figure 5(a) shows the four types of first-order internal multiples generated within a three-reflector earth. If the downward-reflecting layer is chosen to close between the first and second reflectors, the layer-related method can predict the three types of first-order internal multiples shown in Figure 5(b). Notice that for any choice of downward-reflecting layer, there is at least one type of first-order internal multiple which cannot be predicted with the phantom layer approach.

Although these missed multiples that are not predicted in the feedback phantom layer method might seem like some academic nitpick of little real world consequence, in fact this observation is of tremendous practical significance, and the root cause behind the Fu et al. (2010) conclusion on ISS internal multiple effectiveness and stand alone added-value on complex land near surface internal multiple generators.

CONCLUSIONS

In this paper, we continued the Fu et al. (2010) examination of inverse scattering series (ISS) internal multiple capability, in general, and specifically for addressing the daunting challenges of land data with its plethora of complex near surface thin layer internal multiple generators. We describe a set of 'wish list' qualities that the ideal response to pressing and prioritized land and marine multiple removal challenges would satisfy, and show how only the ISS internal multiple method reaches that high bar and standard. All methods have strengths and shortcomings, and as we recognize the shortcomings of the current ISS attenuator, we know that removing the shortcoming resides within the ISS and that upgrade will never require subsurface information, picking events or any interpretive intervention, or stripping as well. What all the ISS methods require is a reasonable source signature, and we are developing onshore Green's theorem methods for that purpose. Adaptive energy minimizing criteria are often employed in an attempt to bridge the conditions and limitations of the real world and the physics behind what our algorithms are assuming. When first introduced by Verschuur et al. (1992) and Carvalho and Weglein (1994) the need was clear and good benefit was derived, especially with isolated primaries and free surface multiples of first order. But as with all assumptions, today's reasonable and necessary assumption will invariably be tomorrow's impediment to progress and increased effectiveness. And that's the case with adaptive subtraction today, especially with land internal multiples. We advocate a three pronged response to land internal multiples: (1) seeking further capability for amplitude fidelity for all orders of internal multiples, including converted wave internal multiples, (2) satisfy prerequisites for the source signature and radiation pattern, and (3) look for a new 'bridge' to replace the energy minimization adaptive criteria, a bridge that is consistent with the underlying physics rather than runs at cross purposes with the greatest strength of the ISS prediction. Our plan is to progress each of these three issues as a strategy to extend the current encouraging results and allow ISS multiple removal to reach its potential: to surgically remove all multiples without damaging primaries under simple, complex and daunting land and marine circumstances.

ACKNOWLEDGMENTS

The authors (AW, PT, SH) wish to thank all M-OSRP sponsors, NSF (Award DMS-0327778) and DOE (BES Award DE-FG02-05ER15697) for their encouragement and support. All authors wish to thank Saudi Aramco for permission to publish this paper. We thank Bill Dragoset and Western Geco for providing the data shown in Example 2 and for permission to publish the results.

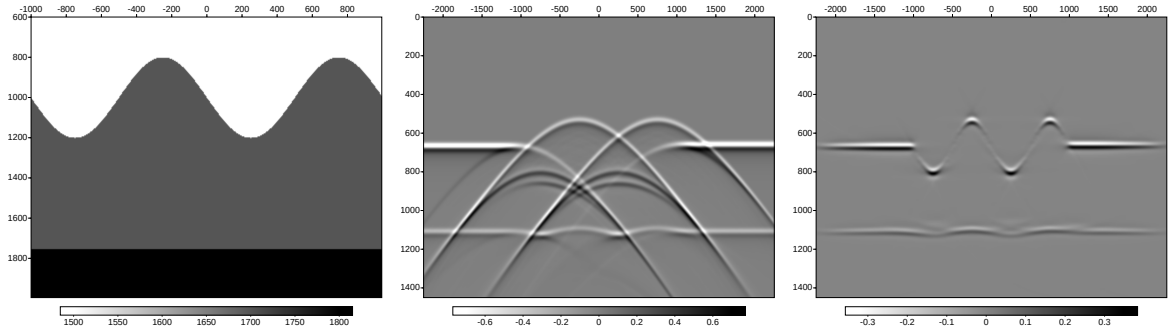

(a) (b) (c)

Figure 3: (a) Velocity model used in Example1. (b): zero offset section of the input data; (c): zero offset section of the water-speed FK migration, first order term in the ISS internal multiple algorithm.

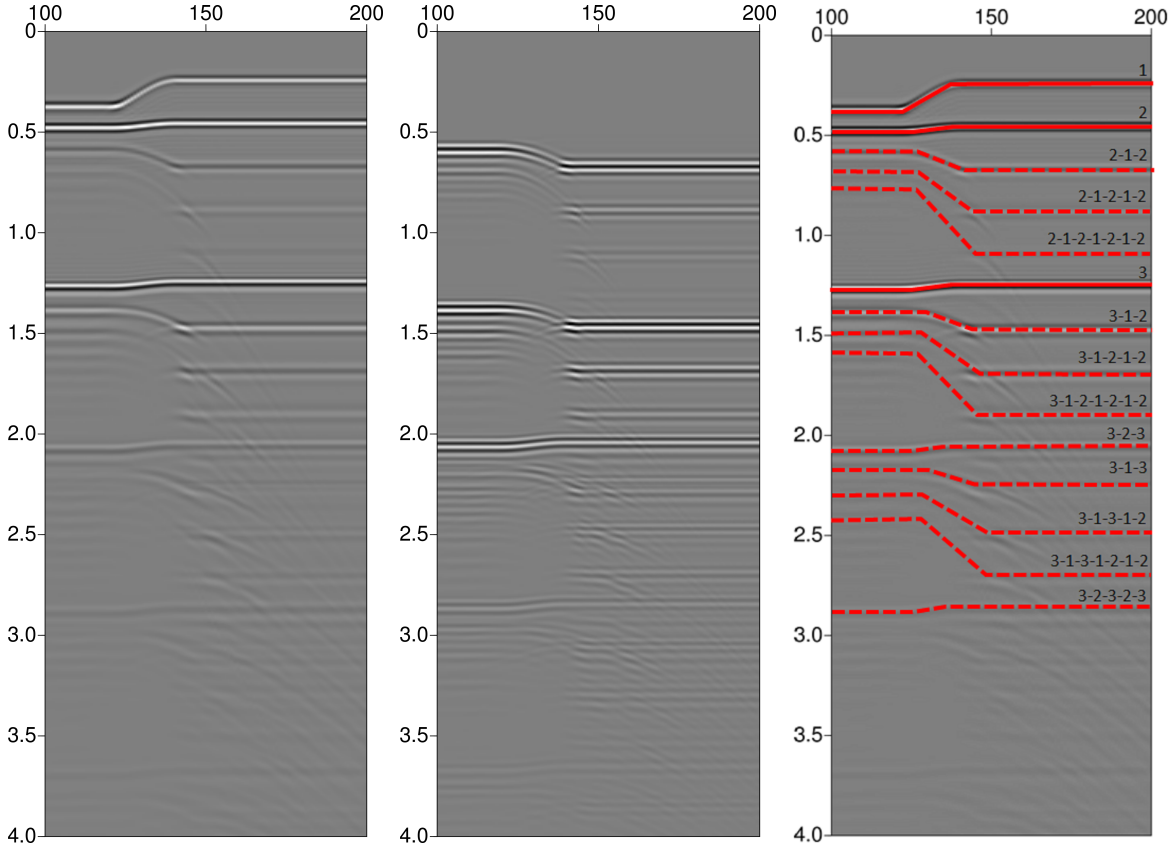

(a) (b) (c)

Figure 4: Zero offset sections from Example2. (a) input data, (b) predicted multiples and (c) labeling of events.

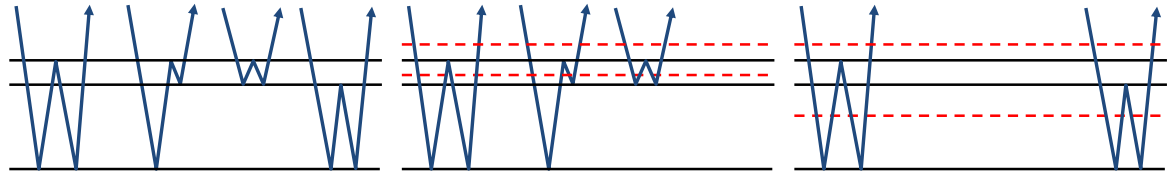

(a) (b) (c)

Figure 5: (a): four type of first-order internal multiples are generated by three reflectors. (b) and (c): the first-order internal multiples predicted by the feedback layer method using different definitions of the downward generator layer (red dashed lines).

REFERENCES

Araújo, F. V., 1994, Linear and non-linear methods derived from scattering theory: backscattered tomography and internal multiple attenuation: PhD thesis, Universidade Federal da Bahia.

Araújo, F. V., A. B. Weglein, P. M. Carvalho, and R. H. Stolt, 1994, Inverse scattering series for multiple attenuation: An example with surface and internal multiples: 64th Annual International Meeting, SEG, Expanded Abstracts, 1039–1042.

Berkhout, A. J., and D. J. Verschuur, 2005, Removal of internal multiples with the common-focus-point (cfp) approach: Part 1 — explanation of the theory: Geophysics, **70**, V45–V60.

Carvalho, P. M., 1992, Free-surface multiple reflection elimination method based on nonlinear inversion of seismic data: PhD thesis, Universidade Federal da Bahia.

Carvalho, P. M., and A. B. Weglein, 1994, Wavelet estimation for surface multiple attenuation using a simulated annealing algorithm: SEG Technical Program Expanded Abstracts, **13**, 1481–1484.

Carvalho, P. M., A. B. Weglein, and R. H. Stolt, 1992, Nonlinear inverse scattering for multiple suppression: Application to real data. part i: SEG Technical Program Expanded Abstracts, **11**, 1093–1095.

Fu, Q., Y. Luo, P. G. Kelamis, S. Huo, G. Sindi, S.-Y. Hsu, and A. B. Weglein, 2010, The inverse scattering series approach towards the elimination of land internal multiples: SEG Technical Program Expanded Abstracts, **29**, 3456–3461.

Jakubowicz, H., 1998, Wave equation prediction and removal of interbed multiples: Society of Exploration Geophysicists International Exposition and 68th Annual Meeting, 1527–1530.

Kelamis, P. G., E. Verschuur, K. E. Erickson, R. L. Clark, and R. M. Burnstad, 2002, Data-driven internal multiple attenuation — applications and issues on land data: SEG Technical Program Expanded Abstracts, **21**, 2035–2038.

Kelamis, P. G., W. Zhu, K. O. Rufaii, and Y. Luo, 2006, Land multiple attenuation — the future is bright: SEG Technical Program Expanded Abstracts, **25**, 2699–2703.

Keydar, S., E. Landa, B. Gurevich, and B. Gelchinsky, 1997, Multiple prediction using wavefront characteristics of primary reflections: EAGE Expanded Abstracts.

Matson, K. H., 2003, Mosrp multiple attenuation review. (www.mosrp.uh.edu/secure/mosrp2005/MOSRPdemultrev_Matson.ppt).

Matson, K. H., D. C. Corrigan, A. B. Weglein, C. Y. Young, and P. M. Carvalho, 1999, Inverse scattering internal multiple attenuation: results from complex synthetic and field data examples: 69th Annual International Meeting, SEG, Expanded Abstracts, 1060–1063.

ten Kroode, 2002, Prediction of internal multiples: Wave Motion, **35**, 315–338.

Verschuur, D. J., A. J. Berkhout, and C. P. A. Wapenaar, 1992, Adaptive surface-related multiple elimination: Geophysics, **57**, 1166–1177.

Weglein, A., and W. Dragoset, 2005, Multiple attenuation: Society of Exploration Geophysicists.

Weglein, A. B., F. V. Araújo, P. M. Carvalho, R. H. Stolt, K. H. Matson, R. T. Coates, D. Corrigan, D. J. Foster, S. A. Shaw, and H. Zhang, 2003, Inverse scattering series and seismic exploration: Inverse Problems, R27–R83.

Weglein, A. B., F. A. Gasparotto, P. M. Carvalho, and R. H. Stolt, 1997, An inverse-scattering series method for attenuating multiples in seismic reflection data: Geophysics, **62**, 1975–1989.

Zhang, J., and A. B. Weglein, 2005, Extinction theorem deghosting method using towed streamer pressure data: analysis of the receiver array effect on deghosting and subsequent free surface multiple removal: SEG Technical Program Expanded Abstracts, **24**, 2095–2098.

———, 2006, Application of extinction theorem deghosting method on ocean bottom data: SEG Technical Program Expanded Abstracts, **25**, 2674–2678.

Inverse scattering series depth imaging: First field data examples

Fang Liu[*], Xu Li[*], Arthur B. Weglein[*], Paolo Terenghi[*], Ed Kragh[†], Hong Liang[*], James D. Mayhan[*], Lin Tang[*], Shih-Ying Hsu[*], Zhiqiang Wang[*], Joachim Mispel[‡], and Lasse Amundsen[‡], M-OSRP/Physics Dept./UH[*], SCR/Schlumberger[†], and Statoil ASA[‡]

SUMMARY

In Weglein et al. (2010) an update and status report were provided on the progress on the inverse scattering series (ISS) direct depth imaging without the velocity model.
In that report, results on synthetics with sufficient realism indicated that field data tests were warranted. This paper documents those first field data tests. These first early tests are encouraging and indicate that ISS direct depth imaging on field data is possible. The next steps, and open issues, on the road between viable and providing relevant and differential added value to the seismic tool-box are described and discussed.

INTRODUCTION / BACKGROUND

All currently applied direct depth imaging methods and indirect imaging concepts firmly believe that depth and velocity are inextricably linked. That cornerstone of all current imaging means that any direct imaging method requires an accurate velocity model to produce an accurate image in depth.

It is essential to understand the significance of the term 'direct' in 'direct depth imaging'. Given an accurate velocity model, all current leading-edge imaging methods (e.g., Kirchhoff, FK, Beam and RTM) are able to directly output the depth (the actual spatial configuration) of reflectors.

Indirect imaging methods (e.g., flat common image gathers, differential moveout, CFP, CRS and 'path integral' approaches) seek to satisfy a property or condition that an image with an accurate velocity would satisfy. Those properties are necessary conditions, but not sufficient, and hence satisfying the indirect proxy for an adequate velocity model is not equivalent to knowing the velocity and direct depth imaging. Hence, satisfying these indirect criteria is no guarantee, and can lead to the correct depth or to any one of a set of incorrect depths. The latter truth is rarely (if ever) spoken and even rarer to find mentioned in print. Most importantly, these indirect approaches fervently believe that a direct depth imaging method would require and demand a velocity model, and that there is absolutely no way around it, and that depth and velocity are inextricably connected. That thinking is clear, and 100% correct within the framework of current imaging concepts and methods.

However, that thinking is superseded by the new broader framework for imaging provided by the ISS.

Amundsen et al. (2005, 2006, 2008) have developed direct inversion methods for 1D acoustic and elastic media. The ISS is the only direct inversion for both a 1D and a multi-D acoustic, elastic and anelastic earth.

In addition to being direct and applicable and applied for a multi-D earth, the ISS (Weglein et al., 2003) allows for all processing objectives (including multiple removal and depth imaging) to be achieved directly and without subsurface information.

In the same 'direct' sense, that current imaging methods can directly output the spatial configuration of reflectors with a velocity model, ISS imaging algorithms can directly output the correct spatial configuration without the velocity model. It is the only method with that capability.

The ISS subseries for direct depth imaging communicates that depth and velocity are not inextricably linked.

The ISS provides a new superseding theory that views the current velocity-depth relationship and framework as a special limiting case, as quantum mechanics and relativity view classical physics as a limiting and special case, within a new comprehensive and broader platform and framework.

The new broader framework for imaging reduces to current imaging algorithms when the velocity model is adequate, and most amazingly it determines on its own for any particular data set, or portion of a data set, whether the new framework is needed, or whether the current conventional imaging framework will suffice. The new imaging framework determines if its services are called upon, and then and only then, will it activate the new ISS imaging framework terms and call them into action.

All current leading edge migration methods, such as, beam, Kirchhoff and RTM, are linear. The ISS direct depth imaging without the velocity algorithm is a non-linear relationship between data and the wavefield at depth.

ISS TASK SPECIFIC SUBSERIES FOR MULTIPLE REMOVAL, DEPTH IMAGING AND DIRECT NON-LINEAR AVO

Each and every term and portion of any term within the ISS is computed directly in terms of data. All tasks associated with inversion (e.g., multiple removal, depth imaging, non-linear direct AVO, and Q compensation) are each contained within the series. Hence, these individual tasks are each achievable directly in terms of data, without subsurface information. Every seismic processing objective is carried out as a subseries of the ISS, and operates without subsurface information, by involving distinct non-linear communication of the recorded seismic data. Only the ISS communicates that all seismic objectives can be achieved in basically the same way that free surface multiples are removed.

The free surface and internal multiple removal subseries have

not only been shown to be viable but have also demonstrated added value and stand alone capability for predicting the amplitude and phase of multiples (See, e.g., Matson et al. (1999); Weglein and Dragoset (2005); Fu et al. (2010)), in particular, demonstrated under complex marine and on-shore circumstances. In this paper, we examine for the first time the issue of ISS depth imaging viability on field data.

All conventional imaging methods require knowledge of the velocity model to determine the spatial locations of reflectors. Hence, the ISS series project began by assuming that only the velocity was variable and unknown. Figures 1-3 illustrate the ISS imaging results for an earth in which only velocity varies. The algorithms are described in Liu (2006); Liu et al. (2005); Zhang et al. (2007).

Imaging methods that require the velocity use only the phase of the data to determine depth. In contrast, all ISS tasks achieve their goals without subsurface information by using both the amplitude and phase of seismic data. The latter difference requires the exclusion of events (and their amplitude and phase) from imaging subseries that do not relate to or contribute towards the task of depth imaging. Reflections that correspond to density only changes must be precluded from depth imaging tasks. The ISS depth imaging in an acoustic earth where V_p and density (and for an elastic earth with V_p, V_s and density), can all vary and all are initially (and remain, completely) unknown was formulated and the results were summarized in Weglein et al. (2010).

THE IMPACT OF DATA LIMITATIONS ON ISS SUBSERIES

Table 1 summarizes the dependence/sensitivity of different ISS subseries on seismic bandwidth. As the latter table indicates, there is an increased dependency as we progress from the ISS free surface multiple case (where the subseries works one frequency at a time, and has absolutely no concern about bandlimited data) to the depth imaging subseries where the absence of low frequency in the data can have a deleterious effect on the ability of the ISS to move from the original linear incorrect depth image to the correct depth.

There are many other issues that need to be taken into consideration in developing practical ISS depth imaging algorithms. Among these issues are: (1) have the appropriate number and types of terms from the inverse series been included to match the imaging challenge due to the difference between the actual and reference velocity, and the duration of that difference; and (2) have the density only reflections been excluded from the ISS depth imaging algorithm. All of these issues need to be addressed to have the ISS depth imaging algorithm produce an accurate depth section. When these requirements are met the ISS image moves until it stops, and when it stops it's there. The moveout becomes flat and the imaging series directly produces a flat common image gather (CIG) at the correct depth.

In contrast to all current imaging methods where CIG flatness is a necessary but not a sufficient condition for depth imaging accuracy, the CIG flatness is a by-product of ISS imaging, and a necessary and sufficient indication that depth has been found. It's a direct depth finding machine, and when it stops it is done. With ISS imaging CIG flatness is an indication that a direct method is done, not an in-direct proxy for velocity used to find the depth, where for the latter conventional use it is necessary but not sufficient for depth location.

The overriding requirement and number one issue for field data application of ISS depth imaging is being able to address the sensitivity to missing low frequency components in the data (or low vertical wave number). If that low frequency sensitivity is not addressed, then gathering or not gathering appropriate and necessary ISS imaging terms or excluding density only reflections will not matter, and will be of no practical consequence. Hence, addressing the bandwidth issue for ISS imaging is the number one priority, the make or break issue for field data application, viability and delivery of its promise of high impact differential added value. A regularization scheme has been developed in Liu and Weglein (2010) to directly address that low frequency challenge. The purpose of this paper is to examine whether this regularization method will allow the ISS imaging algorithms to be effective and work on field data. Therefore, with this first field data examination, we relax all of the other requirements for ISS depth imaging and consider the field data as though it were generated by a velocity only varying earth. Within that parallel world where only velocity varies, the ISS depth imaging will need to address the band-limited nature of field data, and also will require having enough ISS imaging terms (within an acoustic velocity only varying subsurface assumption) to be effective for accurately locating reflectors.

In Figure 4, we present an acoustic model with no density variations and the water speed migration for the data from that model. Figure 5 (a) shows the inverse scattering imaging series ideal result, with full band-width data. In (b), the data has been altered by a sine squared taper up to $10Hz$ which damped the low frequency information and the ISS imaging without regularization is ineffective. In (c), with the regularization applied, the ISS depth imaging successfully corrects the data move-out and reveals the correct depth.

A similar approach is followed for a CMP gather selected from the Kristin data-set (Figure 7, Majdanski et al. (2010)). Figure 8 (a) shows a water-speed migration of the data in Figure 7, while Figure 8 (b) shows the ISS imaging result after regularization.

Event 1 is the water bottom primary, event 2 is the subwater bottom primary, event 3 is the internal multiple between event 1 and 2 and event 4 is a third primary. Event 4, the third primary has a moveout with a water speed migration.

It turns out that event 1, the water-bottom primary, represents a density change but no velocity change. Hence, the layer below the water-bottom has the same acoustic velocity as water. Further, the first order internal multiple (event 3) in that first sub-water-bottom layer also has a water-speed move out. Hence, events 1, 2, and 3 all have flat CIGs with a water-speed FK Stolt migration (Figure 6). Event 4 has move-out due to a

velocity change at the base of the first sub-water-bottom layer.

With a regularized ISS depth imaging the result for the image of event 4 is a shifted and CIG flat output. Hence, the ISS depth imaging is working on the very shallow subsea-bottom portion of the Kristin data set within the context of a velocity only varying earth. The shifted ISS image and flat CIG of event 4, the third primary, indicates that bandwidth issues have been addressed, and sufficient capture of ISS imaging terms are within the ISS imaging algorithm. If for this field data set and ISS depth imaging test, either one of these conditions (addressing bandwidth sensitivity and adequate inclusion of ISS imaging terms) were a remaining and outstanding issue, then event 4 would not have moved and produced a flat CIG. The success of this test is thus defined. The next steps are to apply the regularized ISS depth imaging to an acoustic variable velocity and density model for the very shallow and sub-water-bottom reflectors, and a Vp, Vs and density varying elastic earth model for the deeper reflectors, to preclude density only reflections, and for outputting actual depth. The M-OSRP imaging research team is engaged in moving from the current news and report that demonstrates field data viability for ISS imaging to providing added value. The ultimate goal is to have ISS imaging match the efficacy that ISS free surface and internal multiple removal have provided for the removal of coherent noise, and to extend that capability for extracting information from signal (the collection of all primaries).

CONCLUSIONS

In this paper, we have shown that the ISS depth imaging algorithm can address the most serious practical limitation/challenge field data will place on ISS depth imaging: that is, limitations in seismic bandwidth. With this accomplished, the further steps to extend these tests to variable density and velocity acoustic and elastic media are achievable, and realizing that is within the sphere of issues we can influence and make happen. The most significant difference between synthetic data and field data for ISS depth imaging has been addressed.

ACKNOWLEDGMENT

We thank all the sponsors of M-OSRP for their support and encouragement. We have been partially funded by and are grateful for NSFCMG award DMS-0327778 and DOE Basic Sciences award DE-FG02-05ER15697. The M-OSRP group would like to thank Statoil ASA and Schlumberger/WesternGeco for granting access to the Kristin data and Mark Thompson, Mariusz Majdanski and Einar Otnes for their assistance and cooperation.

Figures

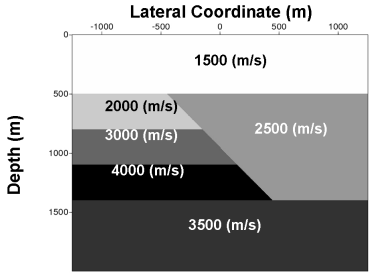

Figure 1: The fault shadow zone model.

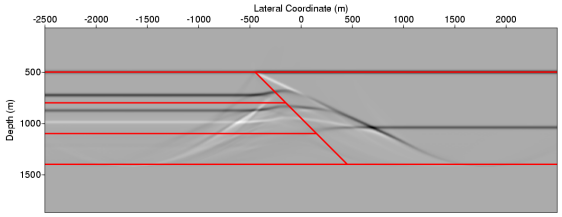

Figure 2: The water speed pre-stack FK Stolt migration for the data from the fault shadow model.

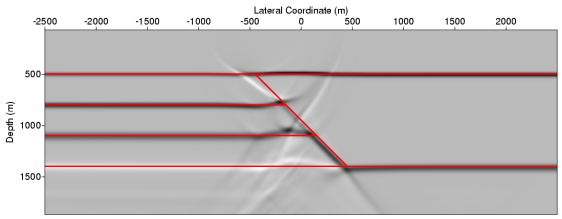

Figure 3: The inverse scattering series image (with partial capture of ISS imaging capability) for the fault shadow model.

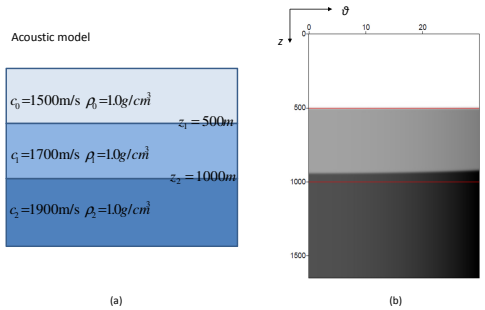

Figure 4: Figure (a) shows the acoustic model we are testing for evaluating the dependence of ISS on seismic bandwidth. Figure (b) is the water speed FK Stolt migration, the red lines represent the true location of the reflectors.

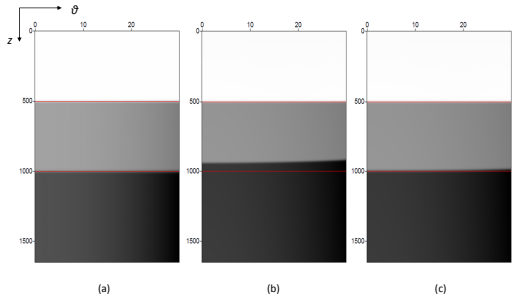

Figure 5: This figure illustrates the imaging result for a velocity varying only earth model. Figure (a) shows ISS imaging with data which has low frequency information. Figure (b) shows ISS imaging with band-limited data. Figure (c) shows the imaging result with the regularization being applied. This ISS imaging bandwidth issue is documented in Shaw (2005).

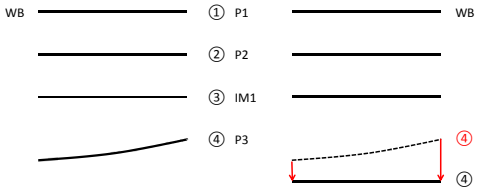

Figure 6: This figure summarizes the results of the initial ISS depth imaging tests on the very shallow, near ocean bottom section of the Kristin data.

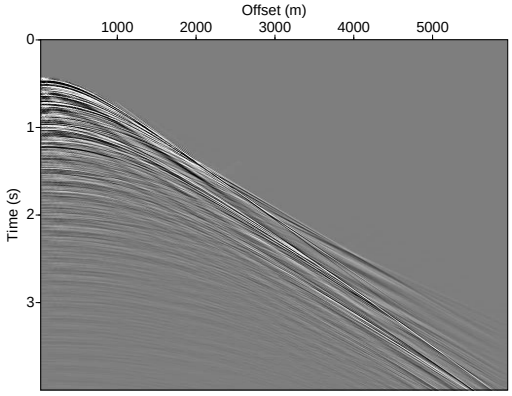

Figure 7: The CMP gather we tested from Kristin data.

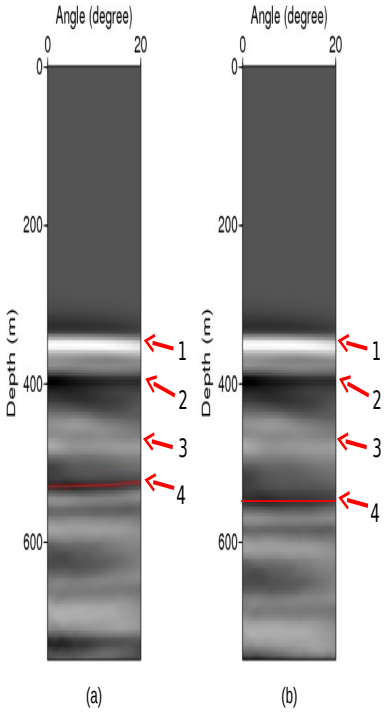

Figure 8: For the Kristin data test: Figure (a) shows water speed migration. The red line indicate water speed migration image for event 4. Figure (b) shows ISS imaging result. The red line shows ISS image for event 4.

Dependence on temporal frequency content of the data	Specific subseries
None	Free surface multiple
Very mild	Internal mulitple
Some	Depth imaging

Table 1: This table shows the dependence of ISS specific subseries on temporal frequency content of the data.

REFERENCES

Amundsen, L., A. Reitan, B. Arntsen, and B. Ursin, 2006, Acoustic nonlinear amplitude versus angle inversion and data-driven depth imaging in stratified media derived from inverse scattering approximations: Inverse Problems, **22**, 1921.

———, 2008, Elastic nonlinear amplitude versus angle inversion and data-driven depth imaging in stratified media derived from inverse scattering approximations: Inverse Problems, **24**, 045006.

Amundsen, L., A. Reitan, H. K. Helgesen, and B. Arntsen, 2005, Data-driven inversion/depth imaging derived from approximations to one-dimensional inverse acoustic scattering: Inverse Problems, **21**, 1823–1850.

Fu, Q., Y. Luo, P. G. Kelamis, S. Huo, G. Sindi, S.-Y. Hsu, and A. B. Weglein, 2010, The inverse scattering series approach towards the elimination of land internal multiples: SEG Technical Program Expanded Abstracts, **29**, 3456–3461.

Liu, F., 2006, Multi-dimensional depth imaging without an adequte velocity model: PhD thesis, University of Houston.

Liu, F., and A. B. Weglein, 2010, Addressing the bandlimited nature of seismic source and rapid lateral variations of the earth: source regularization and cascaded imaging operator: 2009 M-OSRP Annual Report, 72–117.

Liu, F., A. B. Weglein, B. G. Nita, and K. A. Innanen, 2005, Inverse scattering series for vertically and laterally varying media: application to velocity independent depth imaging: M-OSRP Annual Report, **4**.

Majdanski, M., C. Kostov, E. Kragh, I. Moore, M. Thompson, and J. Mispel, 2010, field data results of elimination of free-surface-related events for marine over/under streamer data: EAGE, Expanded Abstracts.

Matson, K. H., D. C. Corrigan, A. B. Weglein, C. Y. Young, and P. M. Carvalho, 1999, Inverse scattering internal multiple attenuation: results from complex synthetic and field data examples: 69th Annual International Meeting, SEG, Expanded Abstracts, 1060–1063.

Shaw, S. A., 2005, An inverse scattering series algorithm for depth imaging of reflection data from a layered acoustic medium with an unknown velocity model: PhD thesis, University of Houston.

Weglein, A. B., F. V. Araújo, P. M. Carvalho, R. H. Stolt, K. H. Matson, R. T. Coates, D. Corrigan, D. J. Foster, S. A. Shaw, and H. Zhang, 2003, Inverse scattering series and seismic exploration: Inverse Problems, **19**, R27–R83.

Weglein, A. B., and W. H. Dragoset, 2005, Multiple attenuation (geophysics reprint no. 24): Soc. Expl. Geophys.

Weglein, A. B., F. Liu, X. L. Z. Wang, and H. Liang, 2010, The inverse scattering series depth imaging algorithms: development, tests and progress towards field data application, *in* 80th Annual Internat. Mtg., Soc. Expl. Geophys., Expanded Abstracts: Soc. Expl. Geophys., 4133–4138.

Zhang, J., F. Liu, K. Innanen, and A. B. Weglein, 2007, Comprehending and analyzing the leading order and higher order imaging closed forms derived from inverse scattering series: 2006 M-OSRP Annual Report, 149–159.

Elimination of land internal multiples based on Inverse Scattering Series

Yi Luo, Panos G. Kelamis, Qiang Fu, ShouDong Huo, Ghada Sindi
(Saudi Aramco, EXPEC Advanced Research Center)
Shih-Ying Hsu and Arthur B. Weglein
(M-OSRP, University of Houston)

Despite the explosion of new, innovative technologies in the area of multiple identification and subsequent attenuation, their applicability is mostly limited in marine environments especially in deep water. In land seismic datasets however, the application of such multiple elimination methodologies is not always straightforward and in many cases poor results are obtained. The unique characteristics of land seismic data, i.e., noise, statics and coupling are major obstacles in the multiple estimation and elimination. The well-defined surface multiples present in marine data are rarely identifiable in land. Particularly in desert terrains with a complex near surface and low-relief structures, surface multiples are rare. In most cases, we are dealing with so called "near surface related multiples". These are primarily internal multiples generated within the complex near surface.

In this paper we use theoretical concepts from the Inverse Scattering Series (ISS) formulation and develop computer algorithms for land internal multiple elimination. The key characteristic of the ISS-based methods is that they do not require any information about the subsurface, i.e., they are fully data driven. Internal multiples from all possible generators are computed and adaptively subtracted from the input data. These methodologies can be applied pre- and post-stack and their performance is demonstrated using realistic synthetic and field datasets from the Arabian Peninsula. These are the first published field data examples of the application of the ISS internal multiple attenuation method to the daunting challenge of land internal multiples.

Introduction

Radon-based methods are commonly employed for multiple reduction in land seismic data processing. However, in land data, the lack of velocity discrimination between primaries and multiples results in unacceptable results. Thus, wave equation based schemes have to be introduced. The research articles of Verschuur *et al.* (1992), Berkhout (1997), Weglein *et al.* (1997), Carvalho and Weglein (1994), Dragoset and Jericevic (1998), Jakubowicz (1998), Berkhout (1999), and Verschuur and Berkhout (2001), to mention a few, offer theoretical insights to wave equation surface and internal multiple elimination along with several applications to synthetic and marine datasets.

Kelamis *et al.* (2002) used concepts from the Common Focus Point (CFP) technology and developed algorithms for internal multiple elimination applicable in land. Luo *et al.*

(2007) and Kelamis *et al.* (2008) have also showed successful applications of land internal multiple suppression. They employed the layer/boundary approaches introduced by Verschuur and Berkhout (2001). In these schemes the user has to define phantom layers/boundaries which correspond to the main internal multiple generators. Thus, some advanced knowledge of the main multiple generators is required. In land, as shown by Kelamis *et al.* (2006), the majority of internal multiples are generated by a series of complex, thin layers encountered in the near surface. Thus, the applicability of the CFP-based layer/boundary approach is not always straightforward since it requires the definition of many phantom layers. In contrast, the ISS theory does not require the introduction of phantom layers/boundaries. Instead, it computes all possible internal multiples produced by all potential multiple generators. Therefore, fully automated internal multiple elimination algorithms can be developed in the pre- and post-stack domains.

Basic Principles of ISS technology

The ISS-based formulation for internal multiple attenuation (Araújo *et al.*, 1994; Weglein *et al.*, 1997) is a data-driven algorithm. It does not require any information about the reflectors that generate the internal multiples or the medium through which the multiples propagate, and it does not require moveout differences or interpretive intervention. The algorithm predicts internal multiples for all horizons at once. This ISS internal multiple attenuation scheme is basically the first term in a subseries of the ISS that predicts the exact time and amplitude of all internal multiples without subsurface information. The ISS attenuation algorithm predicts the correct travel-times and approximate amplitudes of all the internal multiples in the data, including converted wave internal multiples (Coates and Weglein, 1996). Carvalho *et al.* (1992) pioneered the free-surface ISS method and applied it to field data. Matson *et al.* (1999) were the first to apply the ISS internal multiple algorithm to marine towed streamer field data, and Ramírez and Weglein (2005) extended the theory from attenuation towards elimination by including more terms in the subseries, thereby improving the amplitude prediction. Matson (1997) and Weglein *et al.* (1997) extended the ISS methods for removing free surface and internal multiples to ocean bottom and land data.

The ISS internal multiple attenuation algorithm in 2D starts with the input data, $D(k_g, k_s, \omega)$, that is deghosted and has all free-surface multiples eliminated. The parameters, k_g, k_s and ω, represent the Fourier conjugates to receiver, source and time, respectively. The ISS internal multiple attenuation algorithm for first order internal multiple prediction in a 2D earth is given by (Araújo, 1994; Weglein *et al.*, 1997). Figure 1 depicts the mathematical formulation along with a pictorial construction of a first order

multiple. The quantity b1kg,ks,z corresponds to an un-collapsed migration (Weglein *et al.*, 1997) of an effective incident plane-wave data which is given by -2iqsDkg,ks,ω. The vertical wavenumbers for receiver and source, qg and qs, are given by qi=sqn(ω)ω2c02-ki2 for i=g,s; c0 is the constant reference velocity; zs and zg are source and receiver depths; and zi (i=1,2,3) represents pseudodepth. Note that the obliquity factor, -2iqs, is used to transform an incident wave into a plane wave in the Fourier domain (Weglein *et al.*, 2003).
The first order internal multiple is composed of three events that satisfy z'2<z'1 and z'2<z'3. The traveltime of the internal multiple is the sum of the traveltimes of the two deeper events minus the traveltime of the shallower one. The parameter ε introduced in equation (1) to preclude z'2=z1 'and z'2=z'3 in the integrals. For band limited data, ε is related to the width of the wavelet. The output of equation (1), b3IM, is divided by the obliquity factor and transformed back to the space-time domain. When we subtract the estimated internal multiples from the original input data, all first order internal multiples are suppressed and higher order internal multiples are altered.

Synthetic & Field Data

Figure 2 shows a synthetic CMP gather obtained from an 18-layer velocity model. The data contains only primary reflections and internal multiples (Figure 2a). The results of our 1.5D ISS algorithm are shown in Figure 2b and compared with the true primaries-only gather (Figure 2c). Note that almost all internal multiples are attenuated considerably. There is some degradation of the primaries and is due to the adaptive least-squares subtraction. The results of Figure 2 are obtained without any user intervention, i.e., are fully automated and are very encouraging. More full pre-stack tests are currently underway.

Next the application of ISS-based internal multiple attenuation is shown on post-stack data. One of our goals is to study if ISS can successfully predict internal multiples generated by thin layers. Figure 3 depicts the ISS performance on a realistic zero-offset synthetic dataset. The model is composed of a large number of layers with 1 foot thickness and is obtained from a field sonic log shown on the extreme right. The data (primaries and internal multiples) are modeled using the acoustic wave equation. The 1D ISS internal multiple elimination result is shown on the right, while the primaries-only traces are also depicted in the middle panel. The performance of the 1D ISS algorithm is very good. Despite the post-stack application note the complete internal multiple

elimination obtained in the zone of interest between 1.0 and 1.4 secs. At the same time the main primary events are preserved with a minimum degradation.

In Figure 4 a stacked section of land seismic data from Saudi Arabia is shown. The presence of internal multiples is evident. Moreover, note the spatial variability of these multiples that follows the complex near surface. It's an indication that they are all generated within the complex, thin layers of the near surface. Figure 5 exhibits the data after 1D ISS internal multiple elimination, while Figure 6 shows the difference, i.e., the estimated internal multiples. The results are very encouraging. Note the overall reduction of internal multiples. Especially, at the zone of interest between 1.4 and 2.0 secs, the ISS internal multiple elimination has resulted in an improved definition of the primaries and thus increased the interpretability of the data. It is also interesting to examine the difference section where the estimated internal multiples are shown (Figure 6). The spatial variability of the internal multiples is quite obvious along with the "dull", character-free ringing appearance that represents no real geology.

Conclusions

We have developed and employed algorithms from the Inverse Scattering Series theory for the estimation of internal multiples. They can be applied pre-stack (1.5D) in the CMP domain and in zero-offset (1D) data. Their performance was demonstrated with complex synthetic and challenging land field datasets with encouraging results, where other internal multiple suppression methods were unable to demonstrate similar effectiveness. This paper presents the first series of onshore field data tests of the ISS-based internal multiple attenuation technology. ISS technology requires no velocity information for the subsurface or any advanced knowledge of the multiple generators. The main idea is to remove multiples without damaging primaries. In practice, a method like ISS can be used for high-end prediction, and then some form of adaptive subtraction is called upon to address issues omitted in the prediction. The improved multiple prediction offered by ISS is crucial in land seismic data where close interference between primaries and internal multiples occurs. The examples of this paper point to the pressing need to improve the prediction and reduce the reliance on adaptive steps, since the latter can fail precisely when you have interfering events. We will continue our research efforts for more accurate and complete prediction algorithms in order to produce effective, practical and automated internal multiple attenuation methodologies applicable for land seismic data.

Acknowledgements

We thank the Saudi Arabian Oil Company (Saudi Aramco) for support and permission to present this paper. We also thank Kevin Erickson for providing the synthetic datasets and Roy Burnstad for many discussions related to the processing of field data. Arthur B. Weglein and Shih-Ying Hsu thank Saudi Aramco for Shih-Ying's internship with the Geophysics Technology Team of EXPEC Advanced Research Center. They also thank all M-OSRP sponsors for their support.

Araújo, F. V., 1994, Linear and Nonlinear Methods Derived from Scattering Theory: Backscattered Tomography and Internal Multiple Attenuation: Ph.D. Thesis, Department of Geophysics, Universidad Federal de Bahia, Salvador-Bahia, Brazil, 1994 (in Portuguese).

Araújo, F. V., A. B. Weglein, P. M. Carvalho, and R. H. Stolt, 1994, Inverse scattering series for multiple attenuation: An example with surface and internal multiples: SEG Technical Program Expanded Abstracts, **13**, 1039-1041.

Berkhout, A. J., 1997, Pushing the limits of seismic imaging, Part I: Prestack migration in terms of double dynamic focusing: Geophysics, **62**, 937-953.

Berkhout, A. J., 1999, Multiple removal based on the feedback model: The Leading Edge, **18**, 127-131.

Carvalho, P. M., A. B. Weglein, and R. H. Stolt, 1992, Nonlinear inverse scattering for multiple suppression: Application to real data. Part I: SEG Technical Program Expanded Abstracts, 11, 1093-1095.

Carvalho, P. M., and A. B. Weglein, 1994, Wavelet estimation for surface multiple attenuation using a simulated annealing algorithm: SEG Technical Program Expanded Abstracts, **13**, 1481-1484.

Coates, R. T., and A. B. Weglein, 1996, Internal multiple attenuation using inverse scattering: Results from prestack 1 & 2D acoustic and elastic synthetics: SEG Technical Program Expanded Abstracts, **15**, 1522-1525.

Dragoset, W. H., and Z. Jericevic, 1998, Some remarks on surface multiple attenuation: Geophysics, **63**, 772-789.

Jakubowicz, H., 1998, Wave equation prediction and removal of interbed multiples: SEG Technical Program Expanded Abstracts, **17**, 1527-1530.

Kelamis, P. G., E. Verschuur, K. E. Erickson, R. L. Clark and R. M. Burnstad, 2002, Data-driven internal multiple attenuation-Applications and issues on land data: SEG Technical Program Expanded Abstracts, **21**, 2035-2038.

Kelamis, P. G., W. Zhu, K. O. Rufaii and Y. Luo, 2006, Land multiple attenuation-The future is bright: SEG Technical Program Expanded Abstracts, **25**, 2699-2703.

Luo, Y., W. Zhu and P. G. Kelamis, 2007, Internal multiple reduction in inverse-data domain: SEG Technical Program Expanded Abstracts, **26**, 2485-2489.

Kelamis, P. G., Y. Luo, W. Zhu and K. O. Al-Rufaii, 2008, Two Pragmatic Approaches for Attenuation of Land Multiples: 70th EAGE Conference & Exhibition.

Matson, K., 1997, An inverse scattering series method for attenuating elastic multiples from multi-component land and ocean bottom seismic data: Ph. D. Thesis, The University of British Columbia.

Matson, K., D. Corrigan, A. B. Weglein, C.Y. Young, and P. Carvalho, 1999, Inverse scattering internal multiple attenuation: Results from complex synthetic and field data examples: SEG Technical Program Expanded Abstracts, **18**, 1060-1063.

Ramírez, A. C., and A. B. Weglein, 2005, An inverse scattering internal multiple elimination method: beyond attenuation, a new algorithm and initial tests: SEG Technical Program Expanded Abstracts, **24**, 2115-2118.

Verschuur, D. J., A. J. Berkhout, and C. P. A. Wapenaar, 1992, Adaptive surface-related multiple elimination: Geophysics, **57**, 1166-1177.

Verschuur, D. J., and A. J. Berkhout, 2001, CFP-based internal multiple removal, the layer-related case: SEG Technical Program Expanded Abstracts, **20**, 1997-2000.

Weglein, A. B., F. A. Gasparotto, P. M. Carvalho, and R. H. Stolt, 1997, An inverse scattering series method for attenuating multiples in seismic reflection data: Geophysics, **62**, 1975- 1989.

Weglein, A. B., F. Araújo, P. Carvalho, R. Stolt, K. Matson, R. Coates, D. Corrigan, D. Foster, S. Shaw, and H. Zhang, 2003, TOPICAL REVIEW: Inverse scattering series and seismic exploration: Inverse Problems, 19, 27.

Figures

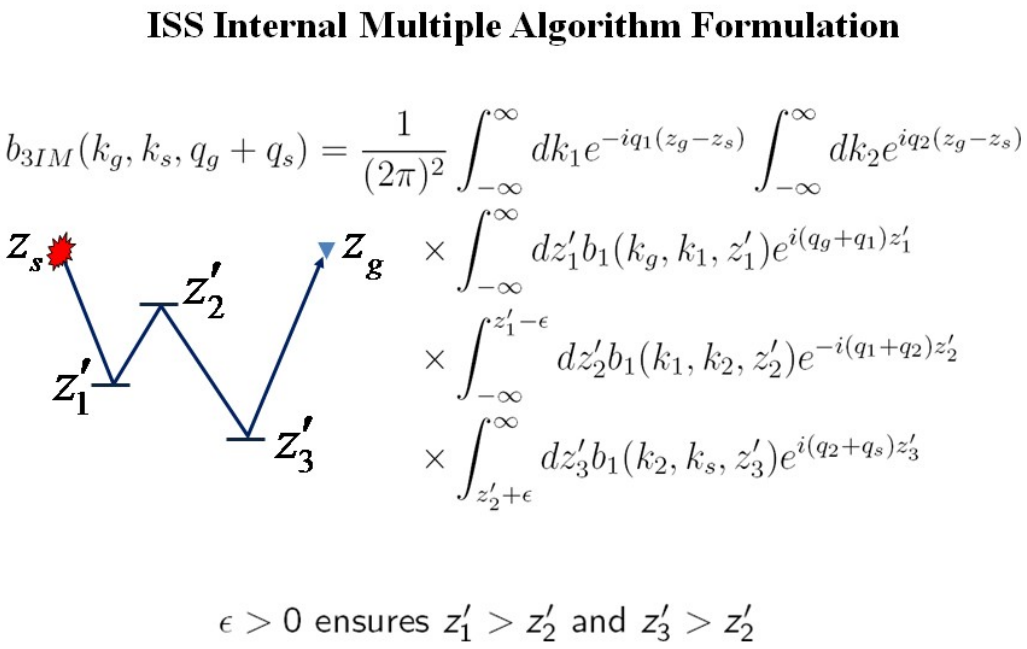

Figure 1: The mathematical formulation of the ISS-based internal multiple elimination technology and a pictorial construction of a first order multiple.

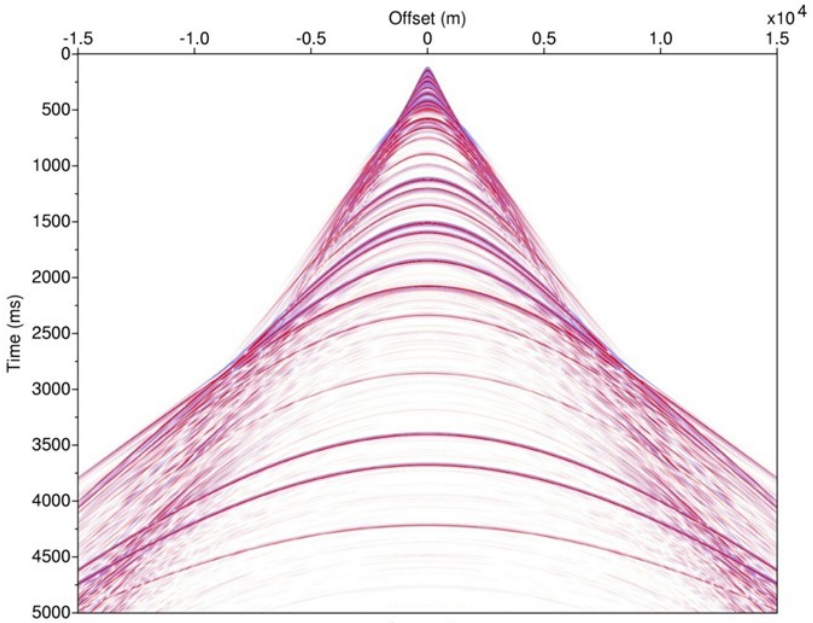

Input

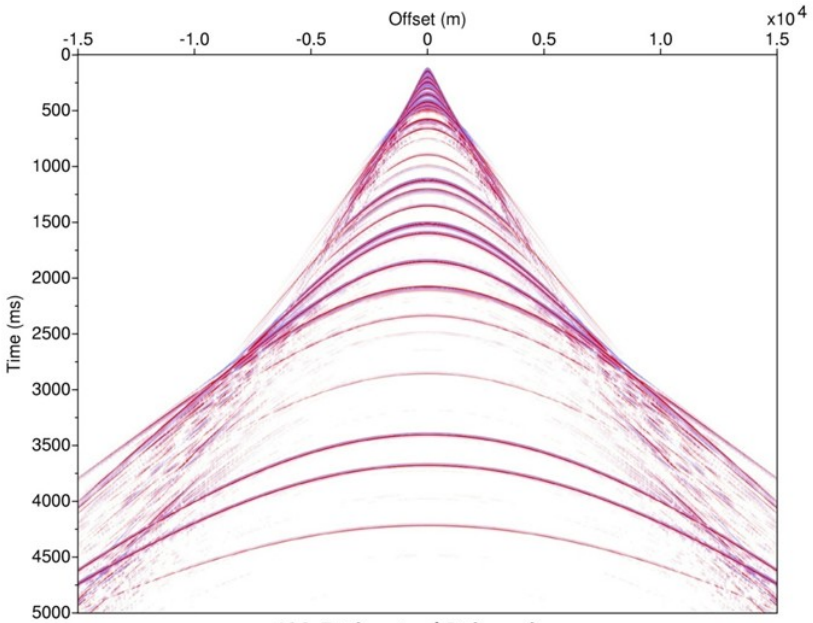

ISS Estimated Primaries

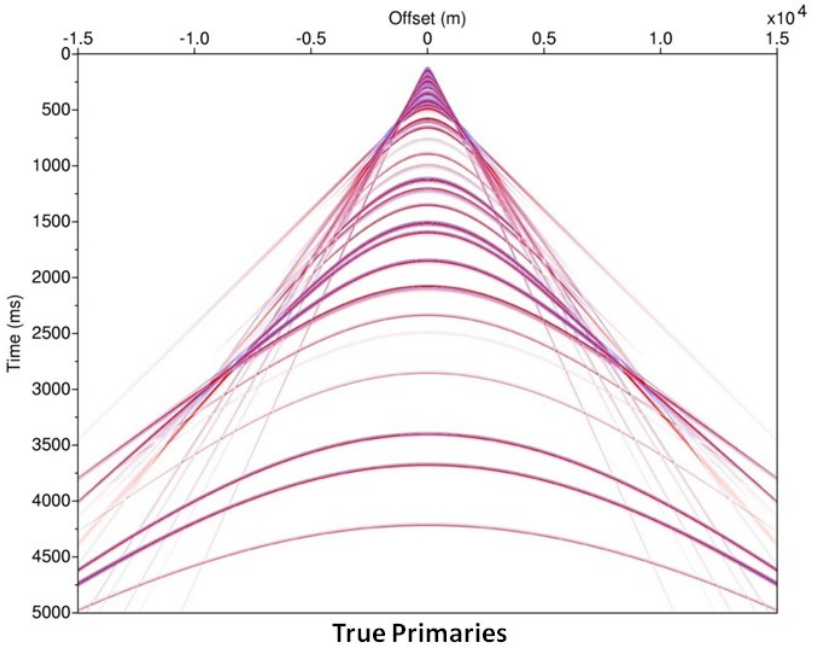

Figure 2: Pre-stack (1.5D) application of ISS internal multiple elimination technology. The input CMP gather (2a) with primaries and internal multiples obtained from an 18-layer velocity model. In the middle (2b), the ISS estimated primaries are shown. The true primaries are depicted on the right (2c).

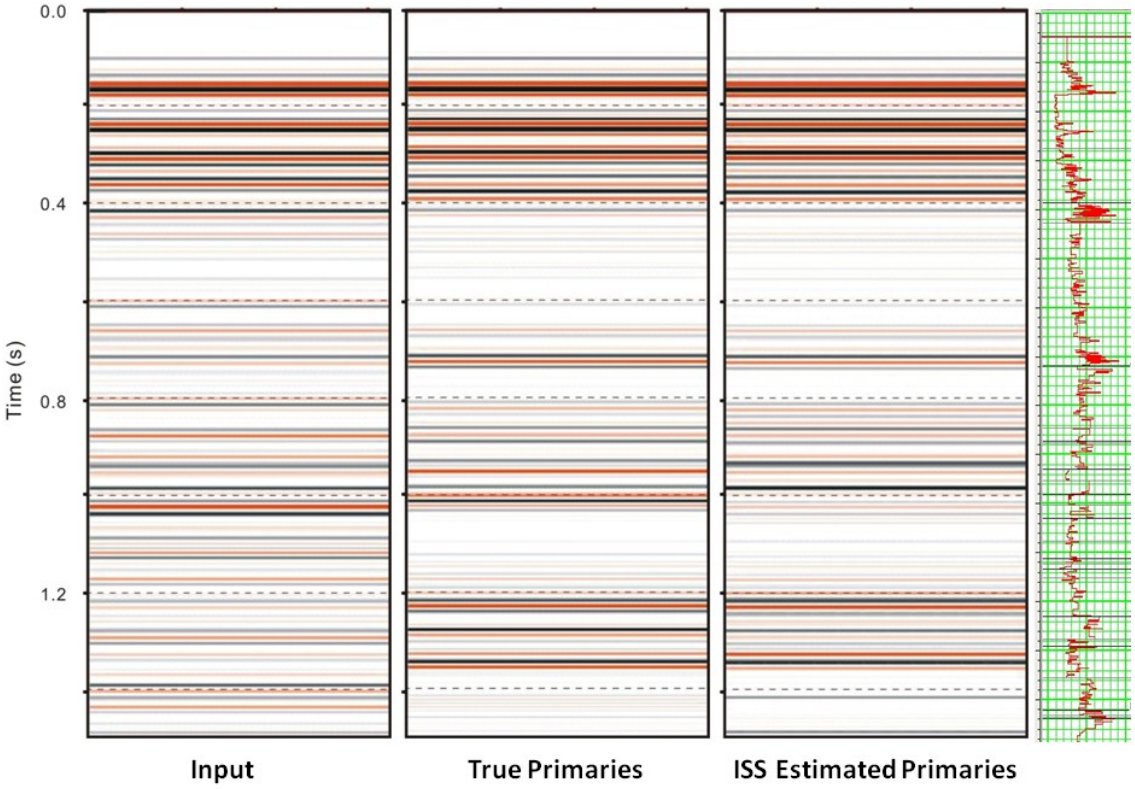

Figure 3: Post-stack (1D) application of ISS internal multiple elimination technology. The data is modeled from a field sonic log shown on the extreme right. The input data (left) has primaries and internal multiples only. The ISS result is shown on the right while the primaries-only section is in the middle.

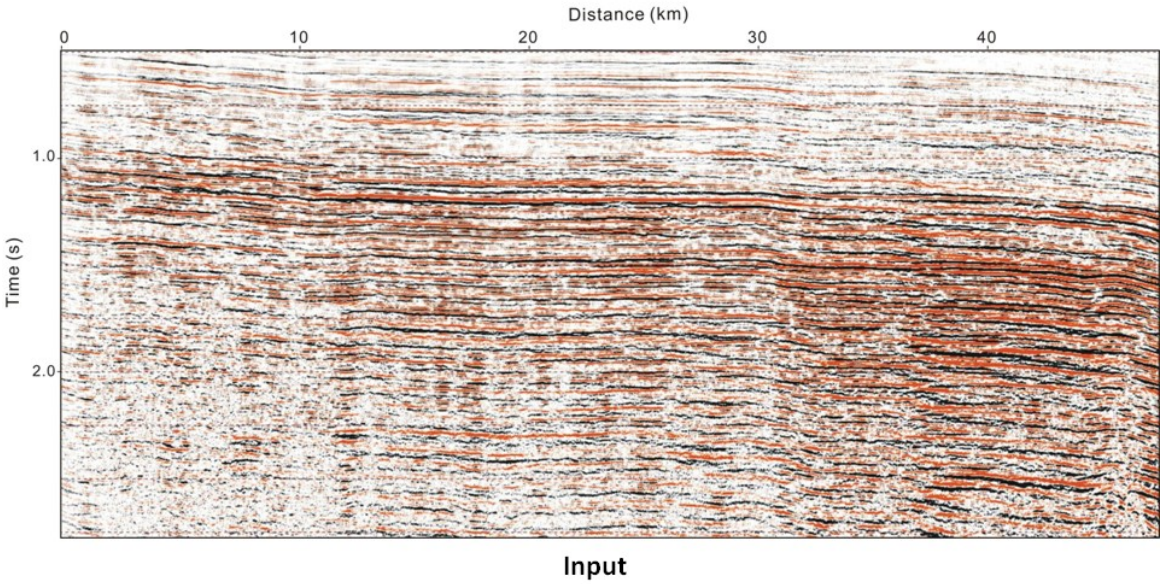

Figure 4: Stacked land seismic data with internal multiples.

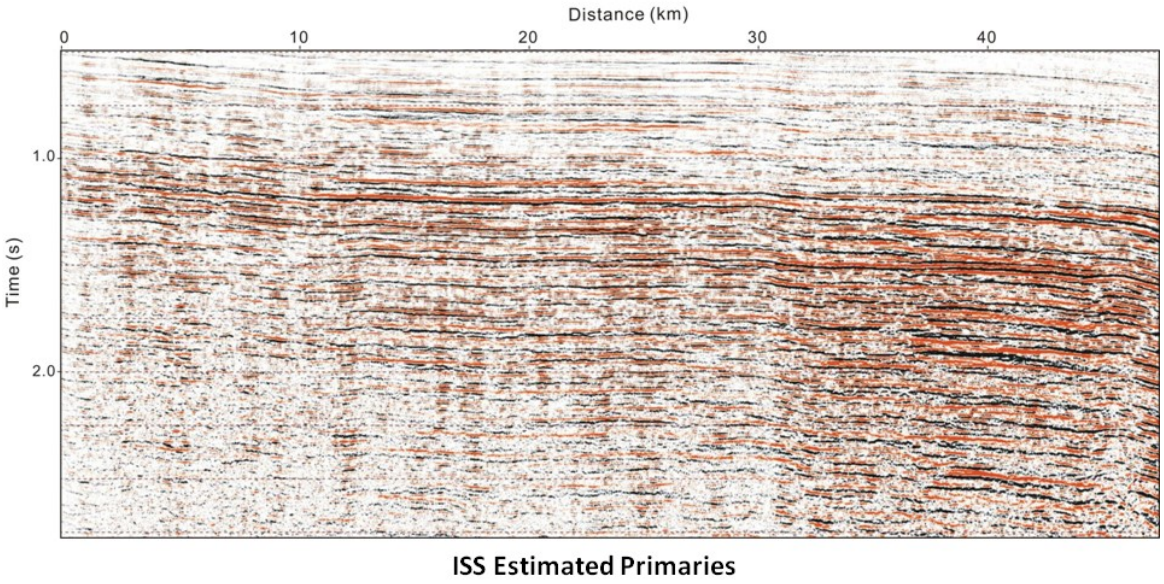

Figure 5: Primaries obtained after applying the 1D ISS internal multiple elimination algorithm.

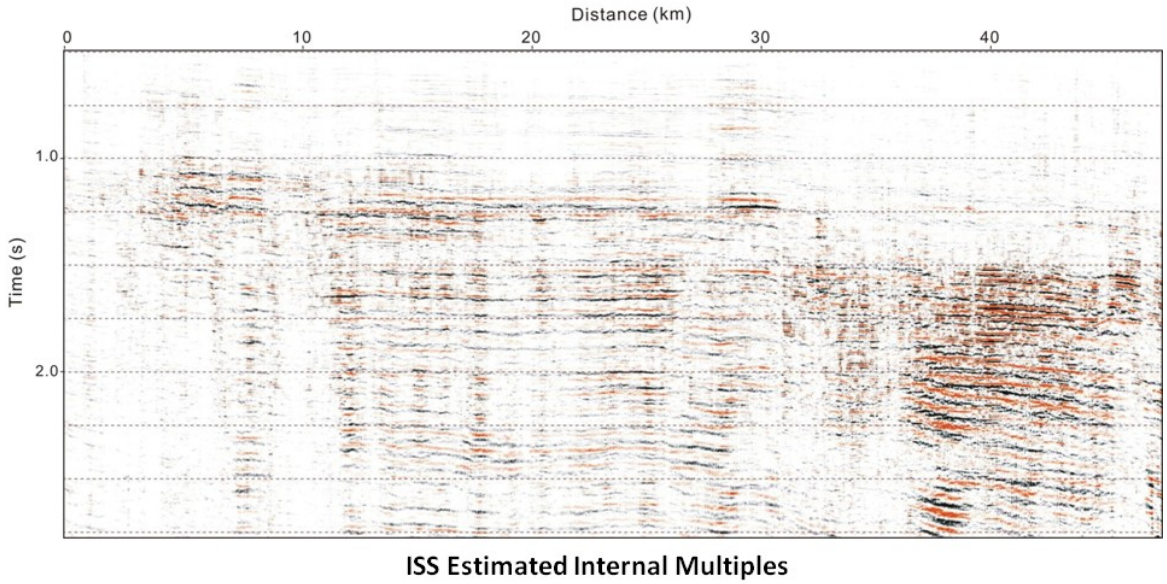

Figure 6: The estimated internal multiples, i.e., the difference between Figures 4 and 5.

Multiple attenuation: Recent advances and the road ahead (2011)

Arthur B. Weglein[1], Shih-Ying Hsu[1], Paolo Terenghi[1], Xu Li[1], and Robert H. Stolt[2]

[1]Department of Physics, University of Houston, Houston, Texas, USA
[2]ConocoPhillips, Houston, Texas, USA

Offshore and onshore multiple removal: Responding to the challenges

In offshore exploration, the industry trend to explore in deep water, by itself, with even a flat horizontal water bottom and a 1D subsurface, immediately caused many traditional signal processing/statistical based multiple removal methods to bump up against their assumptions and break down and fail. In addition, marine exploration plays beneath complex multi-D laterally varying media and beneath and/or at corrugated, diffractive rapid varying boundaries (for example, subsalt, sub-basalt and subkarsted sediments and fault shadow zones) caused a breakdown of many multiple removal methods. Decon, stacking, *f-k*, Radon transform, and wavefield modeling and subtracting multiples are among methods that ran into problems with the violation of any one or combination of the following assumptions: (1) primaries are random, and multiples are periodic, (2) knowledge of the velocity of primaries, and assuming the earth has no lateral variation in properties, with 1D moveout assumptions, (3) velocity discrimination between primaries and multiples, (4) interpreter intervention capable of picking and discriminating primary or multiple events, and (5) determining and defining generators of the multiples, and then modeling and subtracting multiples. The confluence of : (1) high drilling costs in deep water plays, (2) specific deep water hazards and technical challenges, (3) the need to develop fields with fewer wells, and (4) the record of drilling dry holes, drove the need for greater capability for removing marine free-surface and internal multiples, as well as improving methods of imaging.

The estimation and removal of land internal multiples can make the toughest marine-multiple problem pale in comparison. In Kelamis et al. (2006), Fu et al. (2010), and Luo et al. (2011) the basic cause of the land-multiple removal challenge is identified as a series of complex, thin layers encountered in the near surface.

In general, strong reflectors at any depths can be identified as significant sources of internal multiples, especially where geologic bodies with different seismic properties are in contact. Typical examples are alternating sequences of sedimentary rocks and basaltic layers or coal seams, which can give rise to short period internal multiples.

If multiples are a problem due to violation of the assumptions behind methods used to remove them, then the idea is to either develop new methods that remove the violation, and arrange to satisfy the assumption; or develop fundamentally new methods that avoid the limiting or inhibiting assumption altogether. There are cases and issues for which one or the other of these attitudes is called for and indicated. An example of seeking to satisfy a requisite is when a data acquisition is called for by a multiple removal technique, and you seek methods of data collection and interpolation/extrapolation to remove the violation of the need of collecting data by satisfying the requirement. However, if a multiple removal method is, for example, innately 1D in nature, then an interest in removing multiples in a multi-D earth would call for developing a new method that did not assume a 1D earth, hence, calling for developing a new multi-D method that altogether avoids the 1D assumption. The former, e.g., arranging a 3D corrugated boundary subsalt play to satisfy 1D layered earth assumptions, velocity analysis, and moveout patterns, or modeling and subtraction of multiples, where seeking to satisfy those type of assumptions is not really imaginable let alone plausible. That fact drove the search for new methods that avoided those impossible-to-satisfy criteria. These new methods would satisfy the following criteria: (1) be fully multi-D, (2) make no assumptions about subsurface

properties, (3) have no need for interpretive intervention, (4) and be able to accommodate the broadest set of multiples of all orders, (5) where the definitions and meaning of primaries and multiples themselves are extended from their early 1D earth definitions and concepts, extended to prime and composite events as introduced in Weglein and Dragoset (2005), and (6) be equally effective at all offsets, retaining effectiveness in prestack and poststack applications, and (7) last but not least, where multiples are surgically removed by predicting both their amplitudes and phases, and thus do not harm primaries, even if they are proximal and overlapping. The efficacy and choice among multiple removal methods in response to the challenges posed in a world of complex multiple generators, in 1D earth settings, and/or in heterogeneous rapid laterally varying media and boundaries would ultimately be evaluated, judged and selected, by how well they satisfied *all* of these criteria.

Before discussing, classifying, and comparing methods for removing multiples, it would be useful to introduce and briefly discuss three important background topics/subjects that will enhance and facilitate grasping the sometimes counterintuitive ideas we will be describing and attempting to convey.

Modeling and inversion are two entirely different enterprises

Modeling run backwards, or model matching or iterative linear inverse model matching, or any form of indirect inversion, or solving a direct forward problem in an inverse sense, are not equivalent to direct inversion. Nor is any intermediate seismic processing objective within a direct inversion algorithm equivalent to solving for that same goal in some model-matching or indirect manner. The only exception to that rule is when the direct inverse task is linear (e.g., when the goal is depth imaging and **you know the velocity field**, the direct inverse for depth migration is linear, and then modeling run backwards is direct depth imaging). If the direct inverse is nonlinear in either the entire data set or a single event, then modeling run backwards is not the equivalent of a direct inverse solution. See e.g., Weglein et al. (2009) for full detail and examples. And it is worth noting at this point that the inverse scattering series is the only direct inverse for a multidimensional acoustic, elastic, or inelastic heterogeneous earth.

Prediction and subtraction: The plan to strengthen the prediction, and reduce the burden, dependence and mischief of the subtraction

Multiple removal is often described as a two-step procedure: prediction and subtraction. The subtraction step is meant to try to compensate for any algorithmic compromises or real world conditions outside the physical framework behind the prediction. In multiple removal applications the subtraction step frequently takes the form of an energy minimizing criteria based adaptive subtraction. The idea being that a section of data (or some temporally local portion of data) without multiples has less energy than the data with multiples. One often hears that the problem with multiple attenuation is not the prediction but the subtraction. In fact, the real problem is excessive reliance on the adaptive to solve too many problems, with an energy minimizing criteria that can be invalid or fail with proximal or overlapping events. The breakdown of the energy minimization adaptive subtraction criteria itself can occur precisely when the underlying physics behind, e.g., high-end inverse scattering series multiple prediction (that it is intended to serve) will have its greatest strength and will undermine rather than enhance the prediction.

Exact closed forms and perturbative mathematical relationship: closed forms with exact information and series solutions for approximate or no information

There are two general mathematical approaches to solving problems: (1) Exact closed-form or single-term relationships, typically associated with situations where the detail causing the phenomena is well defined; and (2). perturbative approaches, identified with descriptions that allow for imprecise (or no) information about the condition causing the phenomena. The archetypal perturbative statement is the Taylor series

$$f(x) = f(y) + f'(y)(x-y) + f''(y)(x-y)^2/2 + \cdots \quad (1)$$

where the function f at x is given in terms of f and its derivatives at y and the difference between x and y, (x−y).

The value of f, at state x, is given as a perturbation of f about another state, y. An example of an exact closed-form relationship would be, e.g., $f(x)=2+5x$.

Understanding the difference between exact and perturbative relationships is the cornerstone for gaining an appreciation for how the forward and inverse-scattering series approach the construction and removal of events that either owe their existence to well defined and accessible causes (e.g., the free surface) or to causes that uncertain and inaccessible (e.g., reflectors in the subsurface).

For example, free-surface multiples owe their existence to the presence of the air-water free surface. Furthermore, since that physical boundary is as close to well defined and accessible as occurs in exploration geophysics, we will see how the generation and removal of each order of free-surface multiple is accomplished through the action of a single closed-form and exact term. In contrast, internal multiples (i.e., multiples that have their downward reflections below the air-water boundary) have experienced reflectors that are less well defined and, thus, a perturbative description is appropriate. In fact, an entire forward series is needed to construct one order of internal multiple, and one other entire inverse series is required to eliminate that order of multiple, without knowing or needing to know, or determining anything about the subsurface that the multiple has experienced and has generated the multiple.

Scattering theory provides a surface reflection model for surfaces that are close to well defined (e.g.,air-water boundary) and a point scatterer model to model primaries and internal multiples where the details of the medium are uncertain.

The inverse-scattering method assumes a priori information about the location and character of the airwater free surface. However, the method assumes no a priori information below the hydrophones. Internal multiples are described without any a priori information, using a distinct series in both their forward series construction and inverse series removal.

Forward and inverse maps

A forward problem generates data from a model concept; the forward model concept represents the way you visualize data being generated. How the processor conceptualizes and realizes data being generated determines (or locks the processor into) a concept of how they can be inverted to determine inverse or processing goals. The forward description determines how the experiences the event has realized are coded into its character; likewise the inverse decoding of events to determine inversion goals depends on the language and ingredients used to describe those experiences. How to code and decode depends on the processor's degree of confidence in defining the precise nature of the physical phenomena causing those experiences.

The most straightforward and intuitive forward concept describes the formation of data in terms of the actual medium and actual reflections it has experienced between source and receiver. Although conceptually transparent and understandable, with each seismic recorded event being represented by a single term consisting of a product of all propagations, reflections, and transmission that the event had actually experienced. However, to invert, or to perform some inverse tasks within that conventional vision requires the ability to supply or determine the ingredients of the data construction, i.e., actual medium properties and structural information.

Inverse tasks such as the removal of free-surface multiples are coupled to the corresponding concept of their construction. The free surface at the air-water boundary is the physical experience difference that causes the free-surface multiples to exist; it is well defined and well located, hence it is suitable for creation and elimination of the actual air-water reflection that those free-surface multiples have experienced and all other events have not.

We will demonstrate some of these ideas (using the 1D plane-wave normal incidence case) for the inverse scattering free-surface multiple elimination method.

Figure 3 shows a situation in which a unit-amplitude downgoing wave leaves a source in the water column. The upper figure assumes that there is no free surface. $R(\omega)$ denotes the single temporal frequency of the upgoing recorded field. The lower figure corresponds to the same situation with the addition of the free surface. $R_f(\omega)$ is the single temporal frequency of the upgoing portion of the recorded data. $R(\omega)$ contains all primaries and internal multiples. $R_f(\omega)$, on the other hand, is the upgoing portion of the total measured wavefield and consists of primaries, internal multiples, and free-surface multiples. The downgoing source wavefield and the upgoing receiver wavefield would be realized in practice by source and receiver deghosting. The latter source and receiver deghosting is a critically important step to assure subsequent amplitude and phase fidelity of the ISS free-surface multiple removal methods, whose derivation follows below.

Forward construction of data with free-surface multiples, $R_f(\omega)$, in terms of data without free-surface multiples, $R(\omega)$

The downgoing source wavefield of unit amplitude first impinges on the earth and $R(\omega)$ emerges (consisting of all primaries and internal multiples). $R(\omega)$ hits the free-surface and $-R(\omega)$ is the resulting downgoing wave (since the reflection coefficient is -1 for the pressure field at the free surface). This downgoing field, $-R(\omega)$, in turn enters the earth, and $-R^2(\omega)$ emerges, and this repeats in the manner shown in Figure 4.

The total upgoing wavefield in the presence of a free surface, $R_f(\omega)$, is expressed in terms of the total upgoing wavefield in the absence of the free surface, $R(\omega)$,

$$R_f(\omega) = R(\omega) - R^2(\omega) + R^3(\omega) \cdots \tag{2}$$

$$R_f(\omega) = R(\omega)/[1 + R(\omega)] \tag{3}$$

Several items are worth noting about this result.

First, $R(\omega)$ includes primaries and internal multiples; $-R^2(\omega)$ constructs all first-order free-surface multiples; $R^3(\omega)$ constructs all second-order free-surface multiples; and $(-1)^{n+1}R^n(\omega)$ constructs all *n*th order free-surface multiples (*n*th order free-surface multiple means the multiple has n downward reflections at the free surface).

Second, the fact that the free-surface is well located and defined by a known reflection coefficient (-1) allows one closed-form exact expression to create all of those events that correspond to each order of free-surface multiple.

The inverse series for removing free-surface multiples corresponding to the forward series (above) that constructs free surface multiples one above is found by rearranging the second equation into $R=R_f/(1-R_f)$ and then expressing R as the infinite series

$$R = R_f + R_f^2 + R_f^3 + \cdots \tag{4}$$

R_f, as defined, equals the data with all free-surface multiples. R_f^2 predicts (-1) times all first-order free-surface multiples; R_f^3 predicts (-1) times all second-order free-surface multiples, and so forth. Again, one closed-form exact expression (one term) in the inverse series predicts and subtracts all events corresponding to a given order of free-surface multiple. Thus, the above summation for R yields the data with all free-surface multiples eliminated. This expression is, indeed, the 1D normal-incidence version of the inverse-scattering free-surface multiple-attenuation algorithm Carvalho (1992); Weglein et al. (1997). Notice that neither the forward (construction) series for R_f in terms of R nor the removal (elimination) series for R in terms of R_f depend on knowing anything below the receivers.

The ISS free-surface removal series derivation and algorithm does not care about the earth model type and is completely unchanged whether the earth is acoustic, elastic, or anelastic. That property is called 'model type independent' Weglein et al. (2003).

The derivation of these series was based on the difference in the physical circumstances that gives rise to the events we are trying to isolate and separate: Those events are free-surface multiples and the (D_1) reflection coefficient at the free surface is the physical circumstance.

Both the construction and elimination process assume a wavelet deconvolution in the forward problem. The wavelet, $S(\omega)$, plays a role in the forward problem:

$$R_f = SR(\omega)/[1 + R(\omega)] \tag{5}$$

and in the inverse

$$R = (R_f/S)/(1 - (R_f/S)) = R_f/S + {R_f}^2/S^2 + {R_f}^3/S^3 + \cdots \tag{6}$$

Hence, for free-surface multiple removal there is a critical need for the wavelet since the effectiveness of the series has a nonlinear dependence on $1/S(\omega)$.

As mentioned earlier, the single term, closed-form, exact expressions for creating and removing all free surface multiples of a given order reflect their exact, well defined, and well localized source: the free surface.

For those readers interested in the generalization of these simple 1D formulas to the multidimensional earth, we suggest that the simple reflection coefficient (-1) be thought of (in scattering theory) as part of the extra term in the reference Green's functions due to the presence of the free surface called G_0^{FS}.

Free-surface demultiple algorithm: instructive analytic examples

We present an analytic example to illustrate the inner workings of the ISS free surface multiple removal algorithm.

The reflection data in the time domain:

$$R_f(t) = R_1\delta(t-t_1) + R_2'\delta(t-t_2) - R_1^2\delta(t-2t_1) - R_2'^2\delta(t-2t_2) - 2R_1R_2'\delta(t-(t_1+t_2))\cdots \quad (7)$$

In frequency domain:

$$R_f(\omega) = R_1e^{i\omega t_1} + R_2'e^{i\omega t_2} - R_1^2e^{2i\omega t_1} - R_2'^2e^{2i\omega t_1} - 2R_1R_2'e^{i\omega(t_1+t_2)} + \cdots \quad (8)$$

$$R_f^2(\omega) = R_1^2e^{2i\omega t_1} + R_2'^2e^{2i\omega t_2} + 2R_1R_2'e^{i\omega(t_1+t_2)} + \cdots \quad (9)$$

So $R_f(\omega)+R_f^2(\omega)$ precisely eliminates all free surface multiples that have experienced one downward reflection at the free surface. The absence of low frequency (and in fact all other frequency) plays absolutely no role in this prediction. This is a nonlinear direct inverse that removes free surface multiples. There is no imaginable way that one frequency of data could be used to model and subtract one frequency of free-surface multiple. A single frequency of data cannot even locate the water bottom. This is an example of how a direct nonlinear inverse does not correspond to a forward problem run backwards. Model matching and subtracting multiples is inconceivable without knowing or caring about the earth model type for the modeling step. Model matching, iteratively or otherwise, modeling run backwards, and all forms of indirect inversion are not equivalent to a direct inverse solution.

Recovering an invisible primary

Consider a free surface example with the following data:

$$r_t(t) = R_1\delta(t-t_1) + R_2'\delta(t-t_2) - R_1^2\delta(t-2t_1). \quad (10)$$

Now assume

$$R_2' = R_1^2. \quad (11)$$

$$t_2 = 2t_1. \quad (12)$$

for some special case, then from equation **Error! Reference source not found.**,

$$r_t(t) = R_1\delta(t-t_1) \quad (13)$$

The second primary and the free-surface multiple cancel, and

$$r_f(\omega) = R_1e^{i\omega t_1} \quad (14)$$

$$r_f^2(\omega) = R_1^2e^{2i\omega t_1} \quad (15)$$

$$r_f(\omega) + r_f^2(\omega) = R_1e^{i\omega t_1} + R_1^2e^{2i\omega t_1} \quad (16)$$

$$r(t) = R_1\delta(t-t_1) + R_1^2\delta(t-2t_1) = R_1\delta(t-t_1) + R_2'\delta(t-2t_1) \quad (17)$$

resulting in the two primaries by recovering the primary not 'seen' in the original data.

The ISS free-surface multiple removal algorithm with deghosted data can predict and subtract the hidden multiple and recover the hidden primary. If these obliquity factor deghosting ingredients are compromised in the prediction the amplitude will be misplaced and incorrect the prediction and there will be an incorrect primary in the invisible reflector example. When the multiple is removed in the invisible reflector example, the energy goes up not

down, and the adaptive subtraction minimize energy criteria fails and it cannot 'fix' the problem. The lesson: Don't compromise on prediction strengths and assume the subtraction (adaptive) will atone for any shortcomings. The ISS FS multiple prediction has no trouble recovering the hidden reflector.

Jingfeng Zhang (2007)(pp. 37-63) demonstrates with prestack data that with deghosted data the ISS free-surface algorithm precisely predicts the FS multiple without the need for adaptive subtraction. For these same examples and in general the feedback loop free-surface multiple-attenuation algorithm, with its lack of an obliquity factor and retaining the source side ghost, will not accurately predict the amplitude and phase of free-surface multiples.

Internal multiples and scattering theory

Forward scattering theory provides a data construction, and inverse-scattering provides a data inversion based on a reference medium, rather than the actual; and point scatterers at points where reference differs from actual. The most convenient reference medium chosen for the purposes of multiple attenuation is water because no a priori information is required. Internal multiples are now visualized as being constructed by an infinite series, rather than as a single term (i.e., a generalized Taylor series about water speed, instead of a single-term description of actual experiences). The benefit is that there is an analogous inverse series for the removal of those internal multiples that requires only primaries and internal multiples, and water speed as input!

But what is the use of this idea if it requires an infinite set of terms to construct a single internal multiple and an infinite set of terms to eliminate it? The answer is: While it is true that it requires, in principle, an infinite set of terms to completely eliminate an internal multiple (when starting with water as the reference), the remarkable fact is that *the first term in the removal series predicts the exact traveltimes of all internal multiples* (including converted-wave internal multiples) and gets 85-95% of the amplitude predicted for entire P-wave internal multiples. The removal process for internal multiples (i.e., the predictive apparatus in the direct inversion series) is much more efficient than the corresponding first contribution to the forward series that models and constructs internal multiples. That latter first term in the forward series gets the time for all internal multiples wrong and in general is a poor approximation to the amplitude. There are certain classes of internal multiples for which closed form for entire series realizing the elimination of those internal multiples have been developed (Ramírez and Weglein, 2005) and we anticipate further progress on that front.

If the prediction of internal multiples that resides in the inverse-scattering series was as efficient as the construction of internal multiples in the forward series (where it takes an infinite number of terms to get the time right), then the inverse-scattering series for predicting and subtracting internal multiples would be of no practical value.This is not the case.

The reason behind this difference between the efficiency of the prediction in the forward and inverse series is that the inverse has data, with events in time, as input; the forward series does not. Processes that involve data prediction are favored by the inverse series; processes that involve depth (or spatial) issues are the domain of comfort of the forward series.

Forward and inverse-scattering series as generalized Taylor series

The forward-scattering series is a generalized Taylor series for the data generated from the actual medium, $D=D(m)$, in terms of the data from the reference medium, $D_0=D(m_0)$, and the difference between the actual and reference media, $m-m_0$. Similarly, the inverse-scattering series can be viewed as the generalized Taylor series that produces the actual medium, $m=m(D)$ in terms of the reference medium, $m_0=m(D_0)$, and the difference between actual and reference data, $D-D_0$.

The forward-scattering series is

$$D(m) = D(m_0) + D'(m_0)(m - m_0) + D''(m_0)(m - m_0)^2 \cdots \tag{18}$$

and the inverse series is

$$m(D) = m(D_0) + m'(D_0)(D - D_0) + m''(D_0)(D - D_0)^2 \cdots \tag{19}$$

. It turns out that $D'(m_0)$, $D''(m_0)\cdot$ and $m'(D_0)$,$m''(D_0)\cdot$ are all expressible in terms of very simple analytic forms that only involve the wavefield in the reference medium, $D(m_0)$. With water as the reference medium, the forward series derives the actual data in terms of propagation in water and the difference between earth and water, $m-m_0$. The inverse series provides the actual medium, m, in terms of propagation in water and the difference between recorded and reference wavefields, $D(m)-D(m_0)$.

Therefore, the subseries that attenuate free-surface and internal multiples (and that reside within the inverse-scattering series) only input data and the propagation properties of water. This demonstrates the link (propagation in the reference medium) between the forward and inverse scattering series. The choice of reference depends on several factors: the task within the inversion process that is the objective; the need for a priori information to achieve that objective; and the availability of reliable information.

The simpler the reference, the simpler the inverse calculations. The simplest reference medium is water and for the tasks of multiple attenuation there is little or no benefit to choosing anything closer to the actual earth.

In the forward-scattering problem, $m-m_0$ is given, and the spatial location of reflectors corresponds to where $m-m_0$ is rapidly varying. Therefore, for the forward-scattering series the location of reflectors is straightforward. The time of events is difficult to predict in the forward series since the wave is propagating with the reference speed, not actual speed, between reflection points. In contrast, the inverse series starts with the data, D, in time. Hence, it favors tasks (e.g., the prediction of free-surface and internal multiples) that stay in that domain. This is the essence of the difference between prediction in the forward scattering (modeling) and the inverse-scattering (processing) problem.

In sum, forward modeling of seismic data from the forward series generates data from a model, starting with no data (or reference data from a reference model). Either case results in a larger class of events after the modeling operations are completed.

The forward series for modeling seismic data, including primaries and multiples, requires knowledge of every detail of the medium, and is model type specific. The inverse series allows removal of free surface and internal multiples without any interest in subsurface information, and without any interest in what type of model you might consider appropriate for modeling the data from the earth.

In contradistinction, in direct inversion the data-prediction operations start with a combination of event types and then predict and subtract one class of those events from the rest. Hence, the prediction mechanisms within the direct inversion are going in the opposite direction from the prediction mechanisms of modeling. Direct inversion inputs a larger, more extensive set of data and proceeds to separate primaries and multiples of different types and orders. In direct inversion, the data already contain the events to be predicted (and substracted). Data prediction with modeling requires creation of the events to be predicted. In direct inversion, the objective is to separate out a subset of the entire data set that has a certain specific characteristic from those that don't, starting with data that contain all events with and without that characteristic. For example, one characteristic could be a free-surface reflection, another could be no free-surface reflection but one downward reflection anywhere below the free surface. This is the fundamental difference between the data-prediction mechanisms in modeling and direct inversion.

There are different ways in which internal multiples are cataloged and classified, and these characterizations affect the way that inversion methods separate them from primaries. If the construction of primaries and multiples is characterized in terms of their actual propagations and reflections (the interface model used in the feedback method), then actual propagation and reflection properties are required in the removal of those multiples.

However, if primaries are characterized, described, and distinguished from multiples in a forward construction in terms of a reference medium, then the inverse of that construction provides a systematic procedure to separate internal multiples from data (with primaries and internal multiples), using only the data and the reference medium (water). This is the idea behind the inverse scattering series for attenuating internal multiples, and it is in that understanding and logic that the mystery of how the inverse scattering series for attenuating free-surface and internal multiples is demystified. That is also the origin of the difference between the inverse-scattering and feedback-loop methods for internal multiples. These internal multiple procedures appear to have opposite attitudes toward a priori information and complementary regions of technical and cost effectiveness.

ISS internal multiple attenuation algorithm

The ISS internal-multiple attenuation algorithm (Araújo et al., 1994; Weglein et al., 1997) is a data-driven tool. It does not require any information about the reflectors that generate the internal multiples or the medium through which the multiples propagate, and it does not require move-out differences or interpretive intervention. The algorithm predicts internal multiples for all horizons at once. This ISS internal multiple attenuation algorithm is the first term in a subseries of the ISS that predicts the exact time and amplitude of all internal multiples without subsurface information. The ISS attenuation algorithm predicts the correct traveltimes and approximate amplitudes of all the internal multiples in the data, including converted-wave internal multiples (Coates and Weglein, 1996). Carvalho (1992) pioneered the free-surface ISS method and applied it to field data; Matson et al. (1999) were the first to apply the ISS internal multiple algorithm to marine towed streamer field data; and Ramírez and Weglein (2005) extended the theory from attenuation towards elimination by including more terms in the elimination subseries, thereby improving the amplitude prediction. The original ISS free-surface and internal multiple algorithms were designed for a marine towed streamer data experiment. Matson (1997) and Weglein extended the ISS methods for removing free surface and internal multiples to ocean bottom and land data.

The ISS internal-multiple attenuation algorithm in 2D starts with the input data, $D(k_g,k_s,\omega)$, that is deghosted and free-surface multiples eliminated. The parameters, k_g, k_s and ω , represent the Fourier conjugates to receiver, source, and time, respectively. The ISS internal-multiple attenuation algorithm for first order internal multiple prediction in a 2D earth is (Araújo, 1994; Weglein et al., 1997)

$$b_{3IM}(k_g,k_s,\omega)=\frac{1}{(2\pi)^2}\int_{-\infty}^{\infty}dk_1e^{iq_2(z_g-z_s)}\int_{-\infty}^{\infty}dz_1b_1(k_g,k_1,z_1)e^{i(q_g+q_1)z_1}$$
$$\times\int_{-\infty}^{\infty}dk_2\,e^{-iq_1(z_g-z_s)}\int_{-\infty}^{z_1-\varepsilon}dz_2b_1(k_1,k_2,z_2)e^{-i(q_1+q_2)z_2}\times\int_{z_2+\varepsilon}^{\infty}dz_3b_1(k_2,k_s,z_3)e^{i(q_2+q_s)z_3} \quad (20)$$

The quantity corresponds to an uncollapsed migration (Weglein et al., 1997) of an effective incident plane-wave data, which is given by . The vertical wavenumbers for receiver and source, q_g and q_s, are given by $q_i=sgn(\omega)\sqrt{\frac{\omega^2}{c_0^2}-k_i^2}$ for $i=(g,s)$; c_0 is the constant reference velocity; z_s and z_g are source and receiver depths; and z_i (i=1,...,3) represents pseudodepth. Note that the obliquity factor, $2iq_s$, is used to transform an incident wave into a plane wave in the Fourier domain (Weglein et al., 2003).

The first-order internal multiple is composed of three events that satisfy $z_1>z_2$ and $z_3>z_2$. The traveltime of the internal multiple is the sum of the traveltimes of the two deeper events minus the traveltime of the shallower one. The parameter ε introduced in equation **Error! Reference source not found.** preclude $z_1=z_2$ and $z_2=z_3$ in the integrals. For band-limited data, ε is related to the width of the wavelet. The output of equation **Error! Reference source not found.**, , are divided by obliquity factors and transformed back to space-time domain. When we subtract the estimated internal multiples from the original input data, all first order internal multiples are suppressed and higher order internal multiples are altered.

Properties of the first order term in the ISS internal-multiple attenuation algorithm -- uncollapsed *f-k* migration

Stolt uncollapsed migration resolves many complicated wave phenomena within a constant velocity overburden such as diffractions and multipathing. One example of such phenomena is the bow-tie pattern generated by reflections over a sufficiently curved boundary. These effects are common in seismic exploration data and can occur in a variety of geologic features, including salt domes, faults, layer terminations, pinch-outs, fractured and/or irregular volcanic

layers and for a rough sea-bottom. As we mentioned, several internal multiple removal algorithms require picking of events and traveltimes. In some of those methods (Keydar et al., 1997) the picked traveltimes are directly used to mute the wavefield at earlier or later times with respect to the generator, and internal multiples are predicted using auto- and crosscorrelation operations between traces from the resulting fields. In others, e.g. the feedback methods, the traveltimes are used to determine approximated redatuming operators. However, all these approaches are based on the implicit assumption that a one-to-one relationship exists between seismic events (their traveltime) and the earth features that create them (such as layer boundaries). In the presence of diffractions and/or multipathing, a one-to-one relationship does not exist, as, e.g., a single curved interface can produce several seismic arrivals. Picking events, traveltimes, and generators is generally not recommendable even in a normal incidence experiment in a 1D earth, since destructively interfering primary and multiple events are possible and even prevalent in land field data tests (see, e.g., Kelamis et al., 2006; Fu et al., 2010). The ISS method, with its automatic amplitude and phase prediction, and no picking of events nor generators, has no problem and surgically removes multiples that are isolated or interfering with other events.

Example1: Internal multiples from curved or rugose surfaces

We present an example based on a simple three-layer earth model where the shallowest interface is sine shaped. The model in Figure 7a produces the data in Figure 7b where all seismic events except the second primary at 2.2 s can be traced back to their origin at the shallow reflector. Clearly, in this example it is an issue to pick a unique traveltime to represent the curved reflector, as many events are generated which interfere among themselves and even with the second primary. The ISS method provides a natural solution by using as input the uncollapsed prestack FK water-speed migration (Figure 7c). The sketch in Figure 8 describes the case of an internal multiple which would not be predicted if total traveltimes were the basis of the method. The multiple can be shown to trace back to an earth feature where the relationship between total traveltimes and vertical traveltimes (pseudodepth) is inverted due to the presence of a high-velocity layer at depth.

Properties of the leading (third) order term

Let z_1, z_2 and z_3 be the pseudodepths of three generic points in the first-order term of the internal multiples series (uncollapsed constant-velocity prestack migration). As those points span the entire data volume, the leading order attenuation algorithm (which is third order in the imaged data) allows any combination such that $z_1 > z_2$ and $z_3 > z_2$ to contribute the prediction (lower-higher-lower constraint). In contrast with the methods based on the convolution and correlation of wavefields, where the definition of the generator is static, the ISS algorithm's lower-higher-lower constraint does not refer to any particular interface or event in the data. On the contrary, it applies to all of their water-speed images allowing the simultaneous prediction of all first-order internal multiples from any depth without interpretation and traveltime picking of the data or knowledge of the medium.

Example2: A complete one-step prediction

We demonstrate the properties of the ISS internal-multiple prediction algorithm and its difference with the phantom layer approach (Berkhout and Verschuur, 2005; Kelamis et al., 2002) using a set of acoustic 3D finite-difference data. The model shown in Figure 9a is composed of four layers delimited by three interfaces, the first of which has a gap approximately 1.5-km long and 100-m deep. In Figure 9b the travel paths of several internal multiples are drawn schematically using up- and downgoing arrows representing wave propagation. In a zero offset section of the data (Figure 10a) a first train of closely spaced internal multiples characterized by the pattern $2[12]_n$ can be shown to originate from the energy reflected between the two shallow reflectors 1 and 2. A deeper reflector 3 causes the entire train to begin again at around 1.4 s ($3[12]_n$ trend) and once more at 2.1 s ($313[12]_n$ and $323[12]_n$ trends). In general, even in a simple three-interface earth model the number of reverberations recorded at the surface is extremely large as a result of the various ways three reflectors can be combined to form internal multiples. The ISS internal-multiple algorithm predicts all of them at once, without any interpretation required on the data, as shown in Figure 10b and 10c. It is useful to observe that the feedback phantom layer approach and algorithms cannot achieve the same result for any choice of 'layer', even when two or more primaries such as events 1 and 2 form a layer of downward reflecting generators. Figure 11a shows the four types of first-order internal multiples generated within a three-

reflector earth. If the downward-reflecting layer is chosen to close between the first and second reflectors, the layer-related method can predict the three types of first-order internal multiples shown in Figure 11b.

The key point

Notice that for any choice of downward-reflecting layer, there is at least one type of first-order internal multiple which cannot be predicted with the phantom layer approach. Although these missed multiples might seem like some academic nitpick of little consequence, in fact this observation is of tremendous practical significance, and the root cause behind the Fu et al. (2010) conclusion on ISS internal multiple effectiveness and stand-alone added value on complex land near surface internal multiple generators.

The above analysis and examples help to recognize the ISS internal multiple capability for addressing the daunting challenges of land data. We describe a wish-list of qualities that the ideal response to multiple removal challenges would satisfy, and show how only the ISS internal multiple method reaches that high standard. All methods have strengths and shortcomings, and as we recognize the shortcomings of the current ISS attenuator, we know that removing them resides within the ISS and that upgrade will never require subsurface information, picking events or any interpretive intervention, or stripping as well. What all the ISS methods require is a reasonable source signature, and we are developing onshore Green's theorem methods for that purpose (see Zhang and Weglein, 2005; Zhang and Weglein, 2006; and Mayhan et al., 2011). Adaptive energy minimizing criteria are often employed in an attempt to bridge the conditions and limitations of the real world and the physics behind what our algorithms are assuming. When first introduced by Verschuur et al. (1992) and Carvalho and Weglein (1994) the need was clear and good benefit was derived, especially with isolated primaries and free surface multiples of first order. But as with all assumptions, today's reasonable and necessary assumption will invariably be tomorrow's impediment to progress and increased effectiveness. And that's the case with adaptive subtraction today. Especially with land internal multiples, we advocate a three pronged response: (1) seek further capability for amplitude fidelity for all orders of internal multiples, including converted wave internal multiples, (2) satisfy prerequisites for the source signature and radiation pattern, and (3) look for a new 'bridge' to replace the energy minimization adaptive criteria, a bridge that is consistent with the underlying physics rather than runs at cross purposes with the greatest strength of the ISS prediction. Our plan is to progress each of these three issues as a strategy to extend the current encouraging results and allow ISS multiple removal to reach its potential: to surgically remove all multiples without damaging primaries under simple, complex, and daunting land and marine circumstances.

Examples of 2D ISS free-surface and internal multiple removal with marine data

Figure 5 shows an example of the internal-multiple attenuation series algorithm applied to a 2D synthetic. The data set was computed using an earth model characterized by rapid lateral variations shown in Figure 5a. On Figure 5b, from left to right, the three panels show the input data, the predicted internal multiples, and the result of inverse scattering internal multiple attenuation, respectively.

Figures 6a and 6b illustrate the free-surface and internal multiple attenuation algorithms applied to a data set from the Gulf of Mexico over a complex salt body. Seismic imaging beneath salt is a challenging problem due to the complexity of the resultant wavefield. In Figure 6a, the left panel is a stacked section of the input data and the right panel shows the result of the inverse scattering free-surface multiple removal algorithm. Figure 6b illustrates the internal-multiple attenuation method applied to the same Gulf of Mexico data set. An internal multiple that has reverberated between the top of the salt body and the water bottom is well attenuated through this method.

ISS internal multiple application for land

Fu et al. (2010); Weglein et al. (2011); Luo et al. (2011) describe the motivation, evaluation, and comparison of different approaches to removing internal multiples on complex synthetic and onshore tests. Fu et al. (2010) concluded that "Their (ISS internal multiple algorithm) performance was demonstrated with complex synthetic and challenging land field data sets with encouraging results, where other internal multiple suppression methods were unable to demonstrate similar effectiveness".

These wavefield event separation methods can be reviewed as borrowing, extending, and merging the earlier separation idea of 'filters' and wave theory modeling to become the modeling of separation, in wave theory event separation techniques, and finally the separation of events without modeling the separation mechanism. In the Delft approach, the modeling of the event separation requires exact knowledge of the detail of the physical properties defining the difference in experience.

For internal multiples the antecedent of the Delft approach resides in the layer-by-layer stripping methods pioneered by Goupillaud (1961); Kennett (1983). The practical difficulties and failure of realizing the latter ideas and methods on field data and on band-limited noisy synthetic data caused understandable aversion to any use of amplitude for parameter identification. However, as every new generation of geophysicists arrives on the scene the idea is revisited, recently encouraged by the collection of longer offset and lower-frequency data.

The purpose of the following sections is to detail what resides behind the properties of the ISS internal multiple algorithm, and the reports by Fu et al. (2010) and Luo et al. (2011) on the stand alone added value represented by those techniques.

Conclusions

We introduce a classification of methods to attenuate multiples starting with filters and on to wavefield modeling and separation techniques. Filters seek to separate primaries from multiples and rely on either periodicity assumptions of multiples or different assumed transform domain separation properties to find a characteristic to separate and mute primaries from multiples. These methods make assumptions which typically include a 1D earth, and require knowing the velocity of primaries, and/or assume that there are move-out differences between primaries and multiples. The second category, wavefield modeling and subtraction (Morley and Claerbout, 1983; Wiggins,,1988) seeks to model the entire history of a multiple or a set of multiples, and then adaptively subtract the modeled multiple from the recorded reflection data. In principle, every physical property within the earth that the multiple has experienced must be accurately known to model and subtract it. The third class of methods, wavefield data separation, while wave-based returns in some sense to the filter idea of seeking to separate primaries from multiples. Rather than using periodicity or transform domain distinctions, however, wavefield data separation uses a defined and distinguishing difference in the actual history and experiences of the events as a means of separating them into categories. There are two different methodologies within this third class of data separation: (1) the feedback loop methods pioneered by the Delphi group at Delft University (Berkhout, 1982; Berkhout and Verschuur, 1997), and (2) the inverse scattering series methods centered at the Mission-Oriented Seismic Research Consortium, within the Physics Department of the University of Houston.

The filter method (based on modeling a specific physical location that separates events), and modeling and subtraction of multiples (based on modeling entire history) has given way to once again separate not in transform domains and using filters with very restrictive assumptions, but with either (1) a physical experience difference known and available for both free-surface and internal multiples (the feedback method), or (2) the vastly different inverse scattering series (ISS) methods for removing free-surface and internal multiples. ISS methods have the unique and stand-alone message, promise and ability to achieve all processing goals directly in terms of data, and without knowledge of subsurface properties. Processing goals of interest are: (1) removal of free-surface and internal multiples, (2) depth imaging, (3) nonlinear AVO, and (4) Q compensation. The ISS communicates that all processing tasks are directly achievable without subsurface information. Because ISS methods can accommodate a priori subsurface information or a total lack thereof (see, e.g., Weglein (1982)). this unique capability is called upon for different processing goals. Therefore, returning to multiples, the ISS provides for subseries that perform the removal of free surface and internal multiples directly in terms of data. When the separation and distinction can either be in terms of a known physical experience as for the free surface reflection and free surface multiple case respectively - while for ISS methods the internal multiple separation is not in terms of an actual known difference in physical well located and identifiable experience but rather in a more subtle and geometric and collaborative manner, that doesn't require knowing or determining any subsurface property whatsoever. There is no need to know either the entire history of the multiple nor is there any need to know, estimate or identify a part of the subsurface e.g., a reflector where those internal multiples that have experienced a shallowest downward reflection are separated from primaries and deeper downward reflecting internal multiples, the ISS multiple removal methods accommodates either well

known physical differences (free surface multiples) or unknown experience differences (internal multiples) or the entire internal multiples/and primary event separation takes place in terms of the complete measured wavefield and only water speed (in the marine case).

Entire history modeling and subtracting multiples gives way to recognizing that all we want to achieve is a separation of events into categories, and separation depends on identifying what separates them, sometimes explicitly and in closed form, and other times in terms of a separation of reference properties and data only. More collaborative cooperative engagement of the entire recorded wavefield is required when a separation without knowing or being able to achieve physical experience property detail is wanted. The ISS promises that separation can be exactly achieved without the identified separation defining physical property, as effectively as having that information would allow.

Summary

The strategy that we advocate is driven by the industry. It's objectives are: (1) fidelity of both amplitude and phase prediction to allow surgical multiple removal of all multiples without damaging primaries; (2) including all relevant multiples in the algorithms; (3) using appropriate orders of multiple removal terms from ISS multiple removal subseries) in the prediction; (4) strengthen the prediction and reduce the burden on the adaptive subtraction, and (5) develop a replacement to the energy minimization criteria that will align with rather than impede the method its meant to serve. The ISS methods for removing free surface and internal multiples is an essential and uniquely qualified ingredient/component in this strategy. When other priorities (like cost) might reasonably override amplitude and phase fidelity, and inclusiveness of relevant internal multiples is not essential, then the feedback method can be the right choice, provided the cost of drilling dry holes has been taken into account.

In summary, multiple removal prediction methods have progressed and there is much to celebrate. However, the trend to more complex and challenging marine and onshore plays demands inclusiveness of all troublesome multiples in the removal, along with: (1) stronger and more competent prediction, with amplitude and phase fidelity at all offsets, and (2) the development of fundamentally new concepts and criteria for subtraction, that align with rather than undermine the strengths of high-end prediction. There will always be a need for a subtraction step, attempting to deal with issues beyond the framework of the prediction, and there will always be those types of 'beyond the framework' issues. We need a more sophisticated and capable subtraction criteria. The adaptive subtraction concept, has been enormously useful; with a strong record of contribution but now is too blunt an instrument for the more complicated and complex pressing challenges. In the interim, the strategy is to build the strength of the prediction and to reduce the burden on the adaptive subtraction. In this paper we want to communicate our support and encouragement for that future progress and delivery.

Acknowledgement

The authors of this paper would like to express our deepest appreciation and gratitude to Dolores Proubasta, James D. Mayhan and Hong Liang for their excellent technical suggestions and advice that were all worthwhile and have benefited this paper. All authors wish to thank all M-OSRP sponsors, NSF (Award DMS-0327778) and DOE (BES Award DE-FG02-05ER15697) for their encouragement and support. We thank Bill Dragoset and Western Geco for providing the data shown in example 2 and for permission to publish the results.

References

Araújo, Fernanda V. *Linear and non-linear methods derived from scattering theory: backscattered tomography and internal multiple attenuation*. PhD thesis, Universidade Federal da Bahia, 1994.

Araújo, Fernanda V., Arthur B. Weglein, Paulo Marcus Carvalho, and R. H. Stolt. "Inverse scattering series for multiple attenuation: An example with surface and internal multiples." *SEG Technical Program Expanded Abstracts* 13 (1994): 1039–1041.

Berkhout, A. J. *Seismic migration, imaging of acoustic energy by wavefield extrapolation*. Elsevier, 1982.

Berkhout, A. J. and D. J. Verschuur. “Estimation of multiple scattering by iterative inversion, Part I: Theoretical considerations.” *Geophysics* 62 (1997): 1586–1595.

Berkhout, A. J. and D. J. Verschuur. “Removal of internal multiples with the common-focus-point (CFP) approach: Part 1 — Explanation of the theory.” *Geophysics* 70 (2005): V45–V60.

Carvalho, Paulo M. and Arthur B. Weglein. “Wavelet estimation for surface multiple attenuation using a simulated annealing algorithm.” *SEG Technical Program Expanded Abstracts* 13 (1994): 1481–1484.

Carvalho, Paulo Marcus. *Free-surface multiple reflection elimination method based on nonlinear inversion of seismic data*. PhD thesis, Universidade Federal da Bahia, 1992.

Coates, R. T. and A. B. Weglein. “Internal multiple attenuation using inverse scattering: Results from prestack 1 & 2D acoustic and elastic synthetics.” *66th Annual International Meeting, SEG, Expanded Abstracts* (1996): 1522–1525.

Fu, Qiang, Yi Luo, Panos G. Kelamis, ShouDong Huo, Ghada Sindi, Shih-Ying Hsu, and Arthur B. Weglein. “The inverse scattering series approach towards the elimination of land internal multiples.” *SEG Technical Program Expanded Abstracts* 29 (2010): 3456–3461.

Goupillaud, Pierre L. “An approach to inverse filtering of near—surface layer effects from seismic records” *Geophysics* 26 (1961): 754–760.

Kelamis, Panos G., Eric Verschuur, Kevin E. Erickson, Robert L. Clark, and Roy M. Burnstad. “Data-driven internal multiple attenuation — Applications and issues on land data.” *SEG Technical Program Expanded Abstracts* 21 (2002): 2035–2038.

Kelamis, Panos G., Weihong Zhu, Khalid O. Rufaii, and Yi Luo. “Land multiple attenuation — The future is bright.” *SEG Technical Program Expanded Abstracts* 25 (2006): 2699–2703.

Kennett, B. L. N. “Seismic Wave Propagation in Stratified Media.” (1983).

Keydar, S., E. Landa, B. Gurevich, and B. Gelchinsky. “Multiple prediction using wavefront characteristics of primary reflections.” *EAGE Expanded Abstracts* (1997).

Luo, Yi, Panos G. Kelamis, Qiang Fu, ShouDong Huo, Ghada Sindi, Shih-Ying Hsu, and Arthur B. Weglein. “Elimination of land internal multiples based on Inverse Scattering Series.” *Submitted to The Leading Edge* (2011).

Matson, K. H. *An inverse-scattering series method for attenuating elastic multiples from multicomponent land and ocean bottom seismic data*. PhD thesis, University of British Columbia, 1997.

Matson, K. H. *MOSRP Multiple Attenuation Review*. `http://www.mosrp.uh.edu/secure/mosrp2005/MOSRPdemultrev_Matson.ppt`. 2003.

Matson, K. H., D. C. Corrigan, A. B. Weglein, C. Y. Young, and Paulo Marcus Carvalho. “Inverse scattering internal multiple attenuation: results from complex synthetic and field data examples.” *SEG Technical Program Expanded Abstracts* 18 (1999): 1060–1063.

Mayhan, James D., Paolo Terenghi, Arthur B. Weglein, and Nizar Chemingui. “Green’s theorem derived methods for deghosting seismic data when the pressure P and its normal derivative are measured.” *submitted to SEG Technical Program Expanded Abstracts* (2011).

Morley, Larry and Jon Claerbout. “Predictive deconvolution in shot-receiver space.” *Geophysics* 48 (1983): 515–531.

Ramírez, A. C. and A.B. Weglein. “An inverse scattering internal multiple elimination method: Beyond attenuation, a new algorithm and initial tests.” *SEG Technical Program Expanded Abstracts* 24 (2005): 2115–2118.

Verschuur, D. J., A. J. Berkhout, and C. P. A. Wapenaar. “Adaptive surface-related multiple elimination.” *Geophysics* 57 (1992): 1166–1177.

Weglein, A. B., Fernanda V. Araújo, Paulo Marcus Carvalho, R. H. Stolt, K. H. Matson, R. T. Coates, D. Corrigan, D. J. Foster, S. A. Shaw, and H. Zhang. “Inverse Scattering Series and Seismic Exploration.” *Inverse Problems* (2003): R27–R83.

Weglein, A.B. and W.H. Dragoset. *Multiple Attenuation*. Society of Exploration Geophysicists, 2005.

Weglein, Arthur B. “Nearfield inverse scattering formalism for the three-dimensional wave equation - The inclusion of a priori velocity information.” *Journal of the Acoustical Society of America* 71 (1982): 1179–1182.

Weglein, Arthur B. “Multiple attenuation: an overview of recent advances and the road ahead.” *The Leading Edge* 18 (1999): 40–44.

Weglein, Arthur B., Fernanda Araújo Gasparotto, Paulo M. Carvalho, and Robert H. Stolt. “An inverse-scattering series method for attenuating multiples in seismic reflection data.” *Geophysics* 62 (1997): 1975–1989.

Weglein, Arthur B., Paolo Terenghi, Shih-Ying Hsu, Yi Luo, and Panos G. Kelamis. “The inverse scattering series approach to removing internal multiples: delineating and defining its current stand-alone capability, and proposing a plan for additional added value for land application.” *Submitted to SEG Technical Program Expanded Abstracts* (2011).

Weglein, Arthur B., Haiyan Zhang, Adriana C. Ramírez, Fang Liu, and Jose Eduardo M. Lira. “Clarifying the underlying and fundamental meaning of the approximate linear inversion of seismic data.” *Geophysics* 74 (2009): WCD1–WCD13.

Wiggins, J. Wendell. “Attenuation of complex water-bottom multiples by wave-equation-based prediction and subtraction.” *Geophysics* 53 (1988): 1527–1539.

Zhang, Jingfeng. *Wave theory based data preparation for inverse scattering multiple removal, depth imaging and parameter estimation: analysis and numerical tests of Green¡¦s theorem deghosting theor*. PhD thesis, University of Houston, 2007.

Zhang, Jingfeng and Arthur B. Weglein. “Extinction theorem deghosting method using towed streamer pressure data: analysis of the receiver array effect on deghosting and subsequent free surface multiple removal.” *SEG Technical Program Expanded Abstracts* 24 (2005): 2095–2098.

Zhang, Jingfeng and Arthur B. Weglein. “Application of extinction theorem deghosting method on ocean bottom data.” *SEG Technical Program Expanded Abstracts* 25 (2006): 2674–2678.

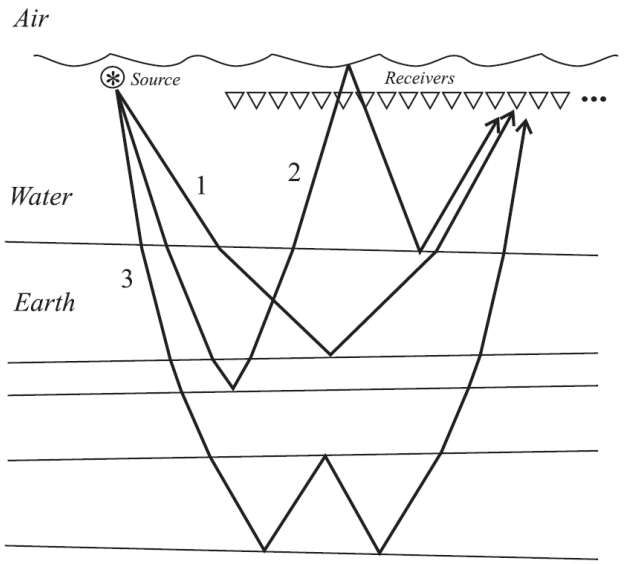

Figure 1: Marine primaries and multiples: 1, 2 and 3 are examples of primaries, free surface multiples and internal multiples, respectively.

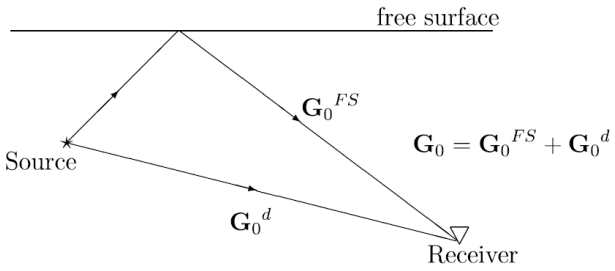

Figure 2: The marine configuration and reference Green Function.

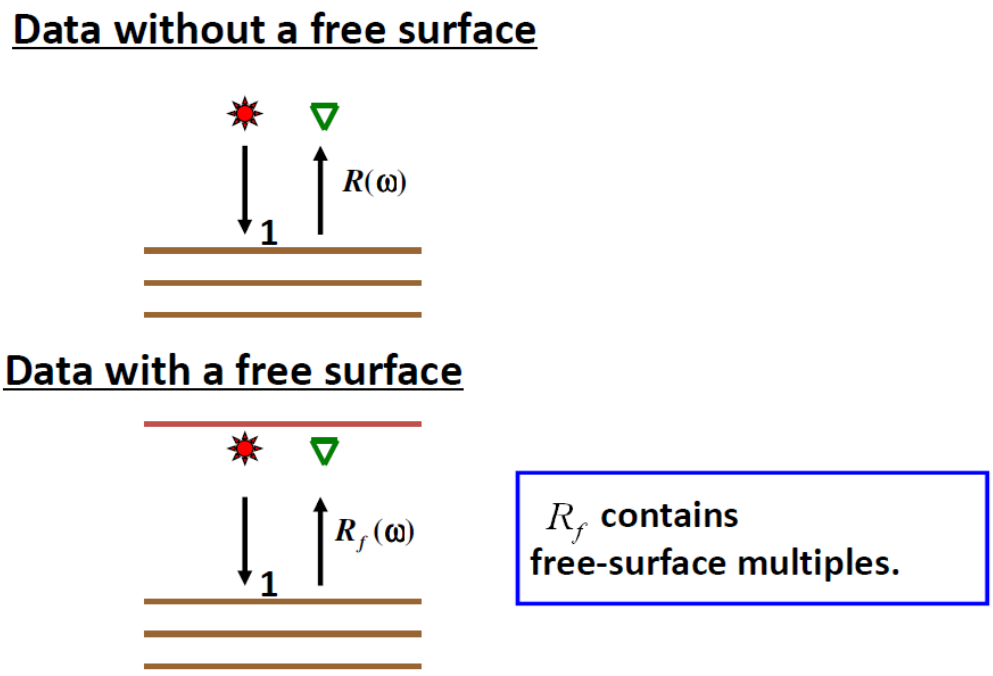

Figure 3: Data without a free surface (top) and with a free surface (bottom).

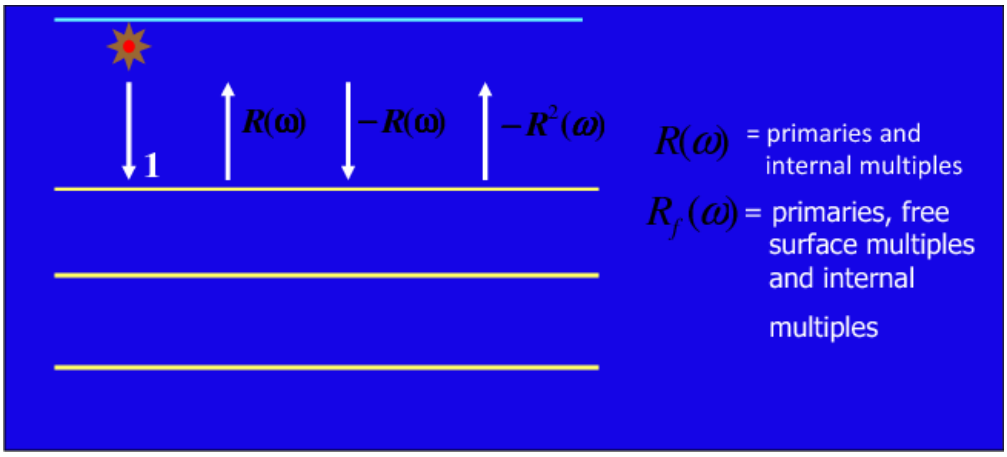

Figure 4: The forward problem. Constructing free surface multiples [i.e., from $R(\omega)$ to $R_f(\omega)$].

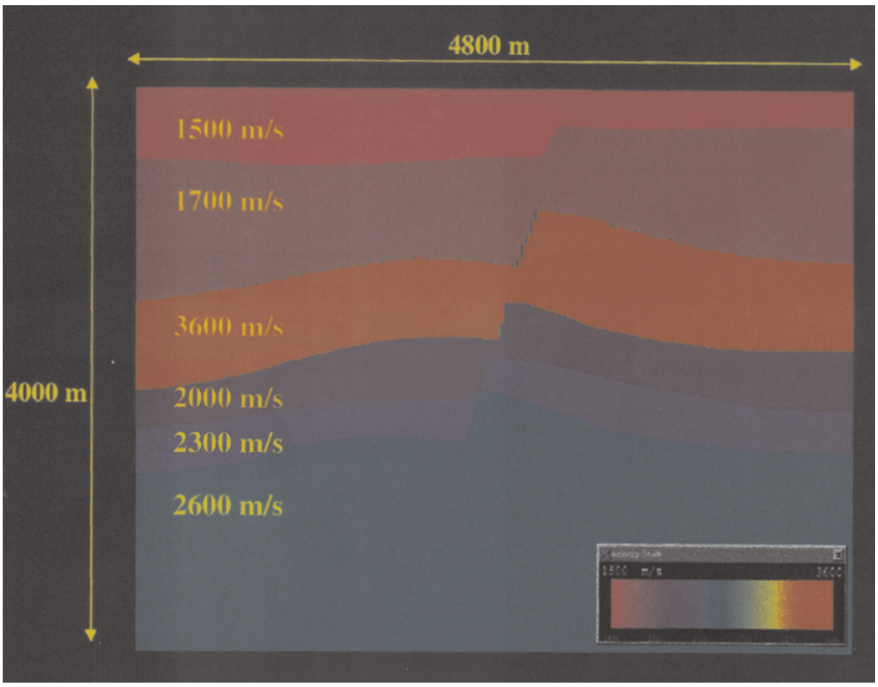

(a)

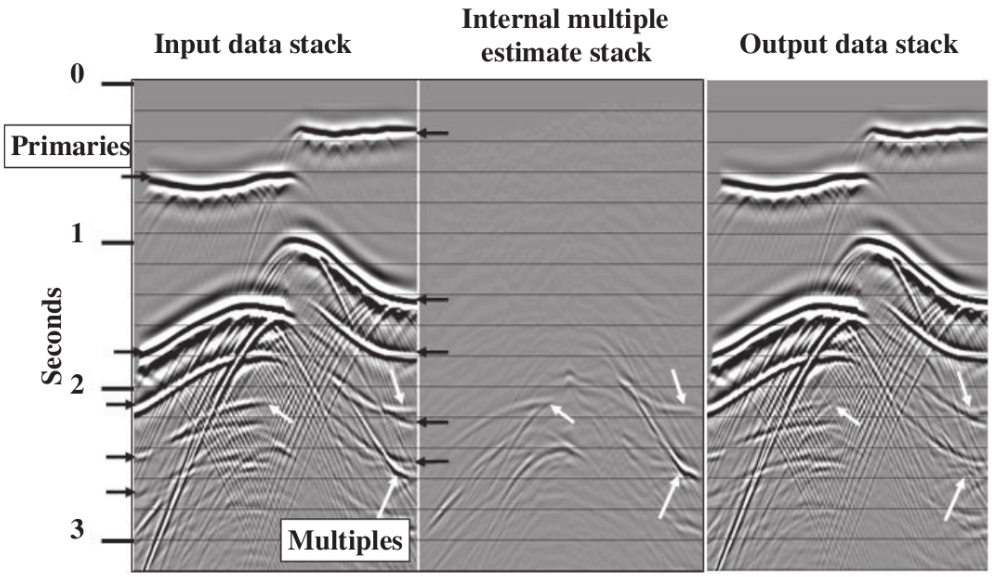

(b)

Figure 5: A 2D synthetic model characterized by gently curved reflectors intersected by a fault (top). The left panel (bottom) shows a common offset display from the synthetic data set created using the model. The middle panel (bottom) shows the predicted internal multiples and the right-hand panel (bottom) is the result after subtracting the predicted multiples from the input data set.

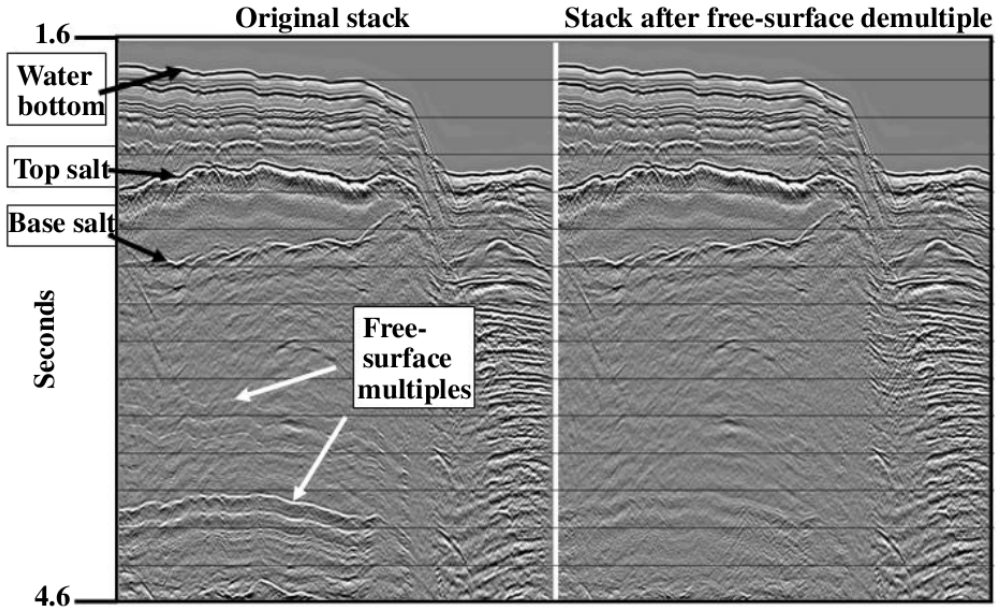

(a)

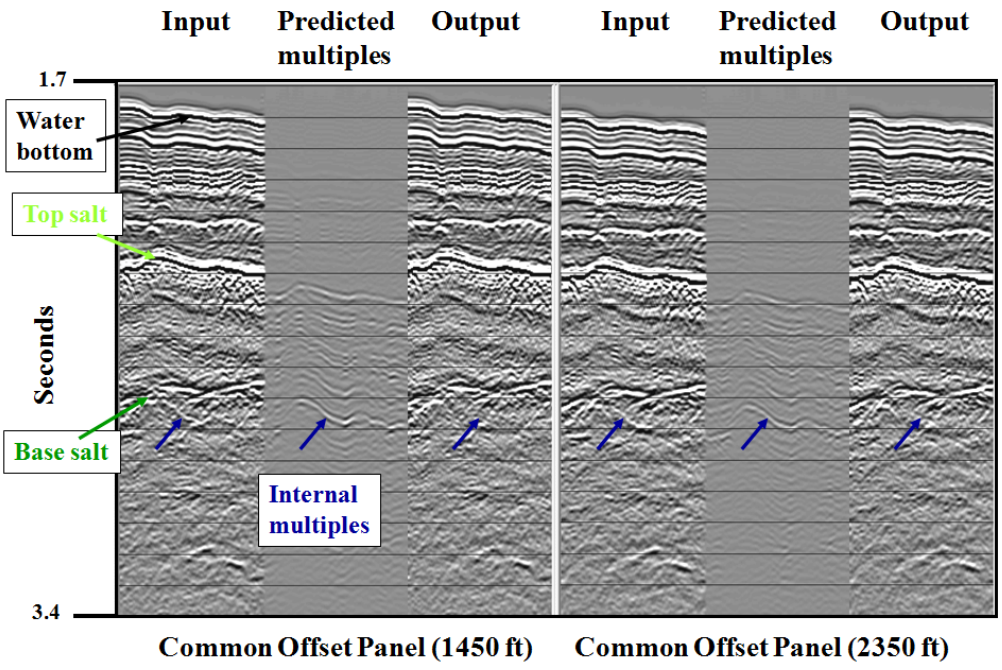

(b)

Figure 6: (a)The left panel is a stack of a field data set from the Gulf of Mexico. The right panel is the result of ISS free surface multiple removal. (b)The ISS internal multiple attenuation method applied to the same data set after free surface multiple removal. Data are courtesy of WesternGeco.

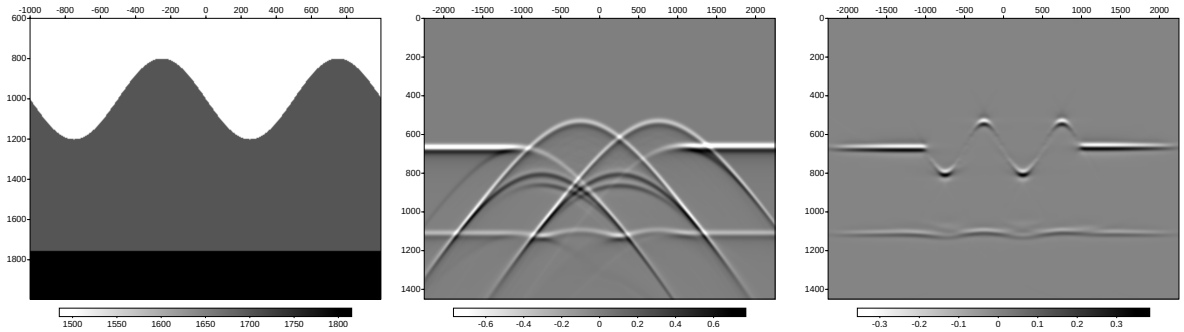

(a) (b) (c)

Figure 7: (a) Velocity model used in Example1. (b): zero offset section of the input data; (c): zero offset section of the water-speed $f-k$ migration, first order term in the ISS internal multiple algorithm.

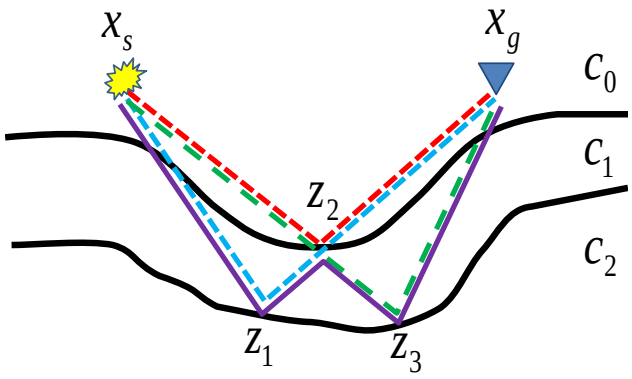

Figure 8: An internal multiple (solid blue) satisfying monotonicity in vertical time but not in total traveltime. If wave-speed c_1 is much greater than c_0, the (dashed blue) and (dashed green) primaries arrive at the surface earlier than the (dashed red) primary. The multiple is removed by the ISS method, but not by methods based on total traveltime monotonicity.

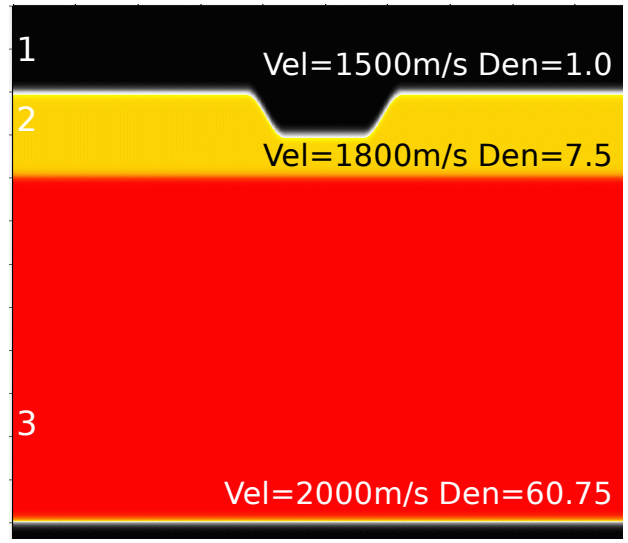

(a)

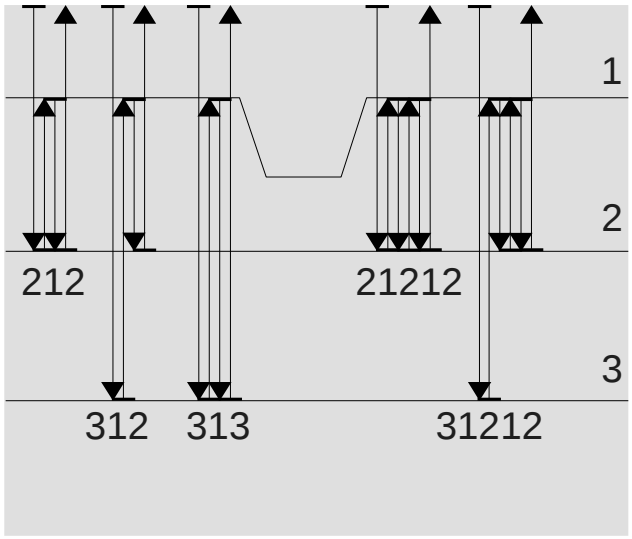

(b)

Figure 9: Earth model (a) and event labeling (b) used in example2. Densities are chosen to yield a vertical-incidence reflection coefficient of 0.8 at all layer boundaries.

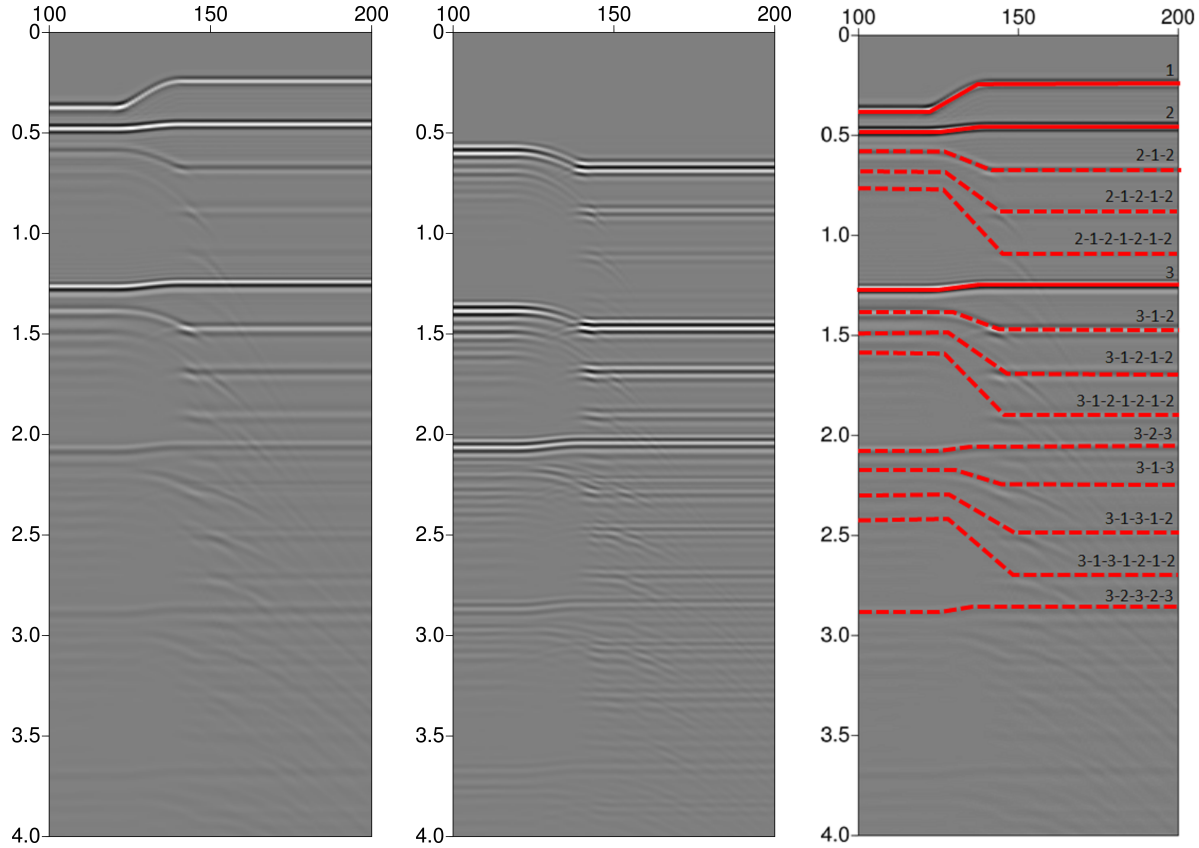

Figure 10: Zero offset sections from example2: (a) input data, (b) predicted multiples and (c) labeling of events.

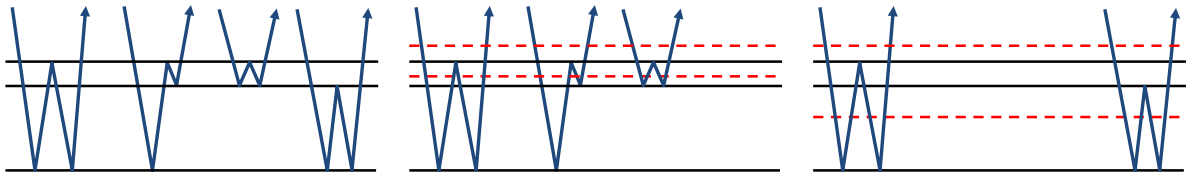

Figure 11: (a) Four types of first-order internal multiples are generated by three reflectors. (b) and (c) The first-order internal multiples predicted by the feedback layer method using different definitions of the downward generator layer (red dashed lines).